Propagation of LF and VLF waves and their use for monitoring space weather events

Dissertation
in fulfilment of the requirements for the degree "Dr. rer. nat."
of the Faculty of Mathematics and Natural Sciences
at Kiel University
submitted by

Daniela Banyś

13 November 2017

Daniela Banyś

German Aerospace Center (DLR)
Institute for Communications and Navigation
Kalkhorstweg 53, 17235 Neustrelitz
Germany

Supervisor: Prof. Dr. Bernd Heber
2. Reviewer: Prof. Dr. Christoph Jacobi

Date of disputation: 13 November 2017

This dissertation is dedicated to my brother, David Wenzel,
for his constant support and encouragement.

Zusammenfassung

Lang- und Längstwellen (in Englisch: LF – low frequencies, VLF – very low frequencies) bezeichnen elektromagnetische Wellen mit einer Wellenlänge von ca. 1 bis 100 km und liegen dementsprechend in einem Frequenzbereich zwischen 3 und 300 kHz. Ihre Signalausbreitung ist maßgeblich bestimmt durch den Zustand der Ionosphäre. Nur durch die dort vorherrschende elektrische Leitfähigkeit ist es möglich, die niederfrequenten Signale starker Sender auf der gesamten Erde zu empfangen. Somit bergen VLF-Messungen nützliche Informationen über die Ionosphäre, insbesondere über deren Unterkante, der D-Schicht in 60 bis 90 km Höhe.

Die Ionosphäre ist täglichen und jahreszeitlichen Änderungen unterworfen. Sie zeigt zudem geographische Abhängigkeiten, die größtenteils auf den Einfluss der Sonne zurückzuführen sind. Vor allem solare Strahlung im extrem ultravioletten (EUV) und Röntgenbereich bestimmt die Elektronendichteverteilung in der Ionosphäre. Somit bewirken insbesondere irreguläre Ereignisse im Röntgenbereich wie Sonneneruptionen (sog. solare Flares) eine abrupte Erhöhung der Ionisation der D-Schicht und verändern infolgedessen die Ausbreitungseigenschaften von VLF-Signalen auf der Tagseite der Erde. Dies äußert sich in einer signifikanten Änderung von Amplitude und Phase. Starke Ereignisse können bestimmte Signale sogar kurzzeitig auslöschen und so zu einem Signalverlust führen.

Diese Arbeit soll die Machbarkeit der bodengestützten Bereitstellung von Flareinformationen mittels VLF-Signalen zeigen. Es wurde ein Algorithmus zur echtzeitnahen Anwendung entwickelt, welcher direkte Störungen in der unteren Ionosphäre aus den Messungen zu extrahieren vermag. Die 24-Stunden-Überwachung erfolgt durch eine Reihe von VLF-Empfängern, die eigenhändig im Verlauf der Arbeit in den mittleren nördlichen Breiten installiert wurden. Dieses Netzwerk aus Empfängern ist Teil des DLR-Projekts GIFDS (Global Ionospheric Flare Detection System). Die Messtechnik wird fortlaufend weiterentwickelt und muss für jeden Messort an die jeweiligen Empfangsbedingungen angepasst werden. Nach systematischer Analyse der Messdaten der verschiedenen VLF-Signale können über geeignete Vorverarbeitung und Kalibrierung zueinander vergleichbare relative Änderungen bestimmt werden. Empirische Studien zeigen, dass die Signalamplituden im VLF-Bereich die erhöhte solare Röntgenstrahlung widerspiegeln. Nach Korrektur der jährlichen Schwankungen wird dieser Zusammenhang noch deutlicher.

Da die empirische Analyse die zugrunde liegenden ionosphärischen Prozesse nicht vollständig abbilden kann, wurden die Messungen an einem klar definierten Beispiel rekonstruiert. Hierfür wurde die 2015er Sonnenfinsternis über Europa ausgewählt. Dazu wurden die Elektronendichteprofile abhängig von der prozentualen Sonneneinstrahlung modelliert und die Wellenausbreitung im Sinne der Modentheorie simuliert. Die Ergebnisse zeigen neben der Sonneneinstrahlung eine deutliche Abhängigkeit der empfangenen Amplitude von Sendefrequenz, Sendeleistung und Entfernung zum Sender. Die aus der Modellierung gewonnenen Daten sind konsistent mit den Messwerten zur Sonnenfinsternis. Ebenso konnte unter Verwendung zusätzlicher Daten über die Gesamtelektronenzahl (TEC, total electron content) und von Ionosondenmessungen die verzögerte Reaktion der über der D-Schicht liegenden Regionen bestätigt werden. Erste Ergebnisse zu VLF-Messungen zeigen großes Potential für das Verständnis von Kopplungsprozessen.

Abstract

Electromagnetic waves with wavelengths from 1 to 100 km, or correspondingly in the frequency range between 3 and 300 kHz, are denoted by low frequencies (LF) and very low frequencies (VLF). Their signal propagation is determined significantly by the state of the ionosphere. Only because of its predominating electrical conductivity it is possible to receive (V)LF signals of powerful transmitters on the whole globe. Hence, VLF and LF measurements contain useful information about the ionosphere, in particular about its bottomside, the D layer in $60 - 90$ km altitude.

The ionosphere is subject to diurnal and seasonal variations. Moreover, there are geographic dependencies, which are in general ascribed to influences of the Sun. Primarily, extreme ultraviolet (EUV) and X-ray radiation determine the electron density distribution of the ionosphere. Therefore, especially irregular events visible in the X-ray range, e.g. solar flares, can cause a sudden enhancement of the D-region ionisation, and as a result, change the propagation characteristics of VLF signals on the dayside Earth. This manifests in significantly changing amplitudes and phases of propagating signals. Severe events can even interrupt specific signals and can cause a loss of lock.

The aim of this thesis is to show the feasibility of a ground-based supply of flare information using VLF observations. Based on such measurements, an algorithm for realtime application has been developed, which is able to detect immediate disturbances in the lower ionosphere. The 24-hour monitoring is the result of combining a couple of VLF receivers, which have been installed in the northern mid-latitudes during the course of this work by myself. This receiver network is part of the internal DLR project GIFDS (Global Ionospheric Flare Detection System). The measuring technique is developed further continuously and has to be adjusted to the respective receiving conditions for every new measuring site. After a systematic analysis of the data of different VLF signals, comparable relative changes can be determined via appropriate preprocessing and calibration. Empirical studies show that the VLF signal amplitude is strongly correlated with the enhanced solar X-ray radiation. After correcting annual variations, the correlation could be increased further.

Since the empirical analysis doesn't picture the actual ionospheric processes, the measurements have been reconstructed on the basis of a clearly defined example, the solar eclipse in 2015 over Europe. Therefore, the electron density profiles have been modelled in dependence of the percentage of solar irradiation, and the wave propagation has been simulated according to the mode theory. The results show, besides by solar illumination, the received amplitude is significantly determined by transmitter frequency and power, as well as the distance to the receiver. The obtained modelling results are shown to be consistent with the measurements taken during the solar eclipse. Furthermore, using additional data on the total electron content (TEC) and ionosonde observations, the delayed reaction of the layers above the D region has been confirmed. First results indicate a high potential of VLF measurements for the understanding of coupling processes.

Contents

List of Tables

List of Figures

Listings

List of abbreviations

Abbreviation	Complete expression
ADC	Analogue/Digital Converter
AGW	Atmospheric Gravity Waves
AM	Amplitude Modulation
BC	Broadcast
BOS	GIFDS receiving station in Boston
CME	Coronal Mass Ejection
CW	Continuous Wave modulation
DGPS	Differential GPS
DLR	Deutsches Zentrum für Luft- und Raumfahrt
DSP	Digital Signal Processing
EFR	Europäische Funk-Rundsteuerung
ELF	Extreme Low Frequency
ERP	Effective Radiated Power
ESP	EUV SpectroPhotometer
EUV	Extreme Ultraviolet
EUVS	EUV Sensor
EVE	Extreme Ultraviolet Variability Experiment
FFT	Fast Fourier Transformation
FPGA	Field-Programmable Gate Array
FSK	Frequency-Shift Keying
GLE	Ground-Level Enhancement
GNSS	Global Navigation Satellite System
GOES	Geostationary Operational Environmental Satellite
GPS	Global Postitioning System
HF	High Frequency
IGS	International GNSS Service
IHY	International Heliophysical Year
IMPC	Ionospheric Monitoring and Prediction Center
IP	Internet Protocol
KRK	GIFDS receiving station in Krakow
LASP	Laboratory for Atmospheric and Space Physics
LF	Low Frequency
LORAN	Long range navigation
LWPC	Long-Wavelength Propagation Capability
LWPM	Long-Wave Propagation Model
MEGS	Multiple EUV Grating Spectrographs
MF	Medium Frequency
MSK	Minimum-Shift Keying

Abbreviation	Complete expression
MUF	Maximum Usable Frequency
NASA	National Aeronautics and Space Administration
NCEI	National Centers for Environmental Information (formerly the NGDC)
NGDC	National Geophysical Data Center
NOAA	National Oceanic and Atmospheric Administration
NTCM	Neustrelitz TEC Model
NTZ	GIFDS receiving station in Neustrelitz
PCA	Polar Cap Absorption
REP	Relativistic Electron Precipitation
R_x	Receiver
SDA	Sudden Decrease of Atmospherics
SDO	Solar Dynamic Observatory
SDR	Software-Defined Radio
SEA	Sudden enhancement of Atmospherics
SFD	Sudden Frequency Deviation
SHF	Super High Frequency
STA	GIFDS receiving station in Stanford
SID	Sudden Ionospheric Disturbances
SILSO	Sunspot Index and Long-term Solar Observations
SITEC	Sudden Increase in Total Electron Content
SPA	Sudden Phase Anomaly
SPE	Solar Proton Events
SWACI	Space Weather Application Center - Ionosphere
SWF	Shortwave fadeout
TCP	Transmission Control Protocol
TEC	Total Electron Content
TID	Travelling Ionospheric Disturbances
TWN	GIFDS receiving station in Taiwan
T_x Transmitter	
UHF	Ultra High Frequency
UTC	Universal Time Coordinated
VHF	Very High Frequency
VLF	Very Low Frequency
VTEC	Vertical TEC

List of symbols

In this thesis, there is a number of various quantities used mainly based on SI units. In order to obtain a clear overview, the list of symbols is structured according to their main field.

Fundamental quantities and general symbols

Symbol	meaning	value/unit
c	Speed of light in free space	$\approx 299,800\,\mathrm{km/s}$
e	Elementary charge	$\approx 1.602 \cdot 10^{-19}$ C
h	Height	[km]
k_B	Boltzmann's constant	$\approx 1.381 \cdot 10^{-23}\,\mathrm{J/K}$
m_e	Rest mass of an electron	$\approx 9.109 \cdot 10^{-31}\,\mathrm{kg}$
T	Temperature	[K]
t	Time	[s]
ε_0	Permittivity of free space	$= 8.854 \cdot 10^{-12}\mathrm{F/m}$
μ_0	Permeability of free space	$= 4\pi \cdot 10^{-7}\mathrm{H/m}$

Solar symbols

Symbol	meaning	unit
b	Brilliance bandwidth	[nm]
$F10.7$	Solar radio flux at 10.7 cm	[sfu]
F_{EUV}	EUV flux	[$\mathrm{Wm^{-2}}$]
F_{HXR}	Hard X-ray flux	[$\mathrm{Wm^{-2}}$]
F_{SXR}	Soft X-ray flux	[$\mathrm{Wm^{-2}}$]
f_s	Total sunspot number	
g_s	Total number of sunspot groups	
I_s	Energy flux	
k_s	Factor of sunspot measuring site	
R_s	Relative sunspot number	
S	Solar constant	[$\mathrm{Wm^{-2}}$]

Atmosphere and Ionosphere symbols

Symbol	meaning	unit
d	Term of transport-induced density change	
foE	Plasma frequency of the E layer	
$foF1$	Plasma frequency of the F1 layer	
$foF2$	Plasma frequency of the F2 layer	
g	Acceleration due to gravity	[$\mathrm{m/s^2}$]
H_p	Pressure scale height	[m]
$hmF2$	Peak density height of the F2 layer	

Symbol	meaning	unit
L	Loss term by destruction	
m	Mean molecular mass	
m_i	Rest mass of an ion	[kg]
N	Electron density	[electrons/m^3]
$NmF2$	Peak electron density	[electrons/m^3]
q	Rate of electron / ion production	
$STEC$	Slant total electron content	$[TECU]$
$VTEC$	Vertical total electron content	$[TECU]$
α	Recombination coefficient	[cm^3/s]
α_e	Electron-ion recombination coefficient	[cm^3/s]
α_{eff}	Effective recombination coefficient	[cm^3/s]
α_i	Ion-ion recombination coefficient	[cm^3/s]
θ	Solar zenith angle	[°]
λ_r	Ratio of negative ion and free electron concentration	
ρ_{air}	Atmospheric density	
ρ_0	Ground level density	
σ_m	Mass absorption coefficient	
τ	Slab thickness	

Wave and propagation symbols

Symbol	meaning	unit
B	Magnetic flux density	[T = (V · s)/m^2]
B_0	Homogeneous magnetic field	
D	Dielectric displacement	[C/m^2]
E	Electric field	[V/m]
f	Frequency	[Hz]
f_N	Plasma frequency	
H	Magnetic field	[A/m]
$H_0^{(2)}$	Hankel function of the second kind	
h'	Reference height of the N_e-profile	
I	Current	
I_a	Average current	
J	Electric current density	[A/m^2]
J_0	Bessel function of the first kind	
k	$2\pi/\lambda$, Wave number	
n	$\mu - i\chi$, Complex refractive index	
n	Multiple of a wavelength	
R	Reflection coefficient	
v	Signal velocity	

Symbol	meaning	unit
X	$(\omega_N/\omega)^2$	
Y	ω_H/ω	
Y_L	Longitudinal component of Y	
Y_T	Transverse component of Y	
Y_0	Bessel function of the second kind	
Z	ν/ω	
β	Sharpness /slope of the N-profile	[km^{-1}]
β_n	Angle between ray and z-axis	
ε	Permittivity	[F/m]
η	Wave impedance	[Ω]
κ	Absorption	[m^{-1}]
λ	Wavelength	[m]
μ	c/v, Real refractive index	
ν	Collision frequency	[collisions/s]
ν_e	Electron-neutral collision frequency	[collisions/s]
$\nu_\pm$	Ion-neutral collision frequency	[collisions/s]
ρ	Volume charge density	
χ	Imaginary part of n	
ω	Angular wave frequency	[rad/s]
ω_N	Angular plasma frequency	[rad/s]
ω_H	Angular gyro frequency	[rad/s]
ω_r	Conductivity parameter	

Other symbols

Symbol	meaning	unit
a^k	Slope of the linear transformation for path k	
A	VLF signal amplitude	[dB]
b^k	y Intersept of the linear transformation for path k	
f_c	Center frequency	
f_m	Bandwidth / Modulation rate	
G	Geomagnetic activity switch	
M	Approached, „modelled“ VLF signal amplitude	[dB]
m_a	Month of the corresponding year	
p_0^k, p_1^k, p_2^k	Parameters of quadratic polynomial regression	
r	Pearson correlation coefficient	
γ	Weighting function of the GIFDS algorithm	
σ	Standard deviation	
φ	Geographic latitude	[°]
ψ	$2\pi(m_a - 0.5)/12$, Seasonal parameter	

„Doubt is the father of invention.“
Galileo Galilei

1

Motivation and objectives

The term *space weather* refers to solar processes as well as varying conditions in the solar wind, the Earth's magnetosphere, ionosphere and thermosphere that may affect space- and ground-based technological systems in their performance and reliability. They can even have an impact on human health. The main source for space weather is the Sun, featuring a large variety of inherent phenomena, i.a., flares, coronal mass ejections, and radio bursts. *Solar flares* are outbursts of electromagnetic radiation primarily in the wavelength range of extreme ultraviolet (EUV) and X-ray. Within a short period of time, such events can cause an enhanced ionisation of the Earth's upper atmosphere – the *ionosphere*. Radio signals passing through the ionosphere can experience reflection, refraction, scattering, and even absorption. So, solar flares can disturb communication and navigation signals, as provided by Global Navigation Satellite Systems (GNSS) such as the United States GPS, the Russian GLONASS, the European Galileo system, and COMPASS from China. Although dual frequency signals allow compensating ionospheric first-order effects, position information still may get inaccurate during strong solar activity. With growing interest in the usage of such satellite systems, especially GNSS applications demand information on accuracy and reliability.

DLR's Ionosphere Monitoring and Prediction Center (IMPC, http://impc.dlr.de/) offers nowcast and forecast services on the state of the ionosphere as well as alerts on space-weather-related issues. Thanks to the project SWACI (Space Weather Application Center - Ionosphere, http://swaciweb.dlr.de/), which has been essentially supported by the state government of Mecklenburg-Vorpommern, IMPC benefits from the historical data archive of the total electron content (TEC) over Europe covering more than twenty years allows the investigation of space weather effects over two full solar cycles. While a permanent monitor of the overall electron density via GNSS measurements is well established, there is only limited information on radio signals of lower frequencies (i.e., VLF to HF bands) propagating within the boundaries of the ground and the ionosphere. For this reason, the DLR establishes the Global Ionospheric Flare Detection System (GIFDS) supplementing the existing services of the IMPC.

GIFDS is a ground-based flare detection system evaluating measurements of VLF signals propagating within the Earth-ionosphere waveguide. The latter is determined by the Earth as the ground plane and the lower part of the ionosphere – the *D region*. Solar flares emit X-rays, which increase the ionisation of the D region. Hence, trans-ionospheric radio signals experience absorption, whereas VLF signals can be even enhanced. Although rocket measurements would be very precise, they provide just a rather limited snapshot, temporally as well as locally. Also common ionosondes cannot be used for studying the D region, because their measuring accuracy isn't sufficient for the associated height. Luckily, VLF measurements provide the required resolution in height. Such signals are almost completely reflected by the D layer, offering high accuracy, too. As a result, a systematic utilisation of VLF data unveils valuable information on the lower ionosphere, and therewith, the response on the enhanced X-ray radiation during solar flares.

When a flare hits the Earth, only the dayside ionosphere is affected. This leads to changed propagation conditions of sunlit radio paths. In order to constitute a specialised monitoring service for ground-based flare detection, the installation of a world-spanning VLF network is needed to continuously picture the dayside lower ionosphere. In this way, VLF measurements can be used to monitor space weather related X-ray effects. The currently five receiving stations are the core of the GIFDS system.

Based on a general analysis of received VLF signals, a flare detection algorithm has to be developed and implemented so that it can operate near real time. The dayside lower ionosphere provides a certain image of solar flare effects. Such *sudden ionospheric disturbances* (SIDs) are marked by a significant increase or decrease in VLF amplitude as well as in phase. Assuming the ionospheric height as the only variable in a waveguide model, a flare that lowers the reflection height of VLF signals is usually indicated by a phase advance. However, depending on the different ionospheric conditions, the actual impact on VLF phase and certainly VLF amplitude may vary. For estimating the interrelation of solar X-ray flare and ionospheric response, comparative studies with solar X-ray flux measurements provided by the Geostationary Operational Environmental Satellite (GOES) are done. Since the Earth's atmosphere absorbs X-ray radiation, for users of the broad radio spectrum from VLF to HF bands, the resulting ionospheric response is more essential than the original solar flux level. Nevertheless, strong links between solar X-ray measurements and ground-based VLF amplitude data exist. As the connection is still somehow

fluent, several adjustments have to be made for increasing this correlation. Therewith, original solar information can be deduced via VLF measurements and a flare detection algorithm can be proposed.

The verification of alerts released by the proposed GIFDS algorithm raises questions about the physical processes. Via modelling VLF propagation within the Earth-ionosphere waveguide, recombination processes in the ionosphere can be reconstructed. For validating the network, the proposed electron density model is examined so that performed measurements and simulated VLF propagation fit together. For this, the solar eclipse on 20 March 2015 covering Northern Europe is used. It provides a unique insight in drastically changing ionospheric conditions that are nevertheless well-defined. During this event, the ionosphere's reflection height varies by several kilometres. In a similar but rather turbulent process, a solar flare influences the ionosphere in the opposite direction. Yet, the impact of a solar eclipse is not as volatile, allowing direct gradual comparisons for different propagation paths of specific obscuration conditions.

In consequence, studying VLF signals and their propagation will unveil lots of potential for monitoring the D-region ionosphere. As solar flares change the propagation conditions of VLF signals, one can derive information on these space weather events. By implementing a VLF-based flare detection in near real-time, the GIFDS system should be able to operate complementary to other space-based warning system like GOES. Therefore, VLF measurements will not only help documenting the D region but also can turn out to be essential for a comprehensive view of the ionosphere and its short-term disturbances. Furthermore, the ground-based measurements provide fundamental information on coupling processes between the middle atmosphere and the thermosphere-ionosphere system.

„[T]he history of science has proved that fundamental research is the lifeblood of individual progress and that the ideas that lead to spectacular advances spring from it.“
Sir Edward Appleton

2

Physical background

The considered very low frequency (VLF, $3 - 30\,\mathrm{kHz}$) and partially low frequency (LF, $30 - 300\,\mathrm{kHz}$) signals may propagate over the whole globe and contain valuable information about the lower ionosphere, which is influenced by space weather and solar irradiation, in particular. The physical background of these processes is given in this chapter. At first, general information about the Sun and its emissions are given. Also, the generation of solar disturbances such as solar flares is described. Of major interest is their impact on the Earth. The main source of atmospheric ionisation is extreme ultraviolet and X-ray radiation coming from the Sun. Therefore, the formation and composition of the ionospheric layers is detailed in section 2.2, and the temporal and spatial variations are explained, together with the ionospheric response during solar events.

Without the reflecting ionosphere, the long distance propagation of radio waves along Earth's curved surface wouldn't be possible. Radio signals would move into space without reaching beyond the horizon. The theory of radio wave propagation is presented in section 2.3, comprising the ionosphere's refractive index introduced by Lassen, Appleton, and Hartree, as well as two approaches of VLF radio wave propagation: the ray (wave-hop) theory and the mode theory. Advantages and disadvantages of both theories are briefly summarised.

2.1 The Sun

In our solar system, the Sun is the most powerful source of energy and provides the base for life on Earth. As our central star heavily influences its surrounding, it is the main engine for the space weather that we are interested in. For an insight into the occurring processes, an overview of physical relations of the Sun as well as a classification of solar events will be introduced in this chapter. In particular, the solar irradiation is addressed with an emphasis on X-rays and extreme ultraviolet (EUV). For a more detailed description of the general physics and the spectrum of the Sun, the reader is referred to Davies (1990), Hanslmeier (2002), Prölss (2003), Schunk and Nagy (2004), Scherer et al. (2005), Bothmer and Daglis (2007), and Moldwin (2010).

2.1.1 Solar irradiation

The Sun is a G-type main-sequence star with a mass of $1.99 \cdot 10^{30}$ kg and a radius of 696,000 km (i.e., 109 times the radius of the Earth). It consists mostly of hydrogen (92.1 %) and helium (7.8 %), with minor portions of oxygen (0.06 %), carbon (0.03 %) and other elements, especially heavy metals (Davies, 1990). The center of the solar system keeps together the planets and further affects its environment primarily in form of electromagnetic radiation. The interior of the Sun can be divided into several spherical layers, see Fig. 1. By nuclear fusion, hydrogen is converted into helium in the Sun's core (occupying about a fourth solar radii). This produces energy (hence, temperatures of 10 million K come across), which propagates outwards by radiative diffusion. As the huge radiation zone is very dense, photons are absorbed and re-emitted again and again, over a long period of time (approximately 100,000 - 200,000 years) until they reach the next layer (depicted in the schematic diagram of Fig. 1). In contrast, in the adjacent 200,000 km-wide zone, energy is transferred much faster by convection. This so-called convective zone is very complex and causes the Sun's turbulent magnetic field. The strong convection flows inside form granules. These are even visible on the solar disk, which has an apparently sharp contour because of a strong density decrease within only a few hundred kilometres of the adjacent sphere.

The solar atmosphere reaches into space up to a distance of 10 solar radii. It is divided into the photosphere, the chromosphere, and the corona. The photosphere emits visible radiation and has a temperature of about 6000 K (close to the convective zone) down to 4500 K (at the outer boundary). The chromosphere still belongs to the inner atmosphere. With a width of merely 4000 km, the thin layer is characterised by a rapid temperature increase up to 25,000 K. The vast outer atmosphere, the corona, holds hot ionised plasma. The tenuous region is characterised by approximately one million K (Bothmer and Daglis, 2007; Schunk and Nagy, 2004). The reasons behind are not yet completely understood. In radial direction, the plasma is flowing away from the Sun due to the high temperatures in the corona. Depending on the magnetic field lines, the solar wind can be highly inhomogeneous. Especially coronal holes are characterised by open magnetic fields and are sources of increased solar wind. The typical solar wind speed is about several hundred km/s. However, in storm periods, it can increase to about 1000 km/s. Plasma from eruptive events (like solar flares, coronal mass ejections or eruptive prominences) is faster than the ambient solar wind. Overtaking the plasma, this forms a shock front (Davies, 1990).

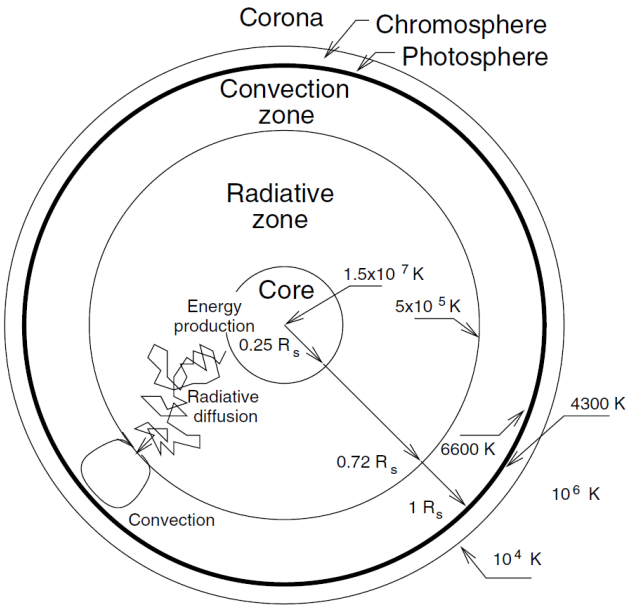

Figure 1: Schematic illustration of the Sun's structure. [taken from Koskinen (2011)]

While the corona with its events is highly variable, the total solar irradiance at the distance of the Earth (1 AU), measured over all wavelengths, remains approximately constant with

$$S = 1367 \pm 3\,\mathrm{Wm}^{-2}, \tag{1}$$

which is known as *solar constant*.[1] Thus, the total radiated power of the Sun, i.e. its luminosity, amounts to $3.8 \cdot 10^{26}$ W. Most of the electromagnetic energy is emitted in the infrared part of the spectrum (52 %), as visible light (41 %), or as ultraviolet radiation relatively steady over time. Fig. 2 shows the spectrum of solar irradiance. The photosphere has an effective temperature of 5762 K and its spectrum (covering the optical, infrared, and shorter radio wavelengths) can be well described by the one of a black-body disk (with a radius of 6.96×10^5 km) at this temperature. Optical emissions are mainly produced in the photosphere. However, during a total solar eclipse, we can also experience some visible light in the corona. Note that in the outer atmosphere the black-body model is no longer appropriate.

The overall picture given in Fig. 2 hides the fact that, for very long and very short wavelengths, the solar irradiance is highly variable. The whole spectrum (extending from gamma-rays to radio waves) is shown in more detail in Fig. 3. In the radio wavelength range (displayed at the right part of the diagram), several other mechanisms produce emissions that cause a differing spectrum (e.g., high-relativistic electrons during flares, free-free emissions of flares and active regions, several kinetic plasma instabilities). In contrast, the steady emissions in the infrared range originate in the quiescent, cooler gas, as it is typical for supergranules and sunspot regions. Optical emissions constitute the peak solar flux and are mainly produced in the photosphere. Furthermore, there are minor contributions to the solar spectrum at shorter wavelengths (i.e.,

[1] The value given in (1) is the current approximation, which is due to Koskinen (2011). Another publication, Kopp and Lean (2011), determined the significantly lower constant $S = 1360.8 \pm 0.5\,\mathrm{Wm}^{-2}$ for the solar minimum in 2008. First estimates to S were made by Pouillet (1838), who specified a *quantity of heat* corresponding to $S = 1228\,\mathrm{Wm}^{-2}$.

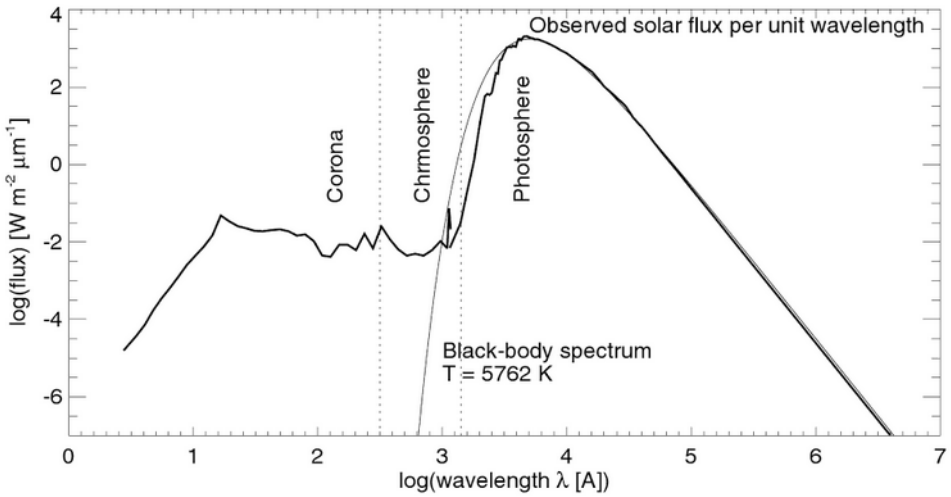

Figure 2: Spectrum of solar irradiance in comparison to a black-body spectrum at a temperature of about 5800 K. [taken from Aschwanden (2004)]

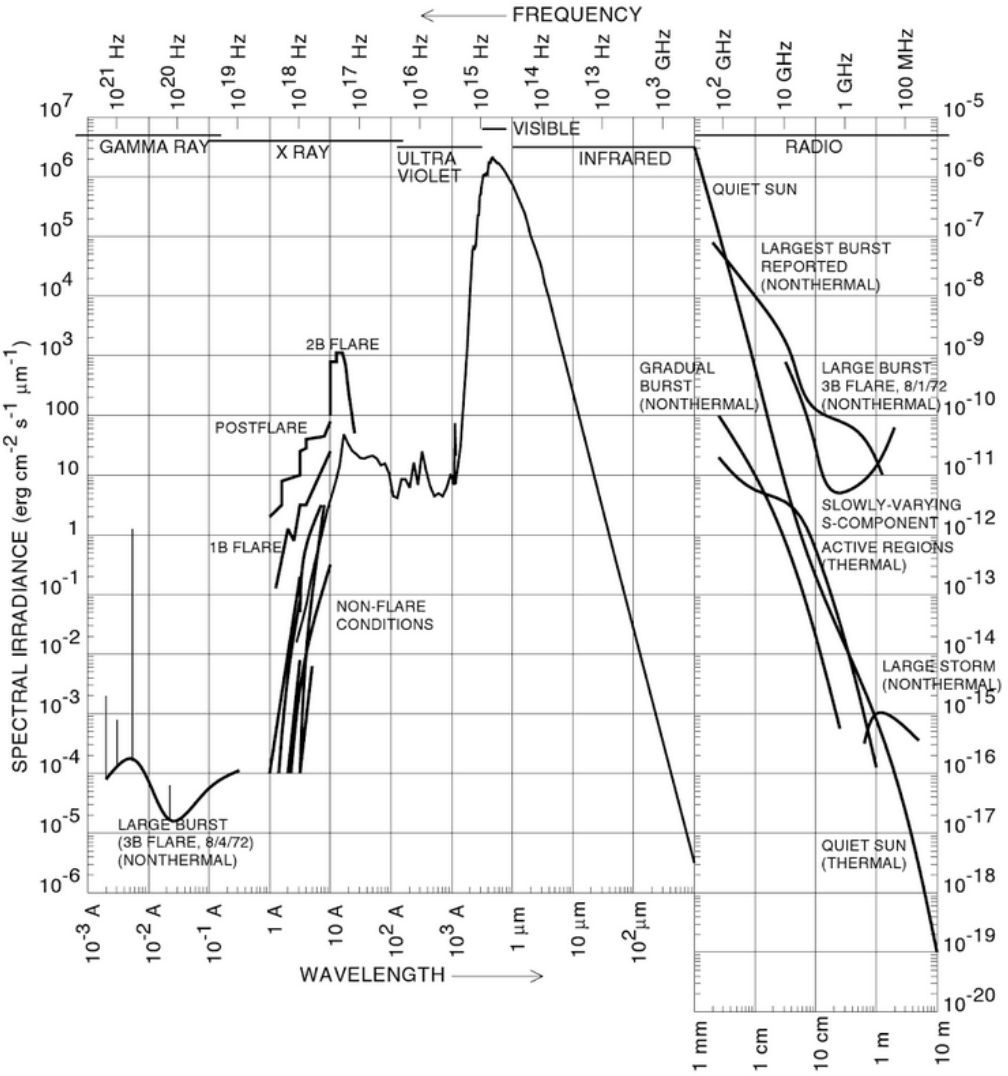

Figure 3: Full spectrum of solar irradiance. [taken from Aschwanden (2004)]

EUV, X-ray, and gamma-ray emissions, presented left in the diagram of Fig. 3). These are subject to large fluctuations.

Gamma rays are produced during flares from nuclear processes in the chromosphere, in interaction with high-energetic particles precipitating from the corona. The solar Bremsstrahlung occurs at different wavelengths, depending on the original energies of the colliding particles. Hard X-rays are generated by nonthermal mildly relativistic electron collisions in the chromosphere. Soft X-rays originate in active regions and flare loops where free-free emissions of electrons are scattered by highly-ionised ions in the corona. EUV emissions are produced similarly to soft X-rays scattered by lower temperature ions. But this part of the spectrum is also emitted continuously by the quiet Sun. Although EUV radiation consumes only 0.1 % of the solar energy, it has a strong effect on the Earth's atmosphere and is the main source of ionospheric plasma, together with X-ray radiation (Schunk and Nagy, 2004). Special high energetic events like solar flares are explained in more detail in section 2.1.3.

2.1.2 The solar cycle

In average, the Sun rotates with a period of 27 days. As the Sun is composed of gaseous plasma, pole regions are rotating slower (about 31 days) than the equatorial region (approximately 25 days). Due to this and the convection of plasma, electric currents are generated and complex magnetic fields are induced. Moreover, the magnetic fields are subject to certain temporal variation.
Within a cycle of 22 years, the activity denotes an increase and decrease, twice, because of a mid-time reversal of the generally dipolar solar magnetic field (Schunk and Nagy, 2004).

One indication of the varying magnetic activity is the behaviour of sunspots. Sunspots are darker regions on the Sun that radiate less electromagnetic energy. Hence, they are with about 3000 K cooler than the surrounding surface with 6000 K (Davies, 1990) These regions correspond to intense magnetic fields breaking through the photosphere and are connected with solar flares and coronal mass ejections. Sunspots may last for a few hours up to even several months. So, the solar activity can be represented by the relative sunspot number

$$R_s = k_s(10g_s + f_s), \tag{2}$$

which was introduced by Wolf in 1848. Here, g_s is the total number of sunspot groups, f_s is the spot number in total, and k_s is an individual coefficient correlated with the measuring and instrument conditions for each observatory. R_s is also known as *Zürich sunspot number*.[2] It varies in an overall increase and decrease within a period of 11 years (known as the solar cycle or Schwabe cycle). So, a full cycle of the magnetic activity takes about 22 years (the Hale cycle) (Davies, 1990; Koskinen, 2011). Fig. 4 shows the sunspot number of the last solar cycles provided by the Solar Influences Data Center (SIDC, http://sidc.be, SILSO data, Royal Observatory of Belgium, Brussels). One can clearly identify the periodic behaviour superimposed by short-term fluctuations. Some solar maxima exhibit a double-peak structure, which is associated with investigations of Gnevyshev (1963).

[2] In 1947, a new counting method was introduced in Zürich. To reduce the bias, all numbers were lowered.

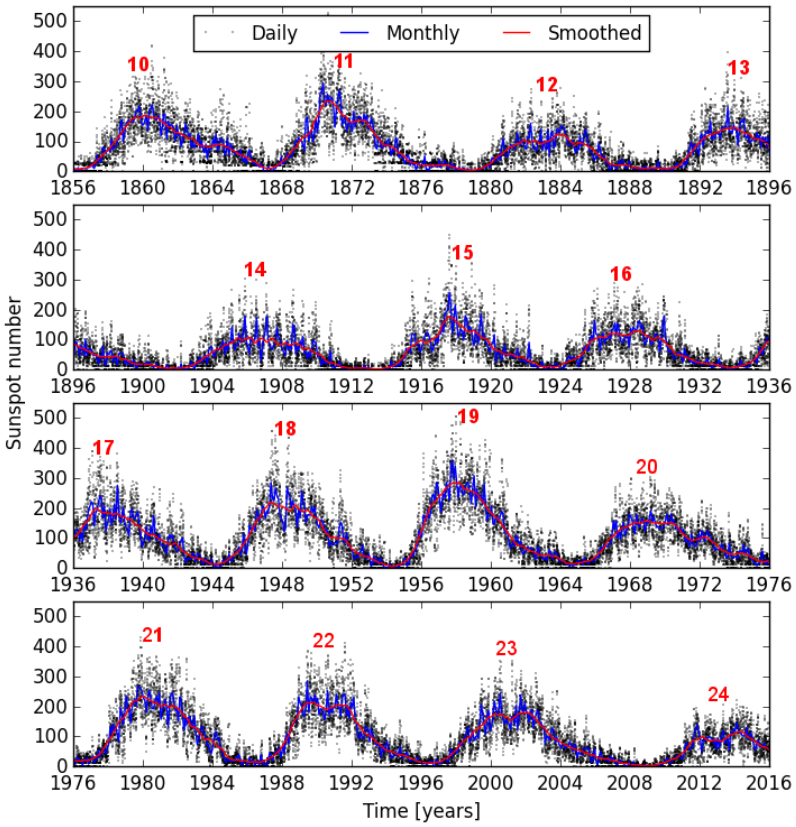

Figure 4: Total sunspot number since solar cycle 10 (data by SIDC, http://sidc.be, SILSO data, Royal Observatory of Belgium, Brussels): The different colours show the daily (black), monthly mean (blue), and 13-months smoothed (red) total sunspot number. Note that the counts follow the improved scale without factor k in (2).

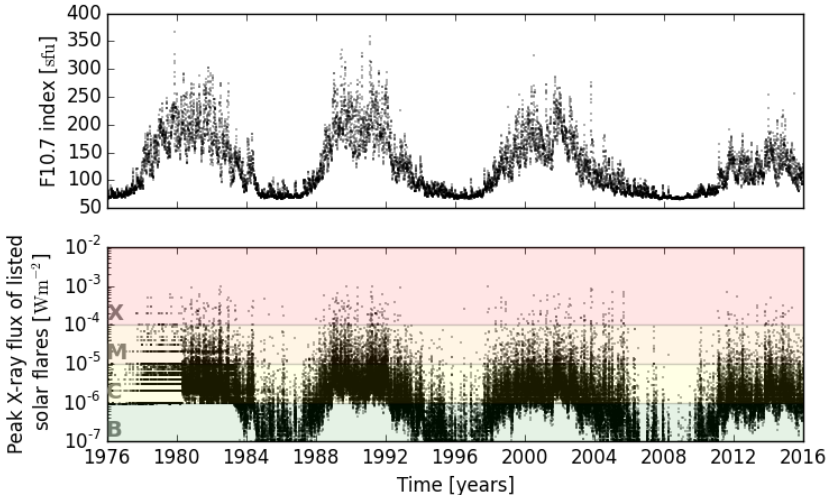

Figure 5: Solar cycle variations indicated via the F10.7 index since first X-ray measurements of the GOES satellites (data by NGDC, https://ngdc.noaa.gov/): The upper picture represents the Ottawa 10.7 cm solar radio flux in solar flux units (1sfu = $10^{-22}\mathrm{Wm}^{-2}\mathrm{Hz}^{-1}$), and the lower picture shows all flares measured by the GOES satellites. The regular-looking points at the first years are due to the chosen flare categories. More accurate classifications are done in the upcoming years.

Currently, we are in the 24th solar cycle according to the enumeration introduced by Wolf, who reconstructed the cycles back to 1755. The recent solar cycle is of less activity. The maximum sunspot number is actually the smallest since cycle 14. Nevertheless, it features a double-peak signature with the first peak in 2012 and the second one in 2014. The present activities of the Sun happen within a declining period after the maxima.

Another indicator for solar activity is the F10.7 index. As seen in the top of Fig. 5, it is in good correlation with the number of sunspots. F10.7 specifies the solar radio flux at 10.7 cm (i.e., 2800 MHz). These radio emissions are originated in the outer solar atmosphere, namely the chromosphere and lower corona. It tracks the average energy output of the Sun and represents a kind of base level behaviour, basically unaffected by abrupt changes.

Such short-term disturbances may have a large impact on the Earth's atmosphere, hence observations of solar characteristics were intensified. As one of the established systems, the GOES satellites were equipped with sensors to monitor the solar X-ray flux. The system issues warnings for flare events and classifies them according to their intensity.

The bottom image in Fig. 5 presents the detected flares since the beginning of respective X-ray measurements archived by the National Oceanic and Atmospheric Administration (NOAA), a division of the National Geophysical Data Center(NGDC, https://ngdc.noaa.gov/).[3] As one can see, the intensity of most flares follows the trend of solar activity (indicated by the sunspot number or the F10.7 index). Of course, sporadic events are significantly off-size. Even during solar minima, there may be severe events, too. They are visible as isolated points, far away from the major cluster.The background on the shortly glimpsed GOES observations will be discussed next to other attempts in section 3.2.2. The classification of solar flares and their physical interrelations are described in the following.

2.1.3 Solar flares

On 1 September 1859, Richard Carrington investigated a group of sunspots and observed a strong brightening of light close to it. He saw a white flare that was followed shortly thereafter by geomagnetic perturbations. About 18 hours later, one of the largest magnetic storms in history was observed (Scherer et al., 2005). Carrington proposed a possible causal connection (Moldwin, 2010). Current knowledge shows that an immediate effect can be seen in the enhanced ionospheric conductivity by increased EUV and X-ray radiation (Scherer et al., 2005). With a delay of one or two days, a shock front of fast plasma may overtake the ambient solar wind and possibly hit the Earth. This is what happened one-and-a-half centuries ago (Davies, 1990).

Evolution Solar Flares are radiation bursts indicated by a brightening of the Hα-line in the chromosphere (Davies, 1990). Fig. 6 illustrates the standard flare model. According to this, the evolution of flares is described by reconnection of magnetic loops. By this, energetic particles

Later, a variable drift was also compensated. The traditional factor $k_s = 0.6$ is no longer in use. The modern count is thus closer to the raw Wolf count and not adjusted to historic scales (see http://sidc.be).

[3] In 2015, NOAA's NGDC and two further data centers – the National Climatic Data Center and the National Oceanic Data Center – have merged into the National Centers for Environmental Information (NCEI). The final integration is projected for 2020.

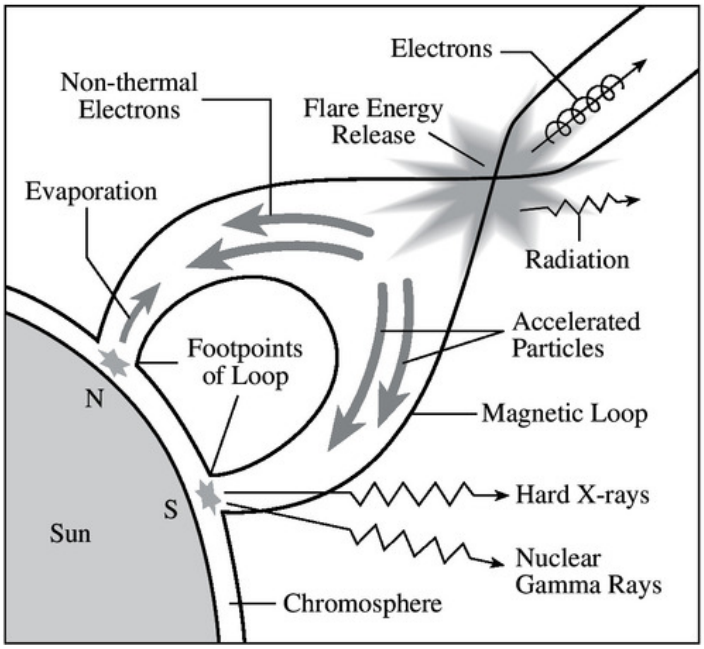

Figure 6: Standard flare model. [adapted from Lang (2009)]

(mostly non-thermal electrons) are accelerated and precipitate along the magnetic loop, down to the chromosphere. During this process radio emissions are generated. When the particles hit the chromospheric footpoints, hard X-rays and H-α are emitted. The coupling between the corona and the chromosphere causes a so-called evaporation, in which chromospheric plasma is heated, leading to a supersonic expansion into the corona and causing soft X-ray emissions.

By an explosive reconnection of the magnetic field lines in a coronal loop, electrons are accelerated up to 10^7–10^8 m/s, with energies of 10–100 keV. High-energetic particles like nuclei may even release tens or hundreds of MeV. The total power of a solar flare is about 10^{20}–10^{22} W, and it can release an energy up to 10^{25} J. The electromagnetic radiation emitted by the particles cover nearly the whole electromagnetic spectrum, ranging from radio waves to X and γ-rays (Koskinen, 2011). The radiation reaches the Earth after about 8 minutes whereas the particles may take much longer, depending on their energy.

As solar flares are often observed close to sunspots, their occurrence is correlated to the 11-years solar cycle. Recalling Figs. 4 and 5, at solar maxima we observe considerably more sunspots (i.e., active regions), and also X-ray measurements tend to feature stronger flare events. But at solar minima there are only few or even no sunspots, and the solar flare activity is very low. The general opinion is that, in the downward phase of one period of the solar cycle, more severe events happen. For instance, around the years 1984 and 2005, the points in Fig. 5 accumulate considerably above the average trend level of the cycle.

Classification The characterisation of a solar flare is non-trivial since the flare spectrum comprises several wavelengths that unveil quite different behaviour. Fig. 7 shows the course of signals exemplary for several frequency ranges as they can be observed during a typical flare.

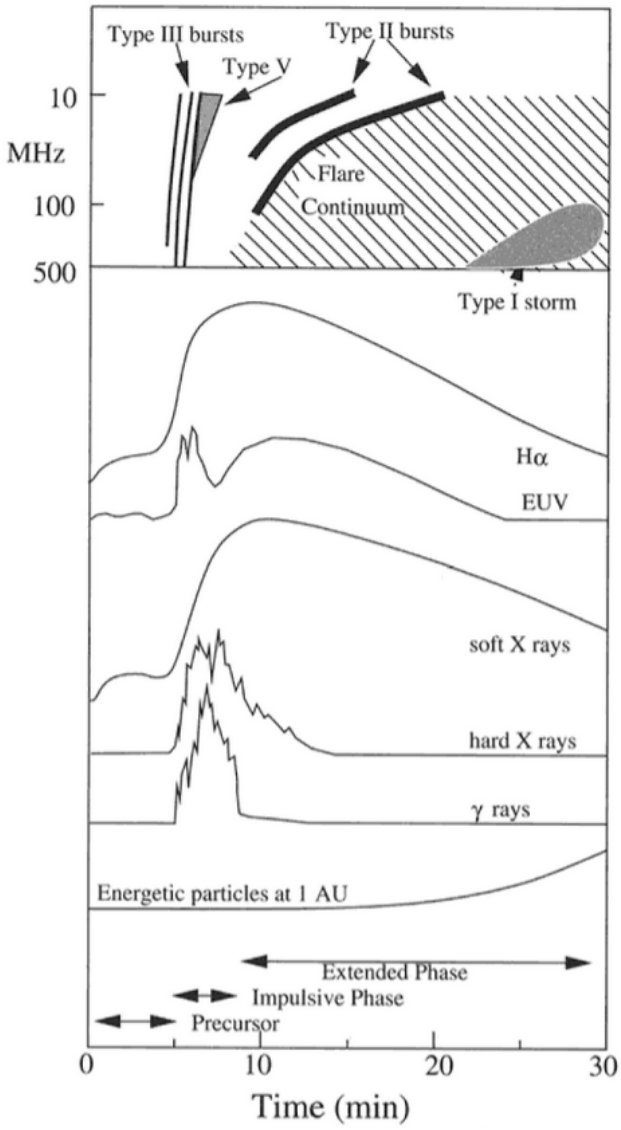

Figure 7: Observations of a flare over various wavelengths. [taken from Kallenrode (2004)]

In the wavelength range of gamma and hard X-ray, an almost immediate increase appears that returns to the base level within short time, whereas in soft X-ray and Hα the decay is very slow and takes about half an hour in the picture, which is the average duration of these events. Notable is also a much smoother progression in the latter channels. Large solar flares (such as the one observed by Carrington) can be accompanied also by a burst in white light.

Generally connected with solar flares are radio emissions that arise from the lower chromosphere via the outer corona up to several solar radii (Davies, 1990). Whereas radio bursts with wavelengths in the range to centimeters (300 – 10000 MHz) are relatively simple with a sharp increase and a slow decay, decimeter waves show a more complicated behaviour due to frequencies changing up or down during lifetime, and meter and decameter bursts (10 – 300 MHz) are rather complex. Fig. 7 moreover illustrates the variability of radio emissions during a solar flare. The burst are subdivided into different types depending on characteristics determined by their energy, frequency, origin, duration, and evolution, amongst others. The interplay of these factors is not consistently captured in the literature. For more information the reader is also referred to Stix (2004) and Lang (2009).

	Hemispheric size [°²]
S (Sub)	≤ 2.1
1	2.1 - 5.1
2	5.2 - 12.4
3	12.5 - 24.7
4	≥ 24.8

	Brilliance bandwidth [nm]
f (faint)	$0.08 < b < 0.12$
n (normal)	$0.12 < b < 0.20$
b (bright)	$0.20 < b$

	Power flux level $F_{SXR}[\mathrm{Wm}^{-2}]$
A	$10^{-8} \leq \phi < 10^{-7}$
B	$10^{-7} \leq \phi < 10^{-6}$
C	$10^{-6} \leq \phi < 10^{-5}$
M	$10^{-5} \leq \phi < 10^{-4}$
X	$10^{-4} \leq \phi$

Table 1: Classifications of solar flares according to their size and brilliance (left table), as well as, to their power flux F_{SXR} in the soft X-ray range between $0.1-0.8\,\mathrm{nm}$ (right table). [adapted from Davies (1990)]

The original definition of flares relies on Hα. Nevertheless, soft X-ray emissions exhibit a qualitatively similar behaviour. Hence, different classification schemes were developed matching to both channels. Optical flares are usually divided by their size and brilliance in the Hα line. Tab. 1 presents the categories, which consist of the two indicators. The size is measured by the area of the visual event in hemispheric square degrees (see first column), and the brilliance is given by the bandwidth (second column), which correlates with the visual brightness. The least important flares are denoted by Sf. The largest and brightest ones are assigned to 4b. As an example, the flare from 5 December 2006, responsible for the damage of the Solar X-ray Imager (SXI) onboard GOES 13, is categorised as an 2n event (see https://ngdc.noaa.gov/).

In X-ray, this flare was classified as X9 according to the data provided by the Space Weather Prediction Center (SWPC, http://www.swpc.noaa.gov/). The different notation based on the wavelength range from 0.1 to 0.8 nm is detailed in the third column of Tab. 1. Here, the main criterion is the power flux level recorded by satellites like GOES in the Earth's orbit. The alphabetic categories determining the power range are supplemented by a number detailing the precise value as a multiple of the respective lower bound (e.g., $3.5 \cdot 10^{-6}\,\mathrm{nm}$ correspond to $C3.5$).

Although the soft and hard X-ray signals have a significantly different shape, they are linked to each other. The soft X-ray flux F_{SXR} corresponds to the cumulative time integral of hard X-rays F_{HXR} during flare emissions, i.e.,

$$F_{SXR}(t) \propto \int_{t_0}^{t} F_{HXR}(t')\,\mathrm{d}t'.$$

This empirical relationship is known as the *Neupert effect*, first observed by Neupert (1968) between soft X-rays and microwave emissions. Later, the connection was found to stay valid also for hard X-rays. This implies the correlation of thermal and nonthermal emissions during flare events. So, in case of a solar flare, accelerated electrons cause hard X-ray emissions and accumulate energies, which heat the plasma and consequently emit soft X-rays. However, observational studies of many flare events show that the hot plasma (responsible for generating soft X-rays) may not be exclusively heated by hard X-rays. For this reason, it is suggested that measurements of soft X-rays yield a flare indication of more significance than hard X-rays (Veronig et al., 2002, 2005).

2.2 The Earth's ionosphere

The ionosphere is the ionised part of the Earth's atmosphere and contains less than 0.1 % of the total atmospheric mass. The main source of its ionisation is the EUV and X-ray radiation coming from the Sun. The following section provides fundamental conditions and characteristics of the ionosphere for a general understanding of our study. Various literature deals with this subject and for further information the reader is referred to Kelley (1989), Davies (1990), Hargreaves (1992), Hunsucker and Hargreaves (2003), and Schunk and Nagy (2004) .

2.2.1 Structure and composition of the upper atmosphere

The ionosphere is the upper, ionised part of the Earth's atmosphere at an altitude between about 60 and 1000 km. So, it covers the upper mesosphere, the thermosphere, and parts of the exosphere. Whereas the atmosphere is structured by the temperature profile, the ionosphere is structured by the plasma density (see Fig. 8). Mainly EUV and X-ray radiation determine the plasma production by photoionisation of neutral atoms and molecules, but also magnetospheric electric fields and particle precipitation form the ionosphere (Schunk and Nagy, 2004).

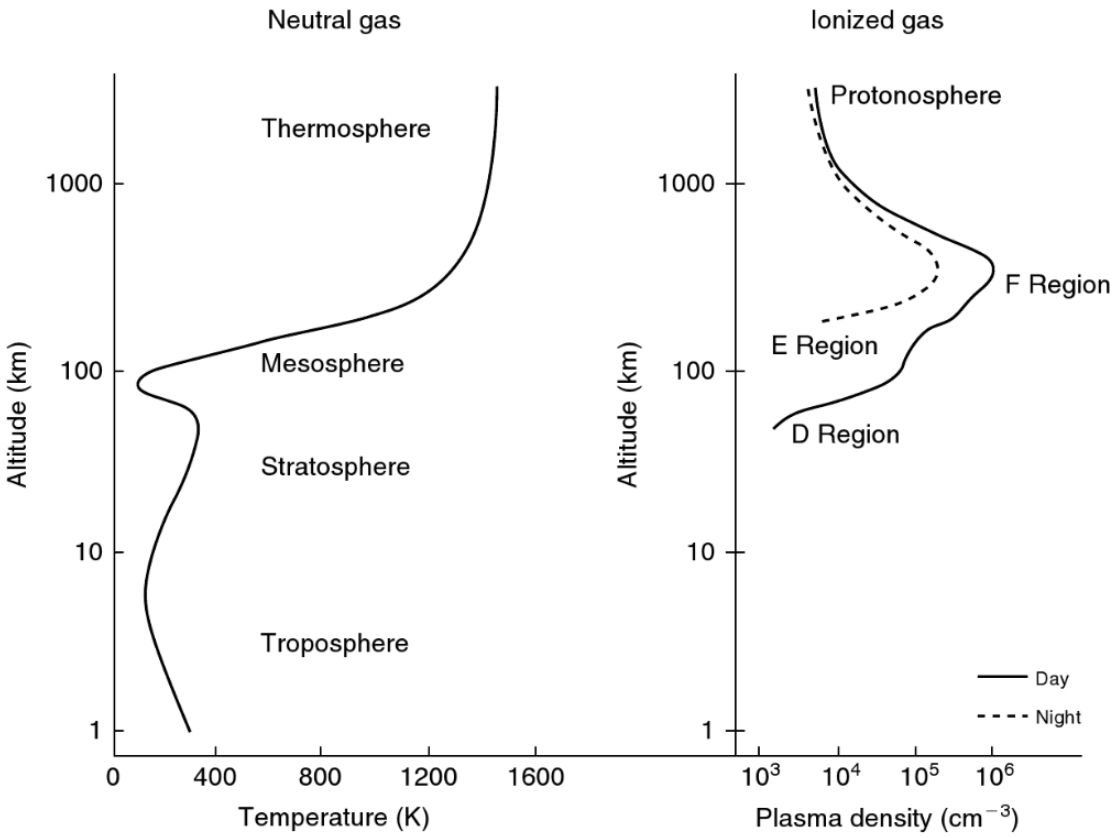

Figure 8: Atmospheric temperature and ionospheric plasma density profile. [taken from Kelley (1989)]

Different latitudes are dominated by different processes. Nevertheless, the ionosphere tends to separate into similar layers that emerge with different characteristics. They are defined by the maximum density at a certain height. Generally, the daytime ionosphere can be divided into three sperically stratified regions: the D, E, and F layers. Fig. 9 gives an overview of their basic composition and the resulting skin depth of radiation of different wavelengths. Although the regions can't be separated strictly and there are varying boundaries, the following paragraphs give a rough distribution of these layers.

The D region occupies altitudes between about 60 and 90 km. Due to the higher pressure, it exhibits more chemical constituents than the other layers. The major ions are NO^+, O_2^+, and N_2^+, although the latter is in a conversion equilibrium with O_2^+ via charge exchange ($N_2^+ + O_2 \rightarrow O_2^+ + N_2$). Minor components are heavy hydrated ions, e.g., $H^+(aq)$, $H_3 =^+ (aq)$, and $NO^+(aq)$.The D layer is mainly produced by Lyman-α radiation (121.6 nm) ionising nitric oxide NO and soft X-ray radiation (< 1 nm) ionising mostly O_2 and other gases. The ionisation potentials of basic atmospheric components are listed in Tab. 3. The D-region electron density is about 10^9 electrons/m^3, and at night the layer disappears (Davies, 1990; Dolukhanov, 1971). Hence, the D region is of special interest for our study. The process of radio wave propagation is discussed in more detail in the next section.

The E region covers altitudes from about 90 km to 150 km. Soft X-rays and EUV radiation ($80 - 102.7$ nm) ionise the thin gas and produce N_2^+, O_2^+, and O^+ (cf. Fig. 9 and see also Hunsucker and Hargreaves, 2003). A so-called sporadic E layer occasionally appears in the lower range. In contrast to the normal one, the sporadic E may reflect radio waves of frequencies up to 100 MHz depending on its current structure (Davies, 1990).

On top, the F region extends up to about 500 km and shows two separate maxima in the plasma density profile. Hence, it is subdivided into two major layers named F1 and F2. The lower F1 region mainly consists of oxygen ionised by EUV radiation [$20 - 90$ nm]. The upper F2 has moreover small contributions by N^+, He^+, and H^+. At daytime, the electron density exceeds 10^{11} or even 10^{12} electrons/m^3. The topside ionosphere is defined to be the region above the F2 peak height hmF2. Beyond the transition height (approximately at 800 km) oxygen loses its dominance, and ionisation decreases within the adjacent protonosphere, containing relatively few H^+ and He^+ (Kelley, 1989; Schunk and Nagy, 2004).

A general description of the ionospheric layers was introduced by Chapman (1931a). The following part will discuss the ion production derived from atmospheric properties, known as Chapman theory.

2.2.2 Formation of ionised layers

In order to model properties of the ionosphere important for radio wave reflection one should describe the electron density $N(h)$ dependant on the height h. In 1931, Chapman introduced a theory of the formation of ionospheric layers (Chapman, 1931a,b). We give a short exposition on the key elements of obtaining $N(h)$.

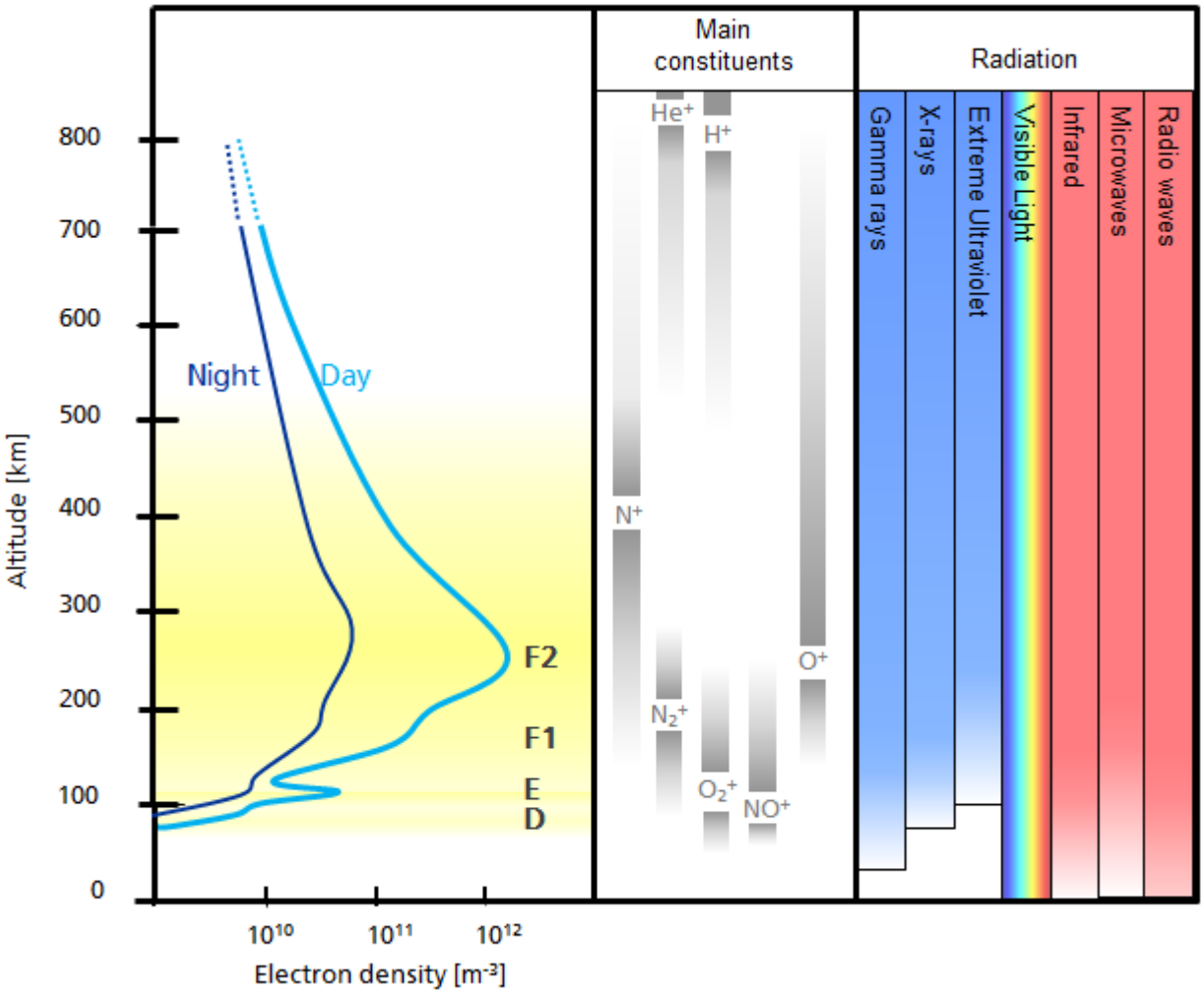

Figure 9: Principles of ionospheric composition and absorption: Whereas X-rays ionise all constituents of the D and E region, EUV is mainly absorbed in the F region.

Gas	Ionisation potential [eV]	Max. Wavelength [nm]
NO	9.25	134.0
O_2	12.1	101.5
O	13.61	91.0
O^+	35.1	35.0
N_2	15.51	79.5
N	14.53	85.0

Table 3: Ionisation potentials of some ionospheric gases. [taken from Hargreaves (1992)]

Assuming a constant air composition and temperature, the atmospheric density ρ_{air} varies exponentially with the height h, i.e., approximately with

$$\rho_{air} = \rho_0 \exp(-h/H_p) \tag{3}$$

(Chapman, 1931b). Here, ρ_0 is the ground level density, and $H_p = k_B T/(gm)$ is the scale height that is determined by Boltzmann's constant k_B, the temperature T, the gravitational acceleration g, and the mean molecular mass m. Since the solar radiation that travels through the atmosphere is reduced proportional to the mass absorption coefficient σ_m, the decreasing energy flux I_s is given by the relation

$$\mathrm{d}I_s = I_s \sigma_m \rho \sec\theta \, \mathrm{d}h, \tag{4}$$

in dependence of the solar zenith angle θ. From (3) and (4), with $h_0 = H_p \ln(\sigma_m \rho_0 H_p)$, follows

$$I_s = I_0 - \exp\Big(-\sec\theta \exp\big(-(h-h_0)/H_p\big)\Big)$$

(Chapman, 1931a). Since the energy absorption is proportional to the rate of electron production, Chapman made the ansatz of a monochromatic solar radiation beam through a homogeneous medium to obtain the rate of production[4]

$$q = q_0 \exp\Big(1 - (h-h_0)/H_p - \sec\theta \exp\big(-(h-h_0)/H_p\big)\Big). \tag{5}$$

This formula is denoted as *Chapman production function* (Hargreaves, 1979). Charge carriers may be produced, especially at daytime by photoionisation. This process is in balance with neutralising chemical reactions, which dominate at nights. In the assumed medium (E and F region), the so-called recombination can be dissociative, i.e., electrons are directly combined with ions to retrieve atoms, or done by charge-transfer between ionised molecules. Thus, the electron recombination is plausibly described by the recombination rate of molecular ions, and the electron density obeys the continuity equation

$$\frac{\mathrm{d}N}{\mathrm{d}t} = q - \alpha N^2, \tag{6}$$

where α is the recombination coefficient and αN^2 is the recombination of molecular ions. By this, neglecting the comparatively small derivative $\mathrm{d}N/\,\mathrm{d}t$, substitution with (5) gives

$$N = N_0 \exp\left(\frac{1}{2}\Big(1 - (h-h_0)/H_p - \sec\theta \exp\big(-(h-h_0)/H_p\big)\Big)\right) \tag{7}$$

(Rishbeth and Garriott, 1969). This simplified mechanism of electron production and loss describes the so-called *Chapman layer*.

[4] More precisely, this is also called the rate of production of ionisation. It is a measure for the produced ion-electron pairs.

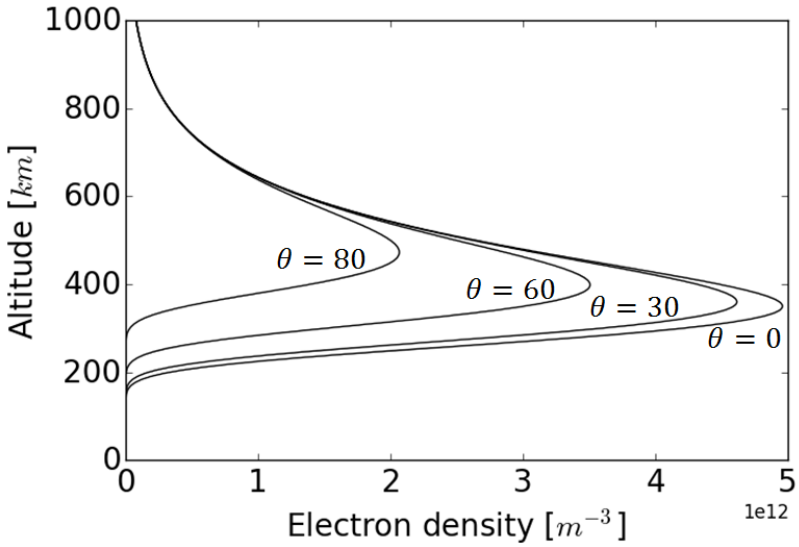

Figure 10: In the major part of the ionosphere, the E and F regions, the electron density distribution is given according to the Chapman's theory (7). We see the results for $N_0 = 4.96 \times 10^{12}\,\mathrm{m}^{-3}$, $H_p = 70\,\mathrm{km}$, and $h_0 = 350\,\mathrm{km}$ using different solar zenith angles θ.

Fig. 10 shows a typical Chapman layer for different solar zenith angles. Integrating such a vertical electron density profile N over the height h gives the total vertical electron content

$$VTEC = \int N(h)\,\mathrm{d}h. \tag{8}$$

This important parameter for describing the ionospheric state (besides the electron density N itself) is measured in TEC units: $1\,\mathrm{TECU} = 10^{16}\,\mathrm{electrons/m^2}$. Analogously, integrating along an inclined path s results into the slant TEC

$$STEC = \int N(s)\,\mathrm{d}s.$$

Considering the D layer, a description solely via the quite stable ions is no longer possible. There are many attachments and detachments of electrons within short time, which have to be taken into account. In consequence, (6) has to be modified to

$$\frac{\mathrm{d}N}{\mathrm{d}t} = \frac{q}{1-\lambda_r} - (\alpha_e + \lambda_r \alpha_i) N^2 \tag{9}$$

(Ratcliffe, 1972), where λ_r denotes the ratio between the concentration of negative ions and free electrons. As there is, e.g., a loss of electrons by conversion into ions, processes within the D layer are more complex. The effective recombination coefficient $\alpha_{eff} = \alpha_e + \lambda_r \alpha_i$ is composed from the electron-ion recombination coefficient α_e and the ion-ion recombination coefficient α_i. Both coefficients, α_e and α_i, are of the same order with a magnitude of about $10^{-13}\mathrm{m}^3/\mathrm{s}$.

In quasi-equilibrium (i.e., $\frac{dN}{dt} = 0$), (9) can be re-written as

$$q = (\alpha_e + \lambda_r \alpha_i)(1 - \lambda_r)N^2.$$

However, this thesis investigates events of high temporal variability (e.g., solar flares in chapter 4 and a solar eclipse in chapter 5). In this case, one instead puts $q = 0$ and regards

$$\frac{\mathrm{d}N}{\mathrm{d}t} = -(\alpha_e + \lambda_r \alpha_i)N^2.$$

With the help of this equation it is possible to derive response delays within the lower ionosphere and to get information on the dominating electron concentration. As the differential equation is more involved, for the comparably narrow D layer other models are preferred over the classical Chapman layers used for the vast E and F regions. We will embark on this in section 2.3.3.

In the ionosphere, quasineutrality is generally assumed to be valid. This means that all charges in an appropriate volume sum up to zero (Koskinen, 2011). The property is quite obvious for heights above 95 km, as electron and positive ion density are the same (Baumann et al., 2013). Below, quasineutrality is no longer maintained solely by negative electrons and positive ions. Further negative charge carriers have to be taken into account. The D layer has a very wide range of molecules, atoms, and ions in comparison to the E and F layers, whence the occurring photochemical reactions are much more complex, too. As the atmospheric density here is about a factor 10^5 higher, the collision frequency exceeds the values known from the upper layers by far. By this, a fast reaction on a sudden disturbance (such as a flare event) is more likely and the short-term characteristics modified by space weather can be observed quite well. Generally, the ionospheric layers are influenced by solar irradiation, which varies more or less periodically. These regional and above all daily variations are discussed below.

2.2.3 Temporal and spatial variations

Due to changing irradiation of the Sun, the solar wind, coronal mass ejections, as well as changes of the Earth's magnetosphere system (see Fig. 11), the ionosphere is subject to temporal and spatial variations. Although one can identify the basic layers at every location, the profile marked by the peak electron densities and their corresponding heights varies strongly in time (in particular with diurnal and seasonal changes, solar cycle) and space (e.g., polar cap absorbtion, auroral oval, and the equatorial fountain). This causes a widely diverged ionisation.

Temporal variations of the plasma density are determined by gain and loss of particles resulting from photoionisation and recombination. In order to detail the also decisive transport processes, the continuity equation may be written as

$$\frac{\mathrm{d}N}{\mathrm{d}t} = q - L + d.$$

Here, q represents the gain by electron production, L the loss by destruction, and $d = -\operatorname{div}(Nv)$ the transport-induced density change, given by the particle flux Nv via its mean velocity v. In

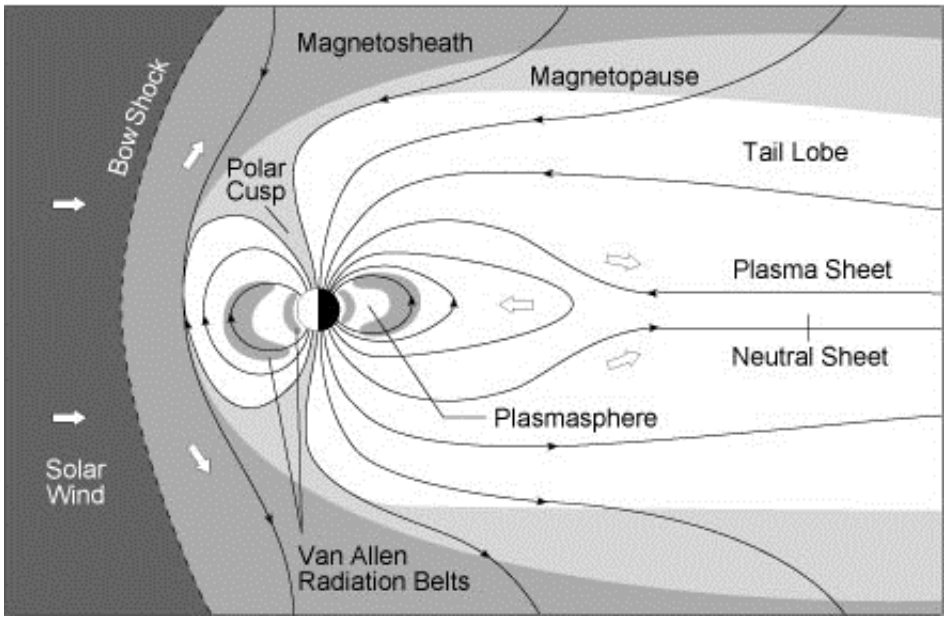

Figure 11: The solar wind hitting the Earth's magnetic field causes different regimes. [taken from Lang (2009)]

the lower ionosphere, the transport is mostly carried by neutral winds. However, the term d, which considers the resulting electron distribution only, is negligibly small (Prölss, 2003). Hence, when the equation reaches the production-loss (or photo-chemical) equilibrium during daytime (in particular near local noon), we obtain $q \approx L$ due to the assumption $\frac{\mathrm{d}N}{\mathrm{d}t} \approx 0$. At night, on the other hand, the production rate reaches zero, and we get $\frac{\mathrm{d}N}{\mathrm{d}t} \approx -L$. With the loss dominating the ionospheric changes, the vague borders vanish and the D, as well as F1 layers disappear (Davies, 1990).

In the upper ionosphere, charged particles are heavily affected by the geomagnetic field and transported along the field lines. At low latitudes, the sunlight almost orthogonally hits the Earth's surface, raising the ionisation level. Close to the geomagnetic equator, the electric field in the E region (directed from East to West) here causes an uplift of the equatorial hmF2 by an electromagnetic drift ($E \times B$), forming the equatorial anomaly, the so-called *ionospheric fountain*.

At high latitudes, vertical diffusion and the anti-solar plasma flow transport particles away from Earth. In contrast to the equatorial region, the ionisation is low because of the large solar zenith angle. Although the polar cap is constantly illuminated half of a year and not subject to the 24 hour change, diurnal variations also can be seen. This is a consequence of plasma convection via electromagnetic transport and neutral winds.

At mid latitudes, such horizontal neutral winds are basically the only source of transport. Since neutral winds are not able to move ions across the geomagnetic field lines, an equatorward wind raises the plasma, whereas a poleward wind lowers it (Davies, 1990).

Because of the lack of sunlight at nights, the plasma density decreases, most noticeable in the equatorial region. In this fashion, ionisation is altered heavily, and the ionosphere shows

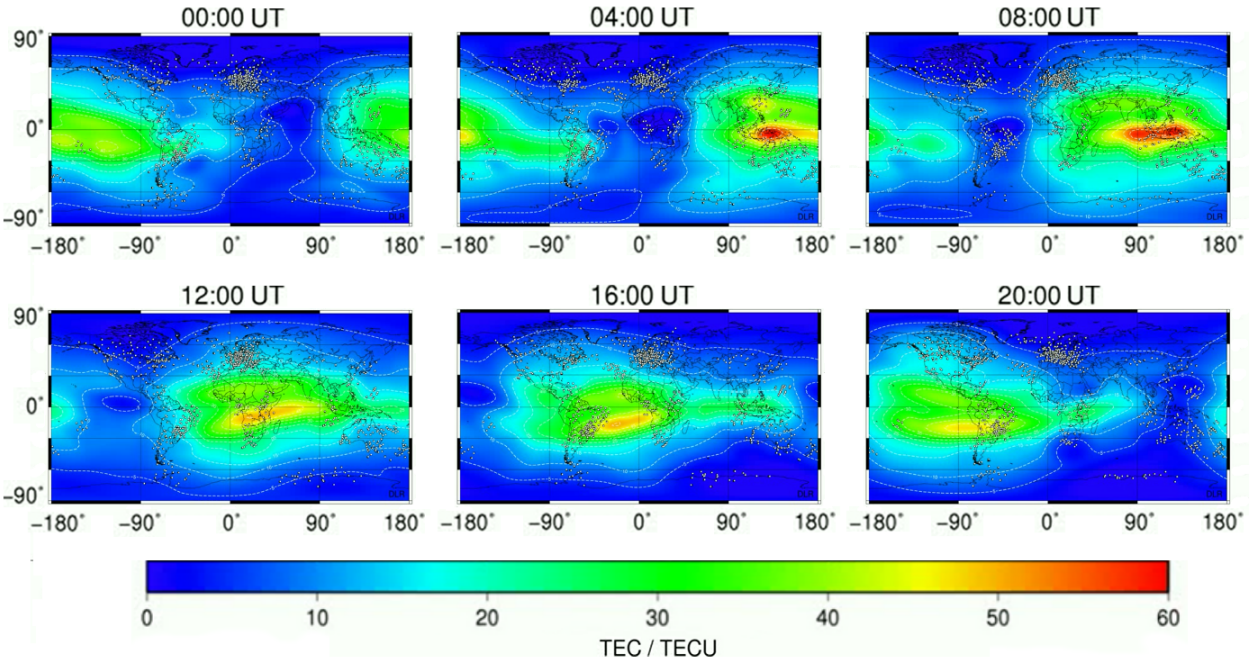

Figure 12: Global maps of vertical TEC distribution over one day: TEC measurements are provided by DLR's IMPC (http://impc.dlr.de/) determined from dual frequency code and carrier phase measurements of Global Navigation Satellite Systems (GNSS). The maps show the TEC variations on 17 February 2011.

especially diurnal and seasonal variations, but also changes mandated by the sunspot cycle and short-term solar disturbances are evident. Fig. 12 shows a sequence of global TEC maps (provided by IMPC, http://impc.dlr.de/) illustrating the variability of the Earth's ionosphere during one day. Irregular disturbances of the ionosphere are described in the following part.

2.2.4 Ionospheric disturbances

When talking about *ionospheric disturbances*, several quite different phenomena may be addressed. The broad variety of fluctuations, which are mostly caused by the Sun in a certain way, ranges from sudden ionospheric disturbances (SIDs) via polar cap absorption events (PCA) to ionospheric storms.

The main interest of this study is focused on SIDs caused by solar flares. Especially X-ray and EUV flares can produce an enhanced ionisation of the D and E region. This leads to a short-term radio wave absorption, known as shortwave fadeout[5] (Davies, 1990; Prölss, 2003). Depending on the respective point of view, these disturbances may be regarded as either obstructive or advantageous. The effects of SIDs on radio signals are presented in section 2.3.4. However, solar flares may also alter the whole total electron content, yielding a sudden increase in total electron content (SITEC, e.g. Jakowski and Lazo, 1977).

Beside SIDs that are caused by electromagnetic radiation, there are different kinds of ionospheric disturbances associated with solar flares. These phenomena are mostly restricted to the

[5] sometimes also termed Mögel-Dellinger effect

polar cap, like solar proton events (SPE), polar cap absorption (PCA), and relativistic electron precipitation (REP). Strong flare events can emit high-energetic protons that propagate along the geomagnetic field lines and couple into the polar ionosphere, manifesting in PCAs. Extremely high-energetic SPEs will pass the atmosphere and are observable on the Earth's surface as so-called ground-level enhancements (GLEs). Similarly, when relativistic electrons enter the atmosphere, their velocity is reduced. This results into bursts of Bremsstrahlung (X-ray emissions). Associated with geomagnetic disturbances, such relativistic electron precipitation (REP) events happen essentially during daytime in the auroral zone. They emit energies of about 500 keV and can be recorded as increases in riometer absorption data and anomalies in VLF phase measurements, too (Davies, 1990). Since GIFDS operates in the mid-latitudes, the system is barely affected by those disturbances.

Variations in the solar wind (i.a. associated with CMEs) lead to compressions of the Earth's magnetosphere and can result into geomagnetic storms (cp., Fig. 11). During such a storm, currents and fields in the Earth's magnetosphere intensify. By this, the electron density can increase (positive ionospheric storm) or decrease (negative ionospheric storm).

Apart from solar influences, the ionosphere is also subject to atmospheric coupling processes like travelling ionospheric disturbances (TIDs). Especially medium-scale TIDs are the ionospheric signatures of atmospheric gravity waves (AGWs) which are caused by local atmospheric buoyant forces. Arising from the troposphere and stratosphere (e.g., via jet stream perturbations, convection, airflow over mountains, earthquakes), gravity waves can propagate up to the thermosphere or can be generated directly in the thermosphere (e.g., via Joule heating, solar terminator movement, solar eclipses). Detailed descriptions of the processes and particular effects can be found in Davies (1990); Hunsucker and Hargreaves (2003); Prölss (2003) and Schunk and Nagy (2004).

2.3 Radio wave propagation

In 1887, Heinrich Hertz proved that radio signals can be produced artificially via a dipole antenna and moreover be detected by a receiving loop. With this demonstration, James Clerk Maxwell's theoretical equations about the existence of electromagnetic fields were confirmed. In the literature, these correlations are explained and further properties of radio wave propagation are derived; see e.g. Budden (1999), Carr and Hippisley (1989), Davies (1990), Dolukhanov (1971), and Volland (1968). In this section, we will provide a short introduction into radio waves with a more detailed demonstration on the propagation of very low frequency (VLF) waves.

2.3.1 Fundamentals of radio wave propagation

Radio waves are electromagnetic waves. Their propagation is subject to Maxwell's equations:

$$\nabla \cdot \mathbf{E} = \frac{\rho}{\varepsilon} \qquad \text{(Gauss's law)}$$

$$\nabla \cdot \mathbf{B} = \nabla \cdot \mu_0 \mathbf{H} = 0 \qquad \text{(Gauss's law for magnetism)}$$

$$\nabla \times \mathbf{E} = -\frac{\partial \mathbf{B}}{\partial t} \qquad \text{(Faraday's law of induction)}$$

$$\nabla \times \mathbf{B} = \mu_0 \left(\mathbf{J} + \varepsilon \frac{\partial \mathbf{E}}{\partial t} \right) \qquad \text{(Ampère's circuital law)}$$

The generation and interplay of electric fields E and magnetic fields H is dependant on the volume charge density ρ, the permittivity ε, the permeability of free space μ_0, the magnetic flux density B, and the current density J. The response of a medium to such fields is defined by the constitutive relations

$$D = \varepsilon E \quad \text{and}$$
$$B = \mu_0 H,$$

where D is the dielectric displacement.

A quarter century after Maxwell established his theory, Hertz confirmed it by demonstrating a wireless, artificial transmission and reception of radio signals between a spark-gap transmitter (consisting of a dipole antenna with a spark gap powered by high voltage pulses from a coil producing a burst of electromagnetic radiation along with a sharp noise) and a loop antenna with a spark gap. Guglielmo Marconi extended the construction plans and built own stations, accomplishing the first transatlantic transmissions from Poldhu (England) to St. John's (Newfoundland) and Glace Bay (Nova Scotia) in 1901/02. Shortly thereafter, Arthur Edwin Kennelly and Oliver Heaviside proposed the existence of an electrically conductive layer in the upper atmosphere, the so-called Kennelly-Heaviside layer, in order to explain Marconi's experiment and therewith the propagation of radio waves beyond the Earth's curvature with the help of reflection. In 1926, Robert Watson-Watt suggested to term the ionised layer *ionosphere*.

Sir Edward Victor Appleton verified the conclusions in regard of the atmosphere with experiments on the frequency modulation considering the angle of the received radio signal. He regarded two separate types of radio wave propagation: a ground wave propagating close to the Earth's surface and a sky wave that is reflected from the ionosphere. Each radio wave is characterised by its frequency, measured in Hz,

$$f = \frac{c}{\lambda},$$

with the wavelength λ in m and the speed of light $c \approx 300,000\,\mathrm{km/s}$. Within the atmosphere, radio wave propagation differs in dependence of this frequency. So, several layers can be identified that will reflect different parts of the spectrum. Fig. 13 illustrates the principal reflection of particular radio waves at ionospheric layers.

The refractive index The common, known real index of refraction is given by $\mu = \frac{c}{v}$, where c is the speed of light in vacuum and v the signal velocity. For describing the propagation and absorption of radio waves, Hans Lassen introduced the *complex refractive index*

$$n = \mu - i\chi$$

(Rawer and Suchy, 1976). Here, the real refraction number is extended by an imaginary part χ that accounts for attenuation. In this way, both the modifications of frequencies (or wavelengths) and amplitudes are taken into account. The complex notation is correlated to geometric interpretations based on quadrics in the plane that is divided into parts representing qualitatively different wave progression. The concept was developed independently in the 1920s also by Edward V. Appleton and Douglas Hartree (Budden, 1999). The extended, new quantity will be governed by

$\omega = 2\pi f$	the angular wave frequency,
$\omega_N = 2\pi f_N$	the angular plasma frequency,
ω_H	the angular electron gyro frequency, and
ν	the collision frequency.

The angular plasma frequency is given by

$$\omega_N^2 = \frac{Ne^2}{\varepsilon_0 m_i}. \tag{10}$$

It describes a phenomenon that is induced by Coulomb forces and depends on the rest mass of an ion m_i, the elementary charge e, and the permittivity $\varepsilon_0 = 8.854 \times 10^{12}\,\mathrm{F/m}$ of free space. Because of electrostatic interaction, an electron can be displaced from the ideal position of a grid. The motion is restricted by other particles in its neighbourhood and hence dependant on the electron density. Due to inertia, counter forces will not stop the electron in the point of balance. Instead, a periodic movement of a specific frequency is established, the plasma frequency.

Ion	Gyro frequency [Hz]	Plasma frequency [Hz]
e^-	$8.8 \cdot 10^6$	$62.8 \cdot 10^6$
p^+	4787.8	$146.4 \cdot 10^4$
O^+	299.7	$36.6 \cdot 10^4$
$NO+$	159.6	$26.8 \cdot 10^4$
O_2^+	149.5	$25.9 \cdot 10^4$
N^+	344.4	$39.3 \cdot 10^4$
N_2^+	172.2	$27.8 \cdot 10^4$

Height [km]	Electron collision frequency [s^{-1}]
60	$22.4 \cdot 10^6$
80	$11.2 \cdot 10^5$
100	$5.6 \cdot 10^4$
150	30.7
200	$17.0 \cdot 10^{-3}$
250	$9.4 \cdot 10^{-6}$
500	$4.9 \cdot 10^{-22}$

Table 4: Estimated values of gyro, plasma and electron collision frequencies occurring in the ionosphere: The left table lists approximated gyro and plasma frequencies based on (11) and (10) (with $B_0 = 0.5 \cdot 10^{-4}$ T and $N = 1.24 \cdot 10^{12}$ ions/m^3). The right table specifies electron collision frequencies according to Wait and Spies (1964), see (13).

The angular gyro frequency

$$\omega_H = \frac{|e|B_0}{m_i} \tag{11}$$

is also known as cyclotron frequency, as it is the frequency of the circular motion of a charged particle in a plane perpendicular to a homogeneous magnetic field B_0. Common values are listed in Tab. 4.

The complete formula for the complex refractive index is given by (Davies, 1990)

$$n^2 = 1 - \frac{X}{1 - iZ - \frac{Y_T^2}{2(1-X-iZ)} \pm \left(\frac{Y_T^4}{4(1-X-iZ)} + Y_L^2\right)^{\frac{1}{2}}} \tag{12}$$

with

$$X = \frac{\omega_N^2}{\omega^2}, \quad Y = \frac{\omega_H}{\omega}, \quad Z = \frac{\nu}{\omega},$$

and is denoted as Appleton or *Appleton-Lassen formula* (Rawer and Suchy, 1976), and also as *Appleton-Hartree formula* (Budden, 1999). The longitudinal and transverse components of any field quantity are indicated by L and T, respectively. Theoretical and experimental information about ν both show an exponential decrease with height (Wait and Spies, 1964). Values can be approximated by the mean molecular mass and the temperature, or the height respectively. So, the electron-neutral collision frequency is estimated by Wait and Spies (1964) with

$$\nu_e(h) = 1.816 \times 10^{11} \cdot e^{-0.15h}. \tag{13}$$

The collision frequency of ions with neutrals is usually taken as

$$\nu_\pm(h) = 4.54 \times 10^9 \cdot e^{-0.15h}, \tag{14}$$

see Morfitt and Shellman (1976).

Eq. (12) is typically used to distinguish several cases with respect to the configurations of X, Y, and Z. The strongest simplification is done for frequencies in the range of and below the plasma frequency (as for, e.g., ionosondes). It is given by neglecting collisions ($Z \approx 0$) and the magnetic field ($Y \ll 1$), yielding

$$n^2 = \mu^2 = 1 - X = 1 - \left(\frac{f_N}{f}\right)^2. \tag{15}$$

For GNSS signals (i.e., in frequency ranges of GHz), the ionosphere can be treated as collisionless plasma ($Z \approx 0$) and hence

$$n^2 = \mu^2 = 1 - \frac{X}{1 \pm Y_L} = 1 - X(1 \pm Y_L + Y_L^2 \pm \cdots).$$

Neglecting higher order terms, one obtains

$$\mu^2 \approx 1 - \frac{f_N^2}{f^2}\left(1 \pm \frac{f_H}{f}\right), \tag{16}$$

where the "+" represents the ordinary and the "−" the extraordinary wave.[6]

Usually, several further simplifications are done depending on the setting. When changes are relatively small, we stay in the same domain of qualitative behaviour mentioned before. For instance, whenever collisions may be neglected, i.e. in the E and F region, $Z = 0$ is assumed. However, down in the D region, this is not appropriate for VLF waves. Here, the electron collision frequency is large (with about 10^5 to $10^6\,\mathrm{s}^{-1}$, cp. Tab. 4) in comparison to the used very low frequencies ($\nu \gg \omega$). Moreover, influences of the magnetic field are mostly negligible, whence squared Y terms more or less vanish ($Y \ll 1$), and (12) can be written as

$$n^2 := (\mu - i\chi)^2 = 1 - \frac{X}{1 - iZ}.$$

Using the previous equations and setting $\chi^2 \approx 0$, we get

$$\mu^2 - i2\mu\chi = 1 - \frac{\omega_N^2/\omega^2}{1 - i\nu/\omega}.$$

After some transformations, one obtains

$$\frac{\omega_N^2}{\omega^2 - i\omega\nu} = 1 - \mu^2 + i2\mu\chi,$$

and thus,

$$\omega_N^2 = \omega^2 - \omega^2\mu^2 + 2\omega\mu\nu\chi + i(\omega^2\mu\chi - \omega\nu + \omega\nu\mu^2).$$

[6] The ordinary mode is left-hand circularly polarised, while the extra-ordinary mode is right-hand circularly polarised.

With $\omega \ll \nu$ and an almost vertical incidence angle (i.e., $\mu^2 \approx 1$), we obtain the simplification

$$\omega_N^2 = 2\omega\mu\nu\chi.$$

Finally, for the D region ionosphere, the absorption is approximately

$$\kappa := \frac{\omega\chi}{c} = \frac{\omega_N^2}{2\mu\nu c}.$$

Substituting ω_N with its definition and estimating measurable and fundamental quantities, the last equation is continued with

$$\kappa \approx 4.6 \times 10^{-2} \frac{N}{\nu}.$$

With larger collision frequencies ν, there is less absorption since electron motion are becoming more restricted. Both, the collision frequency and the electron density mandate the properties of the Earth-ionosphere waveguide. They are approximated from statistics in the applied propagation model detailed in section 2.3.3.

Refraction of radio waves at ionospheric layers When a radio wave travels from one medium to another, the angle with the normal of the bounding interface in the original medium is altered to another value in the target medium. More precisely, due to Snell's law, the quotient of the sines of the two angles is reciprocal to the quotient of the two refractive indices.

The law (12) also justifies the observations in regard of the maximum usable frequency (MUF). When the plasma frequency f_N equals the wave frequency f, i.e. $X = 1$, we have total reflection, and for higher frequencies, the radio wave will penetrate the layer as mentioned above.

On its propagation, a radio signal experiences changes in strength, phase, polarisation, and fading, as well as frequency, depth and time dispersion. The higher the frequency, the deeper a signal penetrates the ionised layers. Beginning from VHF, signals can even pass the whole atmosphere, what enables communication with satellites. Tab. 6 provides an overview of the radio spectrum from ELF to VHF waves presenting their characteristics of propagation and associated applications. As each ionospheric layer is specified by its maximum electron density at a particular height, there is a maximum usable frequency where radio waves of the same frequency and below are still reflected and, hence, applicable for ground-based communication. Frequencies higher than MUF travel through the ionosphere and are transmitted into space. The MUF is limited from above by physical laws that are determined by the refractive index.

2.3.2 Propagation of VLF waves

Extraterrestrial influences, in particular the X-ray flares we are interested in, have a heavy impact especially on the D region of the ionosphere. According to Tab. 6 VLF signals interact with this layer. Consequently, such waves hold valuable information on the originating radiation. So, for our applications, VLF measurements are the right choice.

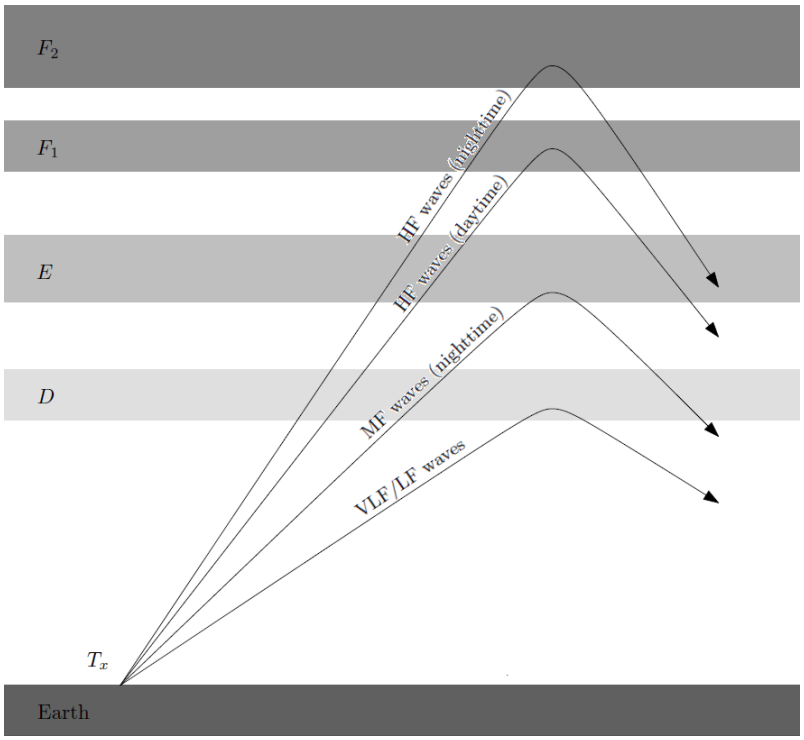

Figure 13: Illustration of radio wave propagation in the Earth's atmosphere

The principle of a general wave's refraction is given by (12). The actual path of an emitted signal is more complicated. Most parts of the journey of the wave front (within a homogeneous medium) are "straight forward." However, in Fig. 13, we see that a reflection at the boundary to another medium (i.e., the ionospheric layers in our situation) turns out to be a gradual change in direction, so that a curve is described. But, for VLF signals, the wavelength very much exceeds the scale of the D region. Due to this, the reflection process can be closely approximated by a classical Fresnel reflection at a sharp boundary (Davies, 1990). Hence, we may work in the following with Snell's law that moreover tells about the critical angle for total reflection.

VLF waves propagate between the Earth's surface and the lower ionospheric layers. At both boundaries they are reflected. These boundaries can be assumed to be pretty sharp compared with the wavelengths of VLF (Klawitter and Herold, 1995). The structure combining the two "plates" (acting like conductor and ground) and the space in between is called the Earth-ionosphere waveguide. It enhances the transport of ELF and VLF signals.

The transmitter – a source of VLF waves – can be considered as a vertical electric dipole on the ground (Wait, 1959) For determining the electric field at the receiver – some other point on the ground plane – there are two approaches for modelling VLF radio wave propagation: the ray theory (or wave-hop theory) and the waveguide mode theory. The efficiency of the methods depends on the signal's frequency and the distance between transmitter and receiver. A short overview on both theories will follow.

Band	Frequency / Wavelength	Propagation characteristic	Application
ELF	≤ 3 kHz / ≥ 100 km	Earth-ionosphere waveguide penetrating sea water	Communication with (submerged) submarines
VLF	$3 - 30$ kHz / $100 - 10$ km	Sky wave: Earth-ionosphere waveguide from ground to lower ionosphere, Ground wave	Submarine communication, Alpha (navigation), Beta (time signal)
LF	$30 - 300$ kHz / $10 - 1$ km	Earth-ionosphere waveguide, Ground wave	Maritime navigation, Loran C (until 2015), AM broadcasting, standard time signals
MF	$300 - 3000$ kHz / $1000 - 100$ m	Ground wave, At night: E-region reflection	Non-Directional (radio) Beacon (NDBs) for maritime and aeronautical navigation, AM broadcasting, Maritime and land mobile
HF	$3 - 30$ MHz / $100 - 10$ m	E- and F-region reflection	Maritime and aeronautical fixed services, shortwave broadcasting, amateur and citizens' band radio
VHF	$30 - 300$ MHz / $10 - 1$ m	Line of sight, Scattered from the ionosphere	Television, FM broadcasting, Public safety, Aeronautical Space communications
UHF	$300 - 3000$ MHz / $1000 - 100$ mm	Line of sight (affected by ionospheric irregularities)	Television, Radar, Broadcasting, Navigation (fixed, mobile)
SHF	$3 - 30$ GHz / $100 - 10$ m	Line of sight (tropospheric, affected by ionospheric irregularities)	Space communications, Television, Radar, Broadcasting, Navigation (fixed, mobile)

Table 6: The radio spectrum, corresponding wavelengths, propagation characteristics and primary applications. [adapted from Davies (1990)]

Ray theory The ray theory is based on the principles of geometric optics for discrete ray paths. The ionosphere, in particular the D layer, works as a mirror-like layer, reflecting VLF radio signals back to the Earth. Fig. 14 illustrates that there are many possibilities for a ray to travel from a transmitter to the receiver. In addition to the single direct wave (the so-called ground wave), there is another one that reaches the receiver by atmospheric reflection half way. Moreover, an integer number of hops (the sky-waves) similarly result from multiple reflections between the ionosphere and the ground. The figure shows the ray paths up to order three, i.e. the VLF wave experiences up to three reflections at the lower ionospheric layer. Theoretically, between a transmitter T_x and a receiver R_x, there is an infinite number of possible propagation paths. In summary, these yield the measured electric field at the receiver. However, the contribution of high-order waves to the total field at the receiving site decreases significantly: the angle of incidence is near vertical and the signal strength reduces too much during the repeated partial absorptions on the ionosphere (Davies, 1990). Hence, only a finite

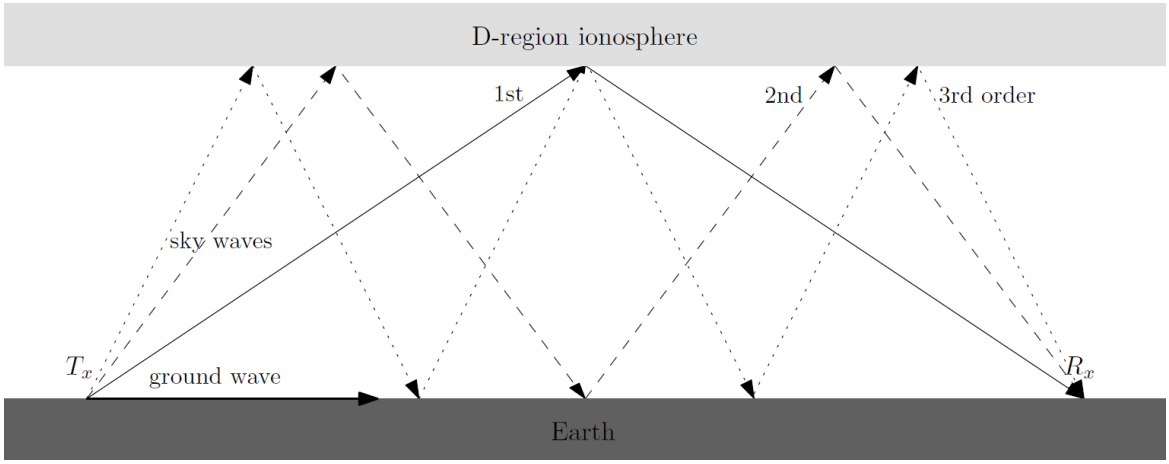

Figure 14: Schematic diagram of VLF radio wave propagation in the Earth-ionosphere waveguide with several possible reflection paths ("hops") according to the ray theory.

number of lower order ray paths is required to calculate the received signal accurately enough. The base for such a computation is Snell's Law, telling that an incident wave is reflected under the same angle. This allows to obtain the sub-reflection points of any order.

Especially for short propagation paths (up to 500 km), just a couple of reflections is needed to derive the resulting signal. The ground wave is dominant only for distances up to 300 km. Afterwards, it is damped because of the spherical Earth. Nevertheless, for long propagation, the ray theory requires a large number of ray paths with relatively low attenuation but similar individual contributions.

Mode theory Whereas the classical ray theory is well known for a long time, but limited in usability, the mode theory has been developed based on Maxwell's equations. It is used to explain VLF propagation within the Earth-ionosphere waveguide. Acceptable waveguides can be constructed with respect to a specific frequency. In general, the lower the transferred frequencies are, the more expanded the waveguide has to be. As the convenient small-sized analogue, consider a rectangular hollow metallic conductor through which a high frequency shall be passed. Such a constellation verifiably demonstrates that in a waveguide electric energy can be transferred via continuous waves with small loss. Fig. 15 illustrates the propagation modes within a hollow rectangular waveguide. If this waveguide is exposed to energy, an electric field is generated at the beginning cross section of the rectangular tube. In the left picture, the field lines are more dense in the middle of the wide side a, and they become weaker towards the narrow sides b. More precisely, the field strength has the form of a sine wave. The electric field induces a perpendicular magnetic one propagating through the hollow waveguide in z direction. This wave propagation is known as transverse electric (TE) mode (cf. left picture of Fig. 15).[7] Depending on the input signal, the electric and magnetic field is changing in intensity and polarity over time. Moving in longitudinal direction of the waveguide, there are alternating maxima and minima with a distance of the half wavelength. This can be identified in the change of direction

[7] A mode is defined as an integral multiple of the half wavelength that fits into the distance.

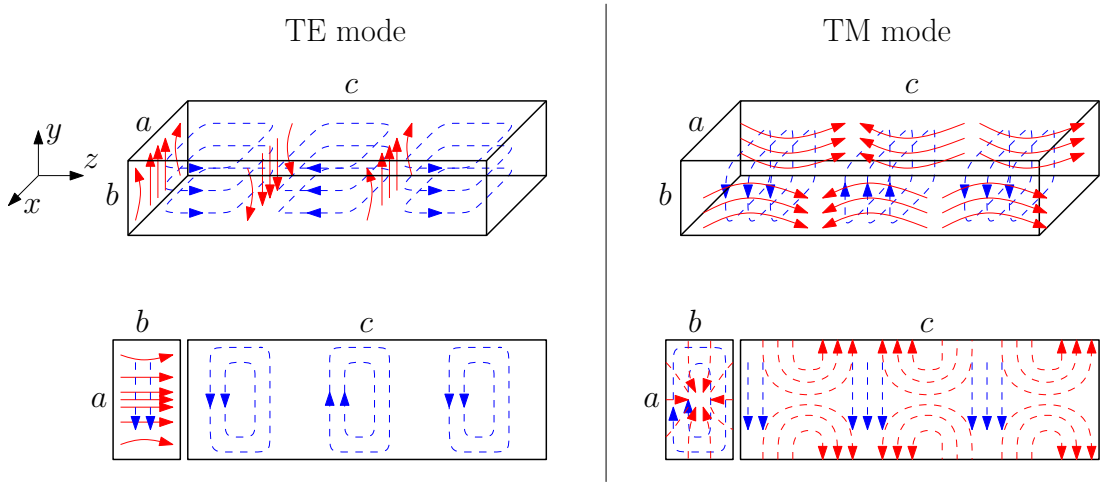

Figure 15: Field pattern of the TE mode (left) and TM mode (right panel) in a rectangular hollow metallic waveguide: Red lines mark electric field and blue lines show the magnetic one.

of the electric field lines. On the other hand, if the electric field is parallel to the propagation direction, the magnetic component fully influences the cross section at the start of the hollow conductor. In a similar fashion, a so-called transverse magnetic (TM) mode is generated. This is illustrated in the right picture of Fig. 15.

The two conductive planes of the Earth's surface and the ionosphere form a natural waveguide in which ELF and VLF waves can propagate similar to microwave transmission in a standard waveguide. For explaining these processes, we use the simple model suggested by Wait (1959), which regards two horizontal planes: one is a perfect electrical conductor – the Earth's surface ($z = 0$, reflection coefficient $R = +1$), and the other is a perfect magnetic conductor – the ionosphere ($z = h$, reflection coefficient $R = -1$); see also Davies (1990). The VLF transmitter can be regarded as a vertical electric dipole on the ground, generating electric and magnetic fields. So, at the receiver, the observed electric field is only given by the vertical component and can be derived from the images of the source, which can be found at integer multiples of $z = h$. They all share the same absolute values, but the sign is flipped for any two neighbours because of the opposite reflection coefficients at the lower and upper boundaries. The even numbers correspond to electric conducting layers, and odd integers represent the magnetic ones.

The even images are linked to signals, for which the common wavefront has a distance of $n\lambda$ to the respective virtual dipole. As they are in phase, the emitted wave is always directed broadside. At large distances, the discrete images virtually merge to a continuous line source with an average current $I_a = \frac{ds}{h} I$ along the z axis, where ds is the dipole height and I its current. The electric field of this line is

$$E_z = \frac{\mu\omega I ds}{4h} H_0^{(2)}(k\rho) \tag{17}$$

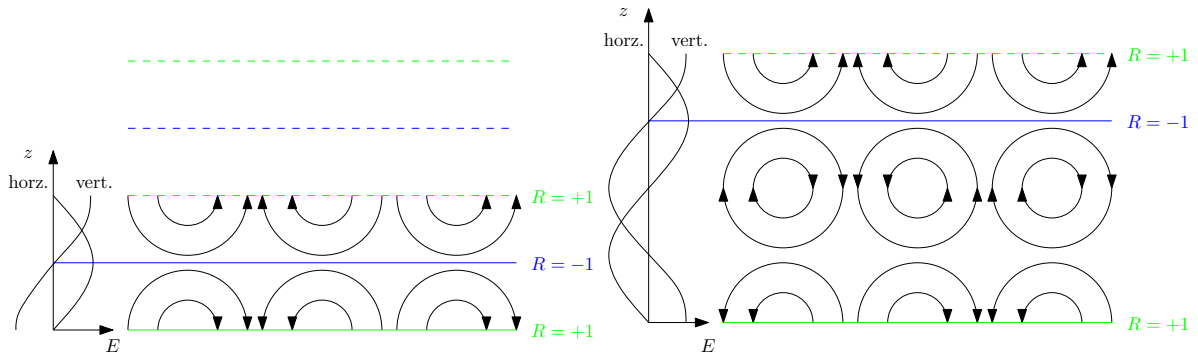

Figure 16: E-field pattern of the first (left) and second order mode (right panel) in an ideal Earth-ionosphere waveguide according to the mode theory [adapted from Davies (1990)]: Green lines mark electric conductor ($R = +1$) and blue lines mark an magnetic conductor ($R = -1$).

with the Hankel function $H_0^{(2)}$ of the second kind.[8] The wave number k and the distance ρ between transmitter and receiver are in its argument. The value is further scaled by the space's permeability μ and the angular frequency ω. For $\rho \gg \lambda$, (17) can be approximated by

$$E_z \cong \frac{\eta}{2} \frac{Ids}{h(\lambda\rho)^{1/2}} e^{-i(k\rho - \pi/4)},$$

with the wave impedance η ($\approx 120\pi\,\Omega$ in free space).[9] A signal at a point is interpreted as a compound of several wavelets coming from the images. The resonance condition of the electric conductor images (for collecting all the waves that are in phase) is

$$2h \cos\beta_n = n\lambda$$

with the angle β_n between the ray to the receiver and the z-axis, where the integer n marks the multiple of the wavelength (cf. Fig. 16, left). When the magnetic conductor images in between are considered, the factor n in the formula above has to be reduced by one half, leading to the angle $\tilde{\beta}_n$.

The contributions add up to the resulting field E_z at the receiver. When the distance is large enough, the far field is represented by

$$E_z \cong \frac{\eta Ids}{h\sqrt{(2\lambda\rho)}}(1+i) \sum_{n=1,2,\ldots}^{\infty} \sin^{3/2}\tilde{\beta}_n e^{-ik\sin\tilde{\beta}_n\rho},$$

where each mode is counted twice (the images on a positive and a negative z-value have the same horizontal velocities, but the vertical components are negatives of each other). Fig. 16 (right)

[8] This is the linear combination $H_0^{(2)} = J_0(z) - iY_0(z)$ of two Bessel functions, one of the first and one of the second kind. The Bessel functions are solutions of the differential equations bearing the same name (like the Laplace equation in cylindrical coordinates). They represent the radial part of the modes of vibration of a circular wave front.

[9] The Bessel functions, up to lower order terms, follow the rules $J_0(z) \approx \sqrt{2}\cos(z - \pi/4)/\sqrt{\pi z}$ and $Y_0(z) \approx \sqrt{2}\sin(z - \pi/4)/\sqrt{\pi z}$. Apart from these asymptotic replacements, only the physical relations $\omega = 2\pi f$, $k = 2\pi/\lambda$, $f = c/\lambda$, $\eta^2 = \mu/\varepsilon$, and $\varepsilon\mu = 1/c^2$ need to be used.

gives an illustration of the preceding explanations and the field pattern under consideration in the ideal Earth-ionosphere waveguide for modes of first and second order. As the electric fields of the waves are polarised vertically, and the magnetic fields are transverse to the propagation plane, we consider TM modes only (recall Fig. 15). Waves will not propagate when their frequency is below

$$f_n = \frac{(n - 1/2)c}{2h}.$$

For the first-order mode in the daytime (i.e. $h \approx 75\,\mathrm{km}$), this minimum cutoff frequency is approximately 1 kHz (Davies, 1990).

The model that is used to obtain the previous conclusion is based on the assumption of two ideal plates of perfect conductivity. In practice, the approach needs further modification in order to adjust the result to real conditions of VLF propagation within the Earth-ionosphere waveguide. This includes the actual height of the source and receiver, boundaries of imperfect reflectors, the curvature of the Earth, and the anisotropy of the ionosphere. For derivations and further approximations of the more complex conditions we refer to Budden (1999); Volland (1968); Wait (1959); and Wait and Spies (1964). The calculation will require complex computer programs like the Long Wavelength Propagation Capability (LWPC) code by Ferguson (1998) that is used in this work and described in section 2.3.3.

Comparison An advantage of the mode theory is that only modes of excitation by the dipole have to be taken into account. In general, only a small number of these is necessary in order to explain the propagation of VLF waves over a long distance. Modes of very high order are largely attenuated and occur with increasingly small amplitudes. On the other hand, propagation paths of short distances have slowly decreasing amplitudes, whence many modes need to be considered. Moreover, the Hankel functions can no longer be approximated by the exponential. In such cases, the ray theory is of more use, as only a few rays are necessary to be investigated. For long distances, the ray theory is unsuitable due to the many reflections that have to be taken into account.

Another important factor is the relation of the transmitted wavelength to the height of the waveguide. With decreasing frequency, also the number of required modes declines. For the lower VLF band, only one to four modes are needed, whereas for the upper band more than 30 modes may be required (Morfitt and Shellman, 1976). At medium distances both methods work reasonably well with similar efforts. However, as we are utilising propagation paths of medium to long length, we will rely on the mode theory for modelling VLF signals. As an example chapter 5 shows the application of this theory to the measurements observed during an solar eclipse.

2.3.3 Long Wavelength Propagation Capability Code

The LWPC suite of computer programs was created for assessing long-wavelength radio communications. It was developed by the Space and Naval Warfare System Center, San Diego

(Ferguson, 1998), and it is implemented in FORTRAN and C. This collection of separated, yet interconnected programs enables the simulation and illustration of VLF signal propagation. For this, the creators rely on the waveguide mode theory. The underlying propagation model itself is implemented in the Long-Wave Propagation Model (LWPM).

The lower boundary of the waveguide is given by the Earth's surface. By default, the effective electrical earth conductivity for VLF waves at an investigation site is modeled with an adaption of the world conductivity map by Morgan (1968). The ground layer is considered to be a smooth, locally homogeneous surface of particular, adjustable conductivity and permittivity. The Earth's curvature is also taken into account via an adjusted refractive index. The upper boundary, i.e. the ionosphere, is highly variable and its state can be well characterised by the conductivity. The ionospheric properties can be modified by means of user-defined conductivity profiles with an arbitrary complex, spatial electron density distribution. According to Wait and Spies (1964), the conductivity of the lower ionosphere is described by the parameter

$$\omega_r = \omega_N^2/\nu,$$

with the plasma frequency ω_N and the effective collision frequency ν. Furthermore, the conductivity of a particular height h within the lower ionosphere is mainly determined by the electron density profile $N(h)$ as

$$\omega_r(h) = 2.5 \times 10^5 \cdot e^{\beta(h-h')} = 3.18254 \times 10^9 N(h)/\nu(h).$$

Here, as usual, h and h' are given in units of km, N in electrons/cm^3, and ν in collisions/s. LWPM uses the collision frequencies as approximated in equation (13) and (14). However, the program also allows to utilise own profiles for conductivity, or electron density, and collision frequency, respectively. Combining the last equations, LWPM simulates conductivity values based on the exponentially increasing electron density profile regarding height

$$N(h, h', \beta) = 1.43 \times 10^{13} \cdot e^{-0.15h'} \cdot e^{(\beta-0.15)(h-h')}. \tag{18}$$

The ionosphere model is tuned by the two parameters, namely the sharpness β and the reference height h' (also denoted as the effective reflection height). The ansatz (18) traces back to analyses by Morfitt (1977); Wait and Spies (1964) and Ferguson (1992). Fig. 17 illustrates the variation of the approximate electron density profiles for lower ionospheric heights. Obviously, the whole profile is shifted in altitude with a change of h'. And by varying β, the slope of the electron density profile is altered. The reference height and sharpness are defined in LWPM depending on the particular frequency, the geographic latitude and longitude, as well as the time of day, and therewith the solar zenith angle and the geomagnetic field. The latter are the determining factors of the day-night and polar cap transitions in the ionospheric profile. They are assumed to be piecewise constant. On arbitrary locations along an investigated VLF path, h' and β can be modified individually for adjusting the current state to real measurements by deriving information on the ionosphere.

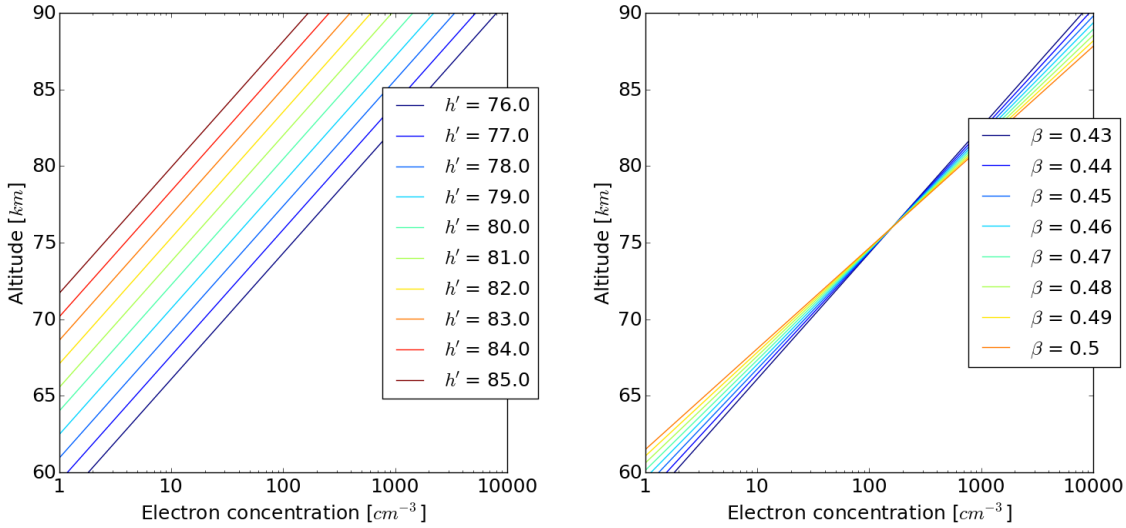

Figure 17: Electron density profiles from 60 to 90 km after (18) by Wait and Spies (1964) for sharpness $\beta = 0.43\,\mathrm{km}^{-1}$ and varying reference height h' (left panel), and for $h' = 76\,\mathrm{km}$ and varying β (right panel).

For regarding the propagation of radio waves within a waveguide, LWPM divides the path under investigation into horizontally homogeneous bins. In accordance with the mode theory (cf. section 2.3.2), fitting modes have to be determined. In order to obtain a starting point for searching these, the algorithm of Morfitt and Shellman (1976) is used. As this calculation is expensive, the procedure is applied only to the first of several bins with similar ground and ionospheric parameters, ordered with increasing distance from the transmitter. The compound mode solution then is obtained by extrapolating existing neighbouring solutions and adapting the values with respect to geomagnetic field effects. If the resulting modes are invalid or the guess is performed over too large distances, the mode-searching algorithm is repeated on a finer scale. The actually necessary full-wave integration (for combining the bin information along the whole path) is replaced by the mode-conversion model of Ferguson and Snyder (1980) because of calculation time issues. This is based on the fact that interaction processes of radio waves are concentrated at the ionospheric reflection height. If a higher accuracy should be in need and the proper data can be provided by the user, LWPC can perform operations also with a full-wave model.

Note that fixing the bunch of parameters over the globe for all times is a huge challenge and will not work with high accuracy, in general. There are several factors that may bear inaccuracies, e.g., the earth conductivity model and the approximated mode-conversion model are potential error sources. In practice, convenient configurations are set up in a trial and error method by recreating output data close to documented observations. In this way, the program has proved quite good reliability in many applications (e.g., Basak et al., 2011; Clilverd et al., 2001; Pal et al., 2012; Schmitter, 2013) and will hence be used later for modelling the solar eclipse's influence on the VLF amplitude measured by the GIFDS station in Neustrelitz.

2.3.4 Disturbances of radio signals

Section 2.2.4 provided an introduction into disturbances of the ionosphere. Changes in the ionosphere cause disturbances in the radio signal that travels via or through the ionosphere. Since this work is aimed to set up a VLF network for solar flare detection, we are focusing on SIDs. In chapter 4, we will present SIDs visible in VLF radio signals as well as in TEC data. However, solar flares cause a variety of disturbances, observable at various wavelengths. Hence, SIDs are further divided into sub-classes that are detectable by different techniques:

Shortwave fadeout (SWF) Connections between X-ray flares and SWFs were observed already about 80 years ago. These anomalies are indicated by a sudden decrease in the HF signal and, depending on the solar X-ray burst, appear as a gradual change or a sudden dropout with a slow recovery.

Sudden Phase Anomaly (SPA) In contrast to SWFs, SPAs are indicated by phase variations in VLF signals resulting from changes of the ionospheric reflection height. The shape of the phase response follows the initiating flare's course well, but the deviation from the pre-flare level may be positive or negative. In particular, SPAs will be monitored. As our VLF network measures the VLF phase in addition to the amplitude (see chapter 4), it is sensitive to SPAs, too.

Sudden Enhancement or Sudden Decrease of Atmospherics (SEA, SDA) An X-ray flare may also modify the atmospherics' field strength. Below 1 kHz or between 10 kHz and 75 kHz, the amplitude increases (termed as SEA), and between 1 and 10 kHz it decreases (so-called SDA). These phenomena are due to solar flare induced D region changes.

Sudden Frequency Deviation (SFD) The E and F regions at higher altitudes are also affected by flares, primarily by ones in the EUV spectrum. SFDs are frequency changes of HF signals that occur mostly without huge absorption but large phase changes.

Sudden Cosmic Noise Absorption (SCNA) A SCNA is observed as a sharp decrease of the cosmic noise signal intensity, followed by a gradual process of recovery. Such events are classified towards their importance or the peak size.

„Only by regular hourly observations can the changes of the ionosphere be surveyed.“
Karl Rawer

3

Instrumentation and data acquisition

Various measurement techniques are possible to survey the ionosphere. The following chapter concentrates on VLF measurements via a software defined radio and on solar radiation measurements using X-ray and EUV observations of the Geostationary Observational Environmental Satellites *GOES* and Solar Dynamic Observatory *SDO* for a comparative study. The measuring instruments as well as data acquisition processes are depicted. The GIFDS network aims at providing a continuous and consistent solar flare detection. The corresponding VLF receivers that were installed during the preparation of this thesis are essential. In section 3.1, the technical setup from the transmitters to the receivers is described, as well as hardware modifications that were made in order to get phase measurements, supplementary to the common amplitude measurements, on which the current flare detection algorithm is based (see chapter 4). The major signal processing and data management of the applied software is specified with the utilised parameters and switches. Some of these aspects, which laid the foundations to our receiver network, were published in Wenzel et al. (2016).

Furthermore, section 3.2 provides a summary of additional data sets that are necessary for comparisons with the VLF measurements made by GIFDS. We distinguish between ground-based measurements (i.e., TEC measurements and the F10.7 index) and space-based measurements (i.e., X-ray and EUV measurements by GOES and SDO).

3.1 GIFDS - Global Ionospheric Flare Detection System

VLF waves are able to propagate over the whole globe via the Earth-ionosphere waveguide and can even penetrate water, so that they are used as one-way communication with submarines. The skin depth depends on the transmitting power, as well as on the size of the antenna and sensitivity of the receiver, but also on the salinity and temperature of the water. As the signals oscillate relatively slow, they are unsuitable for the transport of audio information. The bandwidth is only sufficient to hide text messages within this frequency range. One typically can establish 300 bit/s, covering about 450 standard ASCII words per minute.

However, we can use the information of amplitude and phase alterations of continuously emitted signals to derive conclusions on solar X-ray flares. How the burst of X-radiation leads to an enhanced ionisation in the D region was explained in section 2.2.4. The resulting SIDs abruptly influence the VLF signals that propagate through the lower ionosphere. Other frequencies either do not reach or simply pass the layer we want to observe. So, the VLF band is perfect for our needs.

In the following the GIFDS system is described in detail. With regards to content, parts of section 3.1.1, 3.1.3, and 3.1.4 are published in Wenzel et al. (2016). Figures that have been directly transferred are marked in the caption. Further information of the monitoring software and its framework are taken from Mayer (2011, 2012), who introduced some further developments in terms of stabilised phase measurements in Mayer (2014a,b).

3.1.1 VLF technique for ionospheric flare monitoring

The existing VLF monitoring systems are conceived for analysing geophysical or atmospherical effects and solar activities, some of them by post-processing evaluations that may take a day to be done. Furthermore, many VLF networks are installed on regional scale. Amongst others, the network of the Antarctic-Arctic Radiation-Belt (Dynamic) Deposition - VLF Atmospheric Research Konsortia (AARDDVARK) is designed to study polar events. Similarly, the South America VLF NETwork (SAVNET) concentrates on monitoring the South Atlantic Magnetic Anomaly (Raulin et al., 2009, 2010). In the following, we give an overview over major VLF networks. There may be other isolated receivers with a very special purpose (e.g. in India, Israel, and Egypt). The different kinds of VLF receivers will be introduced in the next section.

AARDDVARK Since 2005, AARDDVARK performs long-range measurements of the lower ionosphere at particularly high latitudes. Objects of investigation are, amongst others, whistler-induced electron precipitation, REPs, SPEs, ionisation of NO_x by Lyman-α, and solar flares (Clilverd et al., 2009). The actual receiving system varies with location. So, AARDDVARK operates different receiver types. The actual positions of all receivers are illustrated in the left picture of in Fig. 18.

SAVNET SAVNET was installed by Brazilian universities and research facilities. Fig. 18 shows the location of the VLF receiver. Each of the receivers is composed of three sensors

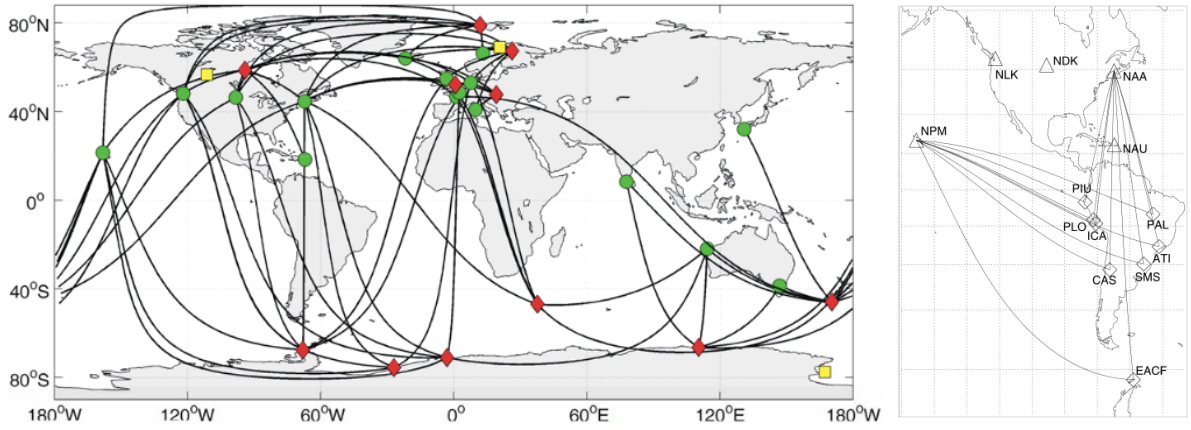

Figure 18: The AARDDVARK network [left panel, taken from Clilverd et al. (2009)] with receivers marked in red diamond, yellow squares as future receiving sites, and VLF transmitter in green circles, and the SAVNET stations [right panel, taken from Raulin et al. (2010)] with squares for receivers and triangles for transmitter, including the corresponding great circle propagation paths of received VLF signals.

(two sensitive to the magnetic field via square loop antennae, and one to the electric field via a whip antenna). The amplified signals are digitalised with help of a commercial audio card. The system was designed and constructed at the Radio Observatorio do Itapetinga-INPE (Brazil). For measuring phase variations that uncover the South Atlantic Magnetic Anomaly, a precise and stable time reference is needed. For achieving accurate phase measurements over hours and days, the system is locked to a 1-pps (one pulse per second) signal of a GPS Raulin et al. (2009).

LAVNet Latin America VLF Network is an extension of SAVNET towards the Northern hemisphere, e.g. in Mexico City. By this, a broader spatial coverage and higher sensitivity for investigating local effects of solar flares are obtained (Borgazzi et al., 2014).

GIFDS network In contrast to the other networks, GIFDS is designed as a service for solar flare detection and warning, whence it is required to finish calculations in near real time. To guarantee a complete daytime observation of the globe (or more precisely, the mid-latitude range of it), a network of receivers is formed, which will monitor the VLF waves provided by Navy stations and reconstruct size and duration of external impacts from the signal's response (Wenzel et al., 2016).

Currently, most VLF systems are confined to regional scale according to their intended applications. In contrast to the heavily disturbed polar regions mid-latitudes are considered as a good region for keeping clear and undisturbed flare information. We want to avoid installations close to the equator as the ionosphere there is dominated by large dynamic daytime variations. However, the target is to cover the areas that are dominated by susceptible technology, i.e. strongly urbanised and technologically developed mid-latitudes. So, the VLF receivers are distributed over the whole longitudinal range at mid-latitudes in the northern hemisphere.

With propagation paths of long east-west spreading, we are able to monitor SIDs continuously and can examine solar flare activity by a ground-based system. Therefore, five GIFDS stations were installed by the author. They are now permanently receiving VLF signals, enabling a continuous monitoring of the lower ionosphere:

NTZ: Neustrelitz / Germany (53.35°N, 13.07°E)
DLR Neustrelitz, Institute of Communications and Navigation

KRK: Krakow / Poland (42.34°N, 71.17°E)
Institute of Nuclear Physics, PAN

BOS: Boston / Massachusetts (50.08°N, 19.92°W)
Boston College, Institute for Scientific Research, ISR

STA: Stanford / California (37.4272°N, 122.1731°W)
Stanford University, WAAS Lab

TWN: Chungli City / Taiwan (24.9679°N, 121.1874°E)
National Central University, Center for Space and Remote Sensing Research

The station KRK was used for early tests by Mayer (2011), who implemented the measuring software *HFMonitor* detailed in section 3.1.4. The receivers monitor existing transmitters in the range from 0 to 500 kHz. Fig. 19 shows the network of transmitters T_x and receivers R_x. The associated great circle paths refer to the mid-latitude scope of observation. Each station is monitoring multiple narrowband channels from Navy stations. A brief introduction into the technique of these VLF transmitters and a summary of frequently received signals is given in the next subsection.

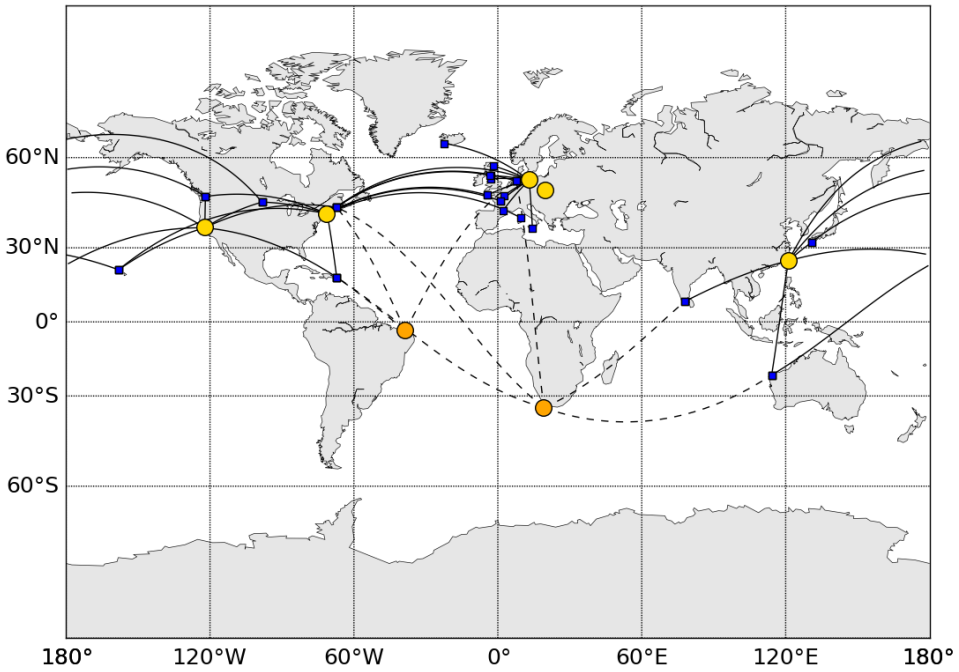

Figure 19: The GIFDS network and associated radio propagation paths: The operating stations (NTZ, KRK, BOS, STA, TWN) are marked by yellow circles. The corresponding great circle propagation paths of received VLF signals are drawn in black. The paths for KRK are not shown, as it receives the same VLF transmitters as Neustrelitz. Planned stations are marked in orange. The dashed lines are the propagation paths of the expected receiving signals. [extended from Wenzel et al. (2016)]

3.1.2 VLF transmitters

For our analysis we need VLF transmitters that operate full time and emit a stable signal of permanent reliable quality (e.g. transmitter power and MSK modulation). Such stations are provided by the navies after the systems were introduced for communications at sea. Today, they are mainly restricted to submarine radio. These VLF transmitters are identified by their call sign at a specific frequency; see Tab. 7 for a list of regularly observed radio stations.

In the following, two specific transmitters are described: Cutler NAA, one of the most powerful radio transmitters in the world, and the German equivalent, Rhauderfehn DHO38, with the special characteristic of ground connection.

Cutler NAA VLF transmitters require large antenna installations that consist of a couple of masts of over 100 m in height in order to transmit signals with powers of 20 kW up to 2 MW. These arrays occupy great areas of many square kilometers. Fig. 20 shows the antenna array of Cutler NAA, which is maintained by the U.S. Navy. It operates at a frequency of 24 kHz. NAA is one of the most powerful VLF transmitters in the world. The antenna field is located at the shore of the Atlantic nearby Cutler, Maine. It is composed of two separate arrays, the north and the south array. Each of them consists of 13 steel masts that are tied by horizontal cables in a hexagonal shape – a *trideco*. The central tower (304 m high) is surrounded by six 266.7 m masts that form the inner ring of 556 m radius. Six outer ring masts of 243.5 m height are placed in a distance of 935.7 m. Both arrays function as one electrically short monopole antenna. The metal towers radiate VLF waves and the network of horizontal cables works as a large capacitor, which improves the performance of the vertical radiator. As the ground ought to have an extremely low electrical resistance, each tower base is additionally connected to earth ground by a radial network of cables in the air (a so-called counterpoise). If the soil conditions are fulfilled as in Rhauderfehn, the cables are usually buried directly in the earth.

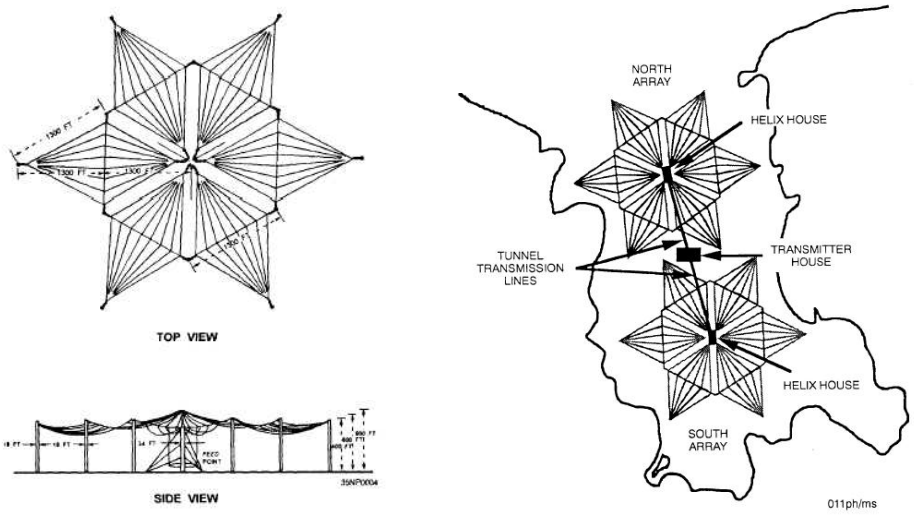

Figure 20: VLF transmitter NAA Cutler Maine: Illustration of the antenna design. [taken from Lombardi and Nelson (2014)]

Frequency [kHz]	Call sign / Country	Latitude	Longitude	Remarks
11.90	RSDN-20 / RU	-	-	Alpha signal, various locations
12.09	RSDN-20 / RU	-	-	Alpha signal, various locations
12.65	RSDN-20 / RU	-	-	Alpha signal, various locations
14.88	RSDN-20 / RU	-	-	Alpha signal, various locations
15.60	RSDN-20 / RU	-	-	Alpha signal, various locations
16.30	VTX1 / IN	8.3870	77.7528	
17.00	VTX2 / IN	8.3870	77.7528	
18.10	RDL / RU	-	-	FSK signal, various locations
18.20	VTX3 / IN	8.3870	77.7528	
19.20	VTX4 / IN	8.3870	77.7528	
19.60	GBZ / GB	54.9000	-3.2667	
19.80	NWC / AU	-21.8163	114.1656	
20.27	ICV / IT	40.9231	9.7310	
20.50	RJHxx / -	-	-	Beta time signal, various locations
20.90	HWU / FR	46.7131	1.2444	
21.10	RDL / RU	-	-	FSK signal, various locations
21.40	NPM / US	21.4202	-158.1511	
21.75	HWU / FR	46.7131	1.2444	
22.10	GQD / GB	54.7318	-2.8830	
22.20	JJI / JP	32.0764	130.8286	
23.00	RJHxx / -	-	-	Beta time signal, various locations
23.40	DHO38 / DE	53.0789	7.6150	Off: Daily, 7:00 - 8:00 UTC
24.00	NAA / US	44.6449	-67.2816	
24.80	NLK / US	48.2035	-121.9168	
25.00	RJHxx / -	-	-	Beta time signal, various locations
25.20	NML / US	46.3660	-98.3356	Off: Tuesdays, 12:00 - 19:00 UTC
26.70	TBB / TR	37.4127	27.3233	
37.50	NRK / IS	63.8503	-22.4668	
40.00	JJY-40 / JP	37.3726	140.8489	Time signal
40.75	NAU / PR	18.3988	-67.1776	
45.90	NSY / IT	37.1257	14.4364	
57.40	GXH / GB	58.5889	-3.6333	
60.00	WWVB / US	40.6777	-105.0472	Time signal
60.00	JJY-60 / JP	33.4654	130.1754	Time signal
62.60	FUG / FR	43.3868	2.0974	
63.85	FTA63 / FR	48.5447	2.5783	
65.80	FUE / FR	48.6377	-4.3507	
68.50	BCP / CH	34.948558	109.542978	Time signal
77.50	DCF77 / DE	50.0154	9.0083	Time signal
81.00	GYN / GB	53.8301	-2.8343	
129.10	DCF49 / DE	50.0142	9.0115	EFR / Mainflingen, FM signal
135.60	HGA 22 / HU	47.3731	19.0048	EFR / Lakihegy, FM signal
139.00	DCF39	52.2869	11.8973	EFR / Burg, FM signal

Table 7: List of transmitters available to the GIFDS network, their call sign, location, and special remarks. [extended from http://www.mwlist.org/, https://sidstation.loudet.org/ and Klawitter and Herold (1995)]

Rhauderfehn DHO38 The radio station Rhauderfehn DHO38 operates at a frequency of 23.4 kHz and belongs to the German Navy. It consists of eight identical umbrella antennas, each with a height of 352.8 m and a width of 2.2 m. Every mast has a transmitting power of 100 kW. So, the total transmitting power of DHO38 is 800 kW. In contrast to the ground connection of Cutler, Rhauderfehn has a network of 200 radial cables, 400 to 450 m long, 30 cm under the ground surface, covering the whole area of influence under each umbrella antenna. The high electrical conductivity was an important factor for the choice of this location. DHO38 is designed to emanate frequencies between 14 and 50 kHz. Due to the very low frequency and the high power, the transmitter's signal can be received worldwide, down to a water depth of 30 m.

3.1.3 VLF receiver systems

Principally, receiving conditions on the ocean and under the sea are good, while urban areas may cause problems. Electronic devices can cause noise over the whole VLF range, and so, close to civilisation, finding quiet locations can be difficult. The issue is to identify and eliminate the disturbances that might interfere with the VLF receiver signal. There are several kinds of VLF receivers that are also used for flare monitoring. Many systems only use the internal audio card of the computer to digitalise the signal, e.g. some receiver systems of AARDDVARK and SAVNET. There is one major disadvantage, as the computer causes direct disturbances on the lower frequency ranges and may contaminate the original signals. On this account there are some VLF receivers developed in order to minimise internal disturbers from the own power network.

The SID monitor, designed by the Stanford Solar Center, is a low cost VLF receiver measuring the narrowband amplitude of a single selected frequency. Within the SID Space Weather Monitor program, receivers are build and installed at high schools all over the world. For this, the SID monitor has been designated by the International Heliophysical Year (IHY) Committee (see http://sid.stanford.edu/). In further developments, Stanford's Solar Center released a second kind of SID monitor, the so-called SuperSID, which is more cost-efficient. Another development by this center is the AWESOME (Atmospheric Weather Electromagnetic System of Observation, Modelling, and Education) monitor. Similar to the SID, AWESOME measures the amplitude, and moreover, the phase enabled by the higher sensitivity via GPS connection and broadband data of 100 kHz over the full ELF/VLF waveform. Both require a computer and an antenna. The monitor itself is no longer available.

In 2007, the national project SIMONE (Solar and Ionospheric Monitoring Network) was initiated within the scope of the IHY by the United Nations in collaboration with the Stanford University and Stanford's Solar Center (Eckelt et al., 2011). Several high schools in northern Germany joined the project in order to investigate solar and terrestrial influences on the propagation of communication and navigation signals. The data is stored at DLR Neustrelitz. Just a few years later in collaboration with associates, the DLR_Project_Lab Neustrelitz developed an own receiver – the SOFIE RX (Solar Flares detected by Ionospheric Effects). The monitor has one specific advantage as it can operate autonomously without any additional computer. Only for the installation a laptop is required. For further information the reader is referred to

Wenzel et al. (2013) and http://www.projectlab-neustrelitz.de/sofie/de/sofie.php.

At the beginning of 2011, the Institute of Communication and Navigation in Neustrelitz (IKN-NZ) also started test measurements on site using a commercial Perseus receiver (http://microtelecom.it/perseus/software.html). It is a software defined radio (SDR) offering an analogue-to-digital converter, a digital down-converter and a PC interface. The following paragraph describes the development of a continuous and reliable VLF monitoring system at IKN Neustrelitz, later known as GIFDS.

The GIFDS monitoring stations The first VLF measurements with the Perseus SDR were performed in connection with the Linutop, a small disk- and fan-less computer. The Linutop processed the received spectrum using the monitoring software by Mayer (2011), commissioned by DLR. The VLF amplitudes of multiple VLF signals were determined and stored every two seconds on an external hard drive. In order to build up a network of receivers, data had to be transmitted to one main server in near real time. In this regard, the software was revised by Mayer (2012) with internet transmission and an enhanced sampling rate of 1 Hz. Due to increasing processing power, the Linutop was replaced by a laptop. Consequently, the whole monitoring system, named GIFDS station, consists of a laptop, a Perseus SDR, and a MiniWhip antenna.

The software defined radio is the core of each monitoring station. The Perseus SDR is suitable for frequencies from 10 kHz to 30 MHz (i.e. from VLF to HF range). In general, a signal is processed by a preamplifier and pre-selectors, whereupon it is converted from an analogue to a digital signal by an ADC (http://microtelecom.it/perseus/software.html). By implementing DSP (digital signal processing) algorithms in a FPGA (field programmable gate array), a specific part of the spectrum is separated. Hence, the computer receives samples for the selected frequency ranges. Subsection 3.1.4 will describe the signal processing software in more detail.

Each GIFDS station receives signals via an active electric field probe. More precisely a Mini-Whip antenna, operating on 5 V DC, developed by Bakker (a,b) is used. The antenna is characterised by a *whip* as capacitance which is coupled to the electric field. In this case, it is a small piece of copper plate directly printed on the circuit board. The antenna was designed for improved LF reception and is capable of covering frequencies ranging from 10 kHz to 30 MHz, just as the Perseus SDR. "To improve signal quality, the antenna is grounded and placed 1 m above the antenna platform, commonly on a roof (see Fig. 22). Since the magnetic component can be shielded by the roof it is less sensitive to magnetic influences. Hence, the system is suitable for use in urban areas. As VLF receiver we are using a software defined radio (Perseus SDR) capable of providing an up to 2 MHz wide part of the spectrum. The corresponding output of complex I/Q samples is processed on a PC where signal amplitudes and phases of each frequency channel are determined. The resulting data of each receiver in the network is streamed to the main server at DLR Neustrelitz (53.35°N 13.06°E) where fast data analysis takes place."[10]

[10] slightly modified quotation from Wenzel et al. (2016), page 235

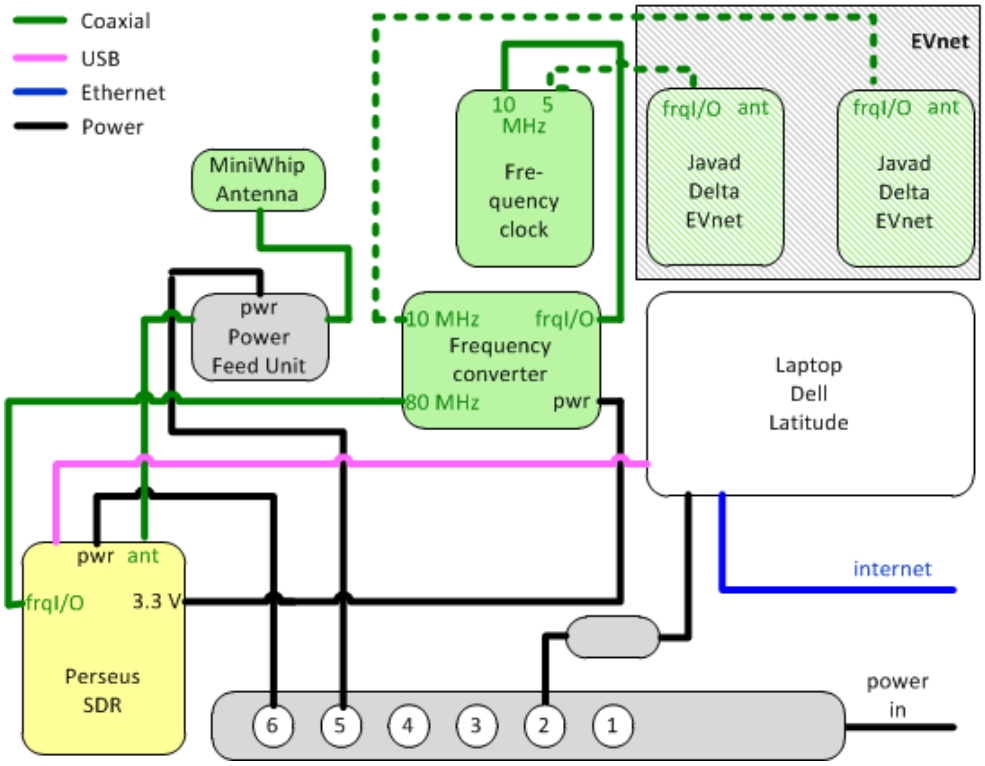

Figure 21: The GIFDS station at DLR Neustrelitz: The left panel shows the set-up of the antenna on the roof. It contains a MiniWhip antenna (detailed view including the remote power supply on the top right). The bottom right picture shows the actual GIFDS setup in Neustrelitz including a frequency standard, a Perseus SDR receiver, a frequency converter, and a laptop.

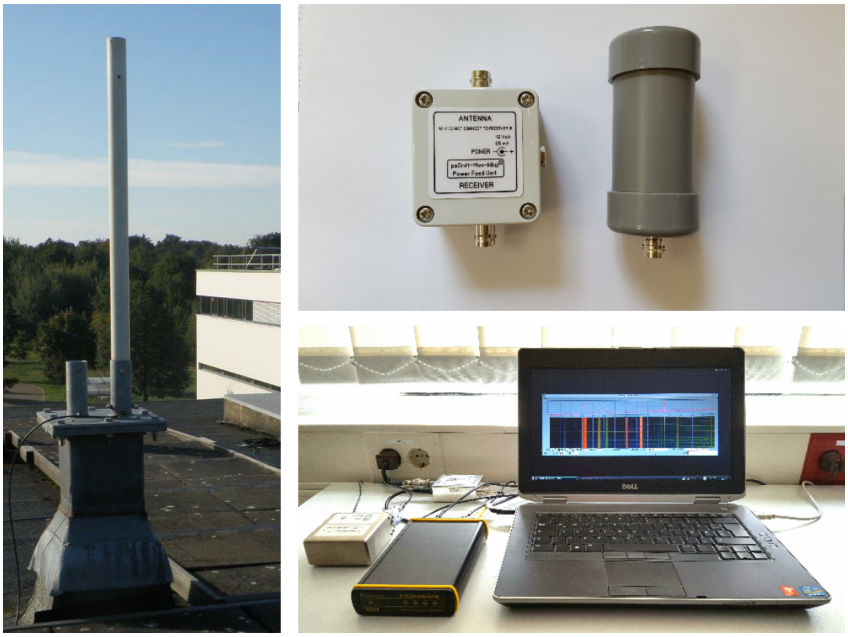

Figure 22: The GIFDS station at DLR Neustrelitz: The left panel shows the set-up of the antenna on the roof. It contains a MiniWhip antenna (detailed view including the remote power supply on the top right). The bottom right picture shows the Perseus SDR receiver. [adapted from Wenzel et al. (2016)]]

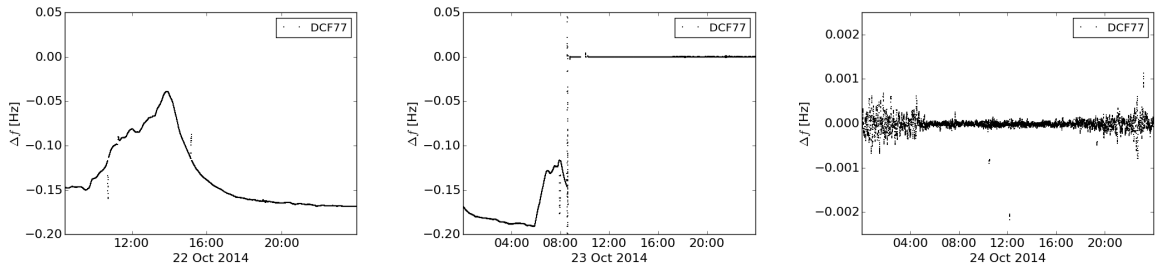

Figure 23: Variation of the frequency offset in Hz for the time signal DCF77 received in Neustrelitz during the test of the prototyp frequency converter: with original Perseus SDR (left panel), during the change with a modified one including a LPFRS frequency standard (middle panel), and using the modified GIFDS setup. Mind the different scaling for the right panel.

In order to improve timing and frequency accuracy, the Perseus SDR was modified and connected to a rubidium standard, which has a stability of $1 \cdot 10^{-12}$ per 100 s and a long-term stability of $1 \cdot 10^{-10}$ per year. However, the measured deviation to the time signal of DCF77 is about $0.2 - 0.5$ ppb during daytime and $1.0 - 1.2$ ppb during nighttime. A constant frequency offset by the rubidium standard is corrected in the first instance, as seen in Fig. 23.

The connection of the Perseus SDR and the frequency standard required minor hardware modifications on the receiver, as no external reference frequency input is provided. By removing the SMD condensator between the 80 MHz quartz oscillator and pin 9 of the LTC2206 AD converter, we could connect it with an 80 MHz input. This is provided by a 10 MHz rubidium standard in connection with a 10-to-80 MHz frequency converter. This converter consumes 3.3 V which is tapped by the chip voltage regulator (cf. Fig. 24). In early 2015, Stanford was the first site installed with a modified Perseus SDR and an external rubidium standard. It is operating without disturbances and has a fixed frequency offset of $1.4 \cdot 10^{-9}\, Hz$. Now, Neustrelitz is also operating with the new set-up and in near future all receiving stations of GIFDS will be equipped with this technological improvement (Wenzel et al., 2016).

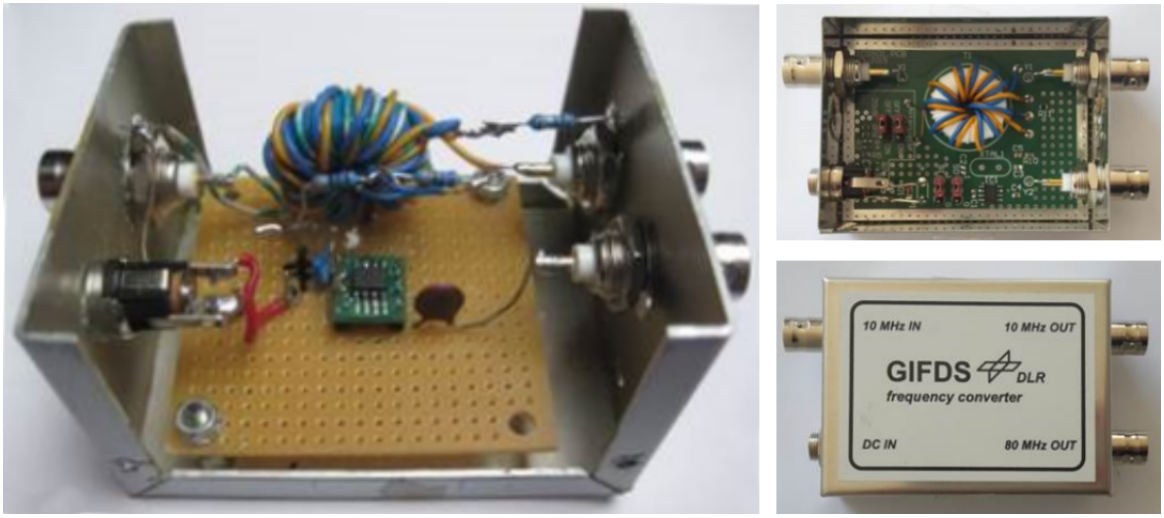

Figure 24: 10 to 80 MHz frequency converter in the first test setup (left) and final installation (middle and right panel): First tests of the prototype where performed in 2014/2015. Afterwards the frequency converter was installed permanently in Stanford, Neustrelitz, and Taiwan.

3.1.4 Monitoring software and signal processing

The monitoring software *HFMonitor*, developed and revised by Mayer (2011, 2012, 2014b), is written in C/C++ and consists of several modules (see https://github.com/hcab14/HFMonitor). List. 1 shows the directory tree of HFMonitor. The top folders contain the tools that are necessary for the software installation. Before a monitoring station becomes operational, several external dependencies need to be compiled and deployed into the Linux operating system.

The actual monitoring source code is stored in *include* and *src*. After the overall installation, each station has to be configured according to its specifications (cp., List. 2). The general workflow is given in input files defined in the *run* directory (see List. 3). An example of input files and xml configuration files can be found in the attachments B.

Listing 1: Directory tree of HFMonitor

```
HFMonitor
|
|
|                          Installation and software operation tools:
|-- bin                    -   Binary programs generated after final installation step
|   |-- fltk_spec              -   Spectrum display of a specified I/Q data stream
|   |-- server_ls              -   Available data-streams from a specified broadcaster
|   |-- save_datastream        -   Storage of data-streams into files
|   `-- read_datastream        -   Play-back of data-streams from specified files
|-- build                  -   Source compilation directory
|-- software               -   Makefiles for installing external dependencies
|
|
|                          Actual monitoring software:
|-- include                - header files
|-- src                    - source files
|-- run                    - input files providing stationwise system configuration
|-- config                 - xml configuration files of the processors
|
|
|                          Software operation:
|-- start.sh               - Start of monitoring software
|-- stop.sh                - Stop of monitoring software
|-- setup.sh               - Installation of missing libraries / Export library path
|-- check_running.sh       - Status of operation
|-- functions.sh           - Contains specification of local user and station name
|-- display_spec.sh        - Spectrum display of combined signal groups, e.g., NavyMSK
|
|
|-- Log                    Log-files recording events
|-- log*.txt               of the single processors
|
|
|-- DataBOS
|-- DataKRK                Recorded amplitude and phase information
|-- DataNTZ                of each GIFDS station (BOS, KRK, NTZ, STA, TWN)
|-- DataSTA                filed per transmitter and per day
`-- DataTWN
```

Listing 2: HFMonitor/config

```
HFMonitor/config
|
|-- multi_client_BOS.xml
|-- multi_client_KRK.xml
|-- multi_client_MUN.xml
|-- multi_client_STA.xml
|-- multi_client_TWN.xml
|
|
|-- multi_client_writer_BOS.xml
|-- multi_client_writer_KRK.xml
|-- multi_client_writer_MUN.xml
|-- multi_client_writer_NTZ.xml
|-- multi_client_writer_STA.xml
|-- multi_client_writer_TWN.xml
|
|-- multi_client_writer_NTZ_fromBOS.xml
|-- multi_client_writer_NTZ_fromKRK.xml
|-- multi_client_writer_NTZ_fromMUN.xml
|-- multi_client_writer_NTZ_fromSTA.xml
|-- multi_client_writer_NTZ_fromTWN.xml
|
|
|-- multi_downconvert_BOS.xml
|-- multi_downconvert_KRK_0.xml
|-- multi_downconvert_KRK.xml
|-- multi_downconvert_MUN.xml
|-- multi_downconvert_NTZ.xml
|-- multi_downconvert_STA.xml
|-- multi_downconvert_TWN.xml
|
|
|-- perseus_server_BOS.xml
|-- perseus_server_KRK.xml
|-- perseus_server_MUN.xml
|-- perseus_server_NTZ.xml
|-- perseus_server_STA.xml
`-- perseus_server_TWN.xml
```

Listing 3: HFMonitor/run

```
HFMonitor/run
|
|-- BOS
|   |-- 0-perseus_server.in
|   |-- 1a-client_multi_downconvert.in
|   |-- 2a-multi_client_to_bc.in
|   `-- 3a-multi_client_writer.in
|-- KRK
|   |-- 0a-perseus_server.in
|   |-- 0b-cuda_mutex.in
|   |-- 1a-client_multi_downconvert.in
|   |-- 2a-client_multi_downconvert.in
|   |-- 3a-multi_client_to_bc.in
|   `-- 4a-multi_client_writer.in
|-- MUN
|   |-- 0-perseus_server.in
|   |-- 1a-client_multi_downconvert.in
|   |-- 2a-multi_client_to_bc.in
|   `-- 3a-multi_client_writer.in
|-- NTZ
|   |-- 0-perseus_server.in
|   |-- 1a-client_multi_downconvert.in
|   |-- 1b-multi_client_writer.in
|   |-- 1c-multi_client_writer.in
|   |-- 1d-multi_client_writer.in
|   |-- 1e-multi_client_writer.in
|   |-- 2a-multi_client_to_file.in
|   `-- 3a-multi_client_writer.in
|-- STA
|   |-- 0-perseus_server.in
|   |-- 1a-client_multi_downconvert.in
|   |-- 2a-multi_client_to_bc.in
|   `-- 3a-multi_client_writer.in
`-- TWN
    |-- 0-perseus_server.in
    |-- 1a-client_multi_downconvert.in
    |-- 2a-multi_client_to_bc.in
    `-- 3a-multi_client_writer.in
```

The core processes of the GIFDS framework with its configuration files (given in List. 2) are depicted in Fig. 25. The SDR delivers digitised data via an interface which is capable of handling half a million samples per second. Through the *perseus_server* processor, the I/Q samples are made available as a data stream centered around 220 kHz. By overlap-save finite impulse response (FIR) filter banks, special segments of the spectrum are selected (see processor *client_multi_downconvert* in Fig. 25). It is possible to obtain multiple channels of different spectral ranges (Borgerding, 2006). These are then shifted and down sampled to I/Q data streams at 1 kHz. As the sampling rate is low and only a fraction of the full bandwidth provided by the SDR is analysed, the demodulation of VLF signals using Minimum Shift Keying (MSK) is computationally more efficient. In order to demodulate MSK signals, *multi_client_to_broadcaster* applies the algorithm detailed in Wescott (1990). Internally, the squared I/Q samples unveil two peaks in the spectrum that are symmetric to the carrier. They are locked with two PLLs

(phase-locked loops). The difference yields the phase. Measuring amplitudes is uncritical. Since it is a coherent demodulation, the resulting carrier can be used for getting a bit stream. Moreover, no time synchronisation is needed. Nevertheless, an additional frequency clock is used in order to avoid thermal drifts at the internal quartz oscillator of the Perseus receiver.

Finally, for obtaining the field strength, the spectrum of the I/Q samples is calculated with the help of a Fast Fourier Transform (FFT)

$$F(X)_k = \sum_{j=0}^{n-1} \exp\left(2\pi kji/n\right) \cdot X_j,$$

where n denotes the number of samples. In order to generate a periodic signal and remove artifacts, first a window function is applied on the input X. The computed signal is then run through a low-pass filter to get rid of highly oscillating noise. The system provides different methods of strength calculation. Within the scope of this work an average density approach is used for getting the amplitudes of the VLF signal. The frequency spectrum is calibrated at a known reference time signal (e.g., DCF77 for Neustrelitz). Formerly using a find peak approach, the frequency is now estimated with a Goertzel filter which is computationally more efficient (see, Goertzel, 1958).

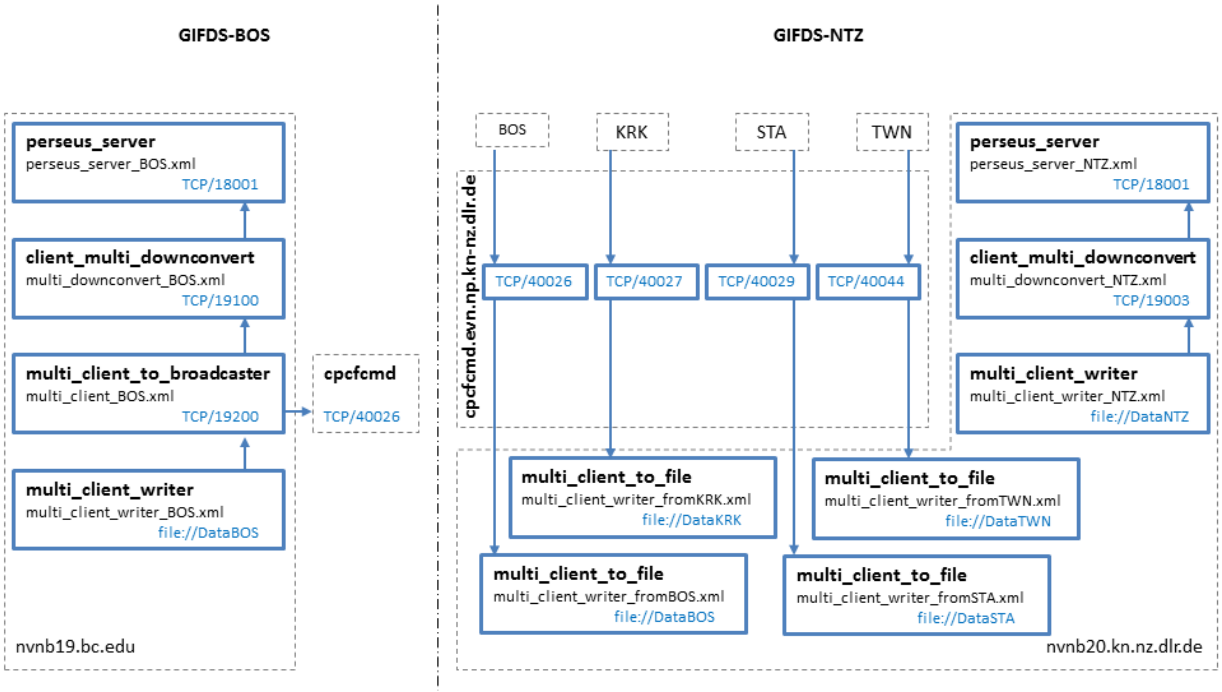

Figure 25: The GIFDS framework and its relevant XML files for configuration: The setup for the GIFDS stations in Boston BOS (left) and Neustrelitz NTZ (right) is pictured. Visibly, NTZ moreover takes care of the administration processes like collecting the other's data. The description of the software, its modules and parameters are documented in Mayer (2011, 2012, 2014b).

Further configurations in *multi_client_to_broadcaster* define the interfaces of transferring desired VLF signals over TCP/IP links to the main server in Neustrelitz. The *multi_client_writer* processor ensures an additional local storage of the data, so no measurements are lost in case of disruptions of the network connections. In Neustrelitz, the server runs additional processors for each incoming data stream of the other receiving sites (see *multi_client_to_file* processors in Fig. 25). The installation and the framework are subject to continuous development and fine-tuning. The last addition was the implementation of phase measurements, which are currently undergoing technical validation.

In order to guarantee a continuous monitoring of the whole GIFDS network, each station computer operates a special system utility which uses a time based job scheduler to check every minute whether all the crucial GIFDS software components are up and running. Additionally, during the boot phase the operating system automatically starts the HFMonitor software, unless its runtime status was explicitly set to *stopped*. Once per day, all the GIFDS measurement data stored on the HFMonitor computer is mirrored on a cluster of network storage devices under the share name *NZ_Measurement_Data*.

Fig. 26 depicts a received signal at several stations of the GIFDS network. Each panel shows the signal strength over the frequencies in the range from 10 to 30 kHz and its corresponding waterfall diagram of the last 6 seconds. The noisy signal over the VLF range (particularly high between 24 and 26 kHz) reflects that the site Neustrelitz is more disturbed than the others. The reason is presumably in the slightly different technical equipment at the location that uses switched-mode power supplies. We could reduce the noise by moving the station to a higher building and apply a grounding for the antenna. Nevertheless, the station is not yet optimal. We have a clear spectrum in Stanford without potential sources of interference except for sferics. Sferics are broadband electromagnetic impulses caused by lightning discharges. As they are only for a short time, they are visible as green-to-yellow horizontal lines in the waterfall diagram. Even lightning strokes from the other hemisphere can generate an electromagnetic wave, a so-called whistler. They travel along the geomagnetic field lines to the other hemisphere, get dispersed through the ionospheric and magnetospheric plasma and can be received as descending sound. Taiwan experiences small-scale interferences from time to time as well as sferics. Nevertheless, TWN can still resolve the Russian Alpha signals in the range between 10 to 15 kHz.

Fig. 27 shows the corresponding spectra for the time signals of the three exemplary stations. A time signal is a continuous wave (CW), i.e., of constant amplitude and frequency. By deriving the precise frequency of the time signals, all measurements are calibrated in the frequency range.

3.1.5 Data management

Each data stream has a unique name. In order to optimally utilise a limited bandwidth, each data stream is given a unique identification number based on its epoch and only those identification numbers are transferred. The clients are provided the association parameters which link the identification number together with the stream name in the form of a so-called stream directory. It is a special data sentence which is broadcast at the establishing of a new connection and

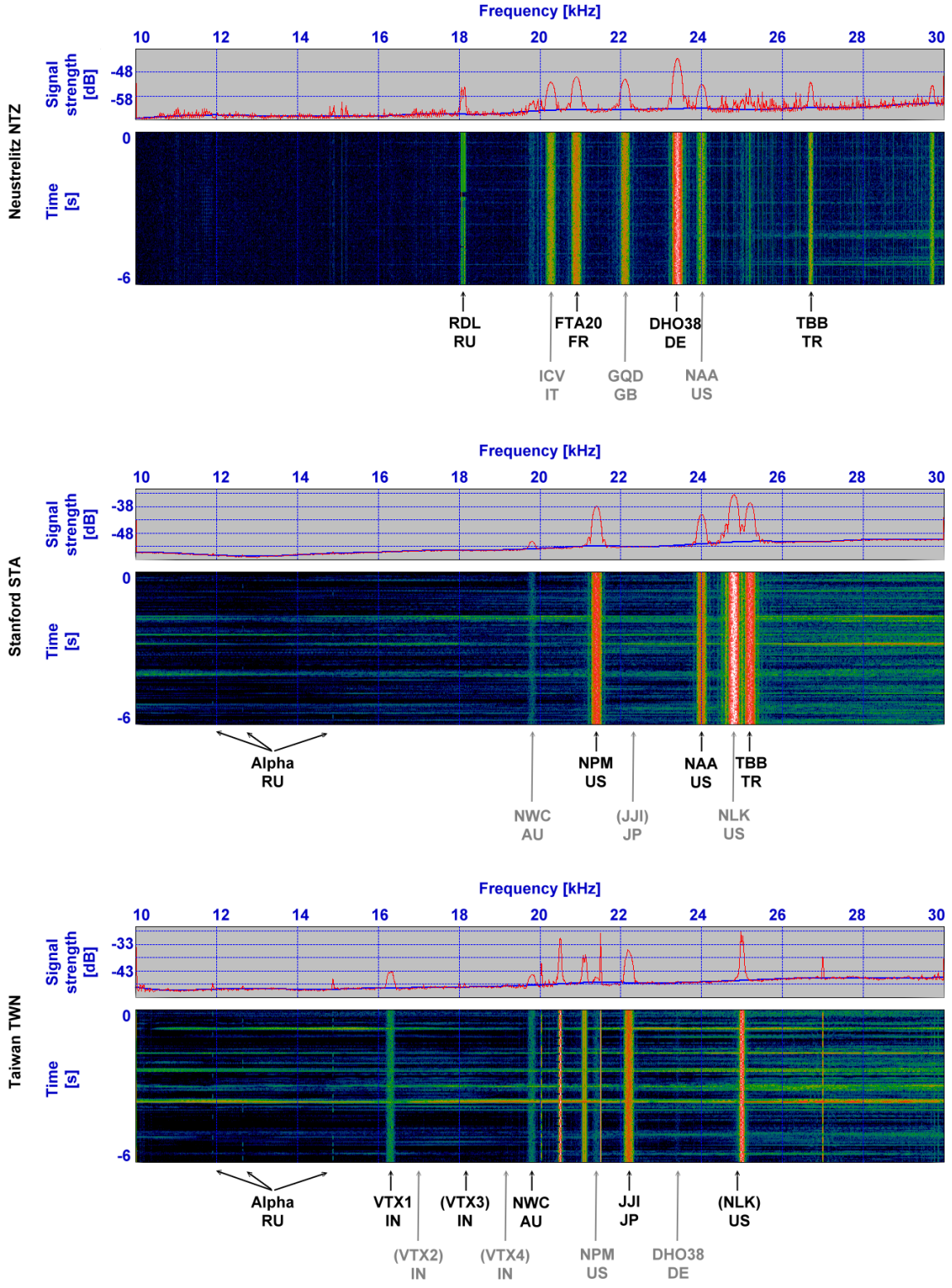

Figure 26: Examples of received VLF signal amplitudes for Neustrelitz, Stanford, and Taiwan over a short period of time, each visualised by a spectrogram and waterfall plot: The receiver sites show a different sensitivity to background noise. Several transmitters (call signs annotated) can be identified in the overall measurement.

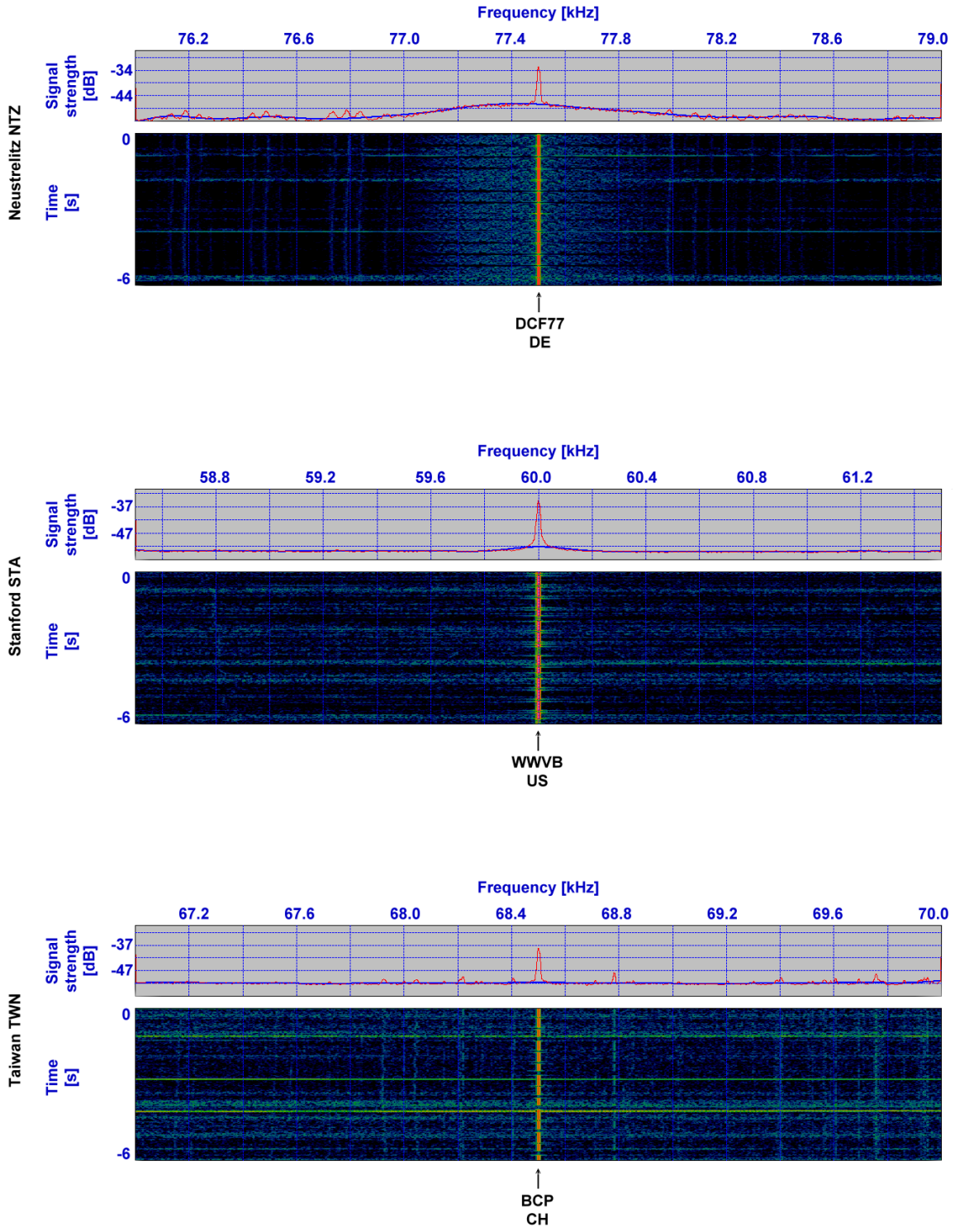

Figure 27: Examples of incoming local time signals (used for frequency calibration) in Neustrelitz, Stanford, and Taiwan: The receiver sites show a different sensitivity to background noise.

whenever the configuration of streams changes. In addition, the server and the client exchange special keep alive pings every second. It helps to ensure that they are communicating with each other. If either the client or the server stops responding, the server will close the connection with the client and the client software will exit, accordingly. The broadcaster uses one TCP/IP socket per client. That is why it is necessary to multiplex several data streams.

All results are stored in ASCII text files (cp., List. 4) which conform to the following format:

- In the beginning of each file there is a header section. All its lines start with a single hash character and contain parameters and their values written in the form parameter=value [unit]. Every data file must contain at least the parameters: Station, Computer, f_c (i.e., the center frequency in Hz) and f_m (i.e, the bandwidth, or the modulation rate in baud, respectively). The last line of the header section lists the names of the data fields.

- The rest of the file contains the lines filled with space separated values corresponding to the above-mentioned data fields. Each line starts with a UTC date (yyyy-mm-dd) and UTC time (HH:MM:SS.ssssss). The timestamp is followed by the measurements.

Listing 4: File format of the stored MSK signal NAA composed of the header with signal and data description and the 1Hz-sampled measurements

```
# Station  = NTZ
# Computer = Latitude E6430 : N-Series Base
# fc[Hz] =  24000.00000000
# fm[Hz] = 200.000
# Time_UTC Amplitude[dB] S/N[db] Phase[rad]
2016-06-01 00:00:00.181024  -45.76   15.47  2.436
2016-06-01 00:00:01.181083  -45.67   12.14  2.437
2016-06-01 00:00:02.181112  -45.78   17.23  2.439
2016-06-01 00:00:03.180906  -45.55   12.16  2.439
2016-06-01 00:00:04.180948  -45.56   11.69  2.438
2016-06-01 00:00:05.180968  -45.89   13.61  2.437
2016-06-01 00:00:06.181003  -45.53   12.39  2.439
2016-06-01 00:00:07.181019  -45.89    8.35  2.438
2016-06-01 00:00:08.181004  -45.90   15.48  2.438
2016-06-01 00:00:09.181039  -45.87   10.64  2.439
2016-06-01 00:00:10.181025  -45.85    5.61  2.438
...
...
...
2016-06-01 23:59:50.144967  -47.30    6.51  0.611
2016-06-01 23:59:51.145002  -46.69   11.86  0.613
2016-06-01 23:59:52.145027  -46.73   11.26  0.613
2016-06-01 23:59:53.145142  -46.84    9.92  0.615
2016-06-01 23:59:54.144953  -46.63   19.18  0.618
2016-06-01 23:59:55.145078  -46.97   15.94  0.621
2016-06-01 23:59:56.145039  -46.82   11.58  0.619
2016-06-01 23:59:57.145093  -46.80   10.50  0.621
2016-06-01 23:59:58.145084  -46.79   14.21  0.621
2016-06-01 23:59:59.145000  -46.84   16.89  0.623
```

3.2 Comparative data sets

3.2.1 Ground-based measurements of the ionosphere

In the context of the solar eclipse in 2015 over Europe (investigated in Chapter 5), other measurements are taken into account in order to derive relations of ionospheric effects. For this purpose, TEC data provided by the IMPC (http://impc.dlr.de/) and the ionosonde data of the stations DB049 in Dourbes/Belgium ($50.1°N$, $4.6°E$) are used. To get an idea of the overall ionospheric behaviour, TEC estimations from GNSS measurements provide a possibility to observe variations over time and space. By the refractive index (16) and the definition of TEC (8), the ionospheric delay of L-band frequencies (L1: $f_1 = 1575.42\,\mathrm{MHz}$, L2: $f_2 = 1227.60\,\mathrm{MHz}$) are given by (Jakowski et al., 1996)

$$d_I = \frac{K}{f^2}\int N(s)ds = \frac{K}{f^2}STEC$$

with $K = 40.3\,\mathrm{m^3 s^{-2}}$. So, the relative TEC can be derived by the carrier phases L_1 and L_2 via

$$STEC^{carr} = \frac{f_1^2 \cdot f_2^2}{K(f_1^2 - f_2^2)} \cdot (L_1 - L_2),$$

with

$$L_x = \rho + \frac{K}{f_x^2}STEC + \lambda_x N_x + \epsilon_{Lx}, \qquad \text{for } x = [1, 2].$$

Geometric distance between satellite and receiver ρ. The wavelength of the carrier phases is assigned by λ_x, and N_x describes the corresponding integer ambiguities, and ϵ_{Lx} describes the remaining errors. Analogously for the code measurements P_1 and P_2, the absolute (but noisy) TEC is given by

$$STEC^{code} = \frac{f_1^2 \cdot f_2^2}{K(f_1^2 - f_2^2)} \cdot (P_2 - P_1),$$

with

$$P_x = \rho + \frac{K}{f_x^2}STEC + \epsilon_{Px}, \qquad \text{for } x = [1, 2].$$

Absolute TEC information is derived from code and carrier phase measurements (Jakowski et al., 2011)

$$STEC^{rel} = STEC^{carr} + \langle STEC^{code} - STEC^{carr} \rangle$$

with the mean offset updated each epoch (indicated with brackets). In order to retrieve the vertical TEC from the slant TEC along the raypath, a mapping function is applied (Jakowski et al., 1996, 2011)

$$VTEC = \left(1 - \frac{R_e \cos\epsilon}{(R_e + h_i)^2}\right)^{-1/2} STEC$$

Empirical models are used to derive maps, like NTCM. However, we will only use the link information directly from the GNSS satellites. These measurements are provided in the framework of the IMPC (http://impc.dlr.de/). For further information on TEC estimation, the reader is referred to Jakowski et al. (1996, 2011).

Furthermore, ionosonde data is consulted to see variations of specific layers of the upper ionosphere. Ionosondes are a special kind of radar for vertical sounding (VS) of the ionosphere by sweeping pulses of frequencies ranging from below 0.1 MHz up to 30 MHz. Hence, the virtual height[11] of reflection h' is given by

$$h' = \frac{1}{2} c t_s,$$

where t_s denotes the signal travel time reflected at the ionosphere until the echo pulse is measured. With increasing frequency, the reflection height increases as described in section 2.3.1. Via (15), under vertical reflection (i.e., refractive index $n = 0$) and an emitted frequency approaching the plasma frequency, the maximum electron density $NmF2$ [electrons/m^3] is given by

$$NmF2 = 1.24 \cdot 10^{-2} (foF2)^2. \tag{19}$$

Here, $foF2$ [Hz] denotes the critical frequency which can still be reflected by the ionospheric F2 layer. In general, frequencies above 30 MHz (i.e., from the VHF range upwards) can penetrate the ionosphere. However, these signals still experience partial absorption. Since the plasma frequency (10) is dependent on the electron density, measurements of reflected radio waves provide information on this and consequently the height of the different ionospheric layers. In this sense, for the F2 region, the maximum plasma frequency, electron density, and the corresponding height are denoted by $foF2$, $NmF2$, and $hmF2$, respectively. Combining the peak electron density $NmF2$ and the TEC measurements at a given location, the width of the electron density profile can be derived by

$$\tau = \frac{TEC}{NmF2}. \tag{20}$$

This is the so-called slab thickness. Section 5.3.2 will present and discuss the resulting TEC maps of Europe and key parameters of one exemplary ionosonde during the 2015 solar eclipse.

3.2.2 Space-based solar radiation measurements

Satellite missions provide direct information of solar irradiation without large atmospheric effects and allow a better understanding of cause and reaction for the Earth's ionospheric system. Analysing solar activity and short-term disturbances, different satellite data is considered and used in this study. We included data of the Geostationary Observational Environmental Satellites (GOES) and a fundamental part of the future analysis deals with the EVE instrument (Extreme Ultraviolet Variability Experiment) of the Solar Dynamics Observatory (SDO). Tab. 8 lists the different characteristics of the satellite data.

[11] The virtual height describes the height where a single reflection takes place. This altitude is higher than the real reflection height, as the signal is bend gradually under Snell's law until the signal travels back. The relation is described by the *secant law*.

A main component of the developed solar flare detection algorithm, that is described in chapter 4, is the X-ray flux by GOES. Since 1976, GOES has provided X-ray measurements via 15 satellite missions. The NOAA satellites SMS-1 and SMS-2 already provided the solar X-ray flux from 1974 to 1976 with a resolution of 3 s. Since 1986, GOES' averaged data of 1 min is available (via NGDC, https://ngdc.noaa.gov/). For this study, we are primarily using GOES 15 data (GOES-West 135°W), as well as secondary measurements by GOES 13 (GOES-East 75°W) in case of outages or data gaps. Both satellites belong to the NOP series and hold an X-ray sensor telescope consisting basically of a collimator, magnets and a dual ion chamber with a detector/filter combination that makes the different measurements of the GOES satellites comparable and almost identical. As the satellite environment can contain high energy electron fluxes of over 2 MeV, the ion chamber is shielded in order to reduce response to Bremsstrahlung. Direct response of electrons is mostly prevented by magnets. So, the X-ray measurements are largely resistent to high electron fluxes. Each GOES satellite observes two soft X-ray channels: a short channel with wavelengths from 0.05 to 0.4 nm and a long channel from 1 to 8 nm. As shown in Tab. 8, samples of 2 s are binned to averages of 1 min and are provided by SWPC (http://www.swpc.noaa.gov/). Due to GOES' geostationary orbit, the satellite is facing eclipse periods caused by the Earth's shadow. These regular interruptions last minutes to over one hour for approximately 45 to 60 consecutive days in spring, and again in fall.

Before analysing the GOES X-ray flux it should be mentioned that the archived spectral bands of GOES 8-15 are scaled to the level of GOES 7. The scaling factors were introduced by SWPC in order to remain consistent flare warning levels. With GOES 8 the spinning satellites were replaced by 3-axis-stabilised satellites. Although rocket measurements confirmed the accuracy of the new sensors the scaling factors remained as many users rely on consistency instead of absolute accuracy (https://ngdc.noaa.gov/). For true fluxes the short channel needs to be divided by 0.85 and the long channel by 0.7. Thus, absolute values are actually higher than indicated. This work maintains the traditional scheme for allowing comparisons with the provided flare alerts by NOAA http://www.swpc.noaa.gov/ and archived data by https://ngdc.noaa.gov/.

Mission	Spectral range	Full time resolution	Used time resolution	Since	
GOES	0.05 - 0.4 nm	2 - 3 s	1 min	1976	G13 unstable until 2014
	0.1 - 0.8 nm	2 - 3 s	1 min	1976	G13 unstable until 2014
	5 - 15 nm	10.24 s	1 min	2006	EUVA
	25 - 35 nm	10.24 s	1 min	2006	EUVB
	115 - 130 nm	10.24 s	1 min	2006	EUVE, H I, Lyman-α
SDO	0.1 - 7 nm	10 s	10 s	2010	
(EVE)	17.1 nm	10 s	10 s	2010	Fe IX-X
	25.7 nm	10 s	10 s	2010	
	30.4 nm	10 s	10 s	2010	He II line
	36.6 nm	10 s	10 s	2010	
	121.6 nm	10 s	10 s	2010	H I, Lyman-α

Table 8: Comparison of available satellite data of GOES and SDO (EVE) in terms of spectral range, time resolution and coverage.

In the context of studying the flare response, we literally extend the spectrum by including EUV measurements. A brief outlook on the opportunities of a spectral analysis is concluded in section 6.2. Therefore, different satellite data was considered, i.e. EUV measurements by GOES and SDO. The EUV sensor (EUVS) onboard GOES has collimators and magnets to provide parallel rays almost free of energetic electrons, and Zeolite blocks absorb any gases. The different spectral bands are provided by filters selecting a broader passband of wavelengths and a transmission grating reducing the passband to the defined wavelengths. Moreover, the grating blocks the visible part of the spectrum and as the filters are mounted directly in front of the silicon diode detectors scattering is reduced (https://ngdc.noaa.gov/). The EUVS shares the control electronics with the XRS of GOES. The whole instrument is pointed at the Sun in order to provide consistent measurements of the various spectral bands of the solar flux.

There are five spectral bands lying between wavelengths from 5 to 130 nm. Four of them are aligned with the maxima of the atmospheric heating rate, and the fifth band EUVA (5 - 15 nm) is essential for studying the production of minor constituents. However, only three channels (EUVA, EUVB, and EUVE) are available as calibrated data (version 2) from 2006 until 2014 (cp., Tab. 8). Within the calibration the count data is converted to an EUV flux

$$F_{EUV}\left[\frac{\mathrm{W}}{\mathrm{m}^2}\right] = \frac{(Counts - B_{EUV}[\mathrm{counts}]) \cdot G_{EUV}[\mathrm{A/count}] - V_{EUV}[\mathrm{A}]}{C_{EUV}[\mathrm{A/(Wm^{-2})}]}$$

with B_{EUV} as background, G_{EUV} as gain, V_{EUV} as visible light contamination, and C_{EUV} as units conversion factor.

SDO is a 3-axis stabilised satellite moving on a geosynchronous orbit. Similarly to GOES, it suffers from breaks during the eclipse seasons twice a year. The EVE instrument onboard SDO consists of different subsystems, e.g., the EUV SpectroPhotometer (ESP) and the Multiple EUV Grating Spectrographs (MEGS). The ESP provides four EUV emission lines in the range of 17 - 38 nm and also one X-ray channel in the range of 0.1 - 7 nm. Since the measurements of 36.6 nm seem to be disturbed, this information is not considered in further observations. The MEGS features a photodiode measuring the Lyman-alpha emission line at 121.6 nm. All SDO data used in our analysis is provided by the Laboratory for Atmospheric and Space Physics (LASP, http://lasp.colorado.edu/).

Fig. 28 presents GOES as well as SDO measurements of a quiet week (22 - 29 January 2013, top) and an active time period (13 - 20 October 2014, bottom). Using level 2 products of SDO, all measurements are averaged from 4 Hz to 10 s data (http://lasp.colorado.edu/). The X-ray measurements of both satellites, GOES and SDO, are comparable to each other, keeping in mind that the EVE instruments observes a broader spectral range. However, the EUV measurements by GOES show signatures of daily variations (as particularly seen in Fig. 28, lower panel, 115 - 130 nm and 123 nm), whereas the ones by SDO are very consistent. Also the EUVB channel by GOES (25 - 35 nm) seems to be noisy during the presented quiet period and is even missing later in 2014. Hence, we will concentrate on the EUV measurements by SDO, but stick to X-ray measurements by GOES. Unfortunately, the Lyman-alpha diode measurement of SDO is noisy and measures only during 20% of the day. Therefore, it is only useful as daily values rather for the spectral analysis of flares.

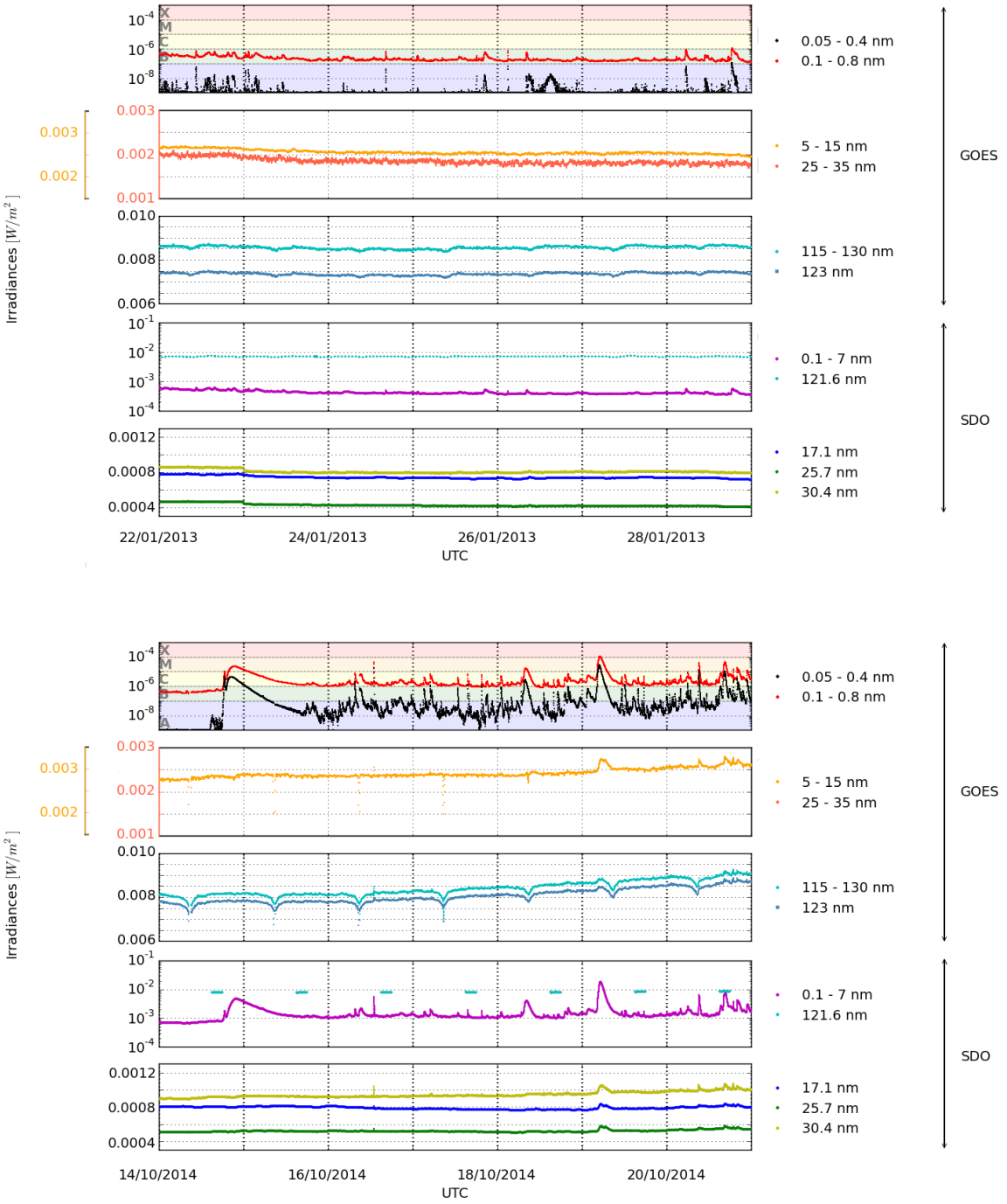

Figure 28: Examples of X-ray and EUV measurements of GOES and SDO (EVE) for a quiet period (upper panels) and an active week (lower panels).

„I do not think that the wireless waves I have discovered will have any practical application.“
Heinrich Hertz

4

Solar flare detection via VLF measurements

We will see that the waves meanwhile have developed high importance. Investigation of VLF measurements provide the opportunity to study the influence of solar flares. Our aim is to develop a warning system for heavy-impact sudden ionospheric disturbances. At first, we study the regular variation of the VLF signal strength in dependence of daytime, annual cycle, and location, as well as short-term perturbations by solar irradiation. After section 4.1, the response in VLF signals provoked by solar flares is subject in section 4.2. Then, in section 4.3, our flare detection algorithm is developed. The principle results of this part were made public in Wenzel et al. (2016). The basic idea for detecting perturbations in measured signals is to estimate the slope of the VLF amplitudes by looking at the most recent values of a channel. In order to eliminate measurement errors and take into account different solar zenith angles, multiple frequencies on several routes have to be combined. However, the general algorithm is adjusted to amplitude measurements, with the option of including phase information in the future.

Due to fluctuating diffusion and absorption taking place in the atmosphere, the original solar flux and the level that can be observed from the ground may differ. While the actual impact on the Earth can be judged quite well with VLF techniques, the original X-ray classification is hard to calculate inversely. For a comparison of flare peak heights and their corresponding base levels, GOES' radiation flux is consulted. To test the working and recognition stability of the proposed detection algorithm, in section 4.4, ground data of Neustrelitz from April 2014 to May 2015 is matched with the space-based records.

4.1 Characteristics of VLF measurements

The VLF spectrum, from the perspective of a receiver recording long-distance signals, is subject to geophysical constraints and hence varies strongly in time. The following sections discusses general observable trends in VLF signals originated in solar illumination, which changes in time over a day as well as over a year. Furthermore, the Earth-ionosphere waveguide determines the propagation of radio waves, whereat the respective propagation path is also significant. In addition, the signal may be influenced on its way from the transmitter to the receiver by local conditions.

4.1.1 Temporal variations

Diurnal variations The Sun causes strong changes in the electron density of the Earth's ionosphere and therewith possibly in the received VLF signals. So, it is reasonable to look for daily as well as seasonal behaviour. Fig. 29 (upper picture) shows the typical diurnal variation of undisturbed VLF measurements. It is rather smooth. It features an increase during sunrise, remains stable throughout the day until sunset, and finally decreases. During nighttime, the VLF signal strength is more unstable and generally larger. This is due to the absence of the absorbing D layer in the ionosphere, which defines the altitude of the Earth-ionosphere waveguide for VLF propagation (seen in the lower picture). All the times of sunrise and sunset, as well as corresponding solar zenith angles were calculated in Python using the PyEphem package (http://rhodesmill.org/pyephem/). The chosen measurement of one received VLF signal displays the strength in dB on 20 May 2016 for the propagation path NAA-NTZ. The corresponding solar altitude of the transmitter and receiver site, as well as of the mid sub-reflective point are given below over a shared time-axis. There is a clearly shaped plateau with a steady signal amplitude between the times of latest sunrise (here for NAA, blue dashed line marked by Tx) and the earliest sunset (here NTZ, red dashed line marked by Rx).

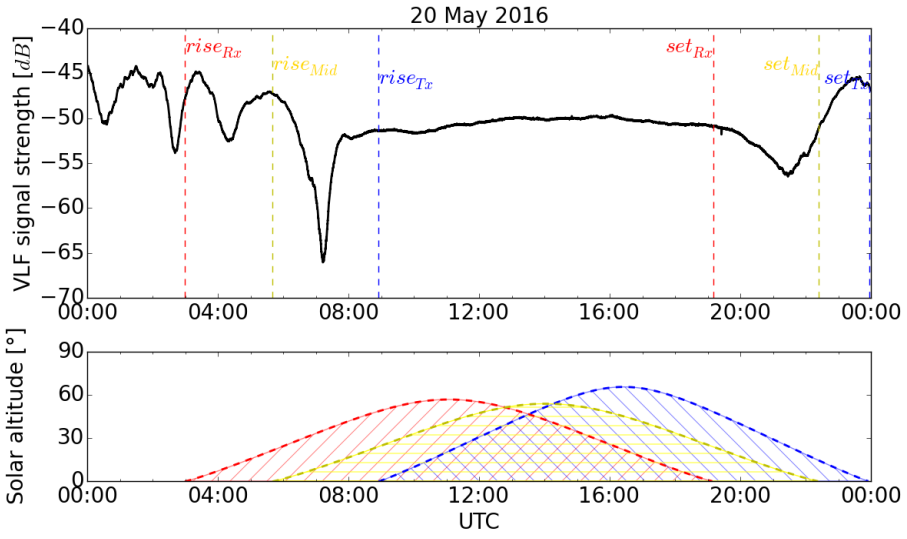

Figure 29: A typical whole day measurement at the example of NAA-NTZ on 20 May 2016 in comparison with the solar altitude of Tx (blue), Rx (red) and the mid sub-reflective point (yellow).

The twilight periods show very oscillating amplitudes which are characterised by lots of minima and maxima. The extremes strongly depend on the actual location of Tx-Rx on the globe, and after all, the spanning points' individual conditions of solar illumination. Note that the indicated sunrise and sunset times are given on site, and not at ionospheric heights of the D layer. The actual ionospheric height sunrise times occur earlier than on the ground, and conversely, the corresponding sunset times later. In fact, in an altitude of the subionospheric waveguide, the sunrise and sunset times of specific locations on the path coincide with the minima in the diurnal VLF signal variations of Fig. 29 (cp., Clilverd et al., 1999).

The day-night transition causes a modal conversion of the VLF signal. Roughly speaking, the number of minima is linked to the number of reflections in terms of the ray theory, although extremes can be superimposed and may cancel each other. The number of reflections can be rather hidden in case of the sunset time in Fig. 29 (here for the mid-point, yellow dashed line marked by Mid). The path of NAA-NTZ performs a long West-East propagation and shows up to three minima, and therewith three reflections can be considered with respect to the wave-hop theory. However, for defining a daytime window of reliable and stable measurements on fully illuminated propagation paths, the flare detection algorithm will use the more conservative times on the ground (see Section 4.3.1).

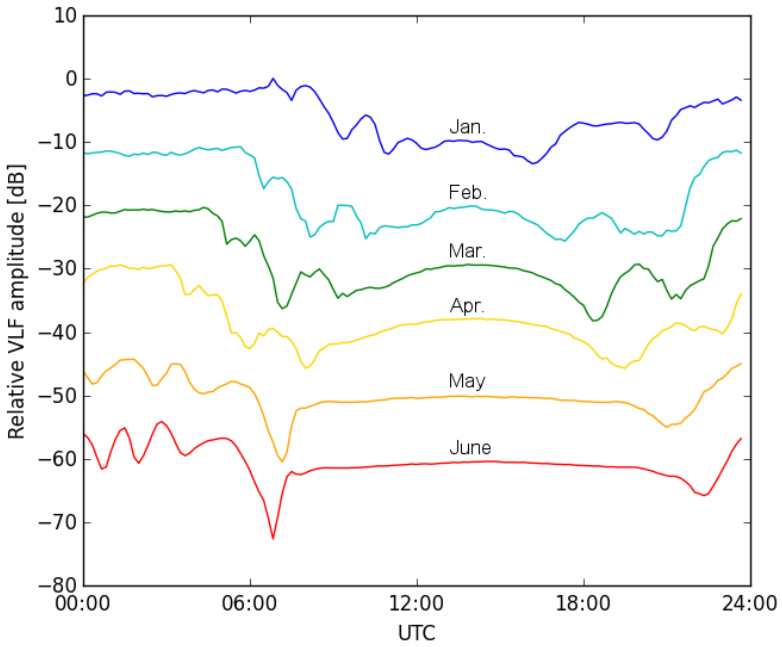

Figure 30: Daily pattern of NAA-NTZ varying in the first half of the year 2016: The graphs of a day representative for one month are calculated from about 30 full-day measurements averaged on 10 min intervals by taking medians over the whole month on every interval. The values were measured on the same relative scale, but their vertical positions in the figure are re-arranged for an easier comparison of the seasonal variation at a specific time.

Fig. 30 illustrates diurnal variations at an example of the propagation path NAA-NTZ. The monthly median over the 10 min averaged measurements exhibit a identifiable plateau, which indicates a clear daytime window. It is restricted by the sunrise and sunset times of the transmitter and receiver. In summer months like June, the signal strength's curve is quite flat on basically the same level. In contrast, the daily values of the winter months draw an arc following the solar zenith angle. In order to get a better understanding of seasonal differences in the amplitude level, we will now examine three consecutive years of VLF measurements.

Seasonal variations A seasonal dependence of VLF measurements seems to be obvious, since the solar radiation, given by the solar zenith angle, is changing over the year. Assuming the solar radiation induced collision of particles, as the only reason for the absorption of radio waves in the ionosphere, one is naturally tempted to believe that the generally lower solar elevation in winter leads to less absorption than in summer, where the reflection height of the bottomside ionosphere is increased. However, long-term observations reveal the opposite behaviour; see Correia and Gavilan (2011); Raulin et al. (2013) or the following GIFDS and SOFIE measurements.

The first row of Fig. 31 shows the development over three consecutive years, monitoring NAA by receivers in Germany: SIDmonitor in Bergen, SOFIE RX in Neustrelitz and the GIFDS station in Neustrelitz. The signal strength, averaged in 10 min intervals, is given as a colour plot. This unveils the changes of the diurnal variations over the year. Note the different ranges in the colour bars for the years 2013, 2014 and 2015; these come from the differently operating receivers that were selected for the respective year. The picture of one station's year is comparable to its others, so we have chosen to depict several stations in order to exclude special characteristics of the receiver. Note that, due to maintenance of either the transmitter or the receiver, unnatural blackouts may occur. These are visible as dark blue coloured segments (Tx) or white gaps (Rx). See section 4.1.3 for manmade and natural disturbances.

Looking at the profiles in the lower row, we can clearly see a yearly cycle, which is not a matter of the receiver configuration. One can see the amplitudes on the times given by the red or orange dashed lines in the colour plot. The two lines are taken at a 12° solar elevation for the transmitter's forenoon (red) or the receiver's afternoon (orange). The values at the intersection through the colour plot were filtered for excluding transmitter outages and result into the profiles below. At all the times determined by these lines, the whole propagation path of each day is under sunlit conditions and has comparable characteristics of solar irradiation over the year. Also note that in July 2015 the GIFDS station in Neustrelitz has been equipped with a modified Perseus and an additional frequency converter. Compensating the resulting abrupt drop, the previous values up to this time were adapted by shifting them to match the new base level (the black part is continued by the red profile and the grey by the orange one).

Analysing the three similarly looking profiles, as hinted before, the annual behaviour of the VLF signal strength contradicts the first speculations that are connected to the solar altitude. At a constantly chosen altitude, the amplitude is generally larger during summer and obviously suffers of strong absorption in winter. This so-called *winter anomaly* cannot be explained by the solar zenith angle. It requires an approach based on the dynamics of the atmosphere.

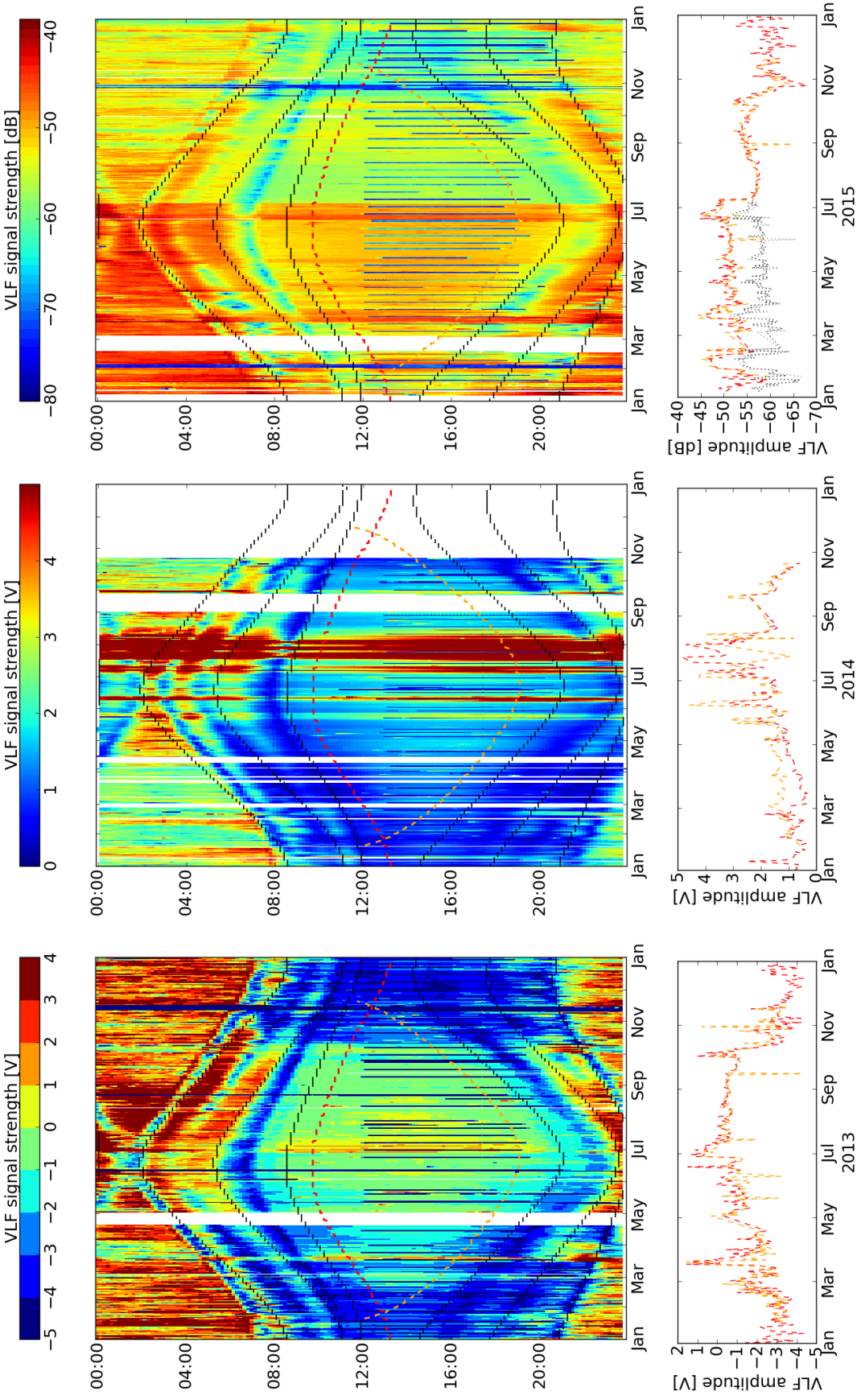

Figure 31: VLF signal amplitude for NAA (averaged over 10 min) measured by the SIDmonitor in Bergen (left column, year 2013), the SOFIE RX in Neustrelitz (middle column, year 2014), and the GIFDS station in Neustrelitz (right column, year 2015): Note the different scales with respect to their varying measurement instrumentation. The lower pictures show the long-term behaviour at the times of 12° solar elevation for the transmitter's forenoon (red) and the receiver's afternoon (orange). The corresponding profiles of constant solar altitude are marked in the upper colour plots.

Note that the profile is obviously not symmetric about the mid of the year. The so-called left-skewness of the annual profile is determined by a slow increase over time until October, followed by a sudden decrease. Pancheva and Mukhtarov (1996) called this behaviour the *October effect*. So far, there are only few papers referring to this phenomenon, let alone describing the physical and chemical processes. Very likely, the coupling of the electron density distribution of the lower ionosphere with mesospheric winds can be made responsible (see future prospects in section 6.2).

4.1.2 Spatial differences

Up to now, we investigated short and long-term trends caused by solar irradiation. A thorough analysis of received VLF measurements should also cover the influences of different propagation conditions. For fixed transmitting frequency and power, the path length and direction of radio propagation are major constraints. Hence, we have chosen six paths of varying propagation parameters representative for a specific group of propagation conditions (i.e. W-E long/short, E-W long/short, N-S and S-N short). For pointing out the consequences of the day length, a quiet summer and a quiet winter day were taken. The resulting VLF measurements can be seen in Fig. 32. All observations are given in local time of the receiving site for a better comparison of the daytime windows. Terminators of local ground-level sunrise and sunset are marked for the particular transmitter T_x (blue), receiver R_x (red) and its mid sub-reflective point (yellow).

Looking at the different measurements, the typical diurnal variation between the last sunrise and the first sunset can be seen in all cases – the daytime window (recall the discussion in section 4.1.1. In regard of the path length, the long ones (NAA-NTZ and NAA-STA) seem to reach their daily level already outside this window. In contrast, for short ones (GQD-NTZ, NSY-NTZ, and NLK-STA, esp. in summer), the VLF amplitude shortly decreases before developing the characteristic plateau, which here may be less flat, even more like a cap. This behaviour comes from the interference pattern on the propagation path. The shorter the distance, the more turbulences are induced by the ground wave. If the path is extremely short, there may be even not enough time to form the cap, leaving a valley only (cp., GQD-NTZ in winter time). This effect is stronger in winter due to the generally lower ionospheric height.

There is always more or less the same shape with a daytime plateau, independent of the propagation direction (however, in winter, it possesses a stronger curvature). Completely inverting the direction, when the positions of Tx and Rx would be exchanged, the measurements are observed to differ. The amplitude level is known to be shifted as a result of the differently experienced geomagnetic field conditions (see, Bickel et al., 1970; Davies, 1990). The non-reciprocity of the VLF propagation leads to less attenuated signals from west to east than from east to west. As our pictures show values between various stations, the configurations are not directly comparable, which is also true for the obtained signal strengths. A similar partial absorption of the signals is invoked by the nature of the ground over which the wave is propagating. Wait (1957a,b) showed average rates for the total attenuation of 1 dB/1000 km for propagation over sea, but 2 dB/1000 km for a transmission over land. Altogether, precise statements relying on spatial information are difficult, however this is not too important as basically only the level is affected.

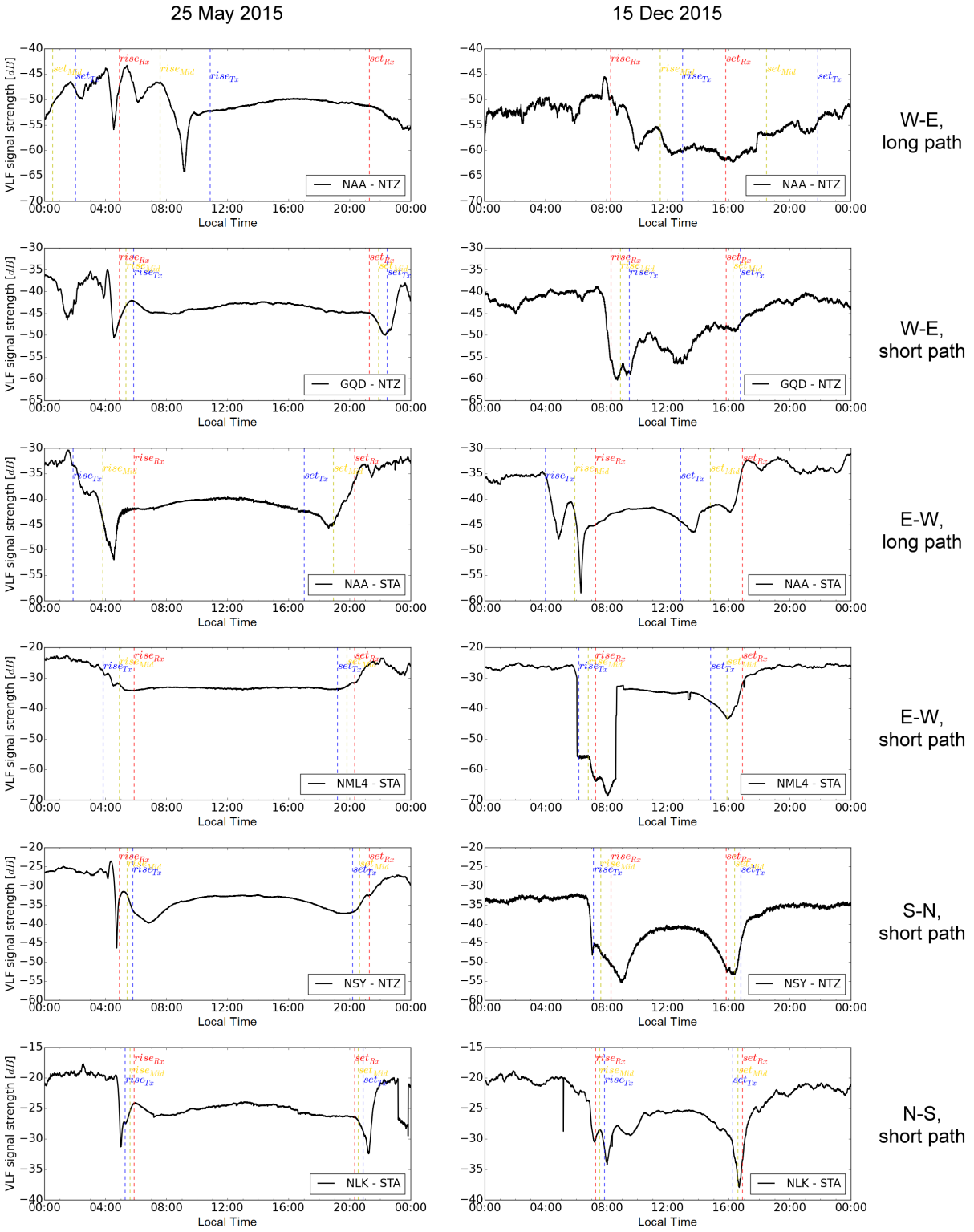

Figure 32: VLF measurements of exemplary propagation paths monitored in Neustrelitz and Stanford: The left pictures show a quiet spring day and the right ones show a quiet winter day. Each row represents different propagation conditions in direction and distance. The actual path is assigned as legend in each panel. The particular sunrise and sunset times are marked by dashed vertical lines for the transmitter (blue), the receiver (red) and the corresponding mid sub-reflective point (yellow).

4.1.3 Disturbances of VLF measurements

There are plenty of disturbances observable in the VLF range, natural influences (recall section 2.3.4 for the primary sources like SIDs and particle precipitation), as well as man-made impacts. This section will shortly illustrate the effects that are important in the context of setting up a global ground-based flare detection system. For this purpose, we distinguish between artificial and natural origins and give a description on the basis of model examples.

Man-made malfunctioning Fig. 33 shows two days of VLF measurements, each of them unveils the effects of a quite different man-made disturbance. The upper picture exhibits alterations typical for disturbances of VLF reception on site. Such impacts close to the receiver are indicated by sudden jumps in amplitude for all received VLF signals. They can be caused by configuration changes of the receiving station or even an exchange of technical equipment in the direct neighborhood. In particular, the switching elements in power supplies change their state quite often and cause a degradation of the received VLF signal. In general, the sudden enhancement of the noise level and therewith an abrupt jump to higher amplitude values can be identified. Furthermore, switching on or off heating installations or air conditioning controls can similarly interfere with the signals.

The lower picture of Fig. 33 features a typical measurement that was influenced by malfunctioning of the transmitter. Since VLF transmitters require maintenance, they are usually switched off occasionally and this can be seen at the receiver as a sudden decrease in the VLF signal strength. This example was caused by a temporary transmission outages of NAA on 20 April 2015, 12:00 - 15:00 UTC and 17:00 - 20:00 UTC (cp., Fig. 33, black curve of the bottom picture). Another possibility is a change of the transmitting power. By this, amplitude levels react in the same way. In the example, a short decrease of power after the restart about 15:30 UTC occurs and can be noted in a reduced signal strength. Transmitter malfunctioning can be clearly separated from disturbances of the reception since the amplitude jumps appear only with single frequencies and not for all VLF signals. Some transmitters are switched off for inspections on a regular basis. Tab. 7 of section 3.1.2 also lists the few known periodic transmitter outages.

Natural disturbances Fig. 34 shows VLF signals recorded by GIFDS that are affected by natural influences. During thunderstorms one can observe additive noise superimposed on the actual VLF signal. The upper picture of Fig. 34 illustrates such effects of a severe storm with lightning over whole Northern Germany on 30 May 2016. According to https://www.lightningmaps.org/ the storm hit the receiver site Neustrelitz around local noon; this is confirmed by our measurements. Depending on the location and dimensions of an atmospheric disturbance and the influenced part of the VLF propagation path, the effects on the measurements may differ in their size.

The focus of this work lies on SIDs caused by solar flares. Their effects on VLF signals can be seen in the bottom picture of Fig. 34. On 12 March 2015, there was a series of flares: a C8.4 at 09:00 UTC , two flares of size M1.6 and M1.4 close to 12:00 UTC shortly after each other,

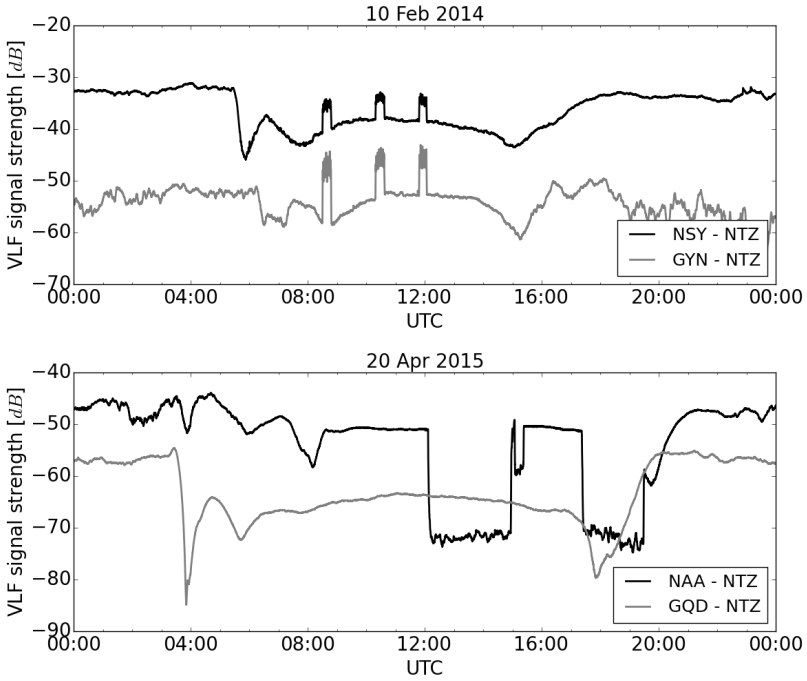

Figure 33: Influences of man-made disturbances on VLF measurements: There are two whole day measurements showing the results of technology caused impacts on site of the receiver (top, three disturbances between 8 and 12 UTC in both signals) and the transmitter (bottom, two big and a small disturbance between 12 and 20 UTC in only one signal).

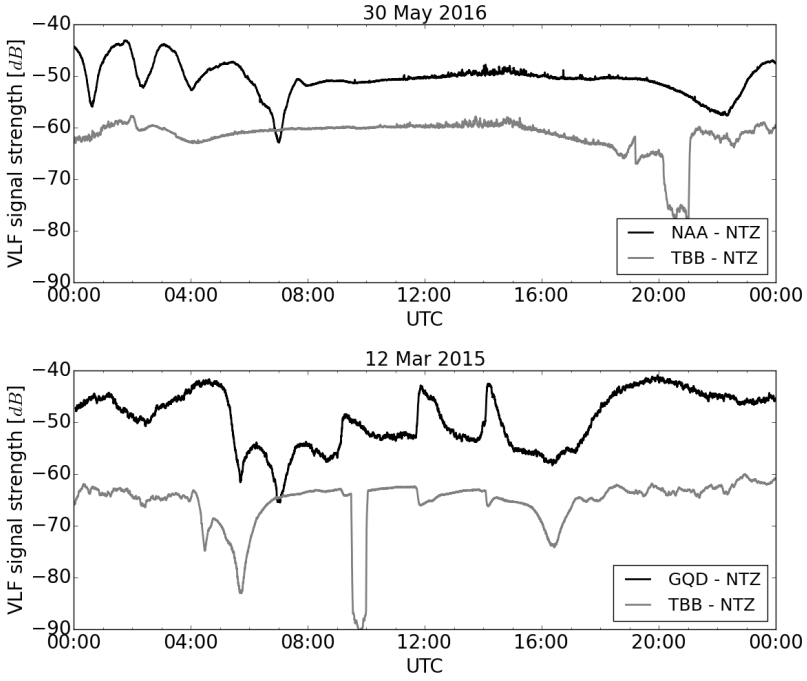

Figure 34: Influences of natural disturbances on VLF measurements: There are two whole day measurements showing the results of external impacts coming from a thunderstorm (top, additive noise between 12 and 16 UTC in both signals) or solar flares (bottom, three clear peaks between 9 and 14 UTC, one signal with increased and one with decreased amplitudes). Note that TBB was switched off at about 10 UTC causing a sudden decrease in amplitude.

and a M4.2 flare at 14:00 UTC.

Striking to the eye are the characteristic peaks of the flare response in the VLF signal strength, which can be positive (e.g., GQD at 14:00 UTC) or negative (see TBB at the same time). Indeed, due to different propagation conditions of the several VLF signals, SIDs may appear in VLF amplitudes as an increase or a decrease. Sometimes the reaction to one event may even swap within in one signal. The shape of the peak strongly depends on the path length, but also on the signal frequency and the ionospheric conditions. Section 5.2 will demonstrate these impacts in more detail at the example of the solar eclipse on 20 March 2015.

4.2 Solar flare response

4.2.1 Variety of solar X-ray flares

As written in section 2.1.3, a solar flare is characterised by an impulsive onset and a decay phase. This is not a precise definition. In order to automatise the detection of the aimed events in the X-ray spectrum, NOAA's SWPC introduced a scheme for determining the times of begin, maximum and end of a flare. In the wavelength range of $0.1 - 0.8\,\mathrm{nm}$ measured by GOES every minute, this works as follows:

1. The begin of an X-ray event is set when the latest X-ray flux is 1.4 times larger than the 3-minute-old value and the sequence of the latest 4 values is increasing monotonically.

2. The maximum is determined as the minute of the maximal flux. If this maximum is exceeded later on, the begin time is reassigned and the determination of the maximum restarts.

3. The end time is defined as the time at which the flux has returned to the value half between the maximum and the initial level of the flare.

In this way, many X-ray events have been detected. We looked at the whole data set of flares measured by GOES, beginning in 1975 as SMS and archived in annual reports by NGDC, https://ngdc.noaa.gov/. Fig. 35 (left picture) shows the dependence of the flare rise time until the maximum over its decay time afterwards. Apparently, there is no clear correlation between the rise and decay times of a flare. Presumably, any combination of them is possible. Note that the scales are logarithmic over a range of values on a minute lattice, whence misleading white gaps occur. On the right picture, the total flare duration in dependence of the size of each event is presented. The duration of solar X-ray flares is strongly diverse and almost not depending on the size. However, small-class flares tend to be shorter in time than events of high X-ray flux.

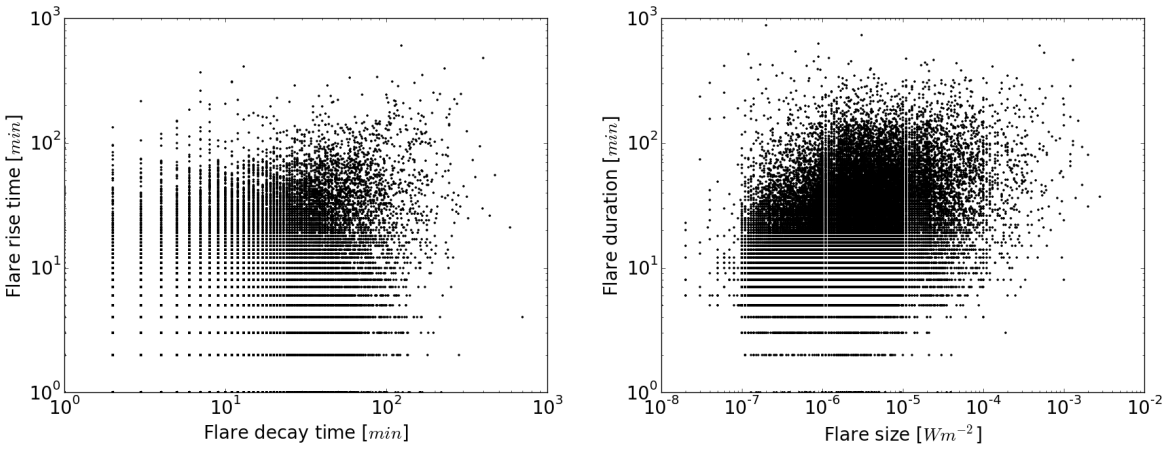

Figure 35: Flare rise time over flare decay time (left panel) and flare duration over flare size (right panel) of all flares listed by the NGDC reports (https://ngdc.noaa.gov/).

The given durations and sizes illustrate a high variety of solar flares. But, this limited information still hides the fact that also the shape is subject to variation. There is a wealth of flare appearances. Examples of this diversity are given in Fig. 36 (upper pictures) by three flares of similar size but very different shape. We see a flare with a sudden increase and a slow decay following (left), an event of sudden increase followed by immediate decay (middle), as well as, another one arising very slowly and taking much time to return to the base level (right). Consequently, the graph may take any form between a needle-like triangle and a wide smooth cap. This can be expected to manifest somehow also in the ionospheric response and therewith in VLF observations.

The resulting amplitude of the three different flares in the VLF spectrum comprising three signals each (NRK, GQD, NAA), measured by the GIFDS station in Neustrelitz, is presented in the lower pictures of Fig. 36. Note that the signal of NRK was instable during the time of the flare on 21 June 2015, possibly due to maintenance work on the transmitter site. The other measurements are fine. Impressively the chosen pictures demonstrate the consequences of the flare passing the atmosphere. An abrupt increase is seen quite similarly in VLF measurements, likely with some time shift depending on the actual composition (we will embark on this below). However, a fast disappearance of the external X-ray flux will not take effect on the atmosphere immediately. In general, the enhanced ionosphere requires time to reach the initial state again. As recombination is slow, decay phases are always long when flares are considered in VLF.

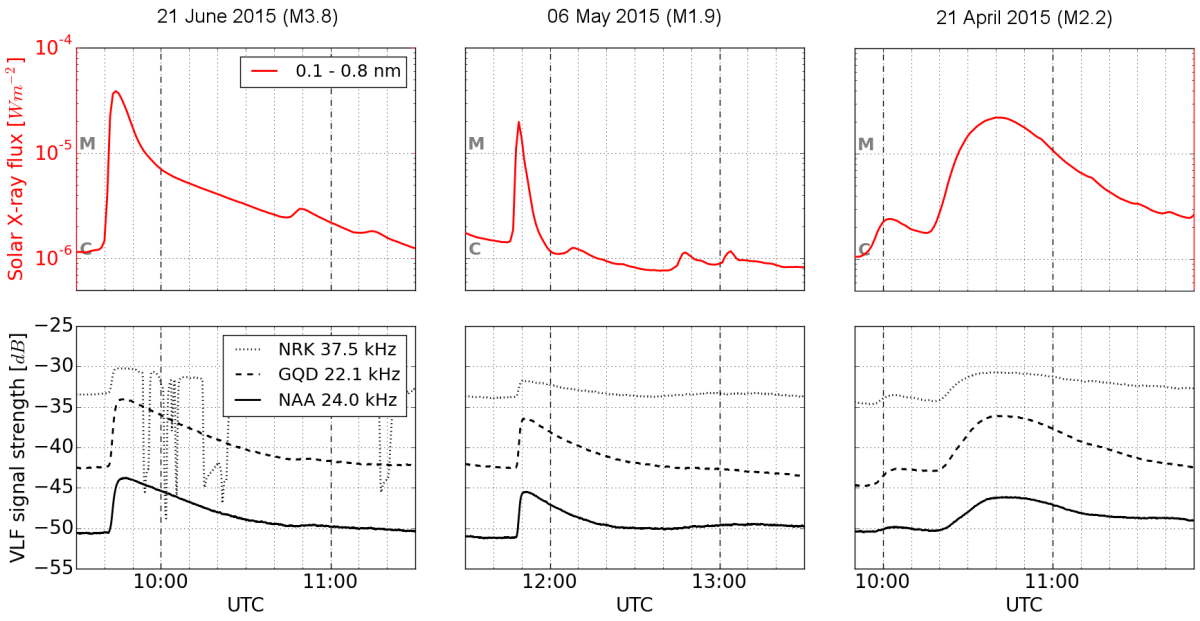

Figure 36: Variety of X-ray events demonstrated by three recorded M-flare events on 21 June, 6 May and 21 April 2015: The upper panels show the X-ray flux measured by the long channel of GOES-15 ($0.1-0.8\,\mathrm{nm}$), and the lower panels reflect their response in the VLF amplitude for three different signals measured by GIFDS in Neustrelitz.

4.2.2 The flare control sample

To investigate the time delay of solar flare effects in VLF signals, a complete set of observed flares from March 2014 to May 2015 was analysed. The annual reports of X-ray events provided by NGDC (https://ngdc.noaa.gov/) was used and filtered systematically. For times in which transmitters or the receiver NTZ were not operating correctly, entries have been deleted. A series of station modifications and test measurements killed whole months. Tab. 9 details parts of the station protocol of NTZ, as well as, transmitter malfunctioning. Hence, only events were taken into account that happened from March to June or September to November in 2014, January, April or May in 2015. Luckily, only a few relevant flares of moderate to severe class were inaccessible.

From the considered periods, all flares of M and X class are taken into account in this study, but only outstanding C flares with a minimum level of C2 are included. In terms of the minimum level of flares recognisable by VLF measurements, the literature gives the threshold varying from mid-size B-class to C-class flares. Kaufmann et al. (2002) investigated statistical correlations the solar X-ray flux and VLF response in the time from 1987 to 1989. The smallest detectable flare belonged to class C5. McRae and Thomson (2004) noted a general sensitivity of VLF measurements down to C1 flares observable in the period from 1994 to 1998. Nevertheless, Raulin et al. (2010) was able to detect even a B2.7 flare in the solar minimum between 2006 and 2009. Clearly, the limitation of flare detection based on VLF data depends on the solar activity. During quiet periods, the ionospheric D region is maintained primarily by the Lyman-alpha radiation (Nicolet and Aikin, 1960) ionising nitric oxide. However, X-rays ionise all constituents. Hence, at times of low solar activity VLF measurements will exhibit higher sensitivities. This study includes X-ray events down to C2, as we are in a time shortly after a solar maximum. In general, detecting M and X-class flares is very important, while many C flares are negligible due to their minor influence on radio systems. Note that in the previous subsection a variety of flare shapes independent of their size was pointed out. So, the following criteria were chosen to exclude C-rated flare events from the study because of their atypical signature:

- lack of a clear abrupt increase and decay phase,
- small peaks shortly after a bigger event,
- rising lasts longer than 15 minutes,
- total increase less than three subclasses.

Year / month	Note
2014 Jul.	Test and preparation of STA in NTZ
2014 Aug.	Transmitter malfunction of GQD
2015 Feb. / Mar.	Test of frequency standard for NTZ
2015 Jul. / Aug.	Set up change NTZ to modified Perseus with frequency standard

Table 9: Extract of the NTZ station protocol and relevant transmitter malfunctioning.

Naturally, only events within the applicable daytime window of the corresponding VLF paths are used for ensuring that flare effects are visible. In the remainder, this statistical sample of all selected solar flare events is referred to as *flare control sample*.

4.2.3 Time delay of VLF responses

Since the ionosphere requires some time for reacting on external influences, obviously, we will face corresponding time delays in VLF flare responses. However, the lower ionosphere, due to its constituents and their comparably high collision frequencies, progresses ionisation quite fast.

For deriving information about the time delay between an X-ray event and its ionospheric response in VLF measurements, we implemented a cross-correlation of both data sets via

$$(A \star \phi)[t] = \sum_{t=-\infty}^{\infty} A^*[t] F_{SXR}[t + \Delta t].$$

Here, A^* is the complex conjugate of the VLF amplitude A, F_{SXR} is the solar X-ray flux ($0.1 - 0.8\,\mathrm{nm}$), and Δt is the displacement or the time delay. The calculation of the cross-correlation depends on the sampling rate of the different signals. We use minute data, as this is the lowest common sampling rate for GOES and GIFDS measurements. The cross-correlation describes the similarity as a function of the variable displacement Δt. Hence, the signal time delay of each event is determined by the shift for which the cross-correlation is maximal. The choice for $\Delta t_{delay} = \arg\max_t((A \star \phi)[t])$ is interpreted so that the displaced signals are most alike. One typical example of a flare signature in GOES and GIFDS is given in Fig. 37 together with the correlation function. The similarity of both signals is high with a clear time delay of 3 min.

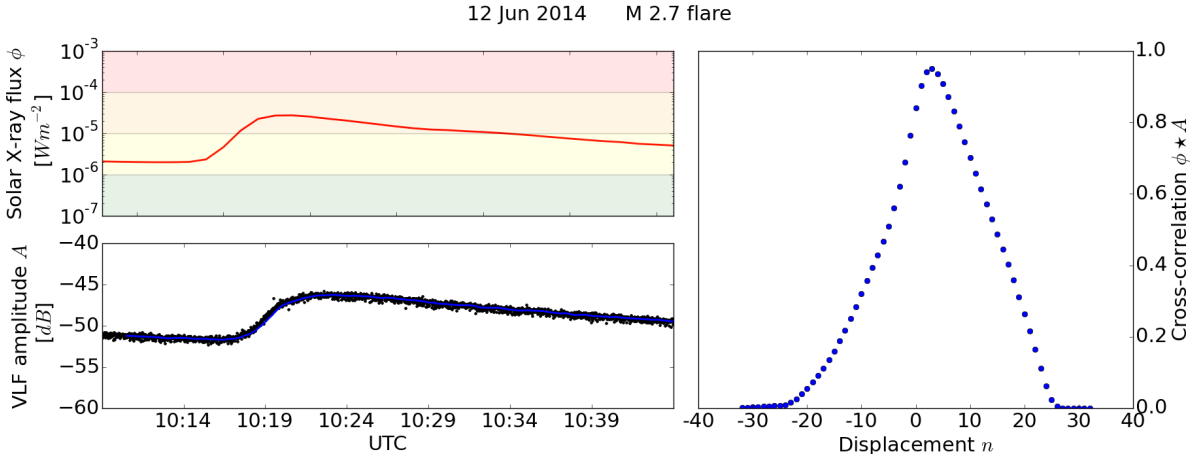

Figure 37: Example of an X-ray event of size M2.7 on 12 June 2014 measured by GOES and GIFDS on the path HWU-NTZ (left) and their correlation function (right): The delay is obtained via cross-correlation of the signals from 5 minutes before event begin to 30 minutes afterwards.

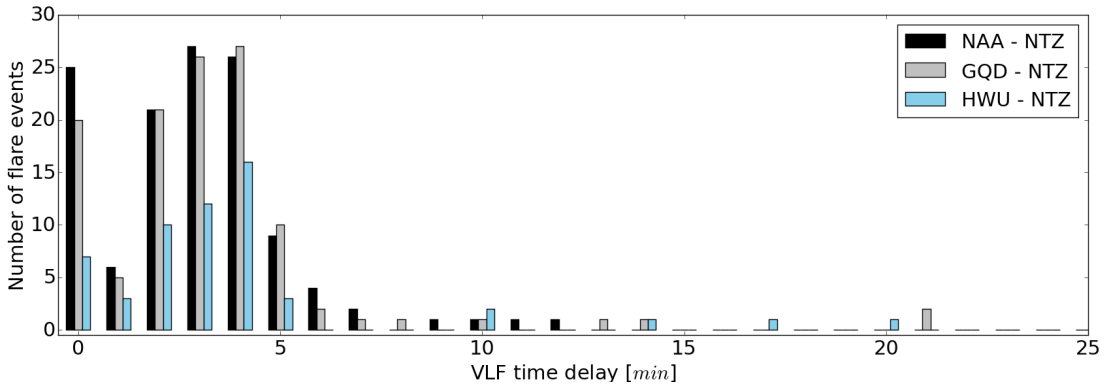

Figure 38: Number of flare events over time delay between the X-ray source and its VLF response: HWU counts less flare events because of more frequent transmitter outages.

The time delay between an X-ray flare and the response in VLF amplitudes is not constant. The delays of the flare control sample from March 2014 to May 2015 on three different propagation paths are shown in Fig. 38. Note that the temporal resolution is limited because of the lowest common sampling rate of 1 min. The statistical distribution reveals an overwhelming accumulation of the time delay up to 5 min. Many events show a delay between 3 and 4 min for all three VLF paths. However, there is also a large number of events showing almost no time delay, at least it is not observable with our techniques. This can be explained by the resampling of GIFDS measurements to the 1 min cycle of GOES, which was only done for the comparison.

Note that Fig. 38 gives only a value resulting from cross-correlation, i.e., in principle the shift between the maxima of the signals. The begin of a flare may be visible in VLF even earlier, maybe reducing the slope during rise time in dependence of turbulent ionospheric conditions. Recognising the beginning of a VLF signal change (and hence the start of external impacts taking effect) is a very important factor of GIFDS' flare detection algorithm. This will be discussed in the next section.

4.2.4 Correlation between VLF and X-ray data

We have seen before that solar flare events of similar size can still strongly vary in their appearance. Fig. 39 (upper picture) shows four flares of similar size. The begin time given by GOES is aligned to 00:00 for allowing better comparisons. As is known, the flare size classification is derived by the peak solar X-ray flux (see 2.1.3 and 4.2.1). The base level of the flare, and hence the general background radiation, isn't taken into account. But, we can only see the relative change in VLF measurements and not the maximum peak size. However, the amount of increase is exactly what is important for limiting technological harms. The picture in the middle shows the responses in the VLF signal strength (on the path NAA-NTZ) of the four similarly sized events (again aligned at the same time of begin). Clearly, X-ray events with small/strong relative change also exhibit small/strong VLF impact.

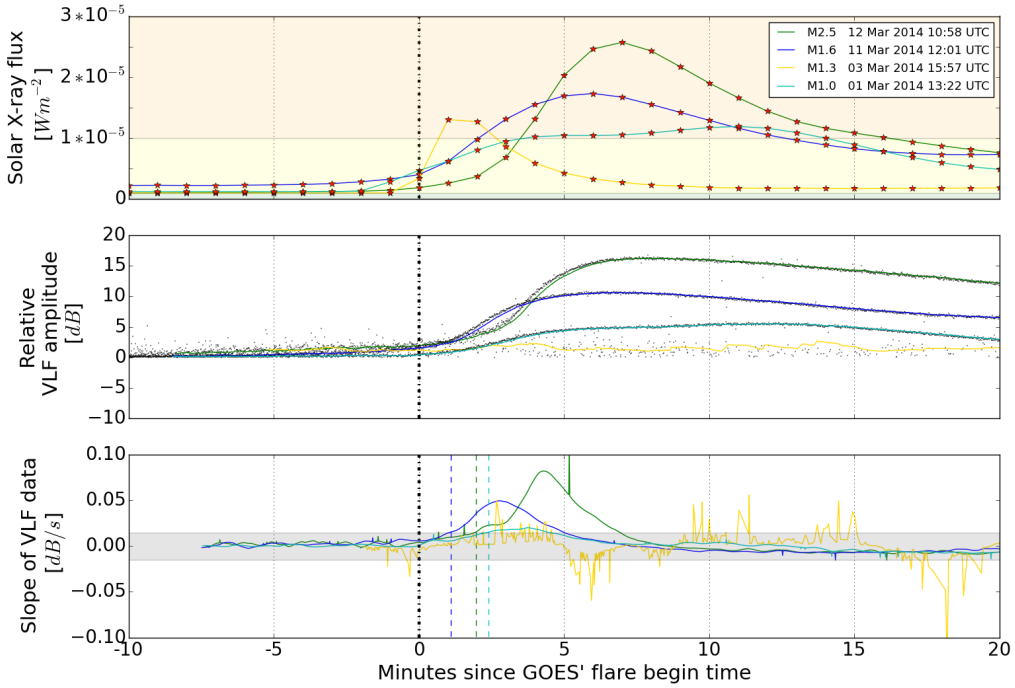

Figure 39: Comparison of four M-flares, similar in size, but different in background level and slope measured by GOES (upper panel) and GIFDS (NAA-NTZ, middle panel): Note that the X-ray flux is shown on linear scale for direct comparison. The lower picture shows the slope derived by the current second-wise polynomial of degree 2 over the last minute. The grey-shaded band marks our threshold for flare alerts of single VLF channels. For the M1.3 flare (yellow), NAA was switched off. Such noisy data is excluded and will not be used for flare detection.

The lower picture of Fig. 39 displays the first derivative of the VLF amplitude. The development of the slope of each VLF signal connected to a SID event gives a primary indicator for flare recognition. All examples experience an increase of more than 0.02 dB/s (grey-shaded band) and are observed within 3 min after GOES' flare begin (vertical dashed lines marking the begin in VLF).The larger flare (M2.5 in green) has a slow initial phase and therewith shows a late response in VLF. This proves the variable reaction time of the ionosphere on flares.

Inversely calculating the flare size of the original X-ray emission from VLF measurements is a naturally appearing question. We have noticed that the absolute flux size is not reflected in equivalent VLF values. However, including knowledge on the radiation background level, there is the chance to use possibly well correlated relative changes. But, the actual ionospheric impact does not match the absolute space-based scale and the disturbances in ground based measurements are better estimated in the relative scale, anyway. Fig. 40 shows the correlation of the relative change in GOES and VLF amplitude measurements (top: NAA, middle: GQD, bottom: HWU) invoked by solar events in the flare control sample. HWU again consists of less events due to a higher transmitter outage rate. Every dot represents an event, and its position relates the two responses. They are coloured according to the time of occurrence. If a flare (with respect to the mid sub-reflective point of the path) happens close to local dawn, it is copper, and if it happens close to local noon, it is black.

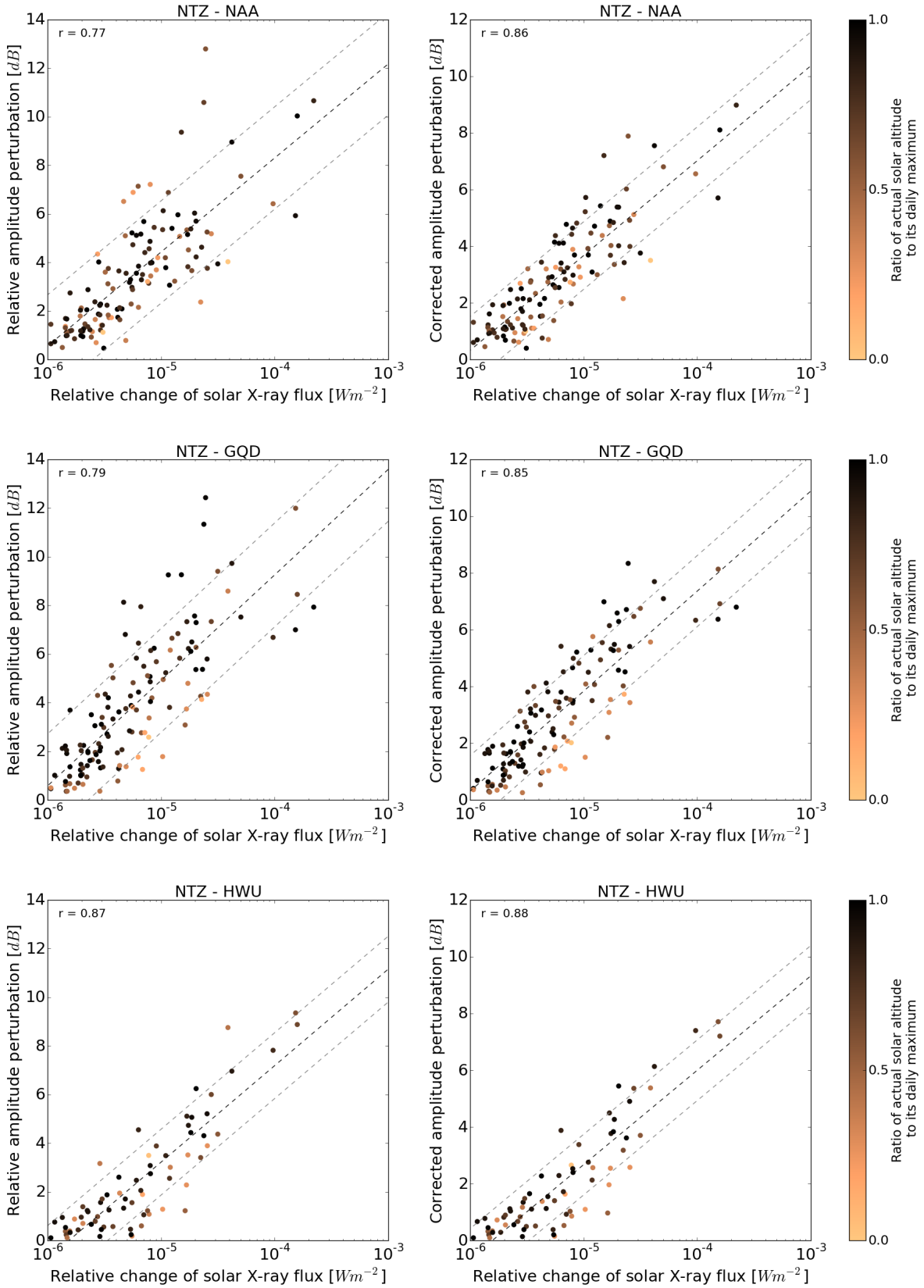

Figure 40: Correlation of VLF and GOES measurements for solar flares from April 2014 until May 2015: Both axes describe the relative change between the base level of quiet conditions and the peak level induced by a solar flare. Only flares within the daytime window are considered. The closer the event occurs to the mid-subreflective's noon, the darker the point is. The black dashed line marks the linear regression and the grey-coloured lines are twice the corresponding standard deviation σ.

The left pictures of Fig. 40 illustrate the unaltered VLF response as a function of the logarithmically scaled relative change in the solar X-ray flux. The pictures indicate a clear linear trend. The regression lines (shown black dashed) have correlation coefficients from 0.77 to 0.87. However, in particular NAA and GQD experience a rather big dispersion for strong events. Some points are quite far away from this mean line. As an orientation, the lines with a distance of twice the standard deviation

$$\sigma = \sqrt{\overline{V^2} - \overline{V}^2}$$

are depicted grey dashed. In the last equation, the bar denotes the expected value and V is the difference of the amplitudes from the regression line. Such an observation is not unfamiliar. We have seen already a strong annual variation of the daytime plateau (cp. section 4.1.1). Apparently, the initial state of the ionosphere may influence the VLF response. For producing the pictures on the right, a logarithmic weighting of VLF intensity was introduced. The weights were chosen according to the particular daytime plateau so that flares under a high solar elevation get more importance. Respecting diurnal and annual variations, events in twilight or in winter are corrected down. By this, the correlation coefficient increases to 0.85 - 0.88. Moreover, the coefficient of HWU, which is already very high, is not degraded. This proves the quality of this approach. Similarly, the standard deviation σ improves (its twice is grey dashed).

The images in Fig. 40 (especially for GQD and HWU) unveil a concentration of light dots (i.e., coloured in copper) in the lower part. A detailed look in particular on the corrected values of the flare events close to dawn reveals that the VLF response is generally lower. The reason may be that the radiation of a flare hitting the atmosphere in an acute angle (as it will happen close to the day-night terminator) has a longer way through the ionosphere and may be attenuated more before being able to affect lower layers. Such constraints need to be considered in the GIFDS flare detection algorithm. They will be included in another weighting presented in the next section. Altogether, the comprehensive study of the flare control sample suggests a narrow dependence between the relative changes in X-ray and VLF. So, VLF measurements may be used to identify SIDs and determine their category in the future.

4.3 Development of the flare detection algorithm

The main aim of our work is to monitor SIDs caused by moderate/severe solar X-ray flares by means of VLF measurements and issue alerts if necessary. This requires an automated mechanism that looks for significant patterns in a continuous stream of data. We here illustrate the ideas of this approach that were introduced by Wenzel et al. (2016). These are concentrated on the direct reaction of VLF amplitudes. It is not intended to deduce exact information on the extraterrestrial source, as the travel through the atmosphere cannot be considered to be prescribed.

There are other studies that focus on the deduction of ionospheric and solar parameters based on VLF measurements, e.g., Raulin et al. (2013) and Palit et al. (2013). Based on the GEANT4 Monte Carlo simulation, the latter describes how to compute the ionisation rate out of VLF perturbations during solar flares. A reduced ionospheric chemistry model is used to calculate the electron density over height. This approach works good with long-term analyses, e.g., for determining environmental relations and quantities.

All of this requires appropriate resources, as the calculations are time-consuming. Fast algorithms are in need to ensure a near real time processing with the desired sampling and update rate of 1 Hz. Thus, our approach on deriving X-ray emissions from VLF data is based on statistical evaluations condensed in an easy-to-compute decision criterion that is monitored all the time.

4.3.1 Data preparation

For a robust prediction, raw measurements cannot be used. In a first step, incoming signals are smoothed immediately with the help of a moving weighted mean, roughly eliminating outliers from the data set. The weights are chosen due to a Gaussian function over the last minute (i.e., 60 measuring points) with emphasis on the recent 5 seconds.

As pointed out before, VLF measurements will allow to recognise impacts of X-ray events only during local day. The daytime window is used to determine a slot for possible flare observation and warning along every VLF path. To get the greatest possible daytime section for every receiver-transmitter combination, we use the times of last sunrise and first sunset calculated on the ground level by utilising the Python package PyEphem (see section 4.1.1). We are not using the ionosphere's reference height at about 75 km, as the signal strength at twilight hours can be quite unsteady.

In order to retrieve reliable flare information from the VLF measurements by GIFDS, only the paths with most stable transmission and good reception conditions are used. Finally, man-made disturbances are eliminated. The filter works by detecting sudden jumps to different amplitude levels (cp. section 4.1.3).

After eliminating technological impacts caused by humans, natural disturbances (other than solar flares) may still be present. Most of them take effect only on a local scale. These phenomena modify small parts of the bottomside ionosphere and hence influence the propagation of only a few associated VLF signals. By combining various VLF measurements of differently distributed

paths, such local effects can be smoothed out via averaging. However, if a non solar flare event has a broad impact on the lower dayside ionosphere, it will be seen by GIFDS. But, this certainly doesn't interfere with the aim of detecting potentially harmful D-region disturbances. Minor atmospheric effects (e.g., atmospheric noise like in section 4.1.3) can be identified by its shape very well and will be ignored.

4.3.2 Adjustment of available VLF data

We will illustrate how the flare detection algorithm of GIFDS processes the VLF signal strength data on an example of two consecutive days which is presented in Fig. 41. For 21 and 22 April 2015, the original measurements (smoothed according to the explanations on data preparation) are seen in the upper half. They are used as a basis for the GIFDS algorithm. The availability of every receiver is limited. Hence, we require several receiving stations with partially overlapping daytime windows. Here we have chosen Neustrelitz-NTZ, Boston-BOS, and Stanford-STA.

In order to confirm that a disturbance originates in a flare, each of these stations has to monitor several transmitters with different propagation paths. The transmitters may vary in their properties, and they are not necessarily the same for all receivers, or for one receiver at all times. They are selected so that propagation conditions are good, excluding the existence of disruptive noise. For eliminating local effects, at least three paths which lie within the daytime slot of active flare observation are used for each receiver.

In the following equations, k numbers the regarded T_x-R_x combinations (ranging from 1 to 9 in our example). The continuously smoothed measurements $A^k(t_i)$ were furthermore truncated to the respective time slot and are now corrected for roughly compensating daytime variations. This is realised by determining a polynomial fitting curve

$$M^k(t) = p_0^k\, t^2 + p_1^k\, t + p_2^k,$$

where $M^k(t)$ denotes the approached, „modelled“ signal amplitude over time of the path k. We achieve a good fitting by minimising the squared error

$$\sum_i |A^k(t_i - \Delta t_{day}) - M^k(t_i)|^2.$$

For accessing past data, times t_i are reduced by a shift about Δt_{day} when the previous day is addressed. We do this to get a good guess for the undisturbed amplitude value at a specific time of the day. This is reasonable, as the diurnal variation changes gradually over the year. The detrending of the daily signal strength variation is obtained from the incoming measurements by reduction with the calculated average daily development

$$\hat{A}^k(t_i) = A^k(t_i) - M^k(t_i).$$

For the example, the detrended measurements are illustrated in the lower half of Fig. 41. However, though temporal variations are compensated, the signal levels are not yet comparable.

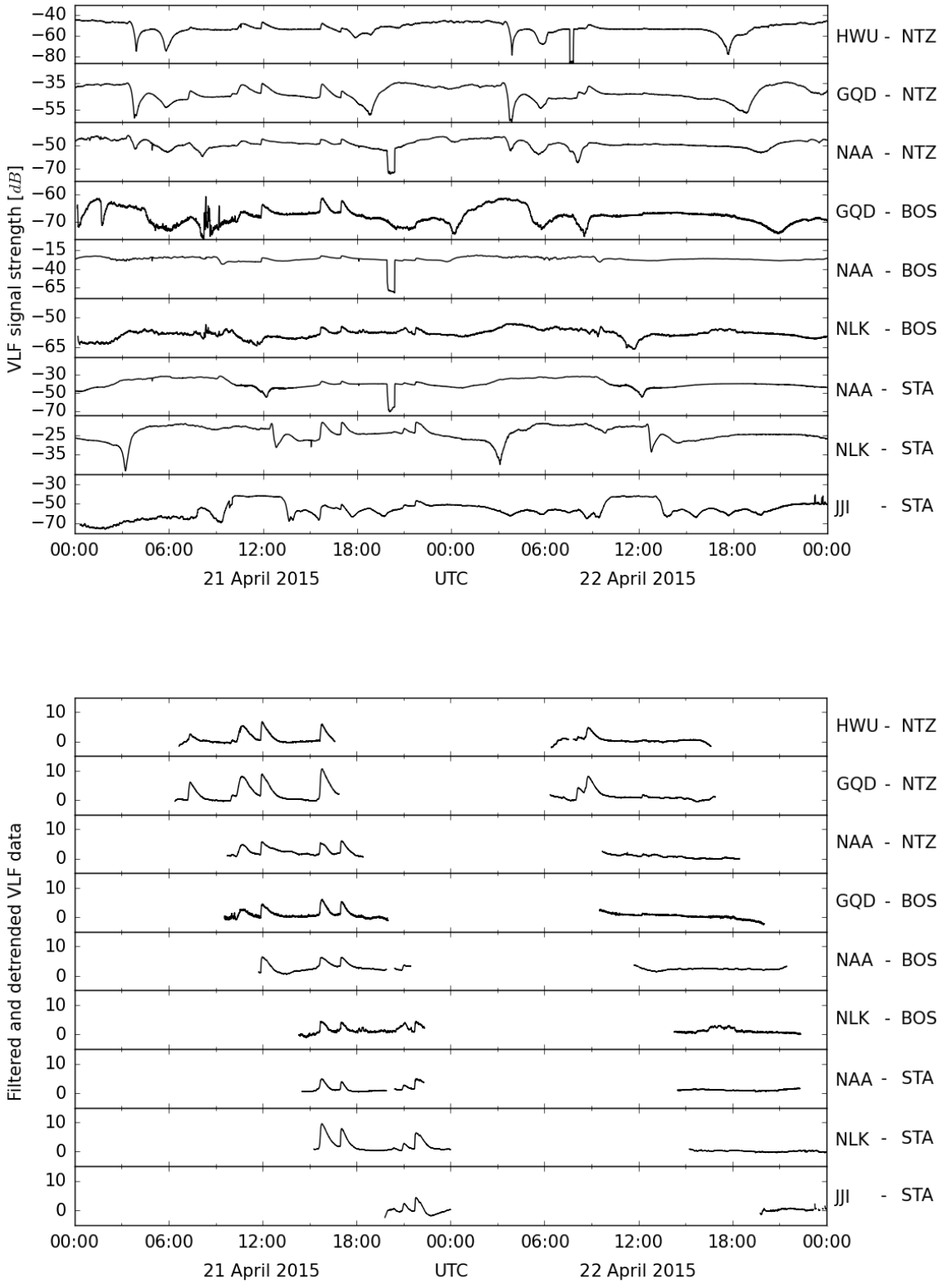

Figure 41: Two consecutive days of several VLF amplitudes: In the upper half, for the three stations NTZ, BOS, and STA, the smoothed measurements of three transmitters each (cf. Tab. 7) can be seen. These raw signals go through the near real-time process of cutting and detrending, yielding the reliable curves shown in the lower half. [taken from Wenzel et al. (2016)]

4.3.3 Compound VLF information

Transmitting powers and propagation conditions are not the same, resulting in signals with unequal average amplitude. These measurements must be calibrated. For this, the data curves are detrended and afterwards transformed linearly, yielding level-adjusted values

$$\tilde{A}^k(t) = a^k \hat{A}^k(t) + b^k.$$

One may glue together the signals by matching them to one specially interesting of the VLF measurements. However, at this place, we take the GOES X-ray flux as reference signal. This allows a direct comparison. The parameters m and b are thus obtained by using the flare's last noted bottom point $A^k_{fl,min}$ and top value $A^k_{fl,max}$ via

$$a^k = \frac{F_{fl,min} - F_{fl,max}}{A^k_{fl,min} - A^k_{fl,max}} \quad \text{and} \quad b^k = \frac{-A^k_{fl,max} \cdot F_{fl,min} + A^k_{fl,min} \cdot F_{fl,max}}{A^k_{fl,min} - A^k_{fl,max}}$$

Here, F_{fl} describes reference measurements of GOES $(0.1 - 0.8\,\text{nm})$ during flares. But in principle, any fixed of the A^k_{fl} may be used in exchange to equalise all the levels with respect to base values and peak heights of a flare. Though we use a linear approach for matching the VLF measurements, we want to point out that the VLF signal strength and the X-ray flux are not necessarily in a linear relation. Of course, the relative change has been observed to obey such a dependence (see section 4.2.4). Instead of relying on only one flare, one could study the general transformation rule for the relative changes over a long time and use this together with an elsewhere provided background level to define m and b. We are using only the recent flares for appropriate levelling as some of the measurements don't have one full year of record yet.

"As encountered in section 4.2.4, relative changes in a VLF signal are distorted during twilight hours. Hence, the aim should be to judge 'fully lighted' paths as more reliable. Especially T_x-R_x paths with a wide East-West spread can suffer less solar irradiation in some sections. Latest studies by Basak and Chakrabarti (2013) showed that the solar zenith angle on a single propagation path plays an important role. A high solar zenith angle for T_x-R_x induces a delay in the VLF response to flares. This can be explained by a lower ionisation, whence the small electron density increases the time to react. So, we will respect the solar zenith angle $\theta^k(t)$, but for simplicity only the one at the mid sub-reflective point is taken into account. The weighting function for the kth great circle path is defined as

$$\gamma^k(t) = \frac{\cos\left(\theta^k(t)\right) - \cos\left(\theta^k_{max}\right)}{1 - \cos\left(\theta^k_{max}\right)}.$$

The values are between 0 and 1. This is realised by aligning the current value $\theta^k(t)$ of the mid sub-reflective point with the maximal solar zenith angle θ^k_{max} (i.e., the angle for sunrise or sunset). Outside the daytime window, or in the case of transmitter outages, the weight of the path will temporarily be set to zero. We obtain small values for transmissions close to night. The weight is 1 for a path with vertical irradiation at the mid point, and it will be

slightly smaller in mid latitudes. Using the zenith angle of the mid sub-reflective point is a first approach to include solar irradiation of VLF propagation paths. One should remember that different portions of paths might still be exposed to less illumination depending on their East-West distance between transmitter and receiver. A more complex algorithm based on a division of each propagation path into small segments is intended to be used in the future.

The final compound of all measurements is then constructed as the weighted arithmetic mean

$$\bar{A}(t) = \frac{\sum\limits_k \gamma^k \cdot \tilde{A}^k}{\sum\limits_k \gamma^k} \tag{21}$$

In this way, we emphasise VLF measurements taken during local noon, whereas signals close to sunrise and sunset remain of minor contribution (recall section 4.2.4) except there is no other. Fig. 42 (middle) shows the resulting weighted superposition facing the original X-ray flux (top)."[12]

The figure demonstrates that we produced a VLF based curve which, at first glance, allows to distinguish between the different classes of flares, similarly to GOES' X-ray flux. For a better understanding of the algorithms work at this concrete example, the number of included T_x-R_x paths is illustrated, as it is a measure of confidence. Nevertheless, note that if too many measurements are used, more noise will disturb the reliability of flare warning. When the last receivers are established spanning the globe, the GIFDS network will continuously monitor multiple suitable propagation paths. Our aim is to guarantee a constant number of three to six fitting paths in order to provide consistency.

4.3.4 Method for alert decisions

In the last paragraphs we generated a signal convenient for flare detection. Fig. 42 compares the newly obtained VLF information with the X-ray flux. They share the same basic progression, though the deduced curve in the middle respects the atmospheric effects altering the signal coming from space shown at the top. The last image gives the first derivative of the compound VLF data above. To eliminate short-term oscillations, the slope is obtained via a polynomial fitting of the discrete point values in the previous minute. This derivative gives the crucial decision criterion.

Every second, the algorithm checks if the slope is unusually high and the resulting compound value outruns a given threshold. The slope is derived via the rise of the last second of a polynomial fit over the last 30 seconds. A resulting value above $0.002\,\mathrm{Wm}^{-2}$ raises an internal warning. For preventing false warnings, a flare alert is given only if this condition is fulfilled for the next two seconds. In this manner, strong noise (i.e., above the threshold level) will likely be ignored, since consecutive values then would jump. The final alert is issued only if such a starting peak is detected in a compound built from at least two T_x-R_x paths of different transmitters. So, we have not only a single indicating signal, but demand a confirmation by

[12] slightly modified quotation from Wenzel et al. (2016), page 238

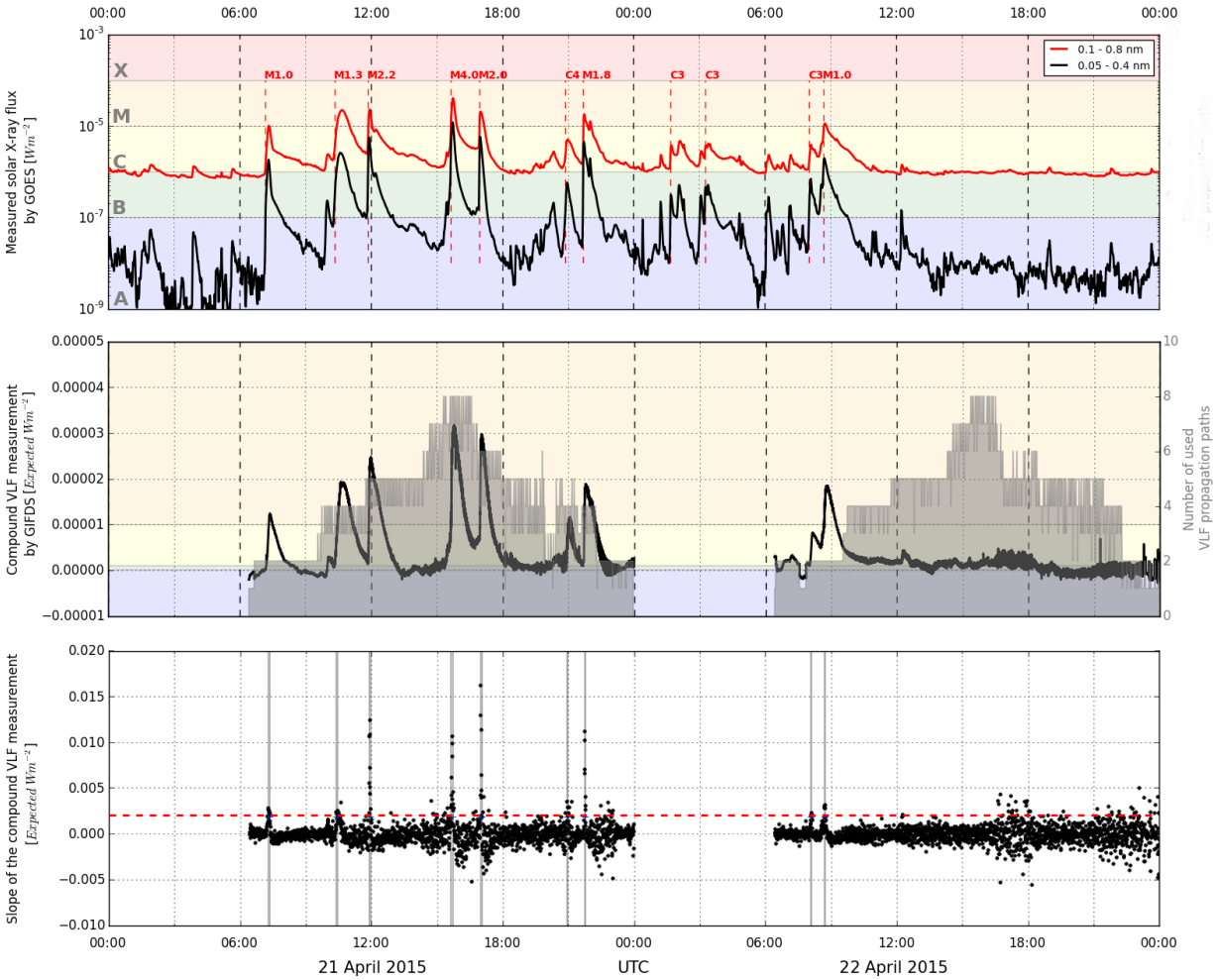

Figure 42: Comparison of the compound VLF measurement, derived by (21), with the GOES X-ray flux: The top image gives the GOES data at the two selected days as a reference. The second image depicts the outcome of the superpositioning of the several single curves from Fig. 41 according to the zenith angle weighting. The number of utilised paths is shaded grey in the background. At the bottom, the slope of the compound (after piecewise polynomial fitting) clearly recognises its peaks. [adapted from Wenzel et al. (2016)]

another. Even if a single transmitter's signal can be temporarily lost (e.g. due to maintenance) the system remains stable by using several VLF channels. As it has been established with the GOES system, a second warning comprising the flare size can follow when the maximum or intermediate classification steps are reached. In GIFDS, these are determined by the VLF peak level adjusted to an "absolute" scale. Here, the $\bar{A}$ coming from empirical analysis is the base.

Tab. 10 suggests good results for estimating the flare size from resulting VLF measurements and proves the fast response of the introduced compound signal. For the given flares, the correlation coefficient of the resulting size in GOES and GIFDS measurements is quite high with 0.91. All M flares are estimated very well. However, the two C flares are overrated which might be due to the linear calibration of the VLF signals using recent flare records only. Appearing parameters in this relation can be adjusted. But this requires long-term observations,

	GOES			GIFDS	
Date	Time [UTC]	Flare class	Size Wm^{-2}	Time [UTC]	Size Expected Wm^{-2}
21-04-15	07:11:00	M1.0	$1.0 \cdot 10^{-5}$	07:12:00	$1.2 \cdot 10^{-5}$
	10:20:00	M1.3	$1.3 \cdot 10^{-5}$	10:22:00	$1.9 \cdot 10^{-5}$
	11:52:00	M2.2	$2.2 \cdot 10^{-5}$	11:52:30	$2.4 \cdot 10^{-5}$
	15:38:00	**M4.0**	$4.0 \cdot 10^{-5}$	**15:38:10**	$\mathbf{3.2 \cdot 10^{-5}}$
	16:58:00	M2.0	$2.0 \cdot 10^{-5}$	16:58:30	$2.9 \cdot 10^{-5}$
	20:53:00	C4.9	$4.9 \cdot 10^{-6}$	20:56:00	$1.1 \cdot 10^{-5}$
	21:42:00	M1.8	$1.8 \cdot 10^{-5}$	21:43:00	$1.9 \cdot 10^{-5}$
22-04-15	08:01:00	C3.8	$3.8 \cdot 10^{-6}$	08:04:00	$8.1 \cdot 10^{-6}$
	08:40:00	M1.0	$1.0 \cdot 10^{-5}$	08:41:00	$1.8 \cdot 10^{-5}$

Table 10: List of selected flares and their properties: The flare time denotes the time of detecting an event by enhanced values with the different systems. [taken from Wenzel et al. (2016)]

as studied in section 4.2.4. For the minor flare examples (C class: grey-coloured in Tab. 10), the compound VLF data by GIFDS shows also a three-minute time delay compared to GOES. Notably, GIFDS exhibits shorter time shifts for M flares (about 30 to 60 seconds), and strong events with an immediate atmospheric reaction (marked bold in Tab. 10) are recognised by both systems almost simultaneously. Palit et al. (2015) explained this size-dependant time delay with the help of the electron density continuity (9) in the lower ionosphere. According to this, C class flares experience quantitatively a longer delay in VLF response in comparison to M or X class flares. This suits the aim of the GIFDS system detecting ionospheric impacts of moderate to severe X-ray events.

4.4 First look on the next tasks

In the previous section, the flare detection based on VLF measurements was applied for two consecutive days. For this special case, the feasibility of the algorithm has been proven. In order to verify the quality of the flare sizes determined by the GIFDS, the results are now investigated for the flare control sample introduced in section 4.2.2.

The validation of size reproduction is a first step to judge on the success rate of flare alerts. Yet, determining the lowest alert level is a task for future studies, as the background radiation level of GOES measurements and the yearly variation in VLF measurements need to be considered. As the accessible VLF data is too limited in time, the lowest level of alert is disregarded. Fortunately, the GIFDS algorithm aims to detect moderate and severe flare events, which can be confirmed to work for the flare control sample.

4.4.1 Performance of the algorithm

Since the set up of the GIFDS system started in 2012, it was subject to further development. Hence, the data for validation is restricted to the flare control sample. It offers consistent and directly comparable measurements over a quite long period of time. Fig. 43 plots our algorithm's flare size estimates over the registered GOES sizes for both variants, without level correction (left picture) and with applying the level correction proposed in section 4.2.4 (right picture). The colours indicate the number of signal paths used for the respective flare information. The original X-ray flux calculation already shows a high correlation to the absolute solar X-ray flux measured by GOES. Taking into account temporal VLF level variations, the Pearson correlation coefficient is further improved from 0.85 to 0.91. In addition, the standard deviation σ has dropped by half. Clearly, the picture has become more defined, showing less driftage from the correlation law. Especially results based on three signal paths are closer to the regression line. Only a few flares, mostly obtained by only two signals, are outside of the narrow 2σ threshold.

Looking at Fig. 44, a slightly different behaviour depending on the season is revealed. Seemingly, the dots for summer events are concentrated below the regression line. In contrast to this, strong flares during spring tend to be overrated. After applying level correction, the calculated event sizes are more in line with the GOES statements. Indeed, the applied correction with respect to diurnal and annual variations of VLF measurements has a huge influence on the solar flare recognition. If one would know the actual conditions of the lower ionosphere, one could try to improve the correlation. Thus, for future studies, it is worth to simulate VLF propagation over a large time scale in order to gain an ionospheric D-region model and conclude general conditions for the specific signal paths.

In the context of our flare control sample, there are some flares which are seen by only one out of the three stable signal measurements. This is below our critical level of at least two valid T_x-R_x paths for making a decision on flare alerts. These events, 10 % of our control sample or 4 % of the moderate and severe events, would have been missed. But in total, this study only used three signal paths arriving at GIFDS-NTZ, because others were still too noisy or subject to technical issues like transmitting power changes. Meanwhile, taking into account all available

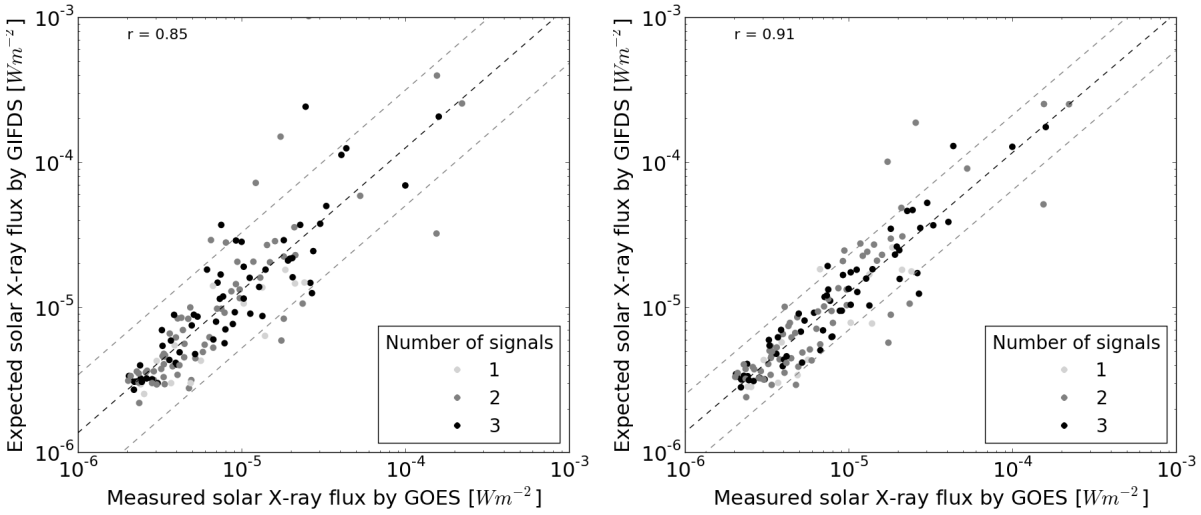

Figure 43: Correlation of VLF and GOES rating for solar flares within the flare control sample from April 2014 until May 2015 monitored by the NTZ station: The results are coloured by the number of utilised signal paths. The left picture presents the original VLF amplitude response transferred into the X-ray flux scale, whereas the right one is corrected by the day level. All axes indicate absolute values of the solar flux. The black dashed line shows the linear regression, and the grey-coloured lines mark twice the corresponding standard deviation σ.

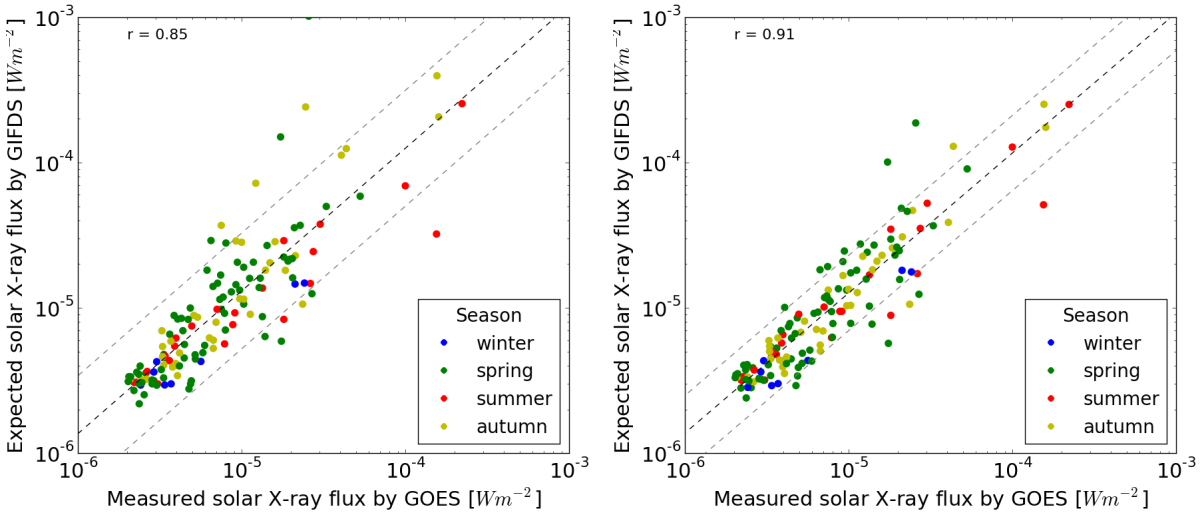

Figure 44: Correlation of VLF and GOES rating for solar flares within the flare control sample from April 2014 until May 2015 monitored by the NTZ station: The data is the same as in Fig. 43 but the events are coloured according to the season in which the flare occurred.

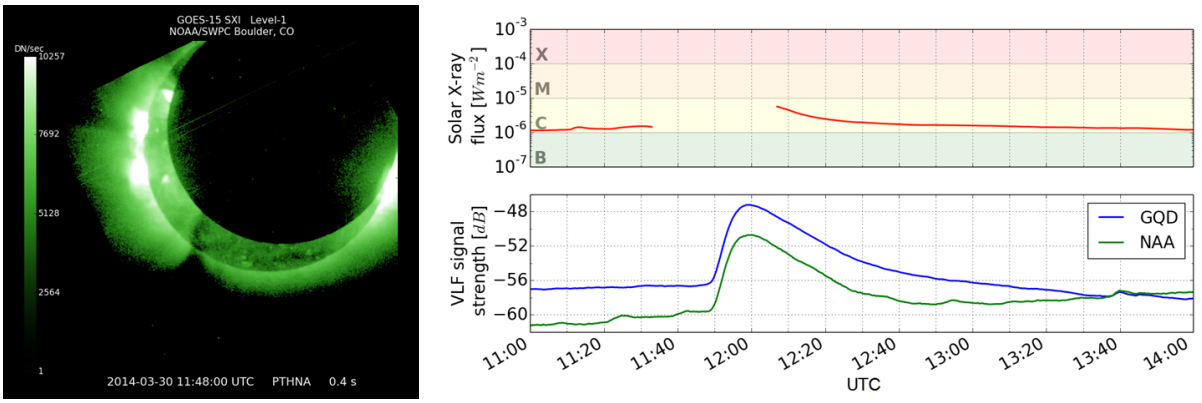

Figure 45: A hidden flare on the time of the partial solar eclipse: The left picture shows the eclipse on 30 March 2014 as seen by the X-ray imager of GOES-15 (provided by SWPC, http://www.swpc.noaa.gov/). The right picture details measurements of GOES' solar X-ray flux (top) and selected VLF amplitudes at GIFDS-NTZ (bottom). During the eclipse gap, GOES was blind for the shadowed region. Coincidentally, GIFDS there detected a moderate-class flare. [adapted from Wenzel et al. (2016)]

signals in Neustrelitz as well as overlapping measurements from the new stations in Boston, Stanford, and Taiwan, there are now at least two potential measurements at any time. Even if a single transmitter's signal is temporarily lost (e.g. due to regular maintenance) the system will remain stable by the use of several VLF channels.

The use of a world-spanning collection of overlapping VLF paths enables flare detection the whole day. The built-in redundancy keeps the network functional even if one signal is unavailable. This is a major difference to the satellite system GOES, which will miss events in case of troubles. Due to regular eclipse periods caused by the Earth or the Moon, these problems arise regularly. Fig. 45 shows an example of such a hidden solar flare during the half hour the Moon covered the GOES-15 satellite on 30 March 2014. However, the GIFDS measurements clearly prove the occurrence of an event. The algorithm classified it as a mid-class moderate flare of M4. Consequently, GIFDS can bridge measuring gaps and is able to work complimentary to satellite detection systems. In the future, a refined GIFDS algorithm shall be integrated as a service into the Ionosphere Monitoring and Prediction Center IMPC (http://impc.dlr.de/). Besides the original VLF measurements, flare alerts will be provided for moderate to severe events that show a direct impact on the lower ionosphere. Furthermore, supplementary phase measurements are planned to be included for increasing the reliability. A brief outlook is given in an instant.

4.4.2 Phase measurements

Phase measurements provide additional information on the state of the lower ionosphere and therewith solar flare effects. Similarly to amplitude measurements, the VLF phase suffers a certain diurnal pattern. Fig. 46 shows an example of amplitude (top) and phase variations (bottom) of two VLF signals measured in Stanford during a quiet period of low solar flare activity on 25 May 2015. The phase is increasing at sunrise, remains on a high stable level

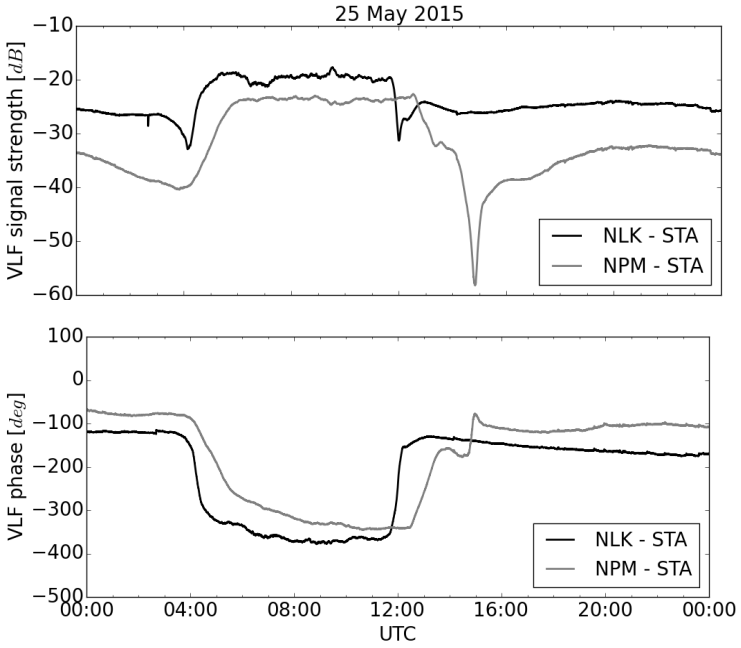

Figure 46: Diurnal amplitude (top) and phase variations (bottom) of NLK-STA (black) and NPM-STA (grey) on 25 May 2015.

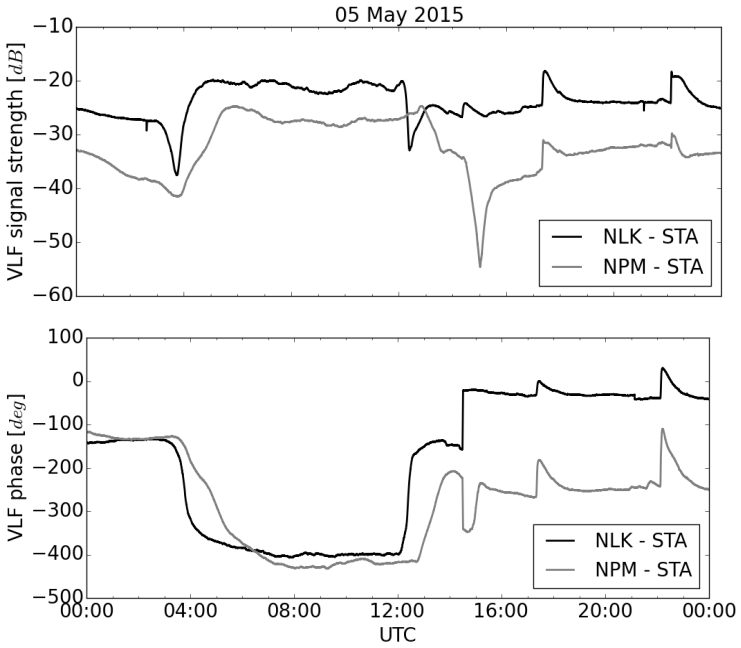

Figure 47: Comparison of solar flare impacts on VLF amplitude (top) and phase measurements (bottom): There are two whole-day measurements showing the results of external impacts coming from solar flares (two clear peaks at 17 and 22 UTC). Note the phase jump about 14:30 UTC in both signals.

during daytime, and decreases with sunset. Amplitude minima correspond to abrupt phase changes. The day-night transition can even feature multiple phase steps, correlated to the number of modes in the Earth-ionosphere waveguide. Such a mid phase step can be seen for NPM-STA around 14:00 UTC. At night, the phase is generally low, as the D layer disappears and the expanded waveguide leads to a higher phase delay.

Considering the lowering of the ionospheric reflection height during solar flares as the only influencing quantity, the phase of VLF signals is expected to be advanced. Fig. 47 presents the effects of two solar flares (M2.6 around 19:00 UTC and X2.7 at about 22:00 UTC) on VLF amplitude (top) and phase measurements (bottom). Indeed, both exemplary signals show a clear phase advance for both flares. Also the flare size seems to be directly correlated in comparison to the amplitude perturbations. In contrast, the amplitude measurements may be illusory. The X-class flare at 22:00 UTC possesses a sudden decrease before reaching its actual maximum in both signals. This phenomenon will be described in section 5.2. However, it strongly depends on specific conditions of ionospheric propagation and did not appear in the flare control sample. Though the phase hence looks to be more accurate, it has to be pointed out that some literature has shown also negative phase changes during flares, e.g. Ohshio (1971) for the long path from Fort Collins (WWVL, 20 kHz) to Japan. Even worse, there may be no apparent reaction at all (cp. Kaufmann et al., 2002), but a combination of the different measurements is promising.

In general, NLK and NPM possess a good phase stability, while other transmitters are unstable or don't preserve the information. So, there can be gradual phase drifts or jumps inside the measurements. Such a jump is visible around 14:30 UTC. This is most probably caused on the receiver site, since both signals are affected. Achieving phase stability at the receiver required modifications of the Perseus SDR (see section 3.1.3). The software is continuously adapted to include the measurements.

„All the variety, all the charm, all the beauty of life is made up of light and shadow. “
Leo Tolstoi

5

Influence and modelling of a solar eclipse

On 20 March 2015, a solar eclipse was noticeable over Northern Europe. For this event, we investigated the obscuration effects on VLF measurements for six different transmitters. The data given in section 5.1 has been presented similarly by the author before in Hoque et al. (2016). A time delay in the D-region response from virtually 0 to merely 11 minutes could be identified. We now will correlate this time to the geographic orientation of the propagation paths.

In order to derive information about the dynamics in the lower ionosphere, half of the VLF links are modelled according to the mode theory with the Long-Wavelength Propagation Capability code. The novel conclusions are detailed in section 5.2. Via an exponential ionospheric profile for the D region, depending on the reference height and the sharpness parameters, we can adapt the ionospheric conditions iteratively for reconstructing the obscuration along the paths. As a simplification, the mid sub-reflective point on the great circle line is taken as the unique referencing replacement for a path. During the time of the considered eclipse, the ionosphere's reflection height is shown to vary by several kilometres, and also the sharpness attains the values that are known from usual nights – although the values are reached in a much faster pace.

Finally, section 5.2 deals with the reproduction of the ionospheric state using VLF, TEC and ionosonde measurements. Hereby, results that were partially published in Hoque et al. (2016) together with the author are incorporated. In addition to this, we will generate electron density profiles of the lower ionosphere via modelling VLF signals under simulated eclipse propagation conditions. They prove a gradual change of the transmitting properties determined by the respective degree of the maximum obscuration of the path.

5.1 Observations

When the Moon passes our view on the Sun, most are impressed by the covering – fully or partially. Also from a scientist's perspective, these uncommon incidents offer the priceless chance for a well-defined study of the Earth's upper atmosphere. Due to the gradual variation of solar illumination (and consequently, EUV and X-ray radiation), dynamic ionisation changes are initiated in the whole ionosphere. Similarly to sunset and sunrise – certainly in a rather fast sequence, limited to a regional scale – we experience measurable ionospheric impacts, which may even last for hours after maximum obscuration.

5.1.1 Selected studies on solar eclipses

There are plenty of articles concerned with the investigation of eclipse effects on the ionosphere. Many studies of the last decades are confined to the E and F region, i.a. Afraimovich et al. (2001); Cohen (1984); Jakowski et al. (1999, 2008); Krankowski et al. (2008); Le et al. (2009); Liu et al. (1998); Mueller-Wodarg et al. (1998); Rashid et al. (2006); Rishbeth (1968). As one of the theoretical pioneers, Rishbeth (1968) demonstrated relations for the ionospheric response – in particular the production and loss rates – during solar eclipses, but restricted to the upper ionospheric regions. In contrast, the D region was not taken into consideration, due to limited data compared to the complex physical processes. Moreover, in many cases, TEC data is evaluated, which is not representative for the D layer.

In order to derive a time delay between the impact from outer space and the reaction of the atmosphere, Cohen (1984) made use of satellite beacon measurements. He unveiled connections of the maximum obscuration with the time of maximum depletion in TEC. Jakowski et al. (1999) determined a delay of ionospheric response in TEC of up to 40 minutes in the lower latitudes. Later, Le et al. (2009) analysed a latitudinal dependence of TEC and NmF2 responses during a solar eclipse by means of GPS TEC observations and ionosonde data. The eclipse's influences were found to be larger in mid latitudes. There, the depletion of TEC reaches from 30 to 40 %, with a time delay of 20 to 40 minutes (see, Jakowski et al., 2001, 2008; Krankowski et al., 2008).

Investigations of the D region ionosphere are quite rare and mostly limited to ELF/VLF measurements. The general task is to model solar eclipse effects in the VLF response for inferring ionospheric parameters. As one of the few, Fleury and Lassudrie-Duchesne (2000) presented VLF simulations of the solar eclipse of 11 August 1999 in Europe. With the help of LWPC (cf. Ferguson, 1998) and an exponential electron density profile (18) introduced by Wait and Spies (1964), they obtained a 5 km increase of the reflection height h' for 50 % obscuration (under the assumptions that h' is proportional to the obscuration and the sharpness β is constant). See section 2.3.3 for more details. Clilverd et al. (2001) studied the same eclipse, but assuming a linear dependence between solar irradiation and electron production instead. For VLF paths suffering a total eclipse, they calculated an increase of h' by 8 km and of β by $0.07\,\mathrm{km}^{-1}$. The fit of the model for the eclipse in 1999 was improved by their approach. However, by studying the solar eclipse of 22 July 2009 in India, Pal et al. (2012) showed very well fitting with the original attempt. Our research object is the eclipse in Northern Europe that happened on 20 March 2015. Its effects on VLF signals and the D layer ionosphere will be explained in more detail below. Some of the recorded data can be found in Hoque et al. (2016).

5.1.2 Observations of the 2015 vernal equinox solar eclipse in VLF signals

On 20 March 2015, a solar eclipse occurred in Northern Europe. The shadow was moving northeast from the North Atlantic over the south of Iceland towards Svalbard (cf. Fig. 48). The penumbra appeared at 07:40 UTC, and the first contact of the umbra was reported around 09:10 UTC. The greatest eclipse (i.e. the shadow of maximum extent) was documented close to Iceland at 09:46 UTC. Finally, the umbra disappeared around 10:20 UTC, and the last contact of the penumbra was observed at 11:50 UTC.

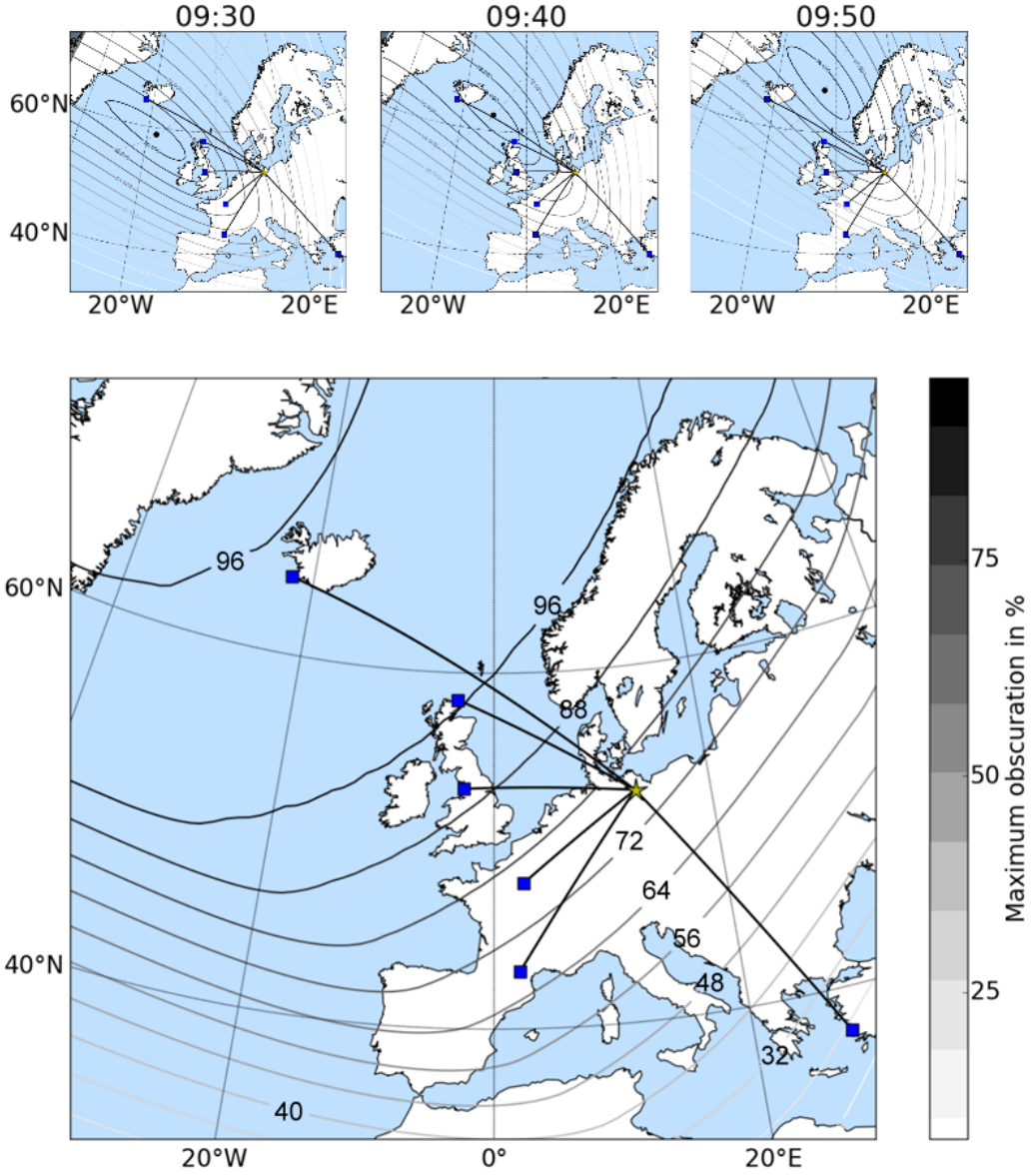

Figure 48: Snapshots of the total solar eclipse on 20 March 2015 (upper panel) and maximum obscuration over Europe (below): The respective obscuration values are indicated by level lines shaded grey according to their percentage. The GIFDS receiver in Neustrelitz is marked by a yellow star and the received transmitters by blue squares. The corresponding great circle propagation paths are shown as black lines.

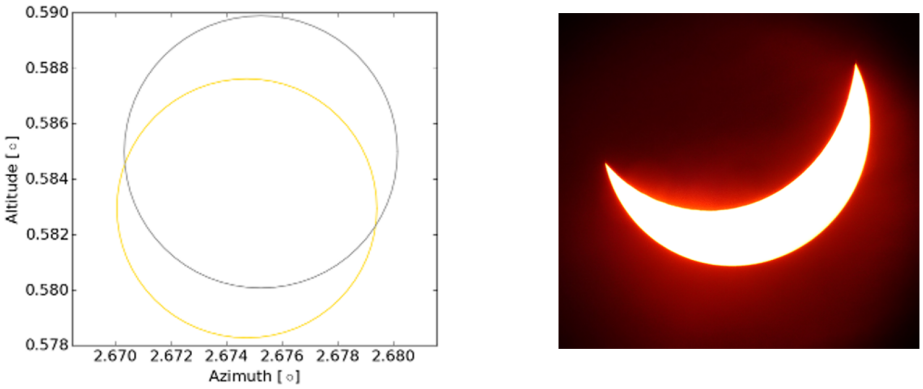

Figure 49: Computed maximal overlap of the Sun's (yellow) and Moon's disc (grey) for Neustrelitz (left) and photo of the eclipse taken through a telescope at DLR site Neustrelitz (right).

The Sun's obscuration data is calculated with help of the PyEphem application (see http://rhodesmill.org/pyephem/), which provides positions of astronomical objects via angular separation on the Earth's surface. We then computed the resulting obscuration values from the overlap of the Sun's and Moon's disc as seen from the Earth at a specific location and time (cf. Fig. 49). We got the obscuration level lines from function maps that were determined on a grid with a resolution of one degree for the geographic coordinates, accumulated for obtaining the maximum.

Whereas the maximum obscuration can be seen in Fig. 48, the diurnal variation of VLF signals on six different propagation paths is shown in Fig. 50. These measurements will be used for judging on the eclipse's effects. The time of obscuration for the corresponding mid sub-reflective points varies with each path. These intervals are highlighted in grey. To exclude the presence of X-ray impacts during this time, the solar X-ray flux by GOES is displayed at the bottom. GOES 15 was in the Earth's shadow. GOES 13 shows no sign of a solar flare. Consequently, we may assume quiet solar conditions during the time of eclipse and rely our study and further modelling on VLF variations that are caused primarily by the eclipse. All VLF recordings were taken at the DLR site Neustrelitz. The six transmitters of investigation are NRK (37.5 kHz) in Iceland, GXH (57.4 kHz) and GYN (81.0 kHz) in Great Britain, FTA63 (63.85 kHz) and FUG (62.6 kHz) in France, and TBB (26.7 kHz) in Turkey (cf. Tab. 11). Whereas the first three stations are close to the totality zone and experience a maximum obscuration at the mid sub-reflection point of over 84 %, TBB undergoes a partial eclipse of only 50 %. Additionally, the selected propagation paths are arranged in different angles with the direction of the eclipse's progression.

A more detailed view on the six recordings of the eclipse period is given in Fig. 51. The original data that was depicted in Fig. 50, is further processed here by detrending the diurnal variations according to the description in section 4.3.1. The respective obscuration function at the mid sub-reflection point can be found below. It was obtained from the PyEphem output similar to the level lines, but we have taken minute-wise values at the precise location (cp., http://rhodesmill.org/pyephem/).

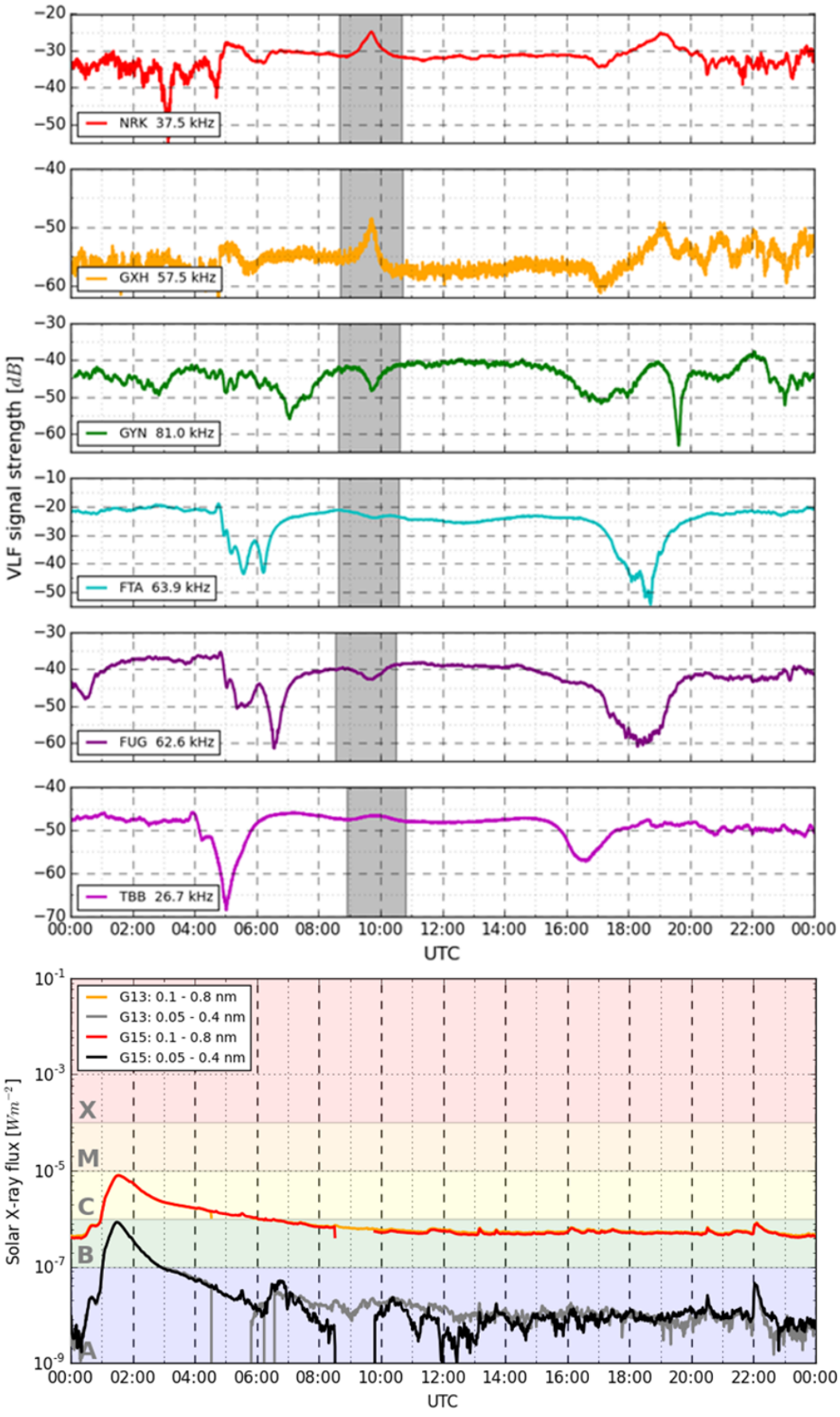

Figure 50: VLF amplitude measurements received in Neustrelitz on the day of the eclipse and the solar X-ray flux measured by the GOES satellites G13 and G15. [extended from Hoque et al. (2016)]]

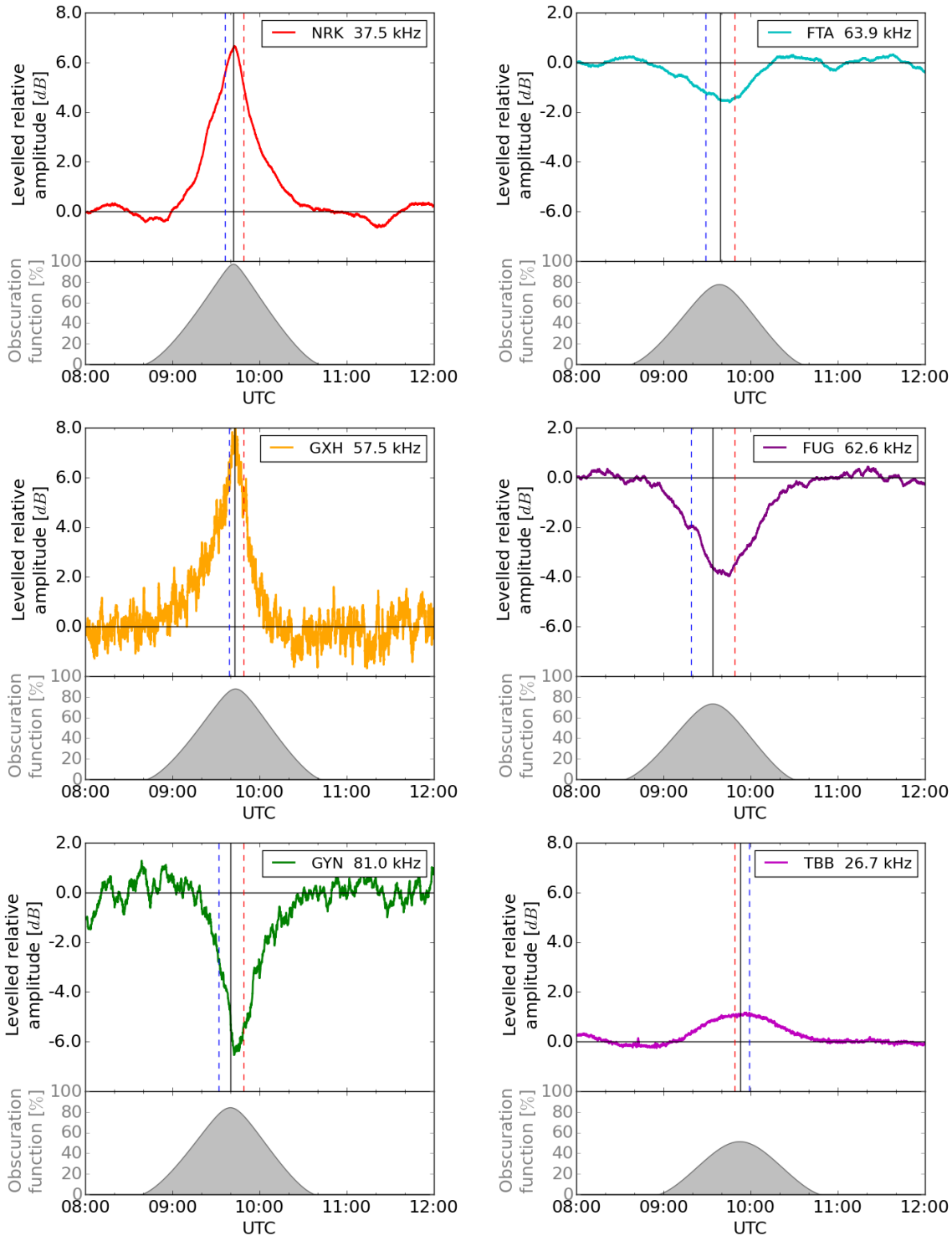

Figure 51: Effects of the eclipse on VLF signals: The same-scale amplitude measurements are corrected by the average daytime trend for adjusting the values at zero. Also seen are the maximum obscuration time at the transmitter (blue dashed) and the receiver site (red dashed). They border the shadow's progression along the respective propagation path. The corresponding time for the mid sub-reflective point is in between (black solid). Its whole obscuration function is pictured below. [adapted from Hoque et al. (2017)]

Call sign, frequency	Location	Distance and bearing	First / last contact	Max. obscur. and time	Max. amp. and time
NRK 37.5 kHz	63.85°N,	2322.95 km	08:41 UTC /	97.0 %	6.66 dB
	22.47°W	314.08°	10:41 UTC	09:42 UTC	09:42 UTC
GXH 57.4 kHz	58.59°N,	1186.77 km	08:42 UTC /	87.6 %	7.97 dB
	3.63°W	306.03°	10:43 UTC	09:43 UTC	09:43 UTC
GYN 81.0 kHz	53.83°N,	1048.66 km	08:39 UTC /	84.1 %	6.55 dB
	2.83°W	279.30°	10:38 UTC	09:40 UTC	09:42 UTC
FTA63 63.85 kHz	48.54°N,	907.08 km	08:38 UTC /	77.3 %	1.61 dB
	2.58°E	238.14°	10:36 UTC	09:39 UTC	09:45 UTC
FUG 62.6 kHz	43.39°N,	1369.29 km	08:33 UTC /	73.1 %	3.98 dB
	2.10°E	220.42°	10:30 UTC	09:34 UTC	09:45 UTC
TBB 26.7 kHz	37.41°N,	2084.28 km	08:56 UTC /	51.2 %	1.16 dB
	27.32°E	142.50°	10:48 UTC	09:53 UTC	09:56 UTC

Table 11: VLF transmitters observed during the solar eclipse of 20 March 2015: In addition to the basic parameters, the event-specific times of first and last contact, as well as, the maximum obscuration at the mid sub-reflective point and the measured peak amplitude are listed. [extended from Hoque et al. (2016)]

We can identify huge deviations in the signal strength of more than 6 dB at the three stations pictured in the first column of Fig. 50. The two British ones exhibit much more noise as they operate with less power in a part of the spectrum that is disturbed at our reception site. The transmitters of the second column experienced less obscuration and show smaller fluctuations but are still affected by the changes of ionospheric conditions.

Although all paths are similarly short (with lengths of about 900 to 2500 km), the peak heights cannot be compared directly because of the fact that different frequencies are reflected at different ionospheric heights. This influences the overall propagation of a signal on its way from the transmitter to the receiver. Moreover, the amplitude variation may be positive or negative depending on the Navy station's transmitting power and the length of the propagation path through the Earth-ionosphere waveguide. In order to conclude information on the lower ionosphere and the resulting effects on wave propagation, a model is required, comprising the varying frequencies, transmitting powers, distances, and bearing angles. The discussion of this model will follow in section 5.2.2.

Nevertheless, the delay of the ionospheric response is reflected more straight in the peak time. We regard the difference of the times of the VLF extremum and the mid point's obscuration maximum as the response delay. With a maximal offset of 11 minutes, our data mirrors that the D region reacts quite fast which is expected and in correlation with previous findings, e.g. Clilverd et al. (2001); Jacobi and Kürschner (2000). This is a fundamentally differing behaviour from what is known of the very inert E and F regions. Comparing the response delay with the so-called maximum eclipse window reveals an approximate linear dependence (see Fig. 52). The latter is defined as the difference between the times of maximum obscuration at receiver and transmitter. A more motivated explanation for the observed relation can be given in terms of geometry. The shadow's shape is roughly elliptical. Its semi-major axis possesses a certain

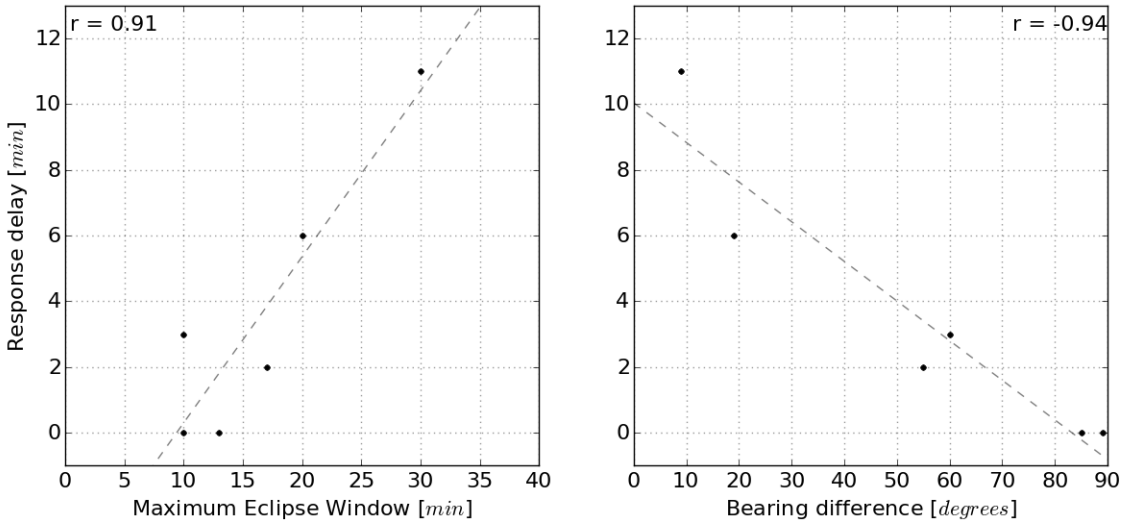

Figure 52: Functional correlations for the response delay: Regressions over the maximum eclipse window (left) and the bearing difference (right) yield very good linear approximations with an absolute Pearson correlation coefficients r close to one.

bearing angle. The absolute value of the difference with the T_x-R_x bearing angle will be referred to as bearing difference. Fitting the response delay over this quantity unveils an even better linear regression. As a consequence, whenever the propagation path completely runs through a fully obscured area, i.e. more or less on the diameter of the afore-mentioned ellipse, an immediate response can be detected. The larger the bearing difference is, the more parts of the path are only partially shadowed and hence less influenced. That's why the maximum obscuration needs some time to move along the path, yielding a delayed maximum for a signal cumulated over its transmission time.

5.2 Modelling of VLF measurements

VLF signals can be modelled using the Long-Wavelength Propagation Capability (LWPC) program. It provides means to simulate the VLF signal propagation using the waveguide mode theory. If one declares a propagation path and a profile for the electron density, LWPC calculates amplitudes and phases.

With a map of the received spatial signal strength distribution of a continuously emitted constant signal one gets a visual impression of the ability for signal propagation through a homogeneous atmosphere. Fig. 53 shows such values for a typical day and a typical night calculated with help of LWPC on a radial grid centered at the Navy transmitter on Iceland. Clearly, signals will propagate very well over regions of water, and they are definitely attenuated by a vast land mass like Greenland. At nighttime, propagation conditions are mostly improved, as the disturbing D layer vanished. At first glance, amplitudes are generally raised (watch out for, e.g., Neustrelitz and Finland). However, there are still areas of reduced signal strength at night – most obvious is the band from Spain over North Italy towards Poland.

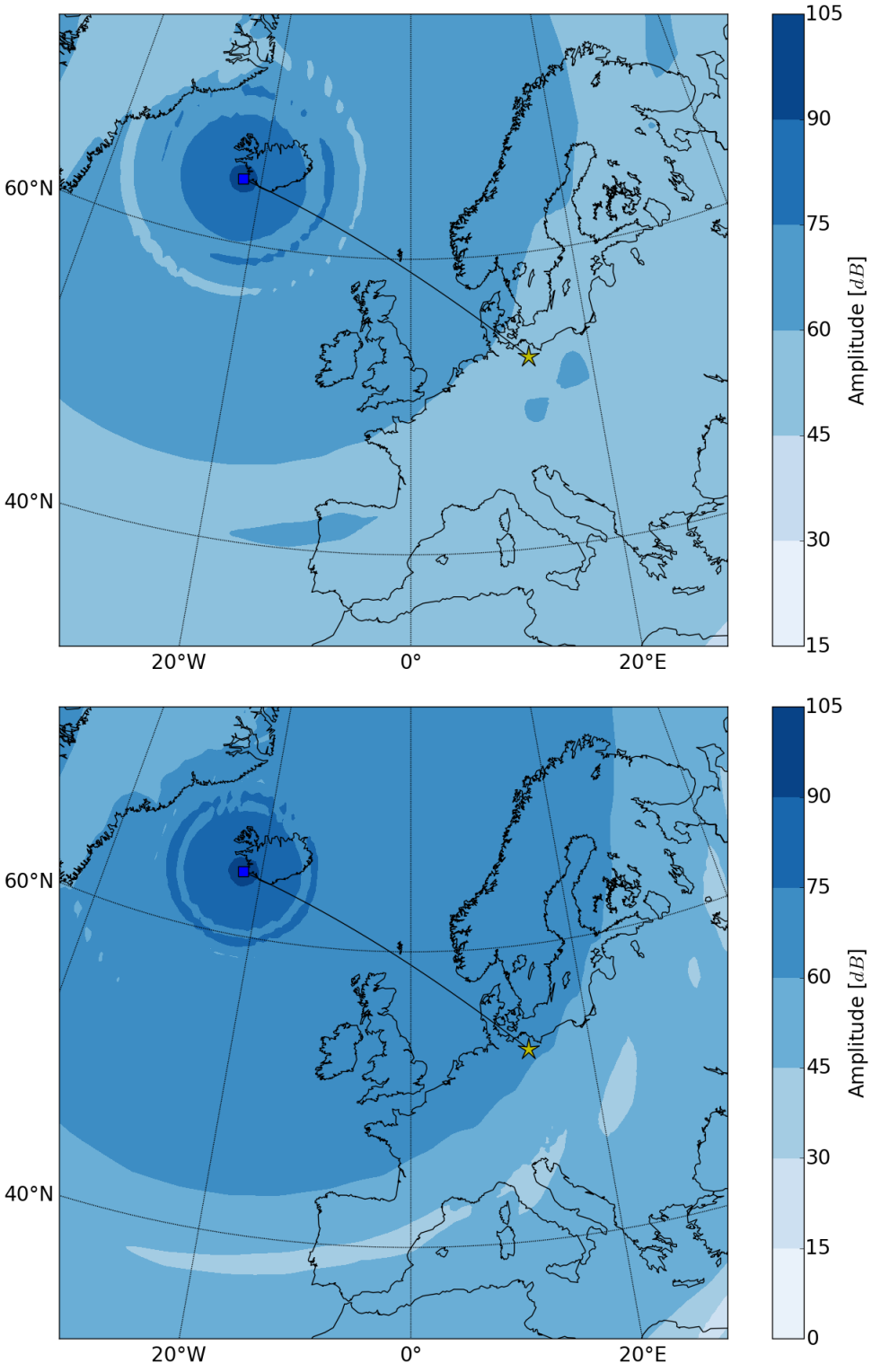

Figure 53: Transmitting properties at day (top) and night (bottom): The images of the signal strength distribution are made for the station NRK at 37.5 kHz (blue square). For reference, Neustrelitz is marked by a yellow star, linked to NRK by the propagation path.

5.2.1 Modelling in LWPC

For analysing the influence of the ionospheric reflection height and the sharpness, we sampled the received amplitude alongside the path between NRK/Iceland and NTZ/Neustrelitz. For fixed $h' = 76\,\mathrm{km}$, with β increasing from 0.3 to $0.5\,\mathrm{km}^{-1}$, Fig. 54 shows the resulting signal strength. In the near field, it oscillates, and it becomes decreasing whenever the distance is large enough. Note that the slope of the trend depends on β. The difference of each of the obtained amplitude curves with the reference level curve of $\beta = 0.3\,\mathrm{km}^{-1}$ unveils a discrepancy getting bigger for larger β.

Conversely, if $\beta = 0.43\,\mathrm{km}^{-1}$ is constant and h' varies between 71 and 84 km, we obtain Fig. 55. Apparently, the amplitude fluctuates more strongly with increasing distance from the source, but with a generally decreasing maximum level. Here, the increasing h' causes a drift of the extremal positions directed away from the source. Knowing the basic shape of the amplitude as a function of the two, h' and β, allows to find a good initial guess for the parameters under concrete conditions, which can be adjusted iteratively. This will now be performed to model the lower ionosphere during the time of the eclipse.

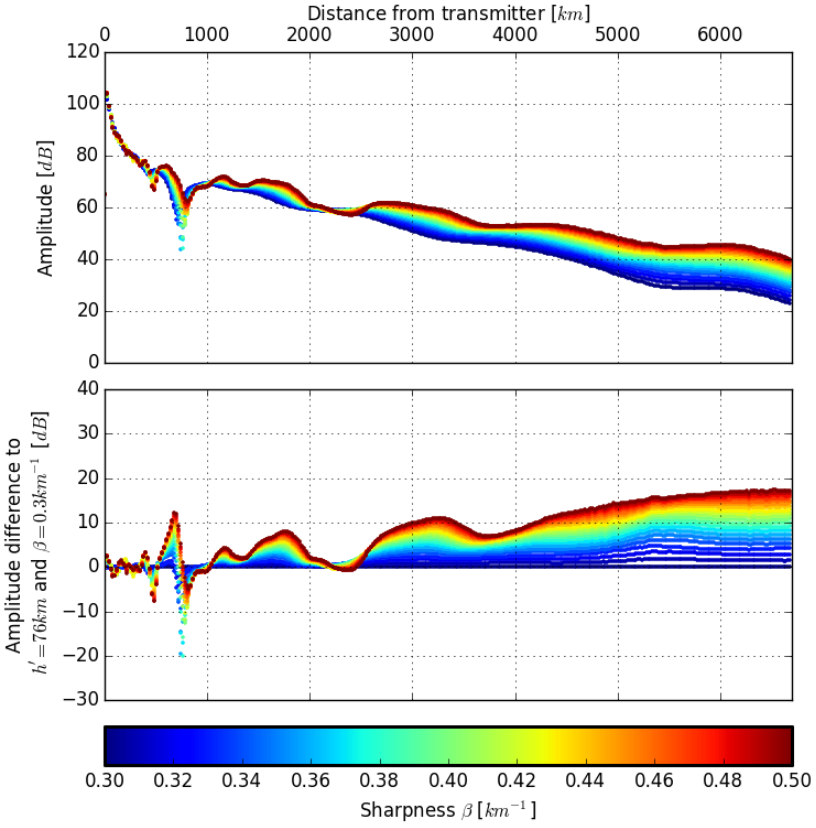

Figure 54: Modelled amplitude's variation with the distance from the transmitter NRK for $h' = 76\,\mathrm{km}$ and selected β: The signal curves for the 21 sharpness values are shown in a common 2D plot (top) in different colours. In the picture at the bottom, the difference of each of the curves with the initial values from $\beta = 0.3\,\mathrm{km}^{-1}$ is seen.

5.2.2 Modelling of the solar eclipse 2015

For simulating the propagation conditions during the eclipse, the temporal development of the determining parameters h' and β is in need. This will be made varying with the gradual change of the electron density, which is in close correlation to the observable obscuration. The actual course of the two parameter functions is prescribed with the initial conditions of h' and β representing the unperturbed ionosphere with respect to the latitudinal, seasonal, and diurnal variation.

From Ferguson (1980), an empirical model is known to specify the reference height and the sharpness of the unperturbed lower ionosphere by

$$\begin{aligned} h' &= 74.37 - 8.097\cos\theta + 5.779\cos\varphi - 1.213\cos\psi - 0.044R_s - 6.038G = [\mathrm{km}], \\ \beta &= 0.5349 - 0.1658\cos\theta - 0.08584\cos\psi + 0.01296G = [\mathrm{km}^{-1}]. \end{aligned}$$

The crucial input factors are given by the solar zenith angle θ and the geographic latitude φ. Moreover, with m_a indicating the month of the year, $\psi = 2\pi(m_a - 0.5)/12$ includes the seasonal change. As constants, we have the Zürich sunspot number R_s, and the geomagnetic activity switch G (which is 0 for quiet and 1 for disturbed conditions).

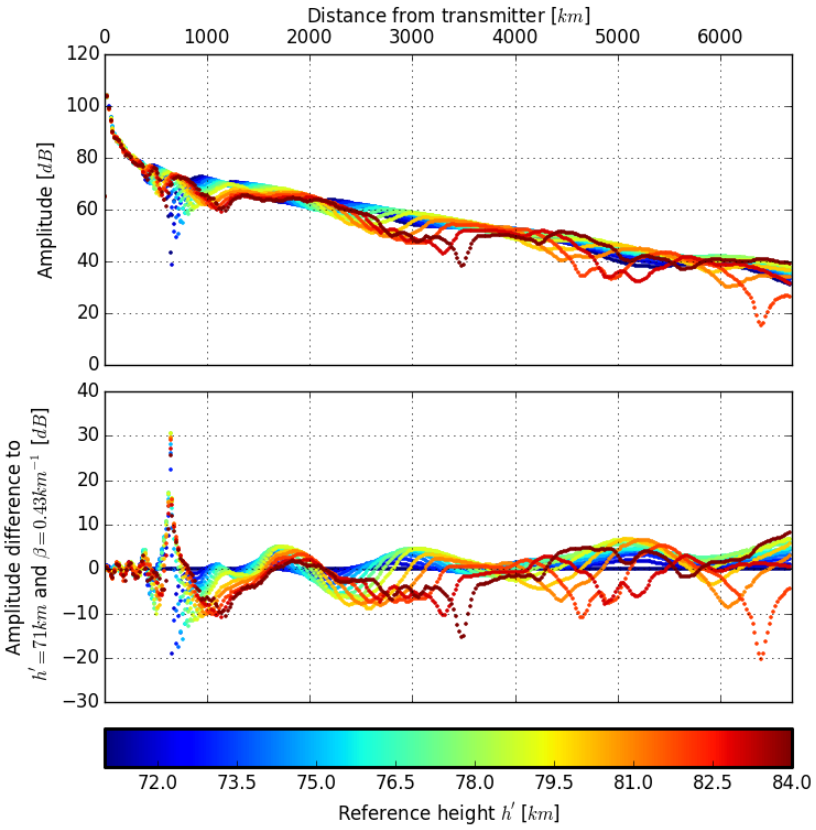

Figure 55: Modelled amplitude's variation with the distance from the transmitter NRK for $\beta = 0.43\,\mathrm{km}^{-1}$ and selected h': The signal curves for the 14 reference height values are depicted analogous to Fig. 54, but with β fixed and h' ranging from 71 km to 84 km.

In the time before the eclipse, the activity was decreasing after a geomagnetic storm. During the time of the eclipse from 9 to 12 UTC, the GFZ data archive lists the index $Kp = 3$, indicating unsettled, almost quiet conditions. Due to the very low activity and since the reaction of the D region is quite fast, $X_5 = 0$ is used. (Note that this is not appropriate for upper layers, see section 5.3.2.) Though the solar activity was increased days before the time of investigation, on this day, the Zurich sunspot number $X_4 = 0$ was already documented.

The geographic latitude and the near-sunrise solar zenith angle of course are not fully constant along the paths. Hence they are drawn at the center of the observation area, which is close to the receiver in Neustrelitz. Fixing the values $\theta = 50°$ and $\alpha_{za} = 75°$ then leads to

$$h'_{quiet} \approx 76\,\mathrm{km}$$

and $\beta_{quiet} \approx 0.46$. Ferguson's reference height formula has proven high reliability in the past (see e.g. Thomson, 1993). However, the sharpness is much more unsteady. In previous experiments, the value had to be corrected in regard of the dependence on latitude and season. In accordance with Clilverd et al. (2001), we hence slightly reduce it to

$$\beta_{quiet} \approx 0.43\,\mathrm{km}^{-1}.$$

Modelling the VLF amplitude values depending on the ionospheric conditions, i.e. h' and β, during the solar eclipse is possible using LWPC. We calculate the resulting signal strength on a grid around the initial conditions, more precisely for β ranging from 0.3 to $0.5\,\mathrm{km}^{-1}$ and h' between 71 and 84 km. The obtained landscape helps to to understand the variability of the signal strength measured in Neustrelitz. It further depends on the transmitter's power, distance and path orientation. We investigated the three different propagation paths from NRK, FUG, and TBB to Neustrelitz only, as the necessary data of the others is not available. The three outputs are seen in Figs. 56 58, and 60, respectively. Now we are left to determine a route through the landscape that corresponds to the actual developments during the time of the eclipse. The initial condition is marked by a triangle. It indicates our starting point of the route. The procedure will be detailed exemplarily on the NRK path; the other two are treated the same way.

We assume a linear dependency of the change of parameters h' and β with increasing obscuration. Therewith, $\Delta h'$ and $\Delta\beta$ are constant for a chosen time step. Both should be positive, since this is the expected behaviour as it is known from the sunset. In the decreasing obscuration phase, we simply return on the same way. Starting from the initial point, the overall change of h' and β remain the only variables. For finding a suitable route, the line between the two points is divided into smaller steps. The intermediate points (marked by the circles in each of the figures) are used for comparing the simulated amplitudes with the measurements. They are restricted to a grid of 0.1 for h' and 0.01 for β because of demands of LWPC. The best fit will be identified via a high Pearson correlation coefficient

$$r = \frac{\sum_{i=1}^{n}(A_i - \bar{A})(M_i - \bar{M})}{\sqrt{\sum_{i=1}^{n}(A_i - \bar{A})^2}\sqrt{\sum_{i=1}^{n}(M_i - \bar{M})^2}}.$$

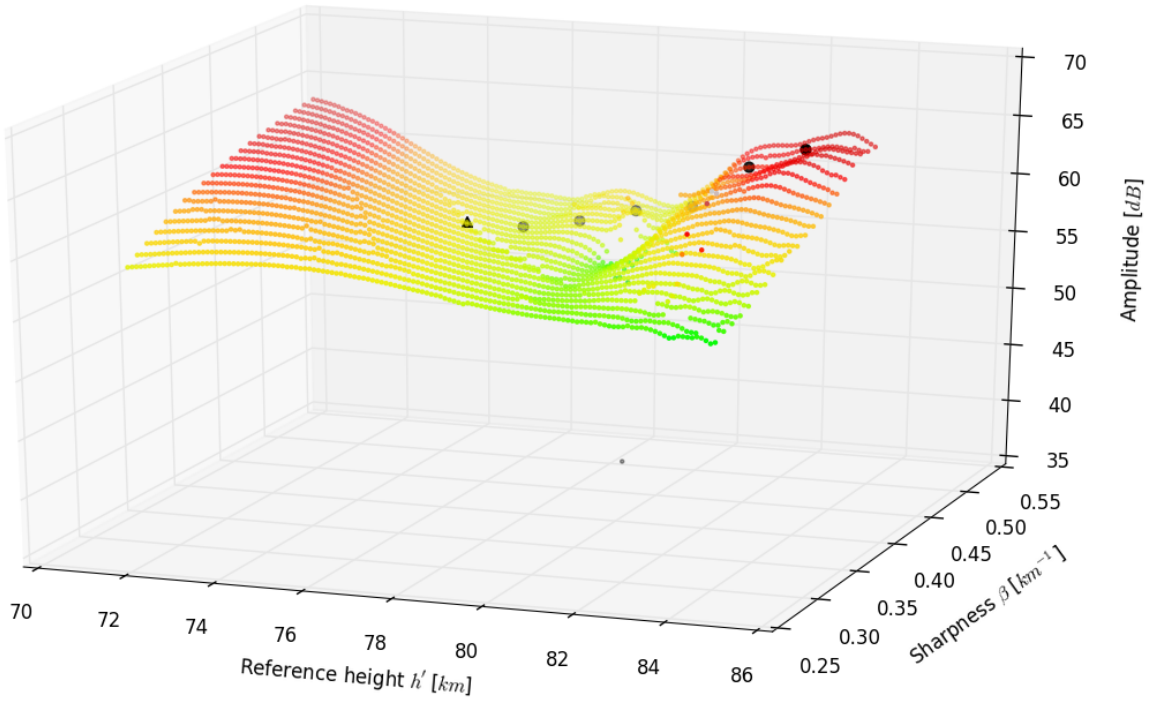

Figure 56: Modelled amplitude variations of NRK at the receiver site NTZ for varying reference height h' and sharpness β: The state of the quiet ionosphere ($h'_{quiet} = 76\,\mathrm{km}$, $\beta_{quiet} = 0.43\,\mathrm{km}^{-1}$) is indicated by a triangle.

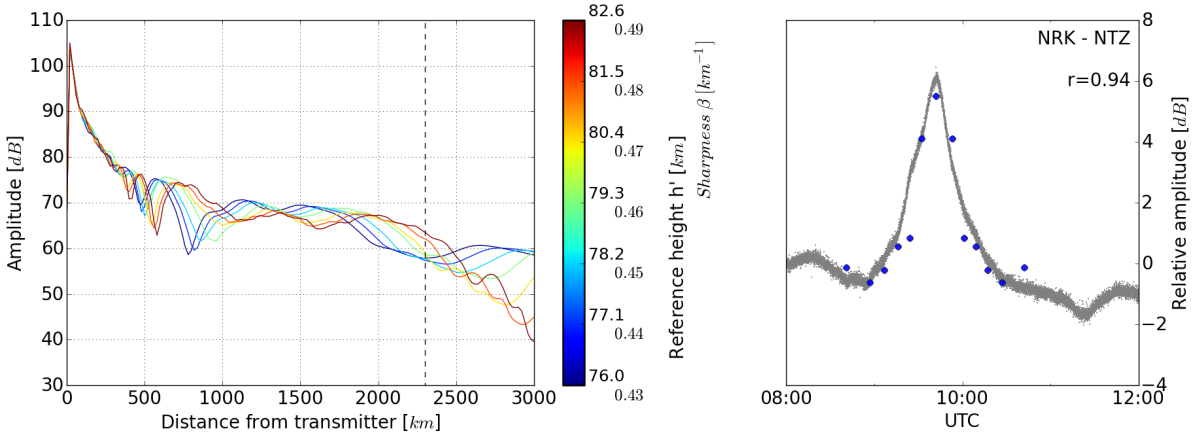

Figure 57: Modelled VLF amplitude over distance from transmitter for the propagation path NRK-NTZ (left) and the resulting signal strength at NTZ (right): On the left picture, the black dashed line marks the distance where Neustrelitz is located. The right picture shows a direct comparison of the modelled values (blue circles) and the original measurements (grey dots).

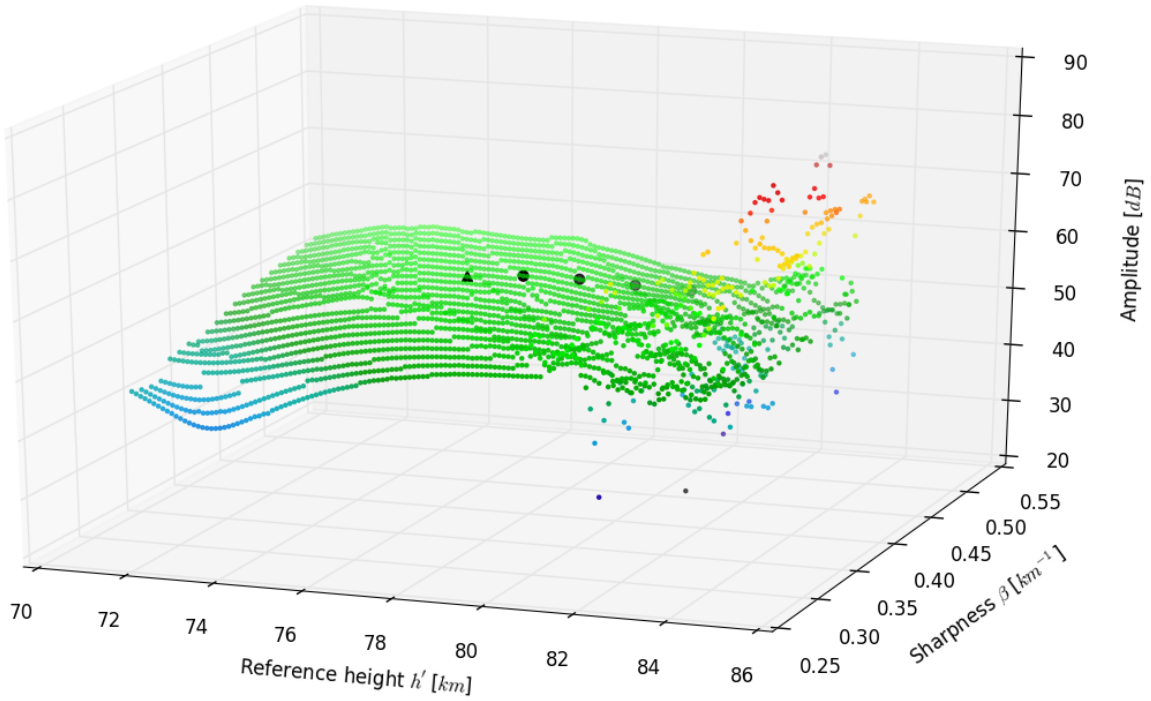

Figure 58: Modelled amplitude variations of FUG at the receiver site NTZ for varying reference height h' and sharpness β: The state of the quiet ionosphere ($h'_{quiet} = 76\,\mathrm{km}$, $\beta_{quiet} = 0.43\,\mathrm{km}^{-1}$) is indicated by a triangle.

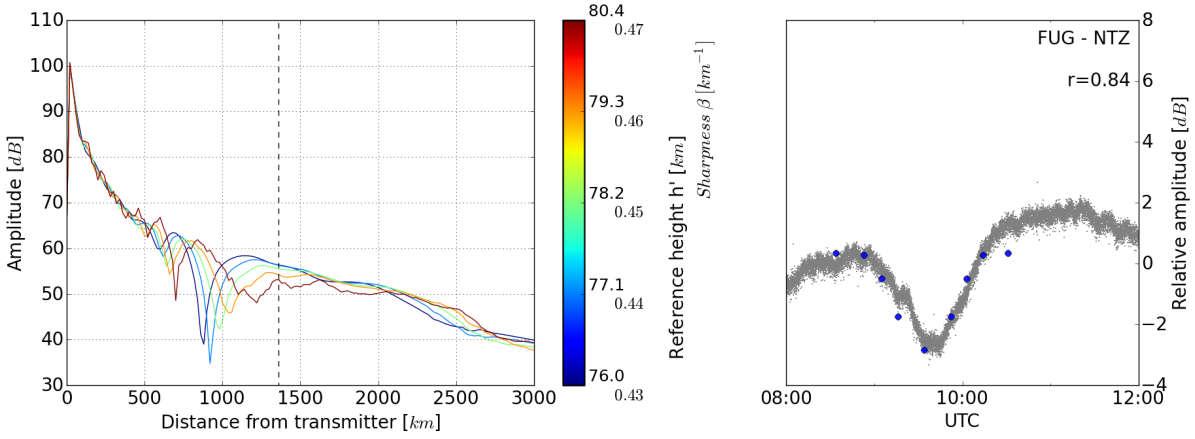

Figure 59: Modelled VLF amplitude over distance from transmitter for the propagation path FUG-NTZ (left) and the resulting signal strength at NTZ (right): On the left picture, the black dashed line marks the distance where Neustrelitz is located. The right picture shows a direct comparison of the modelled values (blue circles) and the original measurements (grey dots).

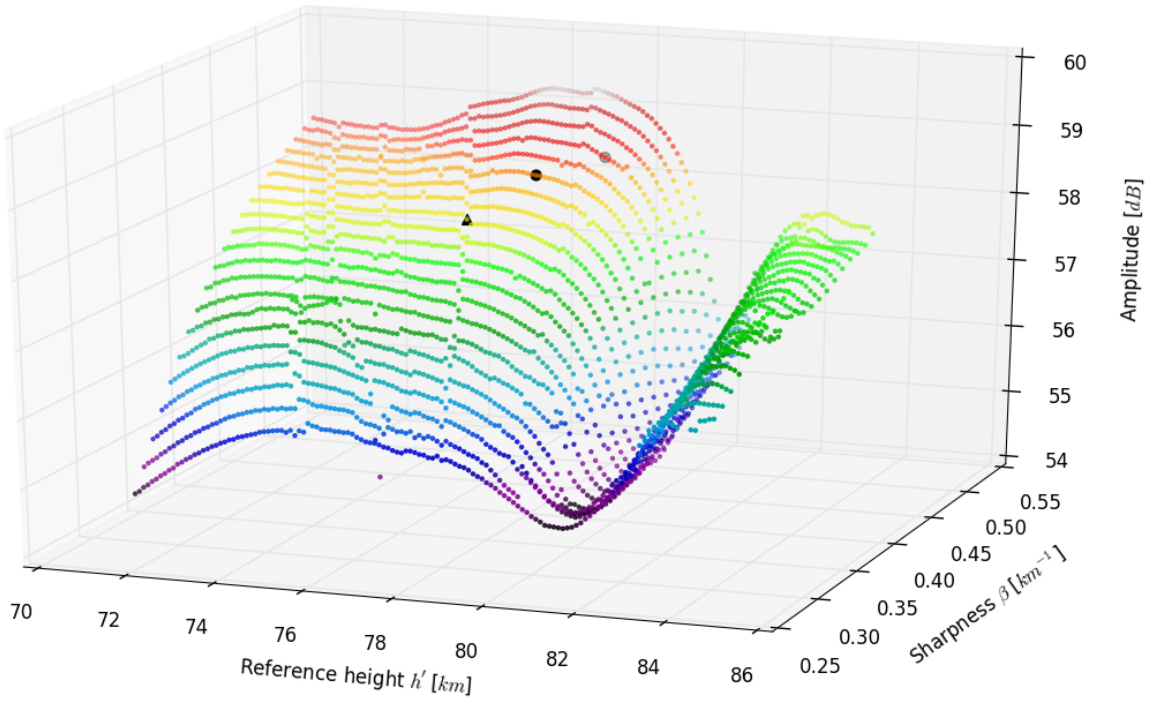

Figure 60: Modelled amplitude variations of TBB at the receiver site NTZ for varying reference height h' and sharpness β: The state of the quiet ionosphere ($h'_{quiet} = 76\,\mathrm{km}$, $\beta_{quiet} = 0.43\,\mathrm{km}^{-1}$) is indicated by a triangle.

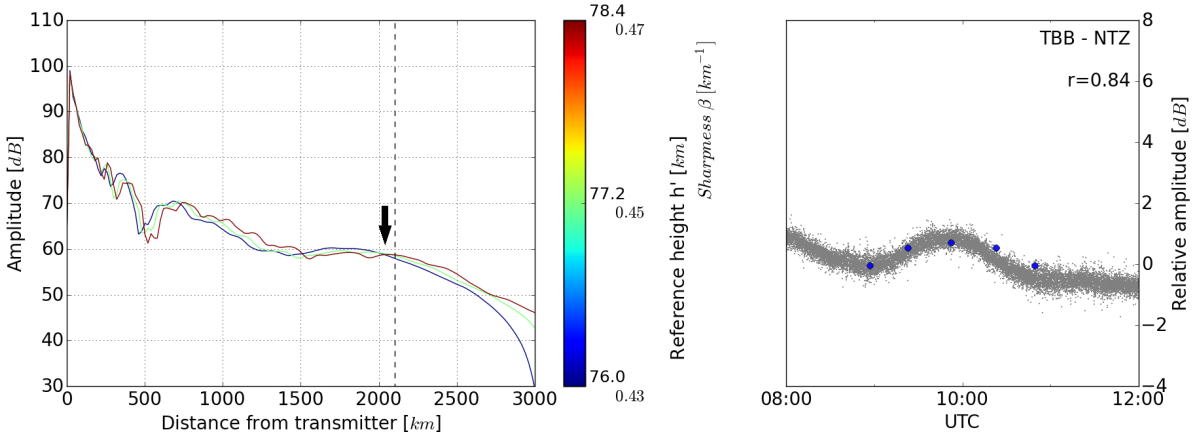

Figure 61: Modelled VLF amplitude over distance from transmitter for the propagation path TBB-NTZ (left) and the resulting signal strength at NTZ (right): On the left picture, the black dashed line marks the distance where Neustrelitz is located. The right picture shows a direct comparison of the modelled values (blue circles) and the original measurements (grey dots).

It is an indicator for how close the model signal strength values M_i are to the corresponding monitored amplitudes A_i. The centering about the mean values $\bar{M}$ and $\bar{A}$, and the normalisation are advantages over the usual least squares method. The total number of steps will be fixed. It is chosen so that the expected fluctuations can be resolved. Clilverd et al. (2001) suggests about six to seven steps for a 100 % obscuration. The NRK-NTZ path experiences an obscuration of 97 %, so we decided to use six steps in order to compensate rounding issues to the grid.

For the considered path NRK-NTZ, Fig. 56 shows the modelled amplitude values at the receiver obtained from LWPC. The route's correlation coefficient of $r = 0.94$ is excellent. The subdivision into six steps yields increases of $\Delta h' = 1.1\,\mathrm{km}$ and $\Delta\beta = 0.01\,\mathrm{km}^{-1}$ on each section. These values comply with the results of earlier investigations (Clilverd et al., 2001; Pal et al., 2012). The end point of the route, i.e. for the time of maximum obscuration, has the parameters $h' = 82.6\,\mathrm{km}$ and $\beta = 0.49\,\mathrm{km}^{-1}$. The increase in height of almost 7 km is typical for a total eclipse.

The parameters obtained for the intermediate times are assumed to be constant on the whole propagation path. Similar to the theoretical studies in Figs. 54 and 55, Fig. 57 (left) displays the resulting amplitudes over the distance from the transmitter NRK under these conditions. Each of the seven times is associated to a colour, and the corresponding parameters h' and β are shown next to the colour bar. The distance of the receiver in Neustrelitz is indicated by a dashed line. The right image of the figure compares the relative amplitudes at this location to the real measurements. They are pictured over the associated time scale.

The second investigated path, FUG-NTZ, is seen in Figs. 58 and 59. As the maximum obscuration is here only 73 %, we used four steps in adapting the ionospheric conditions. Again, a really good fit ($r = 0.84$) was obtained with a route to the end parameters $h' = 80.4\,\mathrm{km}$ and $\beta = 0.47\,\mathrm{km}^{-1}$. The step sizes $\Delta h'$ and $\Delta\beta$ are equal to these of the first example. In contrast to the previous path, the amplitude exhibits a negative peak at the receiver site. This behaviour can only be observed at specific distances and can be understood better by taking a look at the distance plot, in which the amplitude curves for earlier times (blue) are above the one for the maximum obscuration (red), but only in the surrounding of the dashed line of NTZ's position. Note that there is a time delay between the modelled and the measured peak. This is the reaction time on a path perpendicular to the shadow's extent, which was discussed in the previous section, see Fig. 52 and Tab. 11.

Our third path, TBB-NTZ, experienced only 51 % obscuration and the corresponding simulations are detailed in Figs. 60 and 61. Here, already two steps are sufficient. Good results ($r = 0.84$) are received for $\Delta h' = 1.2\,\mathrm{km}$ and $\Delta\beta = 0.02\,\mathrm{km}^{-1}$, leading to $h' = 78.4\,\mathrm{km}$ and $\beta = 0.47\,\mathrm{km}^{-1}$ at the maximum. The peak is not very large, but still remarkable for a half shadow. If the receiver site would be just 50 km closer to TBB, almost no variation during the eclipse time could be noticed. The intersection of all the amplitude curves in the distance plot is marked by an arrow.

5.3 Deductions for the ionospheric state during the eclipse

In order to get an image of the ionosphere's constitution, several different sources of data have to be taken into account. VLF measurements contain valuable information about the ionospheric D region. Via ionosonde measurements, we are able to picture the peak electron densities foE, foF1, and foF2 as well as the height of the F2 layer hmF2 (cp. Section 3.2.1 for the description of the measuring techniques). Finally, GNSS measurements provide the total electron content. All these different measuring techniques help to understand the overall behaviour of the ionosphere and its complex dynamic processes. The geographical distribution of the measuring devices and their specific observation points during the solar eclipse 2015 (e.g., piercing points for GNSS receivers) are illustrated in Fig. 62.

The results of the D-region modelling from the observed VLF measurements during the European solar eclipse 2015 and its impact on the upper ionospheric layers measured by a network of GNSS receivers and one selected ionosonde are discussed in this part.

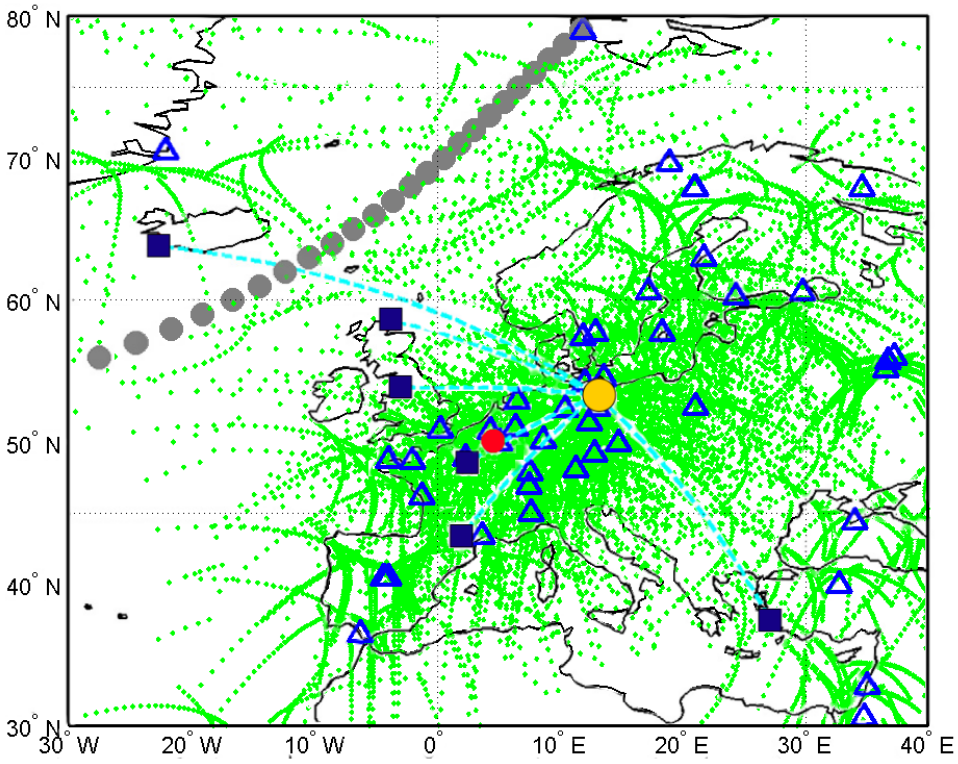

Figure 62: Local distribution of the measurement data available at the time of the eclipse: The GPS receiver network (blue triangles) and their corresponding piercing points (green dots), as well as the ionosonde station DB049 (red circle) and the VLF receiver in Neustrelitz (yellow circle) with the received transmitters (blue squares) can be seen. The grey circles indicate the path of total eclipse at ground level. [adapted from Hoque et al. (2016)]

5.3.1 D-region behaviour

The previous section has shown a good match of the measured and modelled VLF signal amplitudes for the gradual changes during the 2015 solar eclipse over Northern Europe. For this, the exponential ionospheric model (18) introduced by Wait and Spies (1964) was assumed. The results will now be discussed for the different steps of solar illumination.

Fig. 63 shows the modelled variation of the lower-ionospheric electron density distribution for the three different VLF paths NRK-NTZ, FUG-NTZ and TBB-NTZ over time. The gradual decrease of solar illumination leads to a gradual change in electron density with strongest variation at the time of maximum obscuration at the respective path. Note that the time axis of the three pictures in Fig. 63 represents the relevant time window of the local obscuration function. Obviously, electron densities at D-region heights are enhanced for paths with less maximum obscuration, i.e., HWU: 73 %, and TBB: 51 % (see middle and right picture) since parts of solar radiation still provide some photo ionisation.

The resulting profiles during maximum obscuration for the paths NRK-NTZ, FUG-NTZ and TBB-NTZ are shown in the left picture of Fig. 64. For reference, the quiet ionosphere model used for the eclipse day is also shown. Clearly, the ionosphere over the path of near total obscuration, i.e. NRK-NTZ, exhibits the strongest depletion of the electron density profile, but also paths of minor obscuration experience a reduced ionisation. Moreover, the right pictures of Fig. 64 indicate a linear relation between the observed obscuration and the modelled ionospheric reflection height and the sharpness, respectively.

According to our measurements, VLF signals suffer a delay from only a few minutes. This has been expected and is in agreement with earlier findings. However, the size of the delay has been shown to moreover depend on the shadow orientation and movement. For future studies a more detailed evaluation of path segments of different obscuration would be useful in order to simulate VLF signal propagation under more realistic conditions.

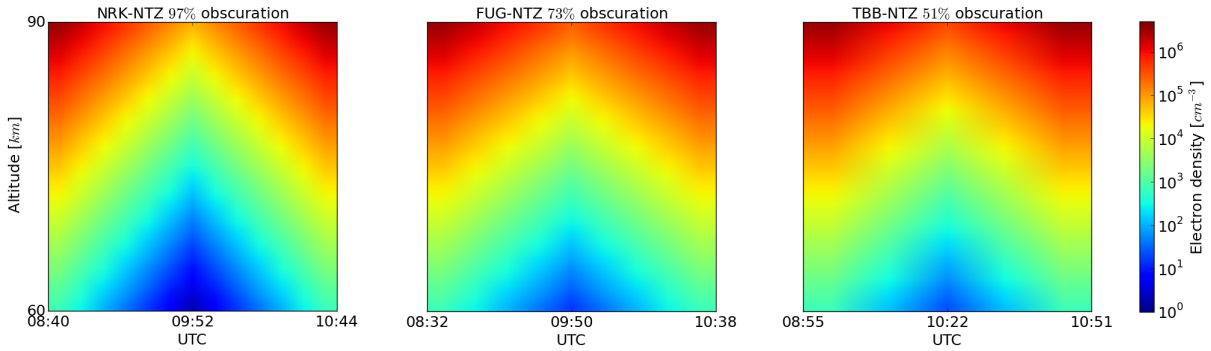

Figure 63: Modelled variation of the electron density distribution between 60 and 90 km over time of the eclipse on the paths from NRK, FUG and TBB to NTZ: For a direct comparison all pictures refer to the same colour bar. The abscissa is adjusted to the time of actual obscuration on each path or rather its mid sub-reflected point.

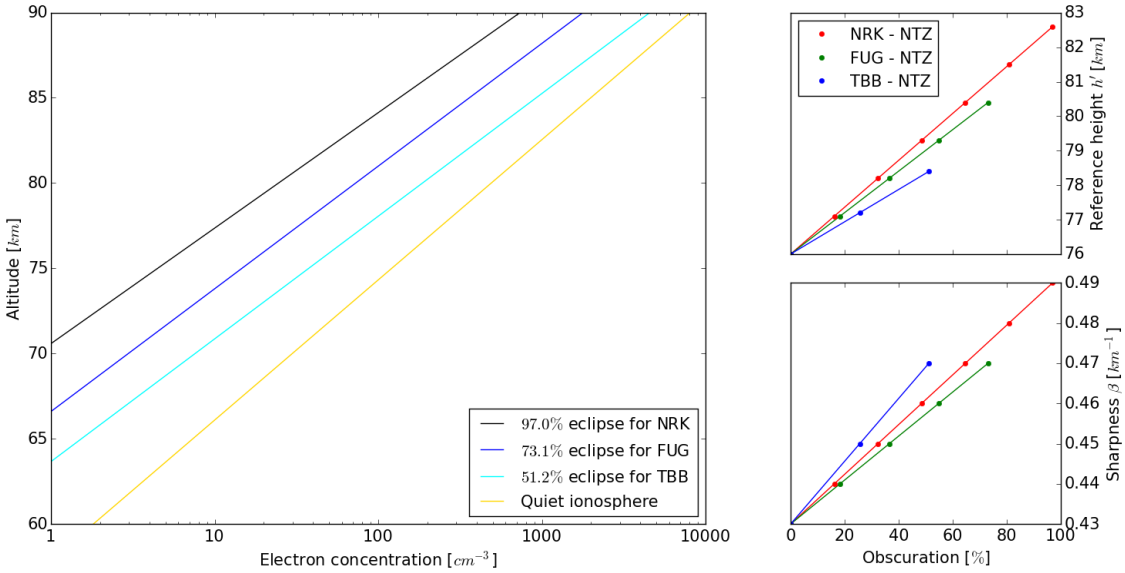

Figure 64: Electron density profiles varying with the solar eclipse's maximum obscuration, the corresponding reference height and sharpness over obscuration: The left picture indicates the ionospheric conditions of the paths TBB (cyan), FUG (blue) and NRK (black) towards NTZ during their maximum obscuration. As a reference, the profile of the quiet ionosphere, with $h'_{quiet} = 76\,\text{km}$ and $\beta_{quiet} = 0.43\,\text{km}^{-1}$ is shown in yellow, based on the exponential model by Wait and Spies (1964). The two pictures on the right illustrate the linear increase of h' and β with growing obscuration.

5.3.2 Impact on the upper ionospheric layers

Whereas VLF measurements offer potential for monitoring the D-region ionosphere, additional measurements, like GNSS and ionosonde data, provide further information on the upper ionospheric layers. To estimate the general ionospheric response, we used GPS dual-frequency precise code (i.e., P1 and P2 signals) and carrier-phase measurements (i.e., L1 and L2 signals) from the International GNSS Service (IGS, Dow et al. 2009) and derived the ionospheric TEC. Therefore, archive data from NASA's Crustal Dynamics Data Information System (CDDIS, ftp://cddis.gsfc.nasa.gov/gnss/data/hourly/) and daily GPS ephemeris data from the Scripps Orbit and Permanent Array Center (SOPAC, http://sopac.ucsd.edu/cgi-bin/dbDataByDate.cgi) were processed by Hoque et al. (2016). During the time of the solar eclipse, about 50 GPS receivers over Europe could be included (cp. Fig. 62).

Fig. 65 shows sequences of the reconstructed European TEC maps during the solar eclipse facing the corresponding 27 day median TEC maps. The path of the total eclipse is traced by circles. Obviously, the regular TEC variations are locally superposed due to the lack of solar radiation below the Moon's shadow. Hoque et al. (2016) found a depletion of up to 6 TEC units. Using the 27 day median, the percentaged deviation has been calculated as

$$\Delta TEC_{perc} = \frac{TEC - TEC_{median}}{TEC_{median}} \cdot 100\%.$$

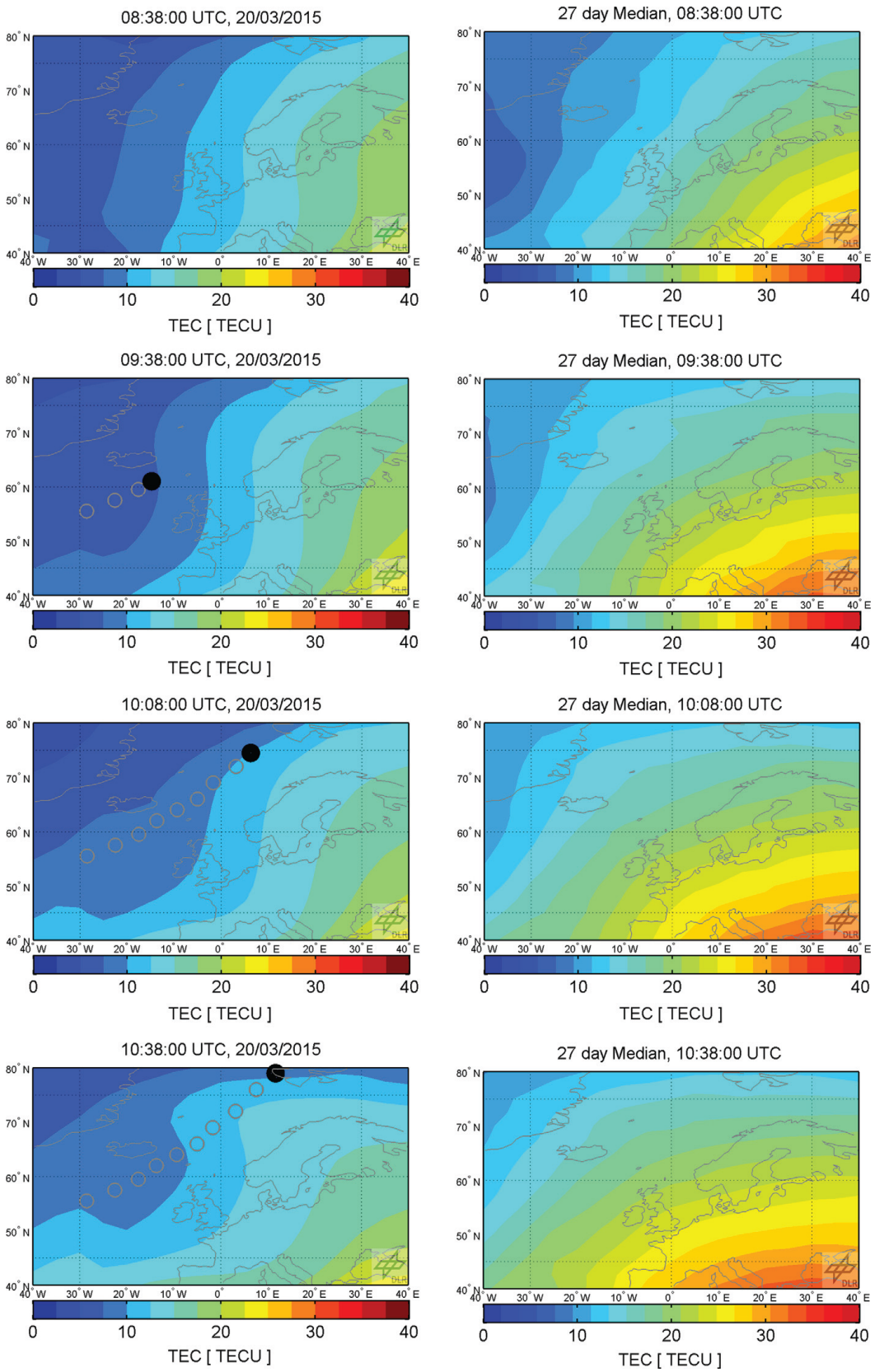

Figure 65: TEC maps over Europe for four times: A comparison is given of the GPS-derived values during the solar eclipse (left) and the previous 27-day median (right). The black disc marks the region of maximum obscuration. [taken from Hoque et al. (2016)]

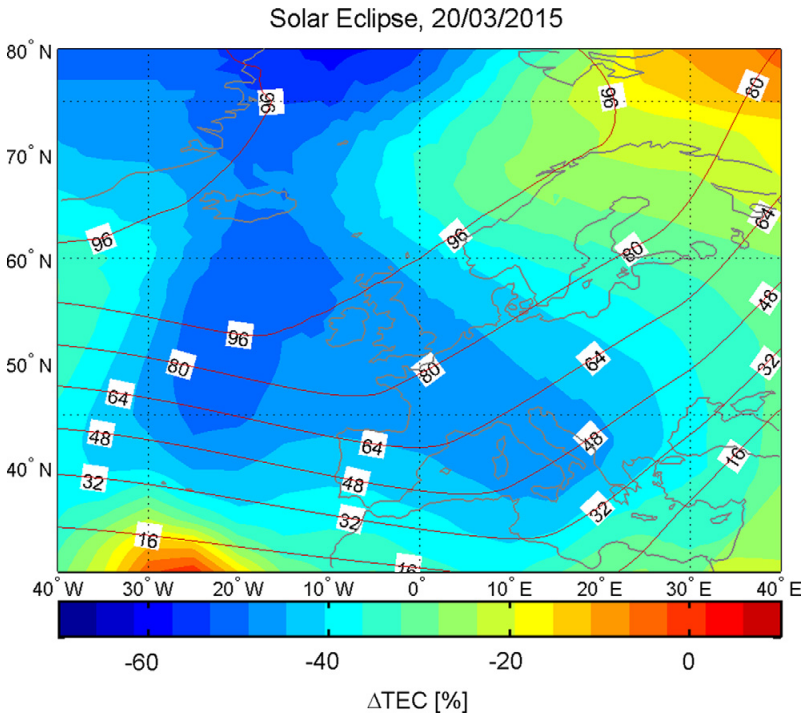

Figure 66: Percentaged TEC deviation with respect to the 27-day median at maximum obscuration times: The respective maximum obscuration values are indicated by level lines. [taken from Hoque et al. (2016)]

For times of maximum obscuration, Fig. 66 shows these values. They reflect the variation in TEC mainly caused by the solar eclipse with respect to the mean TEC level. We can see that the reduction affects much larger areas than the image comparison suggests. It reaches even into low latitudes (take a look at 10° E) and can be seen as an indicator for plasma transport processes caused by the sudden obscuration. Moreover, the extend of the TEC depletion roughly corresponds to the contour lines of the Moon's shadow.

The percentaged deviation reaches values of about 50 %, but note that a big part of this was forced by a geomagnetic storm (with a negative bias of 20 %) unrelated to the solar eclipse. After bias correction, the ionisation decreases about 30 % (for further information see Hoque et al., 2016). However, the overall ionospheric response may be delayed by up to 40 minutes (commonly attributed to an atmospheric height of 400 km), but the reaction gets faster with growing distance from the totality zone. The reduced ionisation persists even for hours, which lets us draw the conclusion of a recovery phase uncorrelated to the obscuration function. Since TEC refers to a mean ionospheric height at about 400 km, these delays primarily correspond to the reaction times of the upper F region. This was also observed in well-known studies.

Investigating the vertical sounding data of DB049 in Dourbes/Belgium (50.1°N, 4.6°E), one can disassemble the overall ionospheric information of TEC to values presenting the single layers at the given location. Fig. 67 shows the corresponding maximum plasma frequencies $foF2$, $foF1$ and foE, the vertical TEC derived by GPS measurements, the peak electron density $NmF2$ and the resulting slab thickness for the day of the solar eclipse on 20 March

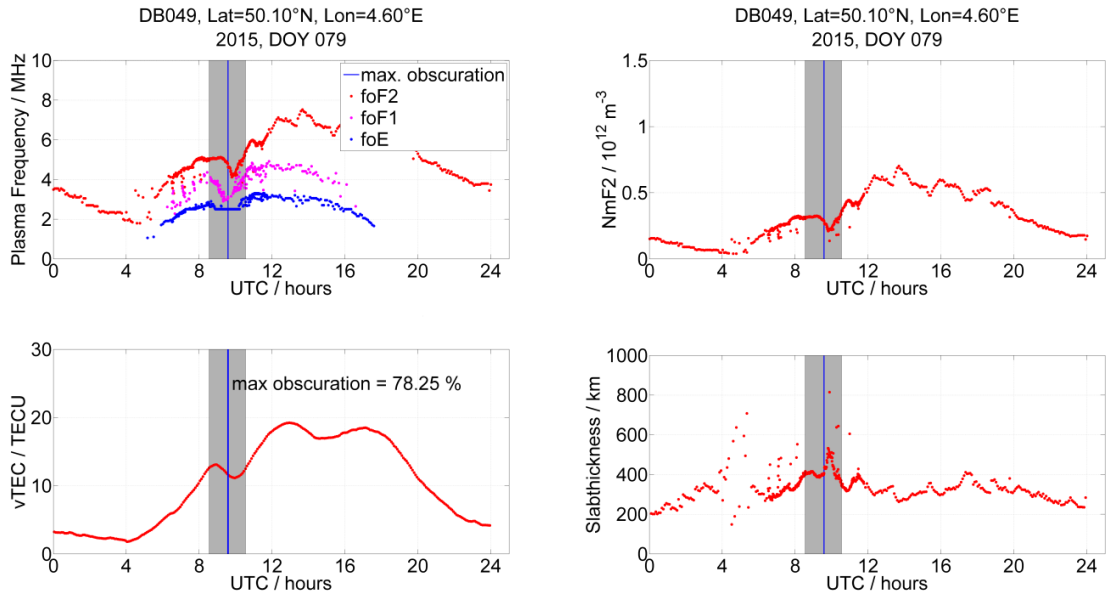

Figure 67: Influence of the eclipse on the diurnal variation of the ionosphere: The ionospheric condition at the ionosonde station DB049 in Dourbes/Belgium is measured with the values of the plasma frequencies $foF2$, $foF1$, foE, the peak electron density $NmF2$, the corresponding $VTEC$ and the slab thickness τ. The obscuration interval is highlighted in grey. [taken from Hoque et al. (2016)]

2015. The plasma frequency $foF2$ experiences a strong depletion, delayed by about 13 min. In comparison, the local TEC response is delayed by 20 min (cp. Fig. 67, bottom left picture). For the plasma frequencies foE and $foF1$, a gradual variation appears shortly after the beginning of the obscuration due to the fast recombination processes in these heights. In fact, the time delay of ionospheric response increases with altitude, in line with previous eclipse studies (e.g., Jakowski et al., 2008). According to (19), the peak electron density $NmF2$ is directly correlated to $foF2$. As noted in section 3.2.1, $NmF2$ and TEC information enable the estimation of the equivalent slab thickness τ, see (20).

Fig. 67 indicates an enhanced slab thickness during local obscuration. Assuming equilibrium diffusion, the slab thickness is proportional to the atmospheric pressure scale height H_p, and hence, proportional to the temperature. Therefore, the increasing slab thickness is in contradiction with the thermospheric cooling under eclipse conditions. This concludes a delayed depletion in the topside ionosphere given by the TEC measurements.

The immediate, approximately linear response in VLF signals, together with the observations of GNSS and ionosonde measurements, demonstrate the effects of the highly dynamic processes within the ionosphere-thermosphere system. For further details, the reader is referred to Hoque et al. (2016). This is a first step to better understand the complex interplay of photoionisation, recombination and plasma redistribution.

„Learn from yesterday, live for today, hope for tomorrow.
The important thing is to not stop questioning.“
Albert Einstein

6

Conclusion

The field of *space weather* involves a broad range of topics associated with solar-terrestrial interrelations. The growing interest in the effects on the Earth pushes the investigation of various measurement techniques. The aim is to protect technological systems in space as well as on the ground. Especially ground-based networks are in demand, as they are easily accessible for maintenance and more economic than satellite missions. The developed GIFDS approach implements a near real-time flare warning system on ground that is able to operate complementary to the well-known service by GOES. The focus of the presented work has been on solar flare detection by means of the ground-based GIFDS network. For this purpose, VLF measurements were considered as an adequate ionospheric image of solar X-ray events with high resolution and potential for continuous global monitoring. Current approaches on solar flare detection rely on satellite missions. Hence, GOES data was used for reference. However, such space-based observations are very important for understanding physical processes in interplanetary space and their origin, the Sun. Nevertheless, they won't represent the actual impact on the ionosphere and the radio signals interacting with it. Users of related technological devices hence will benefit from the new study.

6.1 Resumé

Main objective of this work is establishing a world-spanning ground-based flare monitor, which has lead to the development of the *Global Ionospheric Flare Detection System*. Based on a comprehensive analysis of VLF signals, the feasibility of our network has been proven. For this, the thesis is concerned with the investigation of the terrestrial propagation of VLF waves within the Earth-ionosphere waveguide and its application for space weather monitoring. The analyses were designed to develop a solar flare detection algorithm.

The setup and ongoing maintenance of the necessary VLF receivers required a high degree of cooperation with foreign research institutes. A lot of preparatory work had to be done in order to enable a global monitoring of the lower ionosphere and therewith the observation of solar flare effects. In the process of consolidating my thesis, the following stations were installed:

- NTZ: Neustrelitz / Germany
  DLR Neustrelitz, Institute of Communications and Navigation
- BOS: Boston / Massachusetts
  Boston College, Institute for Scientific Research, ISR
- STA: Stanford / California
  Stanford University, WAAS Lab
- TWN: Chungli City / Taiwan
  National Central University, Center for Space and Remote Sensing Research, CSRSR

Besides the installation and associated technical issues (e.g., mains electricity and usage of appropriate power supplies), granting good receiving conditions on each site needed specific adjustments to the basic software.

After a certain period of operation, one could identify significant variations over time and space. A systematic evaluation and comparison of the VLF measurements has led to a new algorithm for extracting flare information. The following aspects were of particular interest:

- temporal variations of the day/night transition and therewith the development of the diurnal plateau, as well as a seasonal dependency of the daytime signal level,
- spatial differences in VLF signal propagation (e.g., short/long paths, W–E or E–W propagation) that are primarily determined by the local sunrise and sunset times,
- disturbances in VLF measurements caused by man-made malfunctioning as well as noise due to natural influences.

A detailed study of solar flare effects on VLF signals confirms a close relationship between an X-ray event and its VLF response. By level correction, devised with respect to diurnal and annual variations, the correlation has been improved even more. However, only relative comparisons are advised since VLF measurements suffer variations that seem to be independent of the long-term solar activity.

Flares in the X-ray spectrum were observed to have different shapes. The slope in the increase phase determines the reaction time of the ionosphere. The D region reacts quite fast on a sudden

energy flux rise, while gradual changes have almost no noticeable effect. In average, the time delay of the VLF response was determined by cross-correlation as about 3 min. However, the varying decay phases of X-ray are shown to be indistinguishable by looking at the VLF responses only. The inertness can be explained by the complex relaxation process of the ionospheric recombination.

Since the ionosphere smooths out certain values of an impact, reconstructing the original solar radiation function is turned into a challenge. As the established flare classification is based on this information, the desire for deriving the overall original flare intensity can be understood. We rely on the construction of a pseudo-absolute scale by adjusting VLF measurements to the average X-ray background level. The combination of several measurements provides an appropriate image of the flare activity and eliminates transmitter malfunctioning or daytime window gaps. For increasing the reliability of solar flare alerts, we developed the network with the premise of having at least two valid measurements. The algorithm is designed to operate near real-time and can provide alerts for flares of class C2 upwards. Since the VLF amplitude technique aims to help warning the radio community, it is very efficient in operation and enables to judge the direct impact of flares on the ionospheric communication and navigation.

For validating the VLF approach, the simulation of signal propagation usinf the example of the solar eclipse on 20 March 2015 over Europe formed one of the main parts of my thesis. Therewith, the obscuration effects on VLF signals were investigated for six different paths under well-defined conditions. A time delay in the response of the D-region has been identified, varying from virtually 0 to merely 11 minutes depending on the geographic orientation of the signal path. To understand the basic physical processes in the lower ionosphere and their distinct influences on VLF signals, we utilised the mode theory. In this way, the measured signal amplitudes could be reconstructed successfully and the dynamics of the D-region were comprehensibly reproduced. With help of additional measurements like TEC and ionosonde data, it has been confirmed that high ionospheric layers (E and F-region) show a larger response delay. A better understanding of these coupling processes will help to predict radio signal responses to different spectral impacts, and VLF measurements provide detailed insights into specific parts of the ionosphere and its short-term disturbances.

6.2 Prospects

Quite recently, the station in Taiwan became operational. By this, the network is now able to monitor the flare activity 24 hours, which could not be granted before. Apart from a continuous operating surveillance and quality control, there are still some tasks with respect to the GIFDS flare detection:

- adding further stations to increase the overlap of the daytime windows for VLF measurements,
- including phase measurements for supplemental correlation studies,
- investigation of other sensor data (e.g., EUV satellite data by SDO, TEC data),
- integration of GIFDS' VLF measurements into IMPC as fully-operational service, including derived products like flare alerts.

The choice for the current configuration was made with protecting VLF-to-HF radio systems in mind. However, other systems operate in different bands of the spectrum, where influences of a flare may vary. Fig. 68 shows three flares of varying spectral composition. A flare may have peaks in one or both of X-ray (red) and EUV parts (yellow), see first row. Moreover, a rapid X-ray increase may come along with only a small enhancement in the EUV. The latter is harmless for GNSS and UHF applications, so not all flares have an impact on technology. For identifying crucial flares without giving respective false alerts, the X-ray scale (reflected in the VLF, second row) has only a limited information value, and the evaluation of the EUV component is necessary. The last row pictures the influence of EUV flares on the VTEC rate, visible as a jump. Strong EUV flares can even provoke a loss of lock in GNSS measurements. These effects have been studied over the last years by García-Rigo et al. (2007); Hernández-Pajares et al. (2012); Monte-Moreno and Hernández-Pajares (2014); Singh et al. (2015).

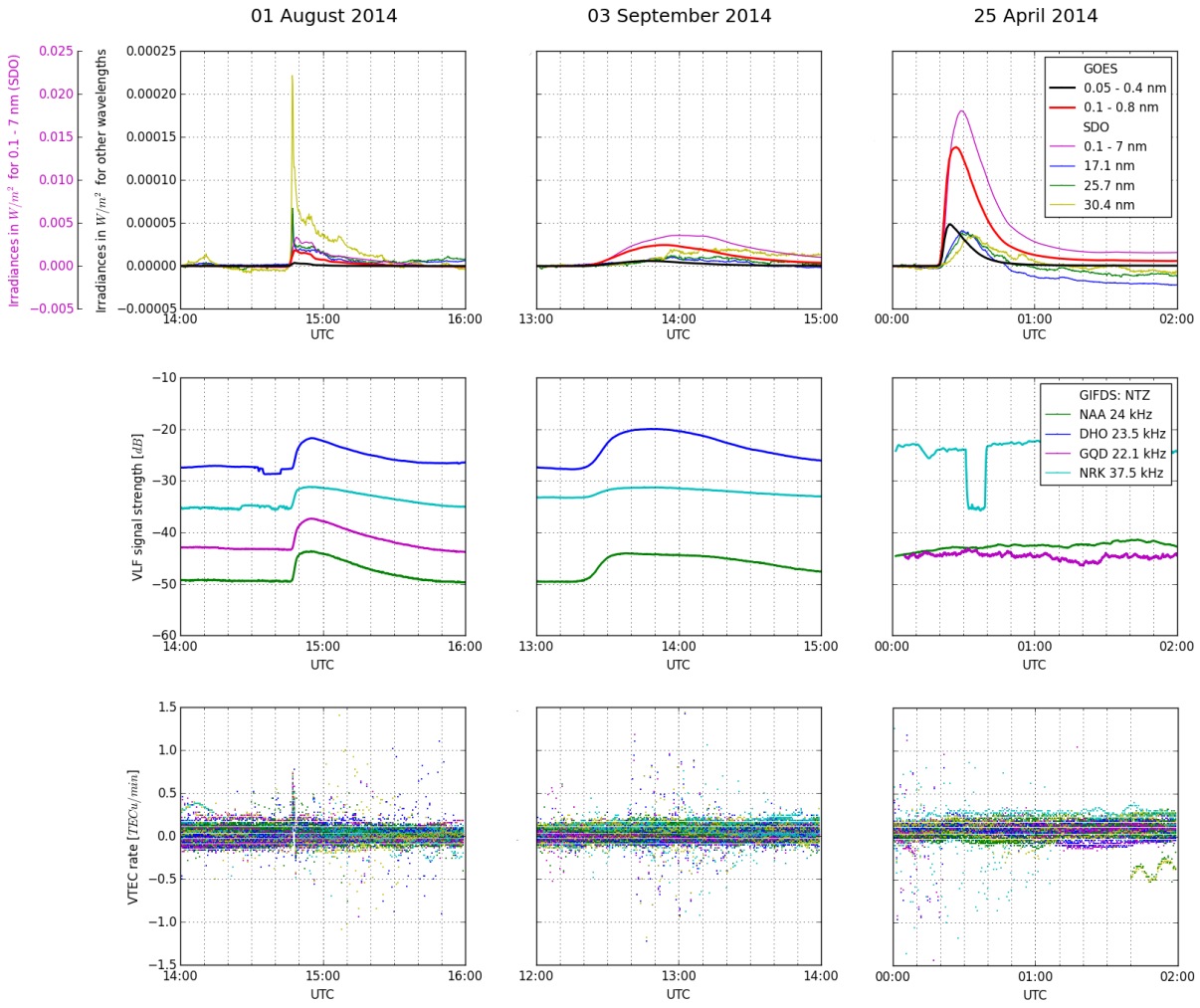

Figure 68: Comparison of measurements by GOES and SDO (upper) to the VLF amplitude by GIFDS-NTZ (middle) and VTEC rate (lower row) during three different flare activities (left: M2, middle: M2.4, right column: X 1.3): For a better comparison of the satellite measurements, all signals are shifted to zero with the flare's beginning and plotted on a linear scale. Note that, during the X class flare, NTZ was in local night, so that no flare impact is observed.

The potential of EUV observations for GNSS users should be combined with the methods of GIFDS for the HF range in order to obtain more detailed information on the performance of technology. Our aim is to derive a classification scheme that respects the affected frequency range and builds upon relative changes compared to an undisturbed base level.

Although we made comprehensive analyses of VLF measurements in this thesis, some issues had to be neglected due to the limited data set in the initial phase. Of course, there are some topics that are worth closer investigation. Firstly, modelling the VLF amplitude and phase in situations other than the exemplified solar eclipse is of interest for determining the reaction time, especially under turbulent conditions like SIDs caused by solar flares. Secondly, apart from the susceptibility to external disturbances, there are variations in the atmosphere itself. By the chosen level correction, the average influence on VLF signals was respected. However, this statistical attempt gives no physical background on the reason for phenomena like the sudden amplitude decrease in fall, the so-called October effect. This is very likely caused by terrestrial mesospheric winds, and cannot be explained by solar processes. The objective of an upcoming research project is to physically understand the coupling processes of the lower ionosphere and the mesosphere-stratosphere system. For observing the interactions inside, ground-based VLF measurements are vital. Consequently, the GIFDS monitor opens the door for documenting these parts of the ionosphere, of which a more detailed view would help in the warning of space weather events.

A

Overview on selected VLF / LF systems

A.1 VLF / LF signals

Alpha signals Alpha is a long range navigation system, developed in Russia concurrently to the U.S. Omega system. Whereas the Omega system was shut down in 1997 and replaced by the GPS navigation system, the Russian system is still in operation. the so-called RSDN-20 pulsed alpha signals are transmitted on the frequencies 11.905 kHz, 12.649 kHz and 14.881 kHz. Via phase difference of these signals, one can determine the position within a range of up to 7 km.

Beta time signals Beta provides a time signal (and rarely also other information) in the VLF range and is maintained by the Russian Navy. The six transmitters (RJH69, RJH77, RJH63, RJH99, RJH66 and RAB99) send primarily unmodulated carriers alternating at fixed times on the frequencies 20.5, 23.0, 25.0, 25.1, and 25.5 kHz.

DGPS signals The Differential Global Positioning System (DGPS) improves the location accuracy of the common GPS, from 15 m to about 10 cm. A network of fixed reference stations on the ground helps to identify the difference between the positions obtained from the satellites and the known location. Every station broadcasts a digital correction signal via short range transmitters to its surrounding.

EFR signals The EFR GmbH (in German: *Europäische Funk-Rundsteuerung* uses FSK modulated long-wave radio in order to transmit telegrams for, e.g., tariff control of electricity meters, demand-side management of energy consumption, or for controlling street or traffic lights (http://www.efr.de/). There are three transmitters located in Mainflingen (129.1 kHz), Burg (139.0 kHz) and Laikihegy (135.6 kHz). Each has a transmission power of 100 kW, reaching an area of 500 km radius, in summary covering Central Europe.

Time signals Radio stations are often used to transmit timing pulses of highest accuracy (i.e. 10^{-10} s). A short-time broadcast can only be ensured with frequencies below 80 kHz (Klawitter and Herold, 1995). Germany operates the DCF77 on 77.5 kHz. Other examples for stations are

WWVB (60 kHz) in the US, MSF 60 kHz in Great Britain, JJY (40*and*60 kHz) in Japan, BPC (68.5 kHz) in China, and RTZ (50 kHz) in Russia.

LORAN signals The LOng RAnge Navigation was a hyperbolic radio navigation system developed in the US in the 1940s. The use of lower frequencies improved the working range up to 2400 km and the accuracy to clearly below 30 km, ideal for ship convoys crossing the oceans, and long-range patrol aircrafts. Loran-C additionally utilised fixed land-based radio beacons. Due to the high expenses, the systems were used mainly by militaries.

Navy signals Several stations around the globe provide one-way communication to marine and submarine forces. The signals are MSK modulated. Frequencies in the lower portion of the VLF spectrum enable a deep penetration into the sea. Though some VLF stations have other purposes, the primary function of most VLF stations is to communicate with military or help them navigate on the ocean or underwater. As they provide a continuous long-range signal, they were chosen as a transmitting component for GIFDS.

NDB signals Non-Directional radio Beacons are fixed-position transmitters are used for navigating in the air or on the sea. The signals follow Earth's curvature, whence they can be received at much greater distances. Nevertheless, they can be heavily affected by atmospheric conditions or land masses.

OMEGA signals The first global radio navigation system was operated by the US and other nations. The ground-based OMEGA network transmitted VLF radio signals in the range 10 to 14 kHz. It was started 1971 parallel to the Russian Alpha system and suspended in 1997 in favour of GPS.

A.2 Modulation techniques

Amplitude modulation (AM) The AM technique is used in electronic communication, most commonly for transmitting information via a radio carrier wave. The amplitude of the carrier is altered so that the information of the transmitting signal is mirrored. It was the earliest modulation method used to transmit voice by radio and is still the base of e.g. walkie-talkies. In contrasts to other techniques, frequency and phase remain constant.

Continuous wave (CW) A continuous waveform is a wave of constant amplitude and frequency. This sinusoidal carrier is switched on and off, so that the varying intervals represent given information, e.g. Morse code. Main applications are for time signals and NDB signals.

Frequency modulation (FM) FM encodes information by modifying the frequency of a carrier wave. The difference between the carrier frequency and its center gives the modulating signal. In telecommunications and signal processing, FM is used for broadcasting news or music.

Frequency shift keying (FSK) An extension of the FM technique is FSK, in which digital information is transmitted through discrete frequency shifts in the carrier wave. A predefined set of frequencies represents digits, e.g., one for the binary 1 and a second for the binary 0. FSK is widespread in modems and also used for EFR signals.

Minimum shift keying (MSK) MSK is a special case of FSK modulation that reduces harms of many receivers by avoiding hard jumps between the binary states. These would create sidebands outside the allowed bandwidth, interfering with other technologies. The method is commonly used with Navy and DGPS signals, as well as for GSM mobile phones.

B

The configuration of GIFDS stations

The preparation of each GIFDS station was not trivial and required several steps of configuration before considering the monitoring itself. The two following sections show the input and xml files using the example of Stanford. After principle installation and configuration of each monitoring system one could adapt the xml files with respect to the actual received transmitters.

B.1 Input files exemplary for STA

Listing 5: HFMonitor/run/STA/0-perseus_server.in

```
#!/bin/bash
# $Id: 0-perseus_server.in 462 2016-02-04 08:25:49Z gifds $

NAME="perseus_server"
CMD="sudo LD_LIBRARY_PATH=$LD_LIBRARY_PATH ./bin/$NAME -c config/${NAME}_STA.xml"
```

Listing 6: HFMonitor/run/STA/1a-client_multi_downconvert.in

```
#!/bin/bash
# $Id: 1a-client_multi_downconvert.in 462 2016-02-04 08:25:49Z gifds $

NAME="client_multi_downconvert"
CMD="./bin/$NAME -c config/multi_downconvert_STA.xml"
```

Listing 7: HFMonitor/run/STA/2a-multi_client_to_bc.in

```
#!/bin/bash
# $Id: 2a-multi_client_to_bc.in 462 2016-02-04 08:25:49Z gifds $

NAME="multi_client_to_broadcaster"
CMD="./bin/$NAME -c config/multi_client_STA.xml"
```

Listing 8: HFMonitor/run/STA/3a-multi_client_writer.in

```
#!/bin/bash
# $Id: 3a-multi_client_writer.in 462 2016-02-04 08:25:49Z gifds $

NAME="multi_client_to_file"
CMD="./bin/$NAME -c config/multi_client_writer_STA.xml"
```

B.2 XML files exemplary for STA

Listing 9: HFMonitor/config/perseus_server_STA.xml

```
<?xml version="1.0" encoding="utf-8"?>
<!DOCTYPE Perseus SYSTEM "DTD/perseus_server.dtd">
<!-- $Id$ -->
<Perseus sn="241"
    fs="500000"
    fc="220e3"
    use_preselector="true"
    attenuator="1"
    usb_transfer_size="510"
    firmware="config/perseus/perseus.hex">
  <rbs fs="125000">config/perseus/perseus125k.rbs</rbs>
  <rbs fs="250000">config/perseus/perseus250k.rbs</rbs>
  <rbs fs="500000">config/perseus/perseus500k.rbs</rbs>
  <rbs fs="1000000">config/perseus/perseus1000k.rbs</rbs>
  <rbs fs="2000000">config/perseus/perseus2000k.rbs</rbs>
  <Broadcaster threadPoolSize="1">
    <Data maxQueueSize_MB="100"
    maxQueueDelay_Minutes="1"
    port="18001"/>
  </Broadcaster>
</Perseus>
```

Listing 10: HFMonitor/config/multi_downconvert_STA.xml

```
<?xml version="1.0" encoding="utf-8"?>
<!DOCTYPE MultiDownConverter SYSTEM "DTD/multi_downconvert.dtd">
<!-- $Id: multi_downconvert_STA.xml 399 2014-05-14 20:43:43Z cmayer $ -->
<MultiDownConverter l="500000"
                    m="125001">
  <StationInfo>
    Station  = STA
    Computer = Latitude E6440
  </StationInfo>
  <Broadcaster>
    <Data maxQueueSize_MB="20"
          maxQueueDelay_Minutes="5"
          port="19000"/>
  </Broadcaster>
  <Repack bufferLength_sec="1"
          overlap_percent="0"/>
  <server host="127.0.0.1"
    port="18001"/>
  <Calibration>
    <FixedOffset offset="1.4e-9"/>
  </Calibration>
  <Processors>
    <TrackingGoertzel name="TGF_JJY"
                      input="DC_040000_JJY"
                      f0_Hz="40.0e3"
                      df_Hz="1"
                      minDf_Hz=".1"
                      maxHistorySize="120"
                      maxNumWithoutLock="5"/>
    <TrackingGoertzel name="TGF_WWVB"
```

```
31                          input="DC_060000_WWVB"
32                          f0_Hz="60.0e3"
33                          df_Hz=".1"
34                          minDf_Hz=".05"
35                          maxHistorySize="120"
36                          maxNumWithoutLock="5"/>
37    </Processors>
38    <Filters>
39      <FIR name="DC_013500_ALPHA" type="lowpass" cutoff="0.009" centerFrequency_Hz="
          13.50e3" decim="100"/>
40      <FIR name="DC_017000_VTX2"  type="lowpass" cutoff="0.009" centerFrequency_Hz="
          17.00e3" decim="100"/>
41      <FIR name="DC_018200_VTX3"  type="lowpass" cutoff="0.009" centerFrequency_Hz="
          18.20e3" decim="100"/>
42      <FIR name="DC_019800_NWC"   type="lowpass" cutoff="0.009" centerFrequency_Hz="
          19.80e3" decim="100"/>
43      <FIR name="DC_020200_JJI"   type="lowpass" cutoff="0.009" centerFrequency_Hz="
          20.20e3" decim="100"/>
44      <FIR name="DC_021400_NPM"   type="lowpass" cutoff="0.009" centerFrequency_Hz="
          21.40e3" decim="100"/>
45      <FIR name="DC_022200_JJI"   type="lowpass" cutoff="0.009" centerFrequency_Hz="
          22.20e3" decim="100"/>
46      <FIR name="DC_024000_NAA"   type="lowpass" cutoff="0.009" centerFrequency_Hz="
          24.00e3" decim="100"/>
47      <FIR name="DC_024800_NLK"   type="lowpass" cutoff="0.009" centerFrequency_Hz="
          24.80e3" decim="100"/>
48      <FIR name="DC_025200_NML4"  type="lowpass" cutoff="0.009" centerFrequency_Hz="
          25.20e3" decim="100"/>
49      <FIR name="DC_040000_JJY"   type="lowpass" cutoff="0.009" centerFrequency_Hz="
          40.00e3" decim="100"/>
50      <FIR name="DC_040800_NAU"   type="lowpass" cutoff="0.009" centerFrequency_Hz="
          40.80e3" decim="100"/>
51      <FIR name="DC_054000_NDI"   type="lowpass" cutoff="0.009" centerFrequency_Hz="
          54.00e3" decim="100"/>
52      <FIR name="DC_055500_UNID"  type="lowpass" cutoff="0.009" centerFrequency_Hz="
          55.50e3" decim="100"/>
53      <FIR name="DC_060000_WWVB"  type="lowpass" cutoff="0.009" centerFrequency_Hz="
          60.00e3" decim="100"/>
54      <FIR name="DC_076200_CKN"   type="lowpass" cutoff="0.009" centerFrequency_Hz="
          76.20e3" decim="100"/>
55      <FIR name="DC_124000_CKN_2" type="lowpass" cutoff="0.009" centerFrequency_Hz="
          124.00e3" decim="100"/>
56      <FIR name="DC_014000_VLF"   type="lowpass" cutoff="0.018" centerFrequency_Hz="
          14.00e3" decim=" 50"/>
57      <FIR name="DC_022000_VLF"   type="lowpass" cutoff="0.018" centerFrequency_Hz="
          22.00e3" decim=" 50"/>
58      <FIR name="DC_030000_VLF"   type="lowpass" cutoff="0.018" centerFrequency_Hz="
          30.00e3" decim=" 50"/>
59      <FIR name="DC_038000_VLF"   type="lowpass" cutoff="0.018" centerFrequency_Hz="
          38.00e3" decim=" 50"/>
60      <FIR name="DC_046000_VLF"   type="lowpass" cutoff="0.018" centerFrequency_Hz="
          46.00e3" decim=" 50"/>
61      <FIR name="DC_054000_VLF"   type="lowpass" cutoff="0.018" centerFrequency_Hz="
          54.00e3" decim=" 50"/>
62      <FIR name="DC_062000_VLF"   type="lowpass" cutoff="0.018" centerFrequency_Hz="
          62.00e3" decim=" 50"/>
63      <FIR name="DC_072000_VLF"   type="lowpass" cutoff="0.018" centerFrequency_Hz="
          70.00e3" decim=" 50"/>
```

```
64      <FIR name="DC_078000_VLF"   type="lowpass" cutoff="0.018" centerFrequency_Hz="
            78.00e3" decim=" 50"/>
65      <FIR name="DC_086000_VLF"   type="lowpass" cutoff="0.018" centerFrequency_Hz="
            86.00e3" decim=" 50"/>
66      <FIR name="DC_288000_DGPS"  type="lowpass" cutoff="0.036" centerFrequency_Hz="
            288.00e3" decim=" 25"/>
67      <FIR name="DC_304000_DGPS"  type="lowpass" cutoff="0.036" centerFrequency_Hz="
            304.00e3" decim=" 25"/>
68      <FIR name="DC_320000_DGPS"  type="lowpass" cutoff="0.036" centerFrequency_Hz="
            320.00e3" decim=" 25"/>
69    </Filters>
70  </MultiDownConverter>
```

Listing 11: HFMonitor/config/multi_client_writer_STA.xml

```
1  <?xml version="1.0" encoding="utf-8"?>
2  <!DOCTYPE MultiClient SYSTEM "DTD/multi_client.dtd">
3  <!-- $Id: multi_client_writer_STA.xml 399 2014-05-14 20:43:43Z cmayer $ -->
4  <MultiClient>
5    <StationInfo>
6      Station  = STA
7      Computer = Latitude E6440
8    </StationInfo>
9    <server host="127.0.0.1" port="19100"/>
10   <FileSink filePath="DataSTA" filePeriod="1d"/>
11   <Streams>
12     <Stream pattern="L.*">Writer</Stream>
13     <Stream pattern="M.*">Writer</Stream>
14     <Stream pattern="A.*">Writer</Stream>
15   </Streams>
16   <Clients>
17     <WriterTXT proc_name="Writer" filePath="DataSTA" filePeriod="1d"/>
18   </Clients>
19 </MultiClient>
```

Listing 12: HFMonitor/config/multi_client_writer_NTZ_fromSTA.xml

```
1  <?xml version="1.0" encoding="utf-8"?>
2  <!DOCTYPE MultiClient SYSTEM "DTD/multi_client.dtd">
3  <!-- $Id: multi_client_writer_NTZ_fromSTA.xml 399 2014-05-14 20:43:43Z cmayer $ -->
4  <MultiClient>
5    <StationInfo>
6      Station  = NTZ
7      Computer = Latitude E6440 : N-Series Base
8    </StationInfo>
9    <server host="cpcfcmd.evn.np.kn.nz.dlr.de" port="40029"/>
10   <FileSink filePath="DataSTA" filePeriod="1d"/>
11   <Streams>
12     <Stream pattern="A.*">Writer</Stream>
13     <Stream pattern="L.*">Writer</Stream>
14     <Stream pattern="M.*">Writer</Stream>
15   </Streams>
16   <Clients>
17     <WriterTXT proc_name="Writer" filePath="DataSTA" filePeriod="1d"/>
18   </Clients>
19 </MultiClient>
```

Listing 13: HFMonitor/config/multi_client_STA.xml

```
<?xml version="1.0" encoding="utf-8"?>
<!DOCTYPE MultiClient SYSTEM "DTD/multi_client.dtd">
<!-- $Id: multi_client_STA.xml 399 2014-05-14 20:43:43Z cmayer $ -->
<MultiClient>
  <StationInfo>
    Station  = STA
    Computer = Latitude E6440
  </StationInfo>
  <Broadcaster>
    <Data maxQueueSize_MB="20"
          maxQueueDelay_Minutes="5"
          port="19100"/>
  </Broadcaster>
  <server host="127.0.0.1" port="19000"/>
  <FileSink filePath="DataSTA" filePeriod="1d"/>
  <Streams>
    <Stream pattern="TGF.*">WriterText</Stream>
    <Stream pattern="DC_013500_ALPHA">DemodALPHA</Stream>
    <Stream pattern="DC_017000_VTX2">DemodMSK_VTX2</Stream>
    <Stream pattern="DC_018200_VTX3">DemodMSK_VTX3</Stream>
    <Stream pattern="DC_019800_NWC">DemodMSK_NWC</Stream>
    <Stream pattern="DC_020200_JJI">DemodMSK_JJI_1</Stream>
    <Stream pattern="DC_021400_NPM">DemodMSK_NPM</Stream>
    <Stream pattern="DC_022200_JJI">DemodMSK_JJI_2</Stream>
    <Stream pattern="DC_024000_NAA">DemodMSK_NAA</Stream>
    <Stream pattern="DC_024800_NLK">DemodMSK_NLK</Stream>
    <Stream pattern="DC_025200_NML4">DemodMSK_NML4</Stream>
    <Stream pattern="DC_040800_NAU">DemodMSK_NAU</Stream>
    <Stream pattern="DC_054000_NDI">DemodMSK_NDI</Stream>
    <Stream pattern="DC_055500_UNID">DemodMSK_UNID</Stream>
    <Stream pattern="DC_076200_CKN">DemodMSK_CKN</Stream>
    <Stream pattern="DC_124000_CKN_2">DemodMSK_CKN_2</Stream>
    <Stream pattern="DataIQ">FFT_Processor</Stream>
  </Streams>
  <Clients>
    <WriterTXT proc_name="WriterText" filePath="DataSTA"    filePeriod="1d"/>
    <WriterIQ  proc_name="WriterIQ"   filePath="DataSTAIQ" filePeriod="5m"
        bitsPerSample="24"/>

    <DemodALPHA proc_name="DemodALPHA" name="ALPHA"/>

    <DemodMSK proc_name="DemodMSK_VTX2"
              name="MSK_VTX2" fc_Hz="17.00e3" fm_Hz="200.0"
              dwl_Hz=".05" period_Sec="1" min_SN_db="2" max_offset_ppb_rms="15"
                  ampl_lowpass_tc_Sec="60"/>
    <DemodMSK proc_name="DemodMSK_VTX3"
              name="MSK_VTX3" fc_Hz="18.20e3" fm_Hz="200.0"
              dwl_Hz=".05" period_Sec="1" min_SN_db="1" max_offset_ppb_rms="15"
                  ampl_lowpass_tc_Sec="60"/>
    <DemodMSK proc_name="DemodMSK_NWC"
              name="MSK_NWC" fc_Hz="19.80e3" fm_Hz="200.0"
              dwl_Hz=".05" period_Sec="1" min_SN_db="1" max_offset_ppb_rms="15"
                  ampl_lowpass_tc_Sec="60"/>
    <DemodMSK proc_name="DemodMSK_JJI_1"
              name="MSK_JJI_1" fc_Hz="20.2e3" fm_Hz="200.0"
              dwl_Hz=".05" period_Sec="1" min_SN_db="1" max_offset_ppb_rms="15"
                  ampl_lowpass_tc_Sec="60"/>
```

```
53      <DemodMSK proc_name="DemodMSK_NPM"
54                name="MSK_NPM" fc_Hz="21.4e3" fm_Hz="200.0"
55                dwl_Hz=".05" period_Sec="1" min_SN_db="1" max_offset_ppb_rms="15"
                      ampl_lowpass_tc_Sec="60"/>
56      <DemodMSK proc_name="DemodMSK_JJI_2"
57                name="MSK_JJI_2" fc_Hz="22200.5893" fm_Hz="200.0"
58                dwl_Hz=".05" period_Sec="1" min_SN_db="1" max_offset_ppb_rms="15"
                      ampl_lowpass_tc_Sec="600"/>
59      <DemodMSK proc_name="DemodMSK_NAA"
60                name="MSK_NAA" fc_Hz="24.00e3" fm_Hz="200.0"
61                dwl_Hz=".05" period_Sec="1" min_SN_db="2" max_offset_ppb_rms="15"
                      ampl_lowpass_tc_Sec="60"/>
62      <DemodMSK proc_name="DemodMSK_NLK"
63                name="MSK_NLK" fc_Hz="24.80e3" fm_Hz="200.0"
64                dwl_Hz=".05" period_Sec="1" min_SN_db="1" max_offset_ppb_rms="15"
                      ampl_lowpass_tc_Sec="60"/>
65      <DemodMSK proc_name="DemodMSK_NML4"
66                name="MSK_NML4" fc_Hz="25200" fm_Hz="200.0"
67                dwl_Hz=".05" period_Sec="1" min_SN_db="1" max_offset_ppb_rms="15"
                      ampl_lowpass_tc_Sec="60"/>
68      <DemodMSK proc_name="DemodMSK_NDI"
69                name="MSK_NDI" fc_Hz="54.00e3" fm_Hz="200.0"
70                dwl_Hz=".05" period_Sec="1" min_SN_db="2" max_offset_ppb_rms="15"
                      ampl_lowpass_tc_Sec="60"/>
71      <DemodMSK proc_name="DemodMSK_UNID"
72                name="MSK_UNID" fc_Hz="55.50e3" fm_Hz="200.0"
73                dwl_Hz=".05" period_Sec="1" min_SN_db="2" max_offset_ppb_rms="15"
                      ampl_lowpass_tc_Sec="60"/>
74      <DemodMSK proc_name="DemodMSK_NAU"
75                name="MSK_NAU" fc_Hz="40.75e3" fm_Hz="200.0"
76                dwl_Hz=".05" period_Sec="1" min_SN_db="2" max_offset_ppb_rms="15"
                      ampl_lowpass_tc_Sec="60"/>
77      <DemodMSK proc_name="DemodMSK_CKN"
78                name="MSK_CKN" fc_Hz="76200" fm_Hz="300.0"
79                dwl_Hz=".05" period_Sec="1" min_SN_db="2" max_offset_ppb_rms="15"
                      ampl_lowpass_tc_Sec="60"/>
80      <DemodMSK proc_name="DemodMSK_CKN_2"
81                name="MSK_CKN_2" fc_Hz="124e3" fm_Hz="300.0"
82                dwl_Hz=".05" period_Sec="1" min_SN_db="2" max_offset_ppb_rms="15"
                      ampl_lowpass_tc_Sec="60"/>
83
84      <FFT_Processor proc_name="FFT_Processor" type="FFTProcessor_DOUBLE" name="
            FFTProcessor"
85                     windowFunction="Blackman"
86                     numberOfCollectedEpochs="1">
87        <Actions calibrationKey="L1.CAL">
88          <L0>
89            <FindPeak name="040000_TS_JJY"
90                      fMin_Hz="39.800e3"
91                      fMax_Hz="40.200e3"
92                      fRef_Hz="40.000e3"
93                      minRatio="1">
94              <Filter type="LowPass" timeConstant_sec="60.0"/>
95            </FindPeak>
96            <FindPeak name="060000_TS_WWVB"
97                      fMin_Hz="59.800e3"
98                      fMax_Hz="60.200e3"
99                      fRef_Hz="60.000e3"
```

```
100                     minRatio="1">
101             <Filter type="LowPass" timeConstant_sec="60.0"/>
102           </FindPeak>
103         </L0>
104         <L1>
105           <Calibrator name="CAL"
106                       maxOffset_Hz="10.0"
107                       maxCorrectionFactor_ppm="20.0">
108             <Inputs>
109               <Input key="L0.040000_TS_JJY"/>
110               <Input key="L0.060000_TS_WWVB"/>
111             </Inputs>
112           </Calibrator>
113         </L1>
114         <L2>
115           <AverageDensity name="017000_VTX2"
116                           fRef_Hz="17.0e3"
117                           bandwidth_Hz="200">
118             <Calibration key="L1.CAL"/>
119           </AverageDensity>
120           <AverageDensity name="017800_unid"
121                           fRef_Hz="17.8e3"
122                           bandwidth_Hz="200">
123             <Calibration key="L1.CAL"/>
124           </AverageDensity>
125           <AverageDensity name="018200_VTX3"
126                           fRef_Hz="18.2e3"
127                           bandwidth_Hz="200">
128             <Calibration key="L1.CAL"/>
129           </AverageDensity>
130           <AverageDensity name="019800_Navy_NWC"
131                           fRef_Hz="19.8e3"
132                           bandwidth_Hz="200">
133             <Calibration key="L1.CAL"/>
134           </AverageDensity>
135           <AverageDensity name="019600_Navy_GQD"
136                           fRef_Hz="19.6e3"
137                           bandwidth_Hz="200">
138             <Calibration key="L1.CAL"/>
139           </AverageDensity>
140           <AverageDensity name="020200_JJI"
141                           fRef_Hz="20.2e3"
142                           bandwidth_Hz="200">
143             <Calibration key="L1.CAL"/>
144           </AverageDensity>
145           <AverageDensity name="020500_Navy_RJHxx"
146                           fRef_Hz="20.5e3"
147                           bandwidth_Hz="100">
148             <Calibration key="L1.CAL"/>
149           </AverageDensity>
150           <AverageDensity name="020900_HWU"
151                           fRef_Hz="20.9e3"
152                           bandwidth_Hz="200">
153             <Calibration key="L1.CAL"/>
154           </AverageDensity>
155           <AverageDensity name="022700_unid"
156                           fRef_Hz="22.7e3"
157                           bandwidth_Hz="200">
```

```
158             <Calibration key="L1.CAL"/>
159           </AverageDensity>
160           <AverageDensity name="021400_Navy_NPM"
161                           fRef_Hz="21.4e3"
162                           bandwidth_Hz="100">
163             <Calibration key="L1.CAL"/>
164           </AverageDensity>
165           <AverageDensity name="022200_JJI"
166                           fRef_Hz="22.2e3"
167                           bandwidth_Hz="100">
168             <Calibration key="L1.CAL"/>
169           </AverageDensity>
170           <AverageDensity name="023400_DHO38"
171                           fRef_Hz="23.4e3"
172                           bandwidth_Hz="200">
173             <Calibration key="L1.CAL"/>
174           </AverageDensity>
175           <AverageDensity name="024000_Navy_NAA"
176                           fRef_Hz="24.000e3"
177                           bandwidth_Hz="200">
178             <Calibration key="L1.CAL"/>
179           </AverageDensity>
180           <AverageDensity name="024800_Navy_NLK"
181                           fRef_Hz="24.800e3"
182                           bandwidth_Hz="200">
183             <Calibration key="L1.CAL"/>
184           </AverageDensity>
185           <AverageDensity name="025200_Navy_NML4"
186                           fRef_Hz="25.200e3"
187                           bandwidth_Hz="200">
188             <Calibration key="L1.CAL"/>
189           </AverageDensity>
190           <AverageDensity name="027200_unid"
191                           fRef_Hz="27.2e3"
192                           bandwidth_Hz="200">
193             <Calibration key="L1.CAL"/>
194           </AverageDensity>
195           <AverageDensity name="037500_Navy_NRK"
196                           fRef_Hz="37.5e3"
197                           bandwidth_Hz="200">
198             <Calibration key="L1.CAL"/>
199           </AverageDensity>
200           <AverageDensity name="040750_Navy_NAU"
201                           fRef_Hz="40.75e3"
202                           bandwidth_Hz="200">
203             <Calibration key="L1.CAL"/>
204           </AverageDensity>
205           <AverageDensity name="076200_CKN"
206                           fRef_Hz="76.2e3"
207                           bandwidth_Hz="300">
208             <Calibration key="L1.CAL"/>
209           </AverageDensity>
210           <FindPeak name="040000_TS_JJY"
211                     fMin_Hz="39.800e3"
212                     fMax_Hz="40.200e3"
213                     fRef_Hz="40.000e3"
214                     minRatio="1">
215             <Filter type="LowPass" timeConstant_sec="10.0"/>
```

```
216             <Calibration key="L1.CAL"/>
217           </FindPeak>
218           <FindPeak name="060000_TS_WWVB"
219                     fMin_Hz="59.800e3"
220                     fMax_Hz="60.200e3"
221                     fRef_Hz="60.000e3"
222                     minRatio="1">
223             <Filter type="LowPass" timeConstant_sec="10.0"/>
224             <Calibration key="L1.CAL"/>
225           </FindPeak>
226           <FindPeak name="068500_TS_BPC"
227                     fMin_Hz="68.300e3"
228                     fMax_Hz="68.700e3"
229                     fRef_Hz="68.500e3"
230                     minRatio="1">
231             <Filter type="LowPass" timeConstant_sec="10.0"/>
232             <Calibration key="L1.CAL"/>
233           </FindPeak>
234         </L2>
235       </Actions>
236     </FFT_Processor>
237   </Clients>
238 </MultiClient>
```

References

Monographic publications

M. Aschwanden. *Physics of the Solar Corona: An Introduction.* Springer, 2004.

J. E. Bickel, J. A. Ferguson, and G. V. Stanley. Experimental observations of magnetic field effects on VLF propagation at night. *Radio Science*, 1970.

V. Bothmer and I. A. Daglis. *Space Weather: Physics and Effects.* Springer, 2007.

K. G. Budden. *The propagation of radio waves - The theory of radio waves of low power in the ionosphere and magnetosphere.* Cambridge University Press, 1999.

J. J. Carr and G. W. Hippisley. *Practical Antenna Handbook, Fifth Edition.* McGraw-Hill, 2012 reprint edition, 1989.

K. Davies. *Ionospheric Radio.* The Institution of Engineering and Technology, 2008 reprint edition, 1990.

M. Dolukhanov. *Propagation of Radio Waves.* Mir Publishers, 1971.

A. Hanslmeier. *The Sun and Space Weather.* Springer, 2002.

J. K. Hargreaves. *The Upper Atmosphere and Solar Terrestrial Relations: An Introduction to the Aerospace Environment.* Van Nostrand Reinhold Company, 1979.

J. K. Hargreaves. *The Solar-Terrestrial Environment.* Cambridge University Press, 1992.

R.D. Hunsucker and J.K. Hargreaves. *The High-Latitude Ionosphere and its Effects on Radio Propagation.* Cambridge University Press, 2003.

M.-B. Kallenrode. *Space Physics: An Introduction to Plasmas and Particles in the Heliosphere and magnetospheres.* Springer, 2004.

M. C. Kelley. *The Earth's Ionosphere: Plasma Physics and Electrodynamics.* Academic Press, Inc., Harcourt Brace Jovanovich, 1989.

G. Klawitter and K. Herold. *Lang- und Längstwellenfunk.* Siebel Verlag, 1995.

H. E. J. Koskinen. *Physics of Space Storms: From the Solar Surface to the Earth.* Springer, 2011.

K. R. Lang. *The Sun from Space.* Springer-Verlag, 2009.

M. Moldwin. *An introduction into space weather.* Cambridge University Press, 2010.

G. Prölss. *Physik des erdnahen Weltraums: Eine Einführung.* Springer, 2003.

J. A. Ratcliffe. *An introduction to the ionosphere and magnetosphere.* Cambridge University Press, 1972.

H. Rishbeth and O. K. Garriott. *Introduction to ionospheric physics.* Academic Press, 1969.

K. Scherer, H. Fichtner, and B. Heber. *Space Weather: The Physics Behind a Slogan.* Springer, 2005. doi: 10.1007/b1000037.

R. W. Schunk and A. Nagy. *Ionospheres: Physics, Plasma Physics, and Chemistry.* Cambridge University Press, 2004.

M. Stix. *The Sun.* Springer, 2004.

H. Volland. *Die Ausbreitung langer Wellen.* Friedr. Vieweg & Sohn GmbH, Verlag, Braunschweig, 1968.

T. Wescott. A DGPS / Radiobeacon Receiver for Minimum Shift Keying with Soft Decision Capabilities. Master's thesis, Worcester Polytechnic Institute (supervisor Per Enge), 1990. URL http://www.wescottdesign.com/articles/MSK/mskTop.html.

Scientific articles

E.L. Afraimovich, A.T. Altynsev, V.V. Grechnev, and L.A. Leonovich. Ionospheric effects of the solar flares as deduced from global GPS network data. *Advances in Space Research*, 27(6 - 7):1333 – 1338, 2001. ISSN 0273-1177. doi: 10.1016/S0273-1177(01)00172-7. printed.

T. Basak and S. K. Chakrabarti. Effective recombination coefficient and solar zenith angle effects on low-latitude D-region ionosphere evaluated from VLF signal amplitude and its time delay during X-ray solar fares. *Astrophys Space Sci*, 348:315–326, 2013.

T. Basak, S. Pal, and S.K. Chakrabarti. VLF study of Ionospheric properties during solar flares of varied intensity for a fixed propagation path. In *General Assembly and Scientific Symposium, 2011 XXXth URSI*, pages 1–4, 2011. doi: 10.1109/URSIGASS.2011.6051004.

C. Baumann, M. Rapp, A. Kero, and C.-F. Enell. Meteor smoke influences on the D-region charge balance - review of recent in situ measurements and one-dimensional model results. *Annales Geophysicae*, 31:2049–2062, 2013. doi: 10.5194/angeo-31-2049-2013.

A. Borgazzi, A. Lara, G. Paz, and J.P. Raulin. The ionosphere and the Latin America {VLF} Network Mexico (LAVNet-Mex) station. *Advances in Space Research*, 54(3):536 – 545, 2014. ISSN 0273-1177. doi: http://dx.doi.org/10.1016/j.asr.2014.03.011. Recent Advances in Equatorial, Low- and Mid-Latitude Mesosphere, Thermosphere-Ionosphere System Studies.

M. Borgerding. Turning overlap-save into a multiband mixing, downsampling filter bank. *IEEE Signal Processing Magazine*, 23(2):158 – 161, 2006.

S Chapman. The absorption and dissociative or ionizing effect of monochromatic radiation in an atmosphere on a rotating earth. *Proceedings of the Physical Society*, 43(1):26, 1931a.

S. Chapman. The absorption and dissociative or ionizing effect of monochromatic radiation in an atmosphere on a rotating earth part II. Grazing incidence. *Proceedings of the Physical Society*, 43(5):483, 1931b.

M. A. Clilverd, C. J. Rodger, N. R. Thomson, J. Lichtenberger, P. Steinbach, P. Cannon, and M. J. Angling. Total solar eclipse effects on VLF signals: Observations and modeling. *Radio Science*, 36(4):773–788, July / August 2001.

Mark A. Clilverd, Neil R. Thomson, and Craig J. Rodger. Sunrise effects on VLF signals propagating over a long north-south path. *Radio Science*, 34(4):939–948, July-August 1999.

Mark A. Clilverd, Craig J. Rodger, Neil R. Thomson, James B. Brundell, Thomas Ulich, János Lichtenberger, Neil Cobbett, Andrew B. Collier, Frederick W. Menk, Annika Seppa, Pekka T. Verronen, and Esa Turunen. Remote sensing space weather events: Antarctic-Arctic Radiation-belt (Dynamic) Deposition-VLF Atmospheric Research Konsortium network. *SPACE WEATHER*, 7(S04001), 2009. doi: 10.1029/2008SW000412.

E. A. Cohen. The study of the effect of solar eclipses on the ionosphere based on satellite beacon observations. *Radio Science*, 19(3):769–777, 1984. ISSN 1944-799X. doi: 10.1029/RS019i003p00769.

P. Kaufmann J.-P. Raulin F. Bertoni Correia, E. and H. R. Gavilan. Analysis of daytime ionosphere behavior between 2004 and 2008 in antarctica. *J. Atmos. Solar-Terr. Phys.*, 73: 2272 – 2278, 2011.

J. A. Ferguson. Computer Programs for Assessment of Long-Wavelength Radio Communications. *Space and Naval Warfare Systems Center, San Diego, CA*, 1998. Technical Document 3030, Version 2.0.

R. Fleury and P. Lassudrie-Duchesne. VLF-LF propagation measurements during the 11 August 1999 solar eclipse. In *IEE Eighth International Conference on HF Radio Systems and Techniques*, pages 391–395, July 2000. Guildford, United Kingdom.

A. García-Rigo, M. Hernández-Pajares, J.M. Juan, and J. Sanz. Solar flare detection system based on global positioning system data: First results. *Advances in Space Research*, 39(5):889 – 895, 2007. ISSN 0273-1177. doi: 10.1016/j.asr.2006.09.031.

M. N. Gnevyshev. The Corona and the 11-Year Cycle of Solar Activity. *Soviet Astronomy*, 7: 311, 1963.

G. Goertzel. An Algorithm for the Evaluation of Finite Trigonometric Series. *American Mathematical Monthly*, 65(1):34–35, 1958. doi: 10.2307/2310304.

M. Hernández-Pajares, A. García-Rigo, J. M. Juan, J. Sanz, E. Monte, and A. Aragón-Àngel. GNSS measurement of EUV photons flux rate during strong and mid solar flares. *Space Weather*, 10(12), 2012.

M. Hoque, D. Wenzel, N. Jakowski, T. Gerzen, J. Berdermann, V. Wilken, M. Kriegel, H. Sato, C. Borries, and D. Minkwitz. Ionospheric Response over Europe during the Solar Eclipse of 20 March 2015. *Space Weather and Space Climate*, 6(A36), 2016. doi: https://doi.org/10.1051/swsc/2016032.

C. Jacobi and D. Kürschner. Ergebnisse ionosphärischer Messungen am Observatorium Collm während der totalen Sonnenfinsternis vom 11. 8. 1999. *Wissenschaftliche Mitteilungen aus dem Institut für Meteorologie der Universität Leipzig und dem Institut für Troposphärenforschung e. V. Leipzig*, pages 88–94, 2000. Band 17.

N. Jakowski and B. Lazo. Die Auswirkungen von Solar Flares auf die Messung der Gesamtelektronenzahl am Beispiel von ATS-6-Beobachtungen. *Phys. Solariterr.*, 5:51–58, 1977.

N. Jakowski, E. Sardon, E. Engler, A. Jungstand, and D. Klähn. Relationships between GPS-signal propagation errors and EISCAT observations. *Annales Geophysicae*, 14(12):1429–1436, 1996. European Geosciences Union.

N. Jakowski, S. Schlüter, and S. Heise. Satellite Technology Glimpses Ionospheric Response to Solar Eclipse. *Eos*, 80(51), 1999.

N. Jakowski, S. Heise, A. Wehrenpfennig, and S. Schlueter. Total electron content studies of the solar eclipse on 11 August 1999. *Proc. IBSS*, pages 279–283, June 2001. CD-ROM, Boston.

N. Jakowski, S. M. Stankov, V. Wilken, B. Borries, D. Altadill, J. Chum, D. Buresova, J. Boska, P. Sauli, F. Hruska, and L. R. Cander. Ionospheric behavior over Europe during the solar eclipse of 3 October 2005. *Journal of Atmospheric and Solar-Terrestrial Physics*, 70:836 – 853, 2008.

N. Jakowski, C. Mayer, M. Hoque, and V. Wilken. Total electron content models and their use in ionosphere monitoring. *Radio Science*, 46, 2011.

P. Kaufmann, L. R. Piazza, J. H. Fernandez, and M. Rocha da Silva. Solar flares not producing sudden phase advances. *Journal of Geophysical Research: Space Physics*, 107(A8):SIA 30–1–SIA 30–4, 2002. ISSN 2156-2202. doi: 10.1029/2001JA000292.

G. Kopp and J. L. Lean. A new, lower value of total solar irradiance: Evidence and climate significance. *Geophysical Research Letters*, 38(L01706), 2011. doi: 10.1029/2010GL045777.

A. Krankowski, I. I. Shagimuratov, L. W. Baran, and G. A. Yakimova. The effect of total solar eclipse of October 3, 2005, on the total electron content over Europe. *Advances in Space Research*, 41(4):628 – 638, 2008.

H. Le, L. Liu, X. Yue, W. Wan, and B. Ning. Latitudinal dependence of the ionospheric response to solar eclipses. *Journal of Geophysical Research: Space Physics*, 114(A7):n/a–n/a, 2009. ISSN 2156-2202. doi: 10.1029/2009JA014072. A07308.

J.Y. Liu, C.C. Hsiao, L.C. Tsai, C.H. Liu, F.S. Kuo, H.Y. Lue, and C.M. Huang. Vertical Phase and Group velocities of internal gravity waves derived from ionograms during the solar eclipse of 24 October 1995. *Journal of Atmospheric and Solar-Terrestrial Physics*, 60:1679 – 1686, 1998.

M. A. Lombardi and G. K. Nelson. WWVB: A Half Century of Delivering Accurate Frequency and Time by Radio. *Journal of research of the National Institute of Standards and Technology*, 119, 2014.

W. M. McRae and N. R. Thomson. Solar flare induced ionospheric D-region enhancements from {VLF} phase and amplitude observations. *Journal of Atmospheric and Solar-Terrestrial Physics*, 66(1):77 – 87, 2004. ISSN 1364-6826. doi: 10.1016/j.jastp.2003.09.009.

E. Monte-Moreno and M. Hernández-Pajares. Occurrence of solar flares viewed with GPS: Statistics and fractal nature. *Journal of Geophysical Research: Space Physics*, 119(11):9216–9227, 2014.

I.C.F. Mueller-Wodarg, A.D. Aylward, and M. Lockwood. Effects of a Mid-Latitude Solar Eclipse on the Thermosphere and Ionosphere - A Modelling Study. *Geophysical Research Letter*, 25 (20):3787 – 3790, 1998.

W. M. Neupert. Comparison of Solar X-Ray Line Emission with Microwave Emission during Flares. *Astrophysical Journal*, 153, 1968. doi: 10.1086/180220.

M. Nicolet and A. C. Aikin. The formation of the D region of the ionosphere. *Journal of Geophysical Research*, 65(5):1469–1483, 1960. ISSN 2156-2202. doi: 10.1029/JZ065i005p01469.

M. Ohshio. Negative Sudden Phase Anomaly. *Nature Physical Science*, 229:239 – 240, 1971.

S. Pal, S. K. Chakrabarti, and S. K. Mondal. Modeling of sub-ionospheric VLF signal perturbations associated with total solar eclipse, 2009 in India subcontinent. *Advances in Space Research*, 50:196 – 204, 2012.

S. Palit, T. Basak, S.K. Mondal, S. Pal, and S.K. Chakrabarti. Modeling of very low frequency (VLF) radio wave signal profile due to solar flares using the GEANT4 Monte Carlo simulation coupled with ionospheric chemistry. *Atmos. Chem. Phys.*, 13:9159–9168, 2013.

S. Palit, T. Basak, S. Pal, and S.K. Chakrabarti. Theoretical study of lower ionospheric response to solar flares: sluggishness of D-region and Peak time delay. *Astrophys. Space Sci.*, 2015.

D. V. Pancheva and P. Y. Mukhtarov. Modelling of the electron density height profiles in the mid-latitude ionospheric D-region. *Annali di Geofisica*, 39(4):819–824, 1996.

C.-S.-M. Pouillet. Mémoire sur la chaleur solaire: sur les pouvoirs rayonnants et absorbants de l'air atmosphérique. *bachelier, imprimeur-libraire pour les sciences*, 1838.

Z.A.A. Rashid, M.A. Momani, S. Sulaiman, M.A.M Ali, B. Yatim, G. Fraser, and N. Sato. GPS ionospheric TEC measurement during the 23rd November 2003 total solar eclipse at Scott Base Antarctica. *Journal of Atmospheric and Solar-Terrestrial Physics*, 68:1219 – 1236, 2006.

J.-P. Raulin, P. Correia de Matos David, R. Hadano, A. C. V. Saraiva, E. Correia, and P. Kaufmann. The South America VLF NETwork (SAVNET). *Earth Moon Planet*, 104:247 – 261, 2009. doi: 10.1007/s11038-008-9269-4.

J.-P. Raulin, F. C. P. Bertoni, H. R. Gavilan, W. Guevara-Day, R. Rodriguez, G. Fernandez, E. Correia, P. Kaufmann, A. Pacini, T. R. C. Stekel, W. L. C. Lima, N. J. Schuch, P. R. Fagundes, and R. Hadano. Solar flare detection sensitivity using the South America VLF Network (SAVNET). *Journal of Geophysical Research: Space Physics*, 115(A7):n/a–n/a, 2010. ISSN 2156-2202. doi: 10.1029/2009JA015154.

J.-P. Raulin, G. Trottet, M. Kretzschmar, E.L. Macotela, A. Pacini, F.C.P. Bertoni, and I.E. Dammasch. Response of the low ionosphere to X-ray and Lyman-α solar flare emissions. *J. Geophys. Res. Space Phys.*, 118:570 – 575, 2013.

Rawer and Suchy. Remarks concerning the dispersion equation of electromagnetic waves in a magnetized cold plasma. *J. Atmos. Terr. Phys.*, 38:395, 1976.

H. Rishbeth. Solar Eclipses and Ionospheric Theory. *Space Science Reviews*, 8(4):543–554, 1968.

E. D. Schmitter. Modeling solar flare induced lower ionosphere changes using VLF/LF transmitter amplitude and phase observations at a midlatitude site. *Annales Geophysicae*, 31(4): 765–773, 2013. doi: 10.5194/angeo-31-765-2013.

T. Singh, M. Hernandez-Pajares, E. Monte, A. Garcia-Rigo, and G Olivares-Pulido. GPS as a solar observational instrument: Real-time estimation of EUV photons flux rate during strong, medium, and weak solar flares. *Journal of Geophysical Research: Space Physics*, 120(12), 2015.

N.R. Thomson. Experimental daytime VLF ionospheric parameters. *Journal of Atmospheric and Terrestrial Physics*, 55(2):173 – 184, 1993. ISSN 0021-9169. doi: 10.1016/0021-9169(93) 90122-F. printed.

A. Veronig, B. Vrsnak, B.R. Dennis M. Temmer, A. Hanslmeier, and J. Magdalenić. The Neupert effect in solar flares and implications for coronal heating. *Magnetic Coupling of the Solar Atmosphere*, June 2002. Proceedings of the Euroconference and IAU Colloquium 188, Santorini, Greece, ed. H. Sawaya-Lacoste, ESA SP-505.

A. M. Veronig, J. C. Brown, B. R. Dennis, R. A. Schwartz, L. Sui, and A. K. Tolbert. Physics of the Neupert Effect: Estimates of the Effects of Source Energy, Mass Transport, and Geometry Using RHESSI and GOES Data. *The Astrophysical Journal*, 621(1):482, 2005.

D. Wenzel, N. Jakowski, J. Berdermann, C. Mayer, C. Valladares, and B. Heber. Global ionospheric flare detection system (GIFDS). *Journal of Atmospheric and Solar-Terrestrial Physics*, 138–139:233 – 242, 2016. ISSN 1364–6826. doi: http://dx.doi.org/10.1016/j.jastp.2015.12.011.

Presentations and posters

M. M. Hoque, N. Jakowski, and J. Berdermann. Ionospheric effects over Europe during the solar eclipse on 20 March 2015. In *EGU General Assembly 2017, Vol. 19, EGU2017-4540*, 2017.

D. Wenzel, N. Jakowski, and W. Andree. Das Schülerprojekt SOFIE - SOlar Flares detektiert über Ionosphärische Effekte. In *73. Jahrestagung der Deutschen Geophysikalischen Gesellschaft (DGG)*, March 2013. Leipzig, Germany.

Technical documents and reports

R. Bakker. *The pa0rdt-Mini-Whip, an active receiving antenna for 10 KHz to 20 MHz*, a. URL http://dl1dbc.net/SAQ/Mwhip/Article_pa0rdt-Mini-Whip_English.pdf.

R. Bakker. *The pa0rdt-Mini-Whip*, b. URL http://dl1dbc.net/SAQ/Mwhip/pa0rdt-Mini-Whip.pdf.

K.-H. Eckelt, V. Bothmer, and B. Bernert. Project SIMONE (Solar & Ionospheric - MOnitoring NEtwork). *ISWI Newsletter*, 3(66), July 2011.

J. A. Ferguson. Ionospheric profiles for predicting nighttime VLF/LF propagation. *Naval Ocean Systems Center*, 1980. Technical Report NOSC/TR 530.

J. A. Ferguson. A Review of the Ionospheric Model for the Long Wave Prediction Capability. *Naval Command, Control and Ocean Surveillance Center RDT&E Division, San Diego, CA*, 1992. Technical Document 2393.

J. A. Ferguson. Computer Programs for Assessment of Long-Wavelength Radio Communications. *Space and Naval Warfare Systems Center, San Diego, CA*, 1998. Technical Document 3030, Version 2.0.

J. A. Ferguson and F. P. Snyder. Approximate VLF/LF waveguide mode conversion model - Computer application: FASTMC and BUMP. *Naval Ocean Systems Center, San Diego, CA*, 1980. Technical Document 400.

C. Mayer. *LOWAMOS (Long Wave Monitoring System): Monitoring Concept, Algorithm Description, and Software Manual*, 2011. Technical Note.

C. Mayer. *LOWAMOS-II: Algorithm Description and Software Manual*, 2012. Technical Note.

C. Mayer. *LOWAMOS-III: 10MHz to 80MHz Frequency Converter*, 2014a. Hardware Description.

C. Mayer. *LOWAMOS-III: Algorithm Description and Software Manual*, 2014b. Technical Note.

D. G. Morfitt. Effective Electron Density Distributions Describing VLF/LF Propagation Data. *Naval Ocean Systems Center, San Diego, CA*, 1977. Technical Report: Jan 1973 - Jun 1977.

D. G. Morfitt and C. H. Shellman. „MODESRCH " An Improved Computer Program for Obtaining ELF/VLF/LF Mode Constants in an Earth-Ionosphere Waveguide. *Defense Nuclear Agency (DNA), Iterim Report 77T (Oct)*, 1976.

R. R. Morgan. World-wide VLF Effective conductivity map. *Westinghouse Electric Corporation, 8013F-1*, 1968.

J. R. Wait. The Mode Theory of VLF Ionospheric Propagation for Finite Ground Conductivity. *Proceedings of the IRE*, 1957a.

J. R. Wait. The Attenuation vs Frequency Characteristics of VLF Radio Waves. *Proceedings of the IRE*, 1957b.

J. R. Wait. Terrestrial Propagation of Very-Low-Frequency Radio Waves. *Journal of Research of the National Bureau of Standards*, 1959.

J. R. Wait and K. Spies. Characteristics of the Earth-ionosphere waveguide for VLF radio waves. *NBS Technical Note*, 300:–, 1964.

Electronic references

Crustal Dynamics Data Information System (CDDIS) archive, a. URL ftp://cddis.gsfc.nasa.gov/gnss/data/hourly/.

Scripps Orbit and Permanent Array Center (SOPAC) archive, b. URL http://sopac.ucsd.edu/cgi-bin/dbDataByDate.cgi.

Perseus Software, June 2016. URL http://microtelecom.it/perseus/software.html.

EFR - Europäische Funkrundsteuerung, May 2016a. URL http://www.efr.de/.

HFMonitor Software, October 2016b. URL https://github.com/hcab14/HFMonitor.

LASP - Laboratory for Atmospheric and Space Physics, University of Colorado Boulder, December 2016c. URL http://lasp.colorado.edu/.

National Oceanic and Atmospheric Administration (NOAA), November 2016d. URL https://ngdc.noaa.gov/.

PyEphem home page, June 2016e. URL http://rhodesmill.org/pyephem/.

SIDC - Solar Influence Data Analysis Center, September 2016f. URL http://sidc.be/.

SID Space Weather Monitor Program, July 2016g. URL http://sid.stanford.edu/.

Space Weather Application Center - Ionosphere (SWACI), Dezember 2016h. URL http://swaciweb.dlr.de/.

Lightning Maps, November 2016i. URL https://www.lightningmaps.org/.

Ionosphere Monitoring and Prediction Center (IMPC), January 2017a. URL http://impc.dlr.de/.

SWPC - Space Weather Prediction Center, January 2017b. URL http://www.swpc.noaa.gov/.

MWLIST - longwave, mediumwave, tropical bands and shortwave radio database, March 2017c. URL http://www.mwlist.org/.

SID Monitoring Station A118, February 2017d. URL https://sidstation.loudet.org/.

SOFIE-Projekt, February 2017e. URL http://www.projectlab-neustrelitz.de/sofie/de/sofie.php.

Acknowledgement

First and foremost, I would like to thank my brother, who always accompanied me in mathematics right from the beginning of primary school until today. His early gift of teaching and endless patience formed my whole life, and not least, his sophisticated review significantly contributed to the outcome of this work. My parents and family deserve my wholehearted thanks, as well, for their constant love and understanding for the mind absence at visits.

I would like to thank my supervisor, Norbert Jakowski, for offering me this chance as PhD student. His continuous advice and guidance throughout the progress of this thesis were outstanding. He has a high impulse for motivation, helpful suggestions and ideas.

I appreciate the many educational discussions with Professor Bernd Heber during our working group meetings as well as at conferences. His suggestions and his extraterrestrial perspective were inspiring. I am moreover very thankful to Professor Christoph Jacobi for his advices from the atmospheric point of view.

All the software and technical developments shouldn't be underestimated. In this regard, Christoph Mayer, the developer of the main frame work, deserves my thanks. He strongly supports the work in further software developments and updates as well as in the assistance during setups and the operation of one of the GIFDS stations. I would like to thank Lutz Heinrich for his technical support, developments and his amazing enthusiasm for fundamental research.

Furthermore, I highly appreciate the effort and maintenance of all hosting partners for GIFDS stations: Patricia Doherty (from the Institute for Ionospheric Research at the Boston College), Todd Walter (WAAS Lab at the Stanford University) and Lung-Chih Tsai (University of Taiwan) for enabling the setup of GIFDS receiver stations, and all their technical support on site. Without their constructive cooperation and the assistance of the institutes I couldn't have finished the thesis in this manner.

To all colleagues at the Institute of Communications and Navigation, especially our working group of *Ionospheric Effects and Corrections*, thank you for the kind and welcoming atmosphere. I am looking forward to joint efforts on further projects.

Statement of originality

I hereby declare that apart from the guidance of my supervisor the content and design of the present thesis is all my own work. No sources have been used in the preparation of this thesis other than those specified in the thesis itself. The source of all graphics, drawings, maps and images not created by myself is indicated. The thesis has not been submitted to another examining body as part of a doctoral degree, neither wholly nor partially. Some results of the scientific work have been published before by me and collaborative authors in reviewed journals in a different form. These are mentioned in the thesis. The only two direct quotations are clearly marked as such on pages 46 and 82f. The thesis has been prepared subject to the Rules of Good Scientific Practice of the German Research Foundation.

Date

Daniela Banyś